Contents

Chapter 1

Introduction

Abstract

In this introductory chapter, I review the properties of low-mass galaxies, with a special focus on starbursting dwarfs. The following properties are discussed in detail: i) the gas distribution and kinematics, ii) the structural parameters of the stellar component, and iii) the resolved stellar populations and the star-formation histories. Possible scenarios for the formation and evolution of dwarf galaxies are discussed. I also briefly review the main results obtained from the study of H I rotation curves of disk galaxies. Finally, I outline the structure and main goals of this Ph.D. thesis.

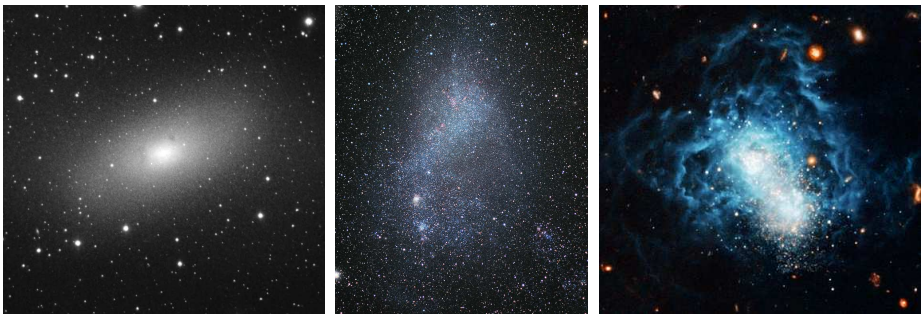

Figure 1.1 – Three different types of dwarf galaxies. *Left*: a prototype dwarf spheroidal (NGC 205). *Middle*: a prototype dwarf irregular (the SMC). *Right*: a prototype blue compact dwarf (I Zw 18).

1.1 A Universe of dwarf galaxies

Low-luminosity, dwarf galaxies are the most common type of galaxies in the nearby Universe (e.g. Ferguson & Binggeli 1994). Understanding their structure, formation, and evolution is a fundamental goal for astronomy and cosmology. Dwarf galaxies are usually defined as stellar systems that have B-band absolute magnitude $M_{\rm B} \gtrsim -17$ ($L_{\rm B} \lesssim 10^9$ L$_\odot$) and are more spatially extended than globular clusters (Tammann 1994). This definition includes several different types of objects, ranging from gas-rich, star-forming galaxies to gas-poor, passively-evolving ones. In the astronomical literature, the taxonomy of dwarf galaxies is vast and, to some extent, confusing (see e.g. Binggeli 1994). Here I will use a minimal nomenclature that distinguishes between 3 types of low-mass galaxies: spheroidals, irregulars, and starbursting dwarfs (or blue compact dwarfs, BCDs).

Spheroidals (Sphs) are gas-poor dwarfs that are *not* forming stars at the present epoch. They are characterized by red colors and smooth optical isophotes, thus resembling a small elliptical galaxy (see Fig. 1.1, left). For this reason, they are sometimes referred to as dwarf ellipticals (dEs) and/or dwarf lenticulars (dS0s) (e.g. Sandage & Binggeli 1984). Following Kormendy et al. (2009), I avoid this nomenclature and indicate any gas-poor dwarf as a Sph. Sphs are typically found in the proximity of massive galaxies (e.g. the satellites of the Milky Way and M31) or in galaxy clusters.

Irregulars (Irrs) are gas-rich dwarfs that are forming stars at a relatively-low rate. They are also referred to as Magellanic irregulars (Im), after the small Magellanic cloud (SMC). The name "irregular" is due to the fact that the star-formation is not organized in spiral arms, as is common for more massive gas-rich galaxies, but is scattered in several "knots" across the galaxy (see Fig. 1.1, middle). Some gas-rich dwarfs, however, can show diffuse and/or broken spiral arms, and be classified (in order of decreasing regularity) as a late-type spiral (Sd) or as a Magellanic spiral (Sm), after the large Magellanic cloud (LMC) (e.g. de Vaucouleurs 1959; Sandage & Binggeli 1984). For the sake of simplicity, I will not distinguish between Sd, Sm, and Im types, but refer to any such gas-rich, low-mass galaxy as an Irr (as in the original morphological classifications of Hubble 1926, 1927 and Lundmark 1926, 1927). Irrs are usually found in the field or in the outskirts of galaxy clusters and galaxy groups.

Starbursting dwarfs (or BCDs) are gas-rich, low-mass galaxies that are forming stars at an unusually high rate. In the literature, they are referred to with different names, often related to the observational technique used to identify the starburst. Common nomenclature includes i) amorphous dwarfs (e.g. Gallagher & Hunter 1987; Marlowe et al. 1999), as they may have peculiar morphologies dominated by a few giant star-forming regions (see Fig. 1.1, right); ii) H II galaxies (e.g. Terlevich et al. 1991; Taylor et al. 1995), as their integrated optical spectra show strong emission-lines similar to those of H II regions in spiral galaxies; and iii) blue compact dwarfs (e.g. Zwicky & Zwicky 1971; Gil

de Paz et al. 2003), since they have blue colors, high surface brightnesses, and low luminosities. I will refer to any starbursting dwarf as a BCD. BCDs are generally found in similar environments as Irrs (the field and/or the outskirts of groups and clusters), but occasionally they can be found close to massive spiral galaxies. A nearby example is the starbursting dwarf IC 10, which is a satellite of M31 and the only known BCD in the Local Group (Gil de Paz et al. 2003).

1.1.1 The Kormendy-Binggeli diagram

Starting from the mid-80's, it has become clear that dwarf galaxies are *structurally* different from other stellar systems, such as globular clusters, elliptical galaxies, and the bulges of disk galaxies (Kormendy 1985; Sandage et al. 1985; Binggeli & Cameron 1991; Bender et al. 1992; Binggeli 1994; Ferguson & Binggeli 1994). This is clearly illustrated by a diagram, firstly made by Kormendy (1985), that plots the absolute visual magnitude $M_{\rm V}$ (proxy for the total stellar mass) versus the central surface brightness $\mu_{\rm V}$ (proxy for the central stellar density) for all these objects. A modern, schematic version of this diagram is shown in Fig. 1.2 (adapted from Tolstoy et al. 2009). Different stellar systems cover different regions of the plot, and follow different trends between $M_{\rm V}$ and $\mu_{\rm V}$:

- elliptical galaxies and the bulges of disk galaxies (red ellipse) lie in the top-left region of the diagram (high stellar masses and high central densities). For these objects, the central surface brightness *decreases* with luminosity (e.g. Kormendy 1985; Kormendy et al. 2009);

- the disks of spirals and lenticulars (blue ellipse) have almost constant central surface brightness $\mu_{\rm V} \simeq 21.5$ mag arcsec^{-2} (Freeman 1970; van der Kruit & Freeman 2011), altough there also exists a population of massive, low-surface-brightness (LSB) disk galaxies with $\mu_{\rm V} \lesssim 23$ mag arcsec^{-2} (not shown in Fig. 1.2; see Bothun et al. 1997; Tully & Verheijen 1997);

- dwarf galaxies form a sequence in the central part of the diagram (blue and yellow symbols), where the central surface brightness *increases* with luminosity. The recently discovered ultra-faint dwarfs (e.g. Willman et al. 2005; Zucker et al. 2006a,b) seem to follow the same relation defined by Sphs, Irrs, and BCDs, thus the "dwarf sequence" may span more than 4 orders of magnitude in both $M_{\rm V}$ and $\mu_{\rm V}$. Note that the canonical separation between dwarfs and "classical" galaxies at $M_{\rm B} = -17$ mag ($M_{\rm V} = -16$ mag, dashed line) also includes low-luminosity ellipticals like M32 (red pentagon), although they are structurally different objects (e.g. Wirth & Gallagher 1984; Kormendy et al. 2009);

- globular clusters (grey dots) define a distinct sequence with respect to dwarf galaxies, where $\mu_{\rm V}$ increases with $M_{\rm V}$ and spans more than 4 orders

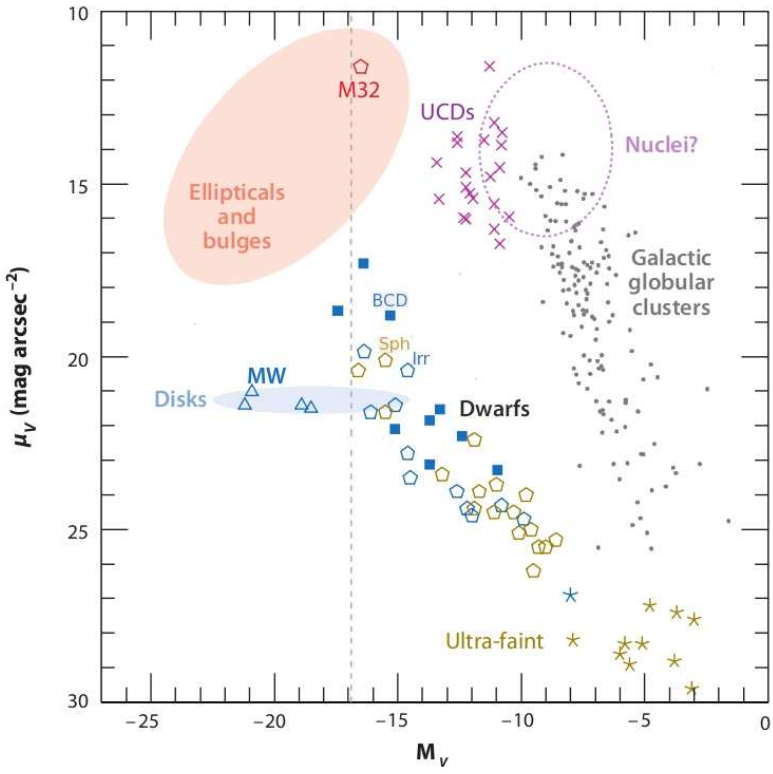

Figure 1.2 – The Kormendy-Binggeli diagram for different stellar systems (adapted from Tolstoy et al. 2009). Dwarf galaxies in the Local Group are shown by open pentagons: blue for gas-rich Irrs, yellow for gas-poor Sphs, and red for the low-luminosity elliptical M32. The recently-discovered ultra-faint dwarfs are indicated by stars. Blue squares, purple crosses, and grey points show starbursting dwarfs (BCDs), ultra-compact dwarfs (UCDs), and globular clusters, respectively. The colored ellipses show the typical location of elliptical galaxies and bulges (light-red), galactic nuclei (dashed purple), and the disks of spirals and lenticulars (light-blue). Starting from the left, the blue open triangles show M31, the Milky Way (MW), M33, and the LMC.

of magnitude. The central nuclei of galaxies (dashed, purple ellipse) may extend this trend to higher surface brightnesses;

- the ultra-compact dwarfs (UCDs), discovered independently by Hilker et al. (1999) and Drinkwater et al. (2000), lie between low-mass ellipticals and high-mass globular clusters. The nature of UCDs is currently under debate: they may simply be the extension of globular clusters to higher masses (e.g. Penny et al. 2012), or be the result of mergers of massive star-clusters (e.g. Fellhauer & Kroupa 2002; Brüns & Kroupa 2012), or be the remnant nuclei of tidally-disrupted dwarfs (e.g. Bekki et al. 2001).

In recent years, the existence of a clear distinction between ellipticals and spheroidals has been strongly debated (e.g. Jerjen & Binggeli 1997; Graham & Guzmán 2003; Gavazzi et al. 2005; Ferrarese et al. 2006). This controversy is not discussed here; I just mention that Kormendy et al. (2009) and Kormendy & Bender (2012) have confirmed the dichotomy between spheroidals and ellipticals using large samples of galaxies.

1.1.2 Evolutionary scenarios

The fact that different stellar systems follow different scaling relations between M_V and μ_V suggests that different physical mechanisms have been driving their formation and evolution (e.g. Kormendy 1985; Dekel & Silk 1986). On the other hand, the fact that Sphs, Irrs, and BCDs approximately lie in the same position of the $M_V - \mu_V$ diagram suggests that evolutionary links between them may exist (e.g. Ferguson & Binggeli 1994; Kormendy & Bender 2012). In this respect, BCDs are particularly interesting because the intense star-formation activity is a short-lived phenomenom, with typical durations of a few 100 Myr (see McQuinn et al. 2010a,b), thus they *must* evolve into a different type of galaxy as the starburst fades. The possibility of morphological transformations between dwarf galaxies is also suggested by the existence of "transition type" dwarfs, a rare class of low-mass galaxies that have intermediate properties between Sphs and Irrs/BCDs (e.g. Sandage & Hoffman 1991; Mateo 1998; Skillman et al. 2003; Dellenbusch et al. 2007, 2008). Several mechanisms (both internal and external) may transform a gas-rich dwarf (Irr or BCD) into a gas-poor Sph:

- the star-formation may consume the entire inter-stellar medium (ISM), if this is not replenished by external, fresh gas. This scenario is quite unlikely because both Irrs and BCDs generally have massive gas reservoirs, and could sustain the current star-formation rates (SFRs) for at least another Hubble time (e.g. Hunter & Elmegreen 2004);

- supernova explosions and stellar winds may blow away the entire ISM from the potential well of the galaxy (e.g. Dekel & Silk 1986). This would require a strong burst of star-formation and efficient stellar feedback (e.g. Mac Low & Ferrara 1999; Ferrara & Tolstoy 2000). In this scenario, any Irr should pass through a BCD-phase in order to evolve into a Sph;

- ram pressure stripping may remove the ISM of a dwarf as it moves through a hot medium, such as the intra-cluster medium (ICM) or the hot coronae that are believed to surround massive galaxies (e.g. Gunn & Gott 1972; Kormendy & Bender 2012; Gatto et al. 2013);

- gravitational interactions with nearby massive companions ("tidal stirring", e.g. Mayer et al. 2006) or with the global potential of a galaxy clusters ("galaxy harassment", e.g. Moore et al. 1998) may strip gas from

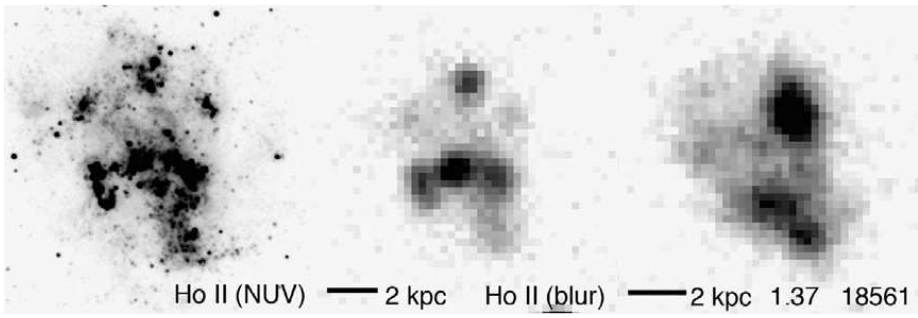

Figure 1.3 – A NUV image of the nearby starbursting dwarf Ho II (*left*), a "blurred" version of the same image (*middle*), and a HST image of the star-forming galaxy COMBO 18561 at $z \simeq 1.4$ (*right*). The blurred image of Ho II and the HST image of COMBO 18561 have the same spatial resolution ($\sim$780 pc) and rest-frame wavelenght ($\sim$2400 Å). COMBO 18561 is $\sim$30 times more massive than Ho II. From Elmegreen et al. (2009).

the outer parts of the galaxy and cause gas inflow towards the center. Depending on the orbits and the initial conditions, Irrs may either evolve directly into Sphs or pass through a BCD-phase.

It is also possible that a Sph may evolve into a BCD if it accretes cold gas from its surroundings, causing a sudden burst of star-formation. In particular, Silk et al. (1987) suggested that Sphs in a galaxy group may expell their ISM through stellar feedback, but this gas remains gravitationally bound to the group potential and, therefore, could fall back onto the galaxies, leading to a cyclic evolution from Sphs to BCDs and vice versa.

1.1.3 The link with the high-redshift Universe

In this section, I point out that nearby, gas-rich dwarfs, especially BCDs, show some striking similarities with more massive star-forming galaxies at high redshifts. In recent years, the development of integral field units, such as SINFONI at the ESO *Very Large Telescope* (VLT), have made it possible to discover a population of star-forming disk galaxies at $z \simeq 1 - 2$ (e.g. Förster Schreiber et al. 2006, 2009), that are thought to be the progenitors of spiral and lenticular galaxies at $z \simeq 0$ (e.g. Bournaud et al. 2007, 2009; Genzel et al. 2008). These star-forming disks have stellar masses in the range 10^{10} to 10^{11} $M_{\odot}$, similar to nearby spirals and lenticulars, but show "clumpy" morphologies, similar to Irrs and BCDs. This is illustrated in Fig. 1.3 (from Elmegreen et al. 2009): the left panel shows a NUV image of Holmberg II (Ho II), a starbursting dwarf at $z \simeq 0$ (e.g. McQuinn et al. 2010b); the middle panel shows how Ho II would look like at $z \simeq 1.4$ if observed with the *Hubble Space Telescope Advance Camera for Surveys* (HST/ACS); and the right panel shows

an actual star-forming galaxy at $z \simeq 1.4$ observed with HST/ACS. Clearly, the two galaxies have very similar morphologies dominated by giant star-forming "clumps", despite the fact that they differ in stellar mass by a factor of ∼30 (see Elmegreen et al. 2009 for details).

The similarity between BCDs and high-redshift, star-forming galaxies is not only morphological. Several physical properties of BCDs are similar to those of high-z galaxies: i) high values of the SFR per unit area $\Sigma_{\rm SFR} = {\rm SFR}/A \simeq 0.1 - 10\,{\rm M}_\odot\,{\rm yr}^{-1}\,{\rm kpc}^{-2}$, where A is the area of the star-forming region (e.g. Kennicutt & Evans 2012), ii) high gas fractions ($M_{\rm gas}/L_{\rm B} \gtrsim 1$; e.g. Salzer et al. 2002), iii) low gas metallicities ($0.2 \lesssim Z/Z_\odot \lesssim 0.02$; e.g. Izotov & Thuan 1999), and iv) relatively-turbulent gaseous disks, where the ratio of the rotation velocity $V_{\rm rot}$ to the velocity dispersion $\sigma_{\rm gas}$ ranges typically from ∼2 to 6 (van Zee et al. 2001; Förster Schreiber et al. 2009). BCDs are, therefore, the best nearby analogs to high-redshift disk galaxies. This has led Elmegreen et al. (2009, 2012) to suggest that similar physical mechanisms may be driving the star-formation activity in both Irrs/BCDs and "clumpy" high-z disks. In particular, they argued that the irregular morphologies of these galaxies are due to gravitational instabilities in a disk that has both a high gas mass compared to the stellar mass and a high turbulent speed compared to the rotational speed. If this analogy is correct, the detailed study of nearby BCDs may shed new light also on the formation and evolution of massive disk galaxies at high redshifts.

1.2 Properties of dwarf galaxies

1.2.1 Gas distribution and kinematics

The *atomic* gas content of nearby galaxies can be investigated using radio observations of the 21-cm line. This is a hyperfine transition of the atomic hydrogen (H I), which traces gas at temperatures $T \simeq 10^2 - 10^4$ K. For massive, metal-rich galaxies, radio and sub-mm observations can be used to study also the *molecular* gas content, by targeting carbon-monoxide (CO) transition lines. This is usually not possible for low-mass galaxies, since they have low metallicities and the CO lines are often undetected (e.g. Taylor et al. 1998). Thus, I focus here on the results from H I observations.

In the past 30 years, the advent of radio interferometers like the *Westerbork Synthesis Radio Telescope* (WRST), the *Very Large Array* (VLA), and the *Giant Metrewave Radio Telescope* (GMRT) have made it possible to investigate the H I distribution and kinematics of nearby galaxies of all morphological types, ranging from disk-dominated spirals (e.g. Bosma 1978; Cayatte et al. 1990; de Blok et al. 1996; Verheijen & Sancisi 2001; Walter et al. 2008), to bulge-dominated spirals (Jore 1997; Noordermeer et al. 2005), to lenticulars and ellipticals (Serra et al. 2012). Several surveys have also been focusing on low-mass, dwarf galaxies. Swaters et al. (2002) studied the H I content

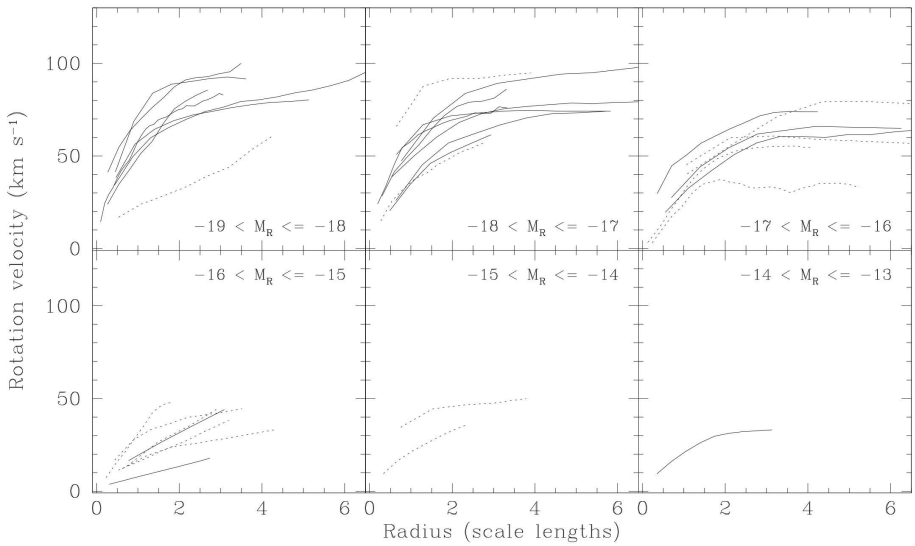

Figure 1.4 – Rotation curves of gas-rich dwarfs (from Swaters et al. 2009), with radii expressed in units of optical scale-lengths. The rotation curves are binned according to the *R*-band absolute magnitude of the galaxy. Full-lines indicate high-quality rotation curves, while dashed-lines indicate rotation curves of lower quality. See Swaters et al. (2009) for details.

of 73 late-type dwarfs, as part of the *Westerbork* H I *Survey of Spiral and Irregular Galaxies* (WHISP). Begum et al. (2008) observed 65 low-mass dwarfs (with $M_{\rm B} \lesssim -13$ mag) as part of the *Faint Irregular Galaxies GMRT Survey* (FIGGS). Cannon et al. (2011) presented the *Survey of* H I *in Extremely Low-mass Dwarfs* (SHIELD), which focuses on dwarf galaxies at the low-mass end of the H I mass function ($M_{\rm H\,I} \simeq 10^6 - 10^7$ M$_\odot$). Hunter et al. (2012) obtained multi-configuration VLA observations of 41 Irrs/BCDs, as part of LITTLE-THINGS (*Local Irregulars That Trace Luminosity Extremes, The* H I *Nearby Galaxy Survey*). Finally, Ott et al. (2012) presented VLA-ANGST (VLA *survey of ACS Nearby Galaxy Survey Treasury*), which provides H I observations of 29 nearby dwarfs that have been resolved into single stars by HST/ACS as part of the ANGST program.

These surveys, together with previous studies, have shown that gas-rich dwarfs generally have "clumpy" H I distributions, characterized by "shells", "holes", and localized overdensities. These structures are thought to be shaped by the star-formation activity, although the detailed connection between the H I distribution and the stellar feedback is still unclear (e.g. Warren et al. 2011). On larger spatial scales (outside the stellar component), about 30% of gas-rich dwarfs show asymmetries in their H I distribution (a so-called "morphological

Table 1.1 – Individual studies of the H I distribution and kinematics of starbursting dwarfs. The stars indicate objects that are in our galaxy sample.

Name	Other names	Reference
NGC 625*	ESO 297-G005	Cannon et al. (2004)
NGC 1569*	VII Zw 16	Stil & Israel (2002); Johnson et al. (2012)
NGC 1705*	ESO 158-G013	Meurer et al. (1998); Elson et al. (2010)
NGC 2366*	DDO 42	Hunter et al. (2001); van Eymeren et al. (2009a)
NGC 2915	ESO 037-G003	Meurer et al. (1996); Elson et al. (2013)
NGC 4670	Haro 9	Hunter et al. (1996)
NGC 4449*	UGC 7592	Hunter et al. (1998, 1999)
NGC 4861	IC 3961	van Eymeren et al. (2009b)
NGC 5253*	Haro 10	Kobulnicky & Skillman (2008); López-Sánchez et al. (2012)
NGC 2537	Mrk 86	Matthews & Uson (2008)
IC 10	UGC 192	Wilcots & Miller (1998)
I Zw 18*	Mrk 116	van Zee et al. (1998c)
I Zw 36*	Mrk 209	Viallefond & Thuan (1983); Ashley et al. (2013)
II Zw 33	Mrk 1094	Walter et al. (1997)
II Zw 40	UGCA 116	Brinks & Klein (1988)
II Zw 70/71	Mrk 829	Cox et al. (2001)
VII Zw 403*	UGC 6456	Simpson et al. (2011)
SBS 0335-052		Pustilnik et al. (2001a); Ekta et al. (2009)
VCC 144	Haro 6	Brosch et al. (1998)
FCC 35		Putman et al. (1998)

lopsidedness", e.g. Swaters et al. 2002), which may indicate recent accretion of cold gas (Sancisi et al. 2008).

The H I kinematics of gas-rich dwarfs is generally regular and characterized by ordered rotation, although mild kinematical asymmetries are common (a so-called "kinematical lopsidedness", e.g. Swaters et al. 2002). Swaters et al. (2009) considered 69 gas-rich dwarfs from the WHISP survey (excluding 4 interacting/merging systems) and could derive rotation curves for 62 of them (∼90%). Figure 1.4 (from Swaters et al. 2009) shows that the rotation curves of Irrs are generally described by a nearly solid-body portion at radii $\lesssim 2-3$ optical scale-lengths, and a flat part in the outer regions, similarly to more massive disk galaxies (e.g. Bosma 1978; Begeman 1987). Swaters et al. (2011) used these rotation curves to investigate the distribution of mass in several Irrs; these results are discussed in Sect. 1.3.

Regarding starbursting dwarfs, many interferometric H I studies have focused on individual objects (see e.g. Table 1.1). Other authors investigated relatively-small samples of BCDs: 5 objects in Taylor et al. (1994), 5 in van Zee et al. (1998a), 8 in Simpson & Gottesman (2000), 6 in van Zee et al. (2001), 7 in Hoffman et al. 2003, 4 in Thuan et al. (2004), 4 in Ramya et al. (2011), and 8 in Most et al. (2013). These studies have shown that BCDs have centrally-concentrated gas distributions, with central H I densities $\sim 2-3$ times higher than in typical Irrs. Regarding the H I kinematics, some BCDs have regularly-rotating gaseous disks (e.g. Meurer et al. 1996, 1998; van Zee et al. 1998b, 2001), whereas others show complex gas kinematics (e.g. Cannon et al. 2004; Kobulnicky & Skillman 2008). To date, high-quality rotation curves and mass models have been derived for only a few BCDs (Walter et al. 1997; Elson et al.

2010; Johnson et al. 2012; Elson et al. 2013). It is unclear what fraction of BCDs have ordered/disturbed H I kinematics, and whether there is a relation between the dynamics and the starburst. In this Ph.D. thesis, I carry out the first systematic study of the H I distribution and kinematics in a relatively large sample of BCDs (18 objects), using both new and archival data.

1.2.2 Structural properties

The structural properties of galaxies can be investigated using surface brightness (SB) profiles, which are usually derived by azimuthally-averaging optical/IR images over a set of concentric ellipses. The SB profiles of Sphs, Irrs, and galaxy disks are generally well-described by an exponential law:

$$I(R) = I_0 \exp(-R/R_\mathrm{d}), \tag{1.1}$$

where R_d is the "disk" scale-length and I_0 is the central SB in $L_\odot$ pc^{-2}. When expressed in magnitudes, this equation becomes a linear relation of the form

$$\mu(R) = \mu_0 + 1.086(R/R_\mathrm{d}), \tag{1.2}$$

where μ_0 is the central SB in mag arcsec^{-2}. Another common fitting-function is the Sérsic profile (Sérsic 1963):

$$I(R) = I_\mathrm{e} \exp\left\{ -b_\mathrm{n}\left[\left(\frac{R}{R_\mathrm{e}}\right)^{1/n} - 1\right]\right\}, \tag{1.3}$$

where R_e is the effective radius (the radius that contains 50% of the total light), I_e is the SB at R_e (in $L_\odot$ pc^{-2}), n is the so-called Sérsic index, and b_n is a parameter that depends on n (see Ciotti 1991 and Ciotti & Bertin 1999 for details). For $n = 1$, the Sérsic profile is equivalent to an exponential with $R_\mathrm{d} = R_\mathrm{e}/1.678$ and $I_0 = \exp(1.678)I_\mathrm{e}$. For $n = 4$, the Sérsic profile reduces to the De Vaucouleurs profile (de Vaucouleurs 1948), which usually describes the SB profiles of ellipticals. If the SB profiles of Irrs and Sphs are fitted with a Sérsic profile, they generally yield values of n between 0.5 and 2 (e.g. Kormendy et al. 2009).

For BCDs the situation is more complicated, as they often show complex SB profiles due to light contamination from the starburst (e.g. Papaderos et al. 1996b; Doublier et al. 1999; Cairós et al. 2001; Gil de Paz & Madore 2005). Two examples (Mkn 178 and VII Zw 403) are illustrated in Fig. 1.5 (from Papaderos et al. 2002). The SB profiles (top panels) are almost exponential in the outer regions, but they show large deviations ($\sim 1-2$ mag) in the inner parts ($R \lesssim 0.6$ kpc) due to the central starburst. The color profiles (bottom panels), indeed, are almost flat in the outer parts at $B - R \simeq 1$ mag, indicative of relatively old stellar populations, but for $R \lesssim 0.6$ kpc they show a sharp transition towards blue colors, indicative of young stellar populations.

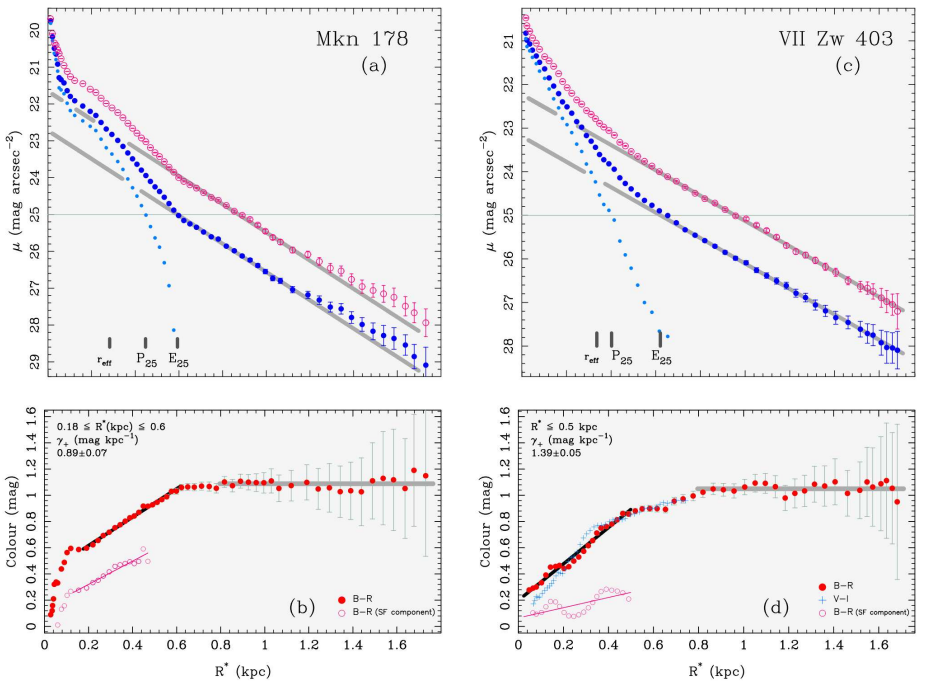

Figure 1.5 – Photometric structure of two BCD prototypes (from Papaderos et al. 2002): Mkn 178 (*left*) and VII Zw 403 (*right*). *Top*: SB profiles in the B-band (blue dots) and in the R-band (purple circles). The grey lines show exponential fits to the outer parts of the SB profiles, while the filled-cyan points are obtained by subtracting the exponential component from the B-band SB profile. The isophotal radii at $\mu_{\rm B} = 25$ mag arcsec^{-2} are indicated for both the exponential component (E_{25}) and the "plateau" component due to the starburst (P_{25}). The effective radii is also indicated. *Bottom:* Color profiles. Red dots and cyan crosses show the $B-R$ and $V-I$ colors, respectively. The purple circles show the $B-R$ color of the starburst component. The steepness of the $B-R$ color profile (γ_+) is given to the top-left. See Papaderos et al. (2002) for details.

To compare the structural properties of BCDs with those of Sphs and Irrs, several authors (e.g. Papaderos et al. 1996b; Marlowe et al. 1999; Gil de Paz & Madore 2005) have fitted exponential and/or Sérsic profiles to the outer parts of the SB profiles of BCDs (see grey lines in Fig. 1.5), which are thought to probe their underlying, old stellar components. The extrapolated values of μ_0, $R_{\rm d}$, and $M_{\rm old}$ (the total magnitude of the old stellar component) have then been used to build $M_{\rm old} - \mu_0$ and $M_{\rm old} - R_{\rm d}$ plots (see Fig. 1.6, adapted from Papaderos et al. 2002). According to these studies, the old stellar component of BCDs generally has higher central SB and smaller scale-length than typical Sphs and Irrs of the same luminosity. This may indicate that the evolution from a BCD to a Irr/Sph is not straightforward, possibly requiring a redistribution of

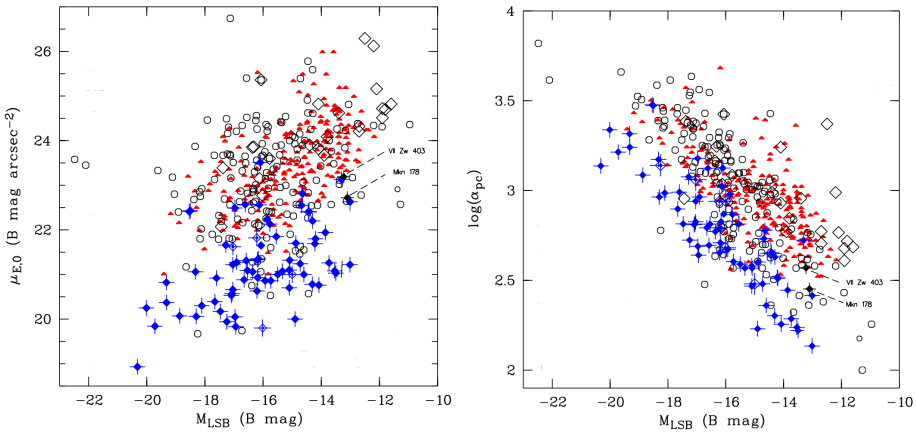

Figure 1.6 – Comparison between the structural properties of the *old* stellar component of BCDs (blue dots) with those of Sphs (red triangles) and Irrs (open circles and open diamonds). In this figure (adapted from Papaderos et al. 2002), the "disk" scale-length $R_{\rm d}$ (in pc) is indicated as $\alpha_{\rm pc}$, while the absolute magnitude of the old stellar component $M_{\rm old}$ is indicated as $M_{\rm LSB}$. The dashed lines show the location of the two BCDs in Fig. 1.5.

the stellar mass (e.g. Papaderos et al. 1996a). Intriguingly, the central SB of the old stellar component of BCDs is, on average, ∼21 B mag arcsec^{-2}, similarly to high-surface-brightness (HSB) disk galaxies (e.g. Freeman 1970; van der Kruit & Freeman 2011). Other authors (Caon et al. 2005; Micheva et al. 2013), however, found that the old stellar components of BCDs have values of μ_0 and $R_{\rm d}$ that are comparable with those of Irrs and Sphs, and argued that evolutionary links between these types of dwarfs are possible. This controversy is likely due to the intrinsic difficulty in obtaining accurate structural parameters for starbursting dwarfs. BCDs often have very irregular morphologies and the young stars may dominate the integrated light over a vast portion of the galaxy. In addition, the values of μ_0 and $R_{\rm d}$ depend on the fitted radial range of the SB profile; the selection of an optimal radial range is not always obvious, and different choices may lead to rather different results.

In this Ph.D. thesis, I tackle this problem using a different approach: I quantify the central mass density of BCDs, Irrs, and Sphs using rotation curves, that directly trace the distribution of the total dynamical mass (including stars, gas, and dark matter). This allows to put solid dynamical constraints on the evolution of dwarf galaxies.

1.2.3 Stellar Populations & Star-Formation Histories

In the past 20 years, the advent of HST has made it possible to resolve nearby galaxies into single stars and to study their stellar content in unprecedented

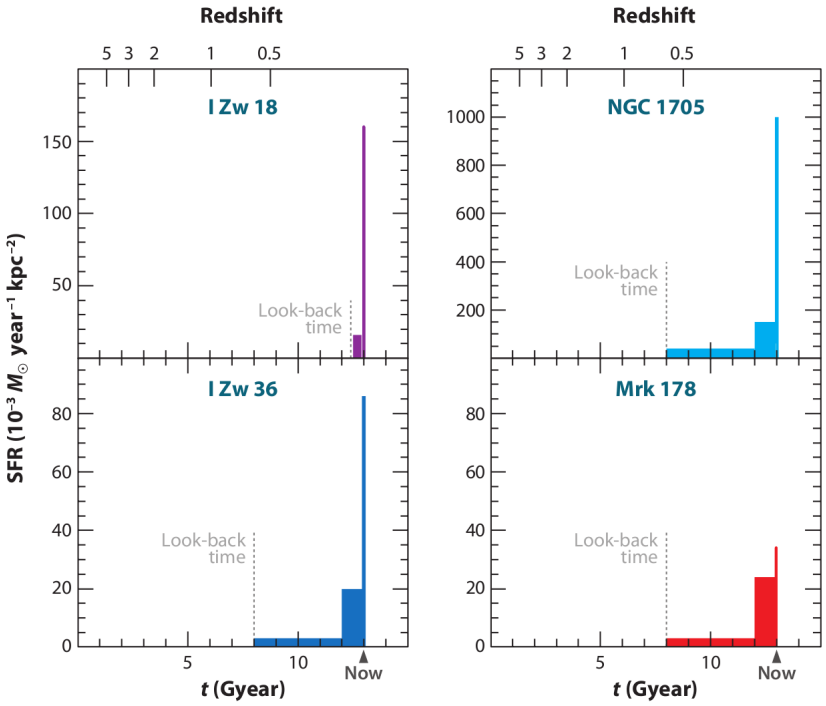

Figure 1.7 – Star-formation histories of 4 BCDs (from Tolstoy et al. 2009). The dashed, grey lines show the look-back time that can be reached by the HST photometry.

detail. Color-magnitude diagrams (CMDs) of the resolved stellar populations have been derived for several galaxies, both inside and outside the Local Group (e.g. Tolstoy et al. 2009; Dalcanton et al. 2009). In addition, the development of the synthetic CMD method (e.g. Tosi et al. 1991; Dolphin 2002) have made it possible to derive detailed star-formation histories (SFHs), i.e. the variation of the galaxy SFR over cosmic time. For details about the synthetic CMD method, I refer to Tolstoy et al. (2009) and Cignoni & Tosi (2010). Briefly, this method creates theoretical CMDs via a Monte-Carlo-based extraction of stars from a given set of evolutionary tracks, taking into account photometric errors, incompleteness, and the effects of stellar crowding. For a given metallicity, initial mass function (IMF), and binary fraction, the method can recover the SFR at different epochs, by comparing the synthetic CMDs with the observed one through a likelihood analysis to find the best-fit solution. In the following, I briefly review the results found for dwarf galaxies, with a special focus on starbursting dwarfs.

The SFHs of dwarf galaxies in the Local Group are generally complex and inconsistent with simple models, such as a single burst, exponentially declining

SFRs, or constant SFRs. They also show a great variety of shapes and SFR values (e.g. Tolstoy et al. 2009). A striking result is that only a few Sphs in the Local Group have experienced a burst of star-formation at early times and then stopped forming stars. Many of them, instead, show extended or recurrent star-formation activity, see e.g. Carina (Hurley-Keller et al. 1998) and Fornax (de Boer et al. 2012). This implies that many Sphs were gas-rich in the recent past and, if observed only ∼1-2 Gyr ago, would have been classified as Irrs or BCDs. Similar results have been found by Weisz et al. (2011), which studied the SFHs of 60 dwarfs *outside* the Local Group and concluded that the mean SFHs of Irrs and Sphs are similar over most of the cosmic time, and begin to diverge only a few Gyr ago.

When one compares the SFHs of different galaxies, a major complication is that the accuracy and the time resolution depend on the photometric depth of the CMDs and, thus, on the galaxy distance. As a result, the SFHs of Sphs and Irrs in the Local Group can be traced back to ∼13 Gyr ago (e.g. Tolstoy et al. 2009), whereas those of BCDs (which are typically at distances $D \gtrsim 2$ Mpc) can be accurately traced only over the last ∼1 Gyr and are quite uncertain at earlier epochs, where one can just obtain an average value of the SFR (see Fig. 1.7, from Tolstoy et al. 2009). Despite this complication, studies of the resolved stellar populations of BCDs have reached the following conclusions:

- all BCDs observed so far contain old stars with ages $\gtrsim$1 Gyr. This is true also for the most metal-poor galaxies, such as I Zw 18 (e.g. Aloisi et al. 2007), which were once considered "young" galaxies undergoing their first burst of star-formation (Searle & Sargent 1972; Izotov & Thuan 2004);

- BCDs show no evidence for long quiescent periods in their SFHs, but have so-called "gaspy" SFHs (Tosi 2004), characterized by long periods of moderate star-formation activity (similar to Irrs) and intense bursts;

- the starbursts correspond to an increase in the SFR by a factor of 2 to 20 with respect to the past, average SFR. This enhanced level of star-formation is sustained for hundreds of Myr with variations on smaller timescales (McQuinn et al. 2010a,b);

- the spatial distribution of the star-formation can vary across the galaxy during the starburst. In some cases, the star-formation remains concentrated towards the center, but in other cases it is strongly off-centered or widespread across the entire galaxy body (McQuinn et al. 2012).

Another important aspect of these CMD studies is that they provide a direct measure of the total stellar mass of a galaxy. This is obtained by integrating the SFH over the Hubble time and assuming that a fraction of this mass (typically 30%) has been returned to the ISM by supernovae and stellar winds.

1.3 Galaxy Dynamics

1.3.1 Basic background

In the early 70's, Ostriker & Peebles (1973) found that stellar disks are unstable against bar-like modes, and speculated that spherical haloes of unseen, dark matter (DM) must surround spiral galaxies in order to stabilize the disk. A few years later, it was found that the H I rotation curves of spiral galaxies remain flat *outside* the stellar component (e.g. Bosma 1978) and do not fall off as expected given the distribution of visible mass (e.g. Casertano 1983), providing observational support to the hypothesis of DM haloes (see Sanders 2010 for a historical review). Nowadays, DM is the backbone of theories of galaxy formation (see Sect. 1.4 for details). I mention, however, that the "mass discrepancies" observed in galaxies can also be explained empirically by alternative models, such as the Modified Newtonian Dynamics (MOND) proposed by Milgrom (1983, see Famaey & McGaugh 2012 for a review).

For gas-rich galaxies, H I rotation curves are the ideal tool to investigate the distribution of mass because i) the H I disk usually is dynamically cold (i.e. random motions give negligible dynamical support), thus its rotation velocity directly traces the gravitational potential, and ii) the H I disk extends far outside the stellar component, probing regions that are clearly dominated by DM (see Fig. 1.8). Other possible dynamical tracers are the ionized gas (observed using inter-stellar recombination lines such as the Hα line) and the molecular gas (observed using transition lines of CO and other species), but they only probe the gravitational potential within the stellar component. For gas-poor galaxies, instead, the mass distribution can be investigated using stellar kinematics, which is studied by fitting the stellar absorption-lines in integrated optical/NIR spectra or, for nearby galaxies in the Local Group, by measuring the radial velocities of individual stars. In the following, I focus on results from H I observations of gas-rich galaxies.

1.3.2 The disk-halo degeneracy

Assuming that a galaxy is axisymmetric and in equilibrium, the radial force $F(R)$ in the galaxy midplane at the galactocentric radius R is given by

$$F(R) = \frac{\partial \Phi}{\partial R} = -\frac{V_{\rm circ}^2}{R}, \tag{1.4}$$

where Φ is the gravitational potential and $V_{\rm circ}$ is the circular velocity. The force $F(R)$ is given by the sum of the gravitational contributions from 3 main mass components: stars, gas, and DM. Thus, $V_{\rm circ}$ can be written as

$$V_{\rm circ} = \sqrt{V_*^2 + V_{\rm gas}^2 + V_{\rm DM}^2}, \tag{1.5}$$

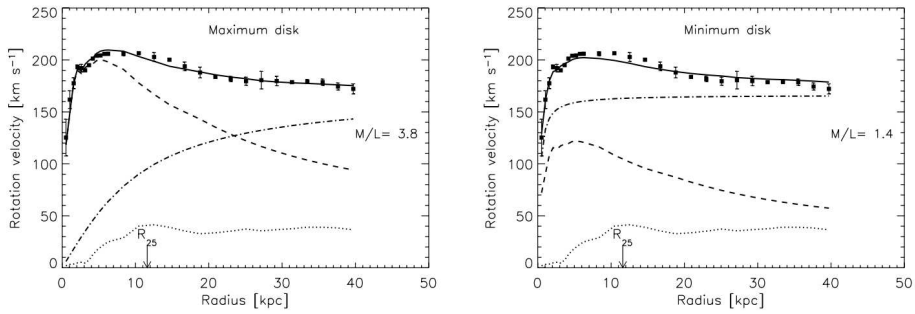

Figure 1.8 – Mass models for the HSB spiral galaxy NGC 5055, that illustrate the disk-halo degeneracy (from Battaglia et al. 2006). Squares show the observed rotation curve. Dotted, dashed, and dash-dotted lines show, respectively, the contributions due to gas, stars, and dark matter. The full line shows the resulting, total rotation curve. The left-panel shows a *maximum-disk* model, while the right-panel shows a *minimum-disk* model, where the contribution of the dark matter halo is maximized. The stellar mass-to-light ratio is in the optical F-band. The optical radius R_{25} (where $\mu = 25$ B mag arcsec^{-2}) is indicated. Note that only the maximum-disk model can reproduce the small feature at $R \simeq 2$ kpc and the gentle decline of the rotation velocity for $R \gtrsim 10$ kpc.

where V_*, $V_{\rm gas}$, and $V_{\rm DM}$ are, respectively, the contributions by the stars, gas, and DM. If the galaxy does not have a significant bulge component, V_* is usually calculated assuming that the stars reside in a disk and using the observed SB profile, scaled by a given value of the stellar mass-to-light ratio (M_*/L). Similarly, $V_{\rm gas}$ is calculated assuming a thin disk and using the observed H I surface density profile, scaled by a factor of 1.33 to take into account the contribution of Helium. For details about the derivation of $V_{\rm circ}$ for a flattened mass distribution, I refer to Binney & Tremaine (1994). Finally, $V_{\rm DM}$ is calculated assuming a given density profile for the DM halo, that generally has 2 free parameters: a scale length and a characteristic density. This component is often assumed to have spherical symmetry, thus the Newton's theorem can be applied.

The stellar mass-to-light ratio generally is an additional free parameter of the mass model, because direct determinations of M_*/L are rarely available. The value of M_*/L is expected to vary from galaxy to galaxy, due to differences in stellar populations, metallicities, and dust attenuation. Attempts have been made to estimate the value of M_*/L from integrated colors by using stellar populations synthesis (SPS) models (e.g. Bell & de Jong 2001), but a large number of assumptions needs to be made about the SFH, the IMF, the metallicity, the dust attenuation, and the binary fraction. As a consequence, the stellar masses from SPS models are very uncertain for galaxies with complex SFHs.

In the mid-80's, van Albada et al. (1985) showed that different combinations of M_*/L and of the DM-halo parameters give equally good fits to the observed rotation curve, leading to large uncertainties in the final mass model. This is the so-called "disk-halo degeneracy" (see Fig. 1.8). The *maximum disk hypothesis* was then introduced (van Albada & Sancisi 1986): the contribution of the stellar disk is maximized, thus the amount of DM is minimized. For HSB disk galaxies (with $\mu_0 \simeq 21.5$ B mag arcsec^{-2}), maximum-disk models can explain the dynamics in the central parts with reasonable values of M_*/L and, in many cases, reproduce detailed features observed in the rotation curve (e.g. Kent 1987; Palunas & Williams 2000; see Fig. 1.8). This suggests that either the baryons dominate the dynamics in the inner parts, or DM closely follows the distribution of light (Sancisi 2004). For low-luminosity and LSB galaxies (with $\mu_0 \gtrsim 23$ B mag arcsec^{-2}), a maximum-disk solution can still reproduce the observed rotation curve in the central parts, but it often requires very high values of M_*/L that are difficult to reconcile with SPS models (e.g. de Blok et al. 2001; Swaters et al. 2011), leading to the interpretation that low-luminosity and LSB galaxies are dominated by DM at all radii. Studies of the stellar kinematics of Sphs in the Local Group (e.g. Tolstoy et al. 2009; Wolf et al. 2010) also support the picture that dwarf galaxies are strongly dominated by DM.

Recently, the DiskMass survey (Bershady et al. 2010) has estimated the values of M_*/L in a sample of 46 face-on spiral galaxies by measuring the stellar velocity dispersion perpendicular to the disk. They found that galaxy disks are generally sub-maximal and contribute only $40\%-70\%$ to the rotational velocity within the stellar disk (Bershady et al. 2011; Martinsson et al. 2013). In Chapter 3 and Chapter 4 of this thesis, I will break the disk-halo degeneracy using a different approach: I will use the values of M_* obtained by HST studies of the resolved stellar populations, under different assumptions for the IMF. In Chapter 7, I will also quantify the coupling between luminous and dynamical mass in the central parts of galaxies by measuring the inner circular-velocity gradient $d_R V(0)$ for a sample of spiral and irregular galaxies with high-quality rotation curves.

1.4 Dwarf galaxies in a ΛCDM cosmology

According to the Λ cold dark matter (ΛCDM) cosmological model, the mass-energy of the Universe is constituted by ∼26% of dark matter, ∼70% of dark energy, and only 4% of ordinary baryonic matter. This model provides remarkable fits to the baryon acoustic power spectrum at $z \simeq 1000$, as derived from observations of the cosmic microwave background (e.g. Komatsu et al. 2009; Planck Collaboration 2013), and of the galaxy power spectrum at $z \simeq 0$, as derived from large galaxy surveys (e.g. Tegmark et al. 2004). The nature of dark matter and dark energy, however, is still not understood. Dark matter is believed to consist of non-relativistic ("cold"), non-baryonic particles, that

interact predominantly through gravity. Indirect evidence for the existence of DM comes from dynamical studies of galaxies and galaxy clusters, as well as gravitational lensing (see Courteau et al. 2013 for a recent review). However, a direct detection of DM candidates by laboratory experiments, as well as an indirect detection by space detectors, is still lacking (e.g. Frenk & White 2012).

In the ΛCDM framework, the formation of large-scale structures, such as filaments and voids, is well-understood by the growth of primordial density perturbations through gravitational forces, mostly due to non-baryonic DM (see Frenk & White 2012 for a review). Galaxies are thought to form by the cooling and collapse of primordial gas into DM haloes, that progressively grow in mass and size by hierarchical merging (e.g. White & Rees 1978; White & Frenk 1991). The details of galaxy formation, however, are not well-understood, because complex baryonic physics (e.g. gas cooling, star-formation, stellar feedback, etc.) plays a major role. In the last years, there has been a substantial increase in the complexity of numerical simulations, which are now able to include several baryonic processes (e.g. Springel & Hernquist 2003; Schaye et al. 2010). Here I briefly discuss two main aspects of galaxy formation in a ΛCDM Universe, that are relevant for our investigation of starbursting dwarfs: i) the hot/cold modes of gas accretion, and ii) the effect of stellar feedback in driving the formation and evolution of dwarf galaxies.

The canonical "hot-mode" of gas accretion (White & Rees 1978; Fall & Efstathiou 1980) dictates that, when primordial gas falls into the DM halo, it is shock-heated to the virial temperature of the potential well $T_{\rm vir} = 10^6 (V_{\rm circ}/168$ km s$^{-1})^2$ K and forms a hot corona of collisionally-ionized gas in quasi-hydrostatic equilibrium with the DM. Subsequently, the gas radiates its thermal energy, loses its pressure support, settles into a rotationally-supported disk, and forms stars (e.g. White & Frenk 1991; Kauffmann et al. 1993). In recent years, however, several theoretical studies have suggested that cold streams of gas can flow along cosmic filaments and reach the central parts of the DM halo, feeding the star formation without being heated to the virial temperature. This is the so-called "cold-mode" of gas accretion (e.g. Birnboim & Dekel 2003; Kereš et al. 2005). According to cosmological hydrodynamical simulations, the "hot mode" dominates the gas accretion rate in massive galaxies (baryonic masses $M_{\rm bar} \gtrsim 10^{10}$ M$_\odot$), while the "cold mode" dominates in low-mass galaxies and might still take place at $z \simeq 0$ in low-density environments (Kereš et al. 2005). Thus, isolated dwarf galaxies in the nearby Universe are prime locations to search for cold gas accretion and test the predictions of this scenario.

When cosmological simulations are compared with observations, several discrepancies emerge. For dwarf galaxies, the main issues are the following:

- bulgeless disk galaxies, which constitute the vast majority of galaxies with $V_{\rm circ} \lesssim 100$ km s^{-1}, are not easily reproduced by simulations (the so-called "angular momentum problem", see e.g. Thacker & Couchman 2001);

- the central "cusps" of DM haloes, found in N-body simulations (e.g. Navarro et al. 1996), are not observed in actual dwarf galaxies (the so-called "cusp-core problem", see e.g. de Blok et al. 2001; Oh et al. 2011);
- the number density of low-mass galaxies is overpredicted by N-body simulations by at least one order of magnitude (the so-called "missing satellites problem"; see e.g. Kauffmann et al. 1993; Kravtsov 2010).
- the baryonic Tully-Fisher relation (BTFR), a fundamental scaling-relation between the total baryonic mass of a galaxy and its circular-velocity along the flat part of the rotation curve, has an observed slope of $\sim$4 (McGaugh et al. 2000; Verheijen 2001; McGaugh 2005), whereas ΛCDM models with a *constant* baryonic fraction in the disk predict a slope of $\sim$3 (e.g. McGaugh 2012). This suggests that galaxies with lower circular velocities should systematically have lower baryonic fractions within their disks and, thus, be progressively more and more dominated by DM. Despite the exact value of the slope, the fact that HSB and LSB galaxies appear to have different baryonic fractions within their disks but can be found *on the same position* of the BTFR (de Blok & McGaugh 1996; Tully & Verheijen 1997) is another major challenge for the ΛCDM model.

These discrepancies are generally explained by invoking complex physical processes involving baryons, in particular strong feedback from supernovae and stellar winds, that *might* be able to expell large amounts of gas from the low potential wells of dwarf galaxies (e.g. Dekel & Silk 1986). According to recent simulations, strong supernova feedback *might* have the following effects: i) prevent the formation of a bulge by the removal of low-angular-momentum gas (e.g. Governato et al. 2010; Brook et al. 2011); ii) turn a DM "cusp" into a "core" (e.g. Governato et al. 2012); iii) suppress star-formation in low-mass DM haloes, explaining the "missing satellites problem" (e.g. Okamoto et al. 2010; Sawala et al. 2013); and iv) reduce the baryonic fraction in low-mass galaxies, reproducing the BTFR (e.g. Stringer et al. 2012; Vogelsberger et al. 2013). It is unclear, however, whether the strong stellar feedback assumed in these simulations is really taking place in dwarf galaxies. Dynamical studies of nearby starbursting dwarfs are, therefore, very important to constrain the real efficiencies of these baryonic processes.

1.5 This Ph.D. Thesis

1.5.1 Open questions

In this Ph.D. thesis, I investigate the H I distribution and kinematics of starbursting dwarf galaxies. I consider 18 nearby galaxies that satisfy two criteria: i) they have been resolved into single stars by HST and high-quality SFHs are available, and ii) the SFHs show an increase in the recent SFR by a

factor $\gtrsim$3 with respect to the past, average SFR. This allows the identification of a representative sample of nearby starbursting dwarfs (see Chapter 4 for details). A detailed study of these objects allows addressing the following issues.

What triggers the starburst in BCDs?

The mechanisms that trigger the starburst in BCDs are not understood. Tidal interactions and galaxy mergers have been proposed as external triggers (e.g. Bekki 2008), but optical studies of the environment of BCDs have led to contradictory results (e.g. Telles & Maddox 2000; Pustilnik et al. 2001b; Noeske et al. 2001). H I studies of individual BCDs have shown that, in several cases, interactions/mergers between gas-rich dwarfs (e.g. Cox et al. 2001; Ekta et al. 2009) or cold gas accretion from the IGM (e.g. López-Sánchez et al. 2012) might be important, but other BCDs seem relatively unperturbed and isolated (e.g. Elson et al. 2010; Simpson et al. 2011). In this Ph.D. thesis, I carry out a systematic H I study of a relatively-large sample of BCDs, attacking the problem in two ways: i) high-resolution H I data are used to study the internal dynamics and the possible link with the starburst, while ii) low-resolution H I data, that are sensitive to the diffuse emission, are used to investigate the large-scale H I distribution and the possible role of external triggers. In particular, the information provided by the SFHs allows comparing the dynamical timescales with the starburst timescales, and studying the detailed link between H I morphology and starburst activity.

What is the dark matter content of BCDs?

The DM content of BCDs is largely unknown. To date, high-quality rotation curves and mass models have been derived for only a few BCDs, leading to contradictory results. Elson et al. (2010, 2013) studied the H I kinematics of NGC 2915 and NGC 1705, and argued that these two BCDs are dominated by DM at all radii (see also Meurer et al. 1996, 1998). On the contrary, Walter et al. (1997) and Johnson et al. (2012) studied the starbursting dwarfs II Zw 33 and NGC 1569, respectively, and concluded that there is no need for DM to explain their inner kinematics. These discrepancies may be due to the following reasons: i) the H I kinematics of BCDs is often complex and several effects can complicate the data analysis, such as the "clumpy" H I distribution, the relatively-high ratio between H I rotation velocity and velocity dispersion, and possibly non-circular motions; ii) it is generally difficult to estimate the stellar masses of BCDs using optical colors and stellar populations models, since the starburst may increase the total luminosity by $\sim 1-2$ mag. In this Ph.D. thesis, I takle these issues as follows: i) I study the H I kinematics using state-of-the-art 3D disk models, that take into account the effects of the gas distribution, velocity dispersion, and non-circular motions; and ii) I use the stellar masses

provided by the HST studies of the resolved stellar population to break the disk-halo degeneracy.

What are the progenitors and descendants of BCDs?

As discussed in Sect. 1.2.2, it is unclear whether there are evolutionary connections between BCDs and other types of dwarfs. There are indications that the old stellar component of BCDs generally has a higher μ_0 and smaller $R_{\rm d}$ than typical Irrs and Sphs (e.g. Papaderos et al. 1996b; Gil de Paz & Madore 2005), but the light contamination from the starburst complicates the analysis of optical images and SB profiles. Using H I observations, van Zee et al. (2001) suggested that BCDs have a higher central concentration of mass (gas, stars, and DM) than Irrs of similar luminosities, although they did not derive accurate rotation curves. In this Ph.D. thesis, I use high-quality rotation curves to directly quantify the central dynamical mass density in BCDs. The comparison with typical Irrs and rotating Sphs puts strong dynamical constraints on the properties of the progenitors and descendants of BCDs.

1.5.2 Thesis outline

The structure of this Ph.D. thesis is as follows.

In Chapters 2 and 3, I present a detailed study of two BCD prototypes: I Zw 18 and UGC 4483. I describe in detail several 3D disk models, that are used to derive rotation curves and estimate non-circular motions. The rotation curves are then decomposed into luminous and dark matter components, and compared with those of typical Irrs of similar dynamical mass.

In Chapter 4, I describe the full sample of 18 BCDs and present H I datacubes at relatively-high spatial resolutions. These are used to investigate the distribution and kinematics of the high-column-density gas associated with the stellar body of BCDs. For galaxies with relatively-regular H I kinematics, I derive rotation curves and estimate baryonic fractions. In Appendix 4.C, I also present an optical-H I atlas that illustrates the high-resolution H I data.

In Chapter 5, I compare the dynamical properties of BCDs with those of Irrs and rotating Sphs. For these galaxies, the central dynamical mass density (gas, stars, and DM) is estimated using the inner circular-velocity gradient $d_R V(0) \simeq V_{R_{\rm d}}/R_{\rm d}$, where $R_{\rm d}$ is the "disk" scale length. I show that $V_{R_{\rm d}}/R_{\rm d}$ correlates with several properties of dwarf galaxies. In light of these new results, several scenarios for the evolution of dwarf galaxies are discussed.

In Chapter 6, I present H I datacubes at low spatial resolutions, which are used to study the diffuse H I emission on large scales. This provides clues to the mechanism that triggers the starburst in BCDs. I also investigate the nearby environment of the 18 objects in our sample.

In Chapter 7, I extend the investigation of the inner circular-velocity gradient $d_R V(0)$ to more massive galaxies. I show that, for spiral and irregular galaxies,

$d_R V(0)$ strongly correlates with the central surface brightness. This is a scaling relation for disk galaxies.

In Chapter 8, I draw my conclusions and discuss prospects for future research.

References

Aloisi, A., Clementini, G., Tosi, M., et al. 2007, ApJL, 667, L151
Ashley, T., Simpson, C. E., & Elmegreen, B. G. 2013, AJ, 146, 42
Battaglia, G., Fraternali, F., Oosterloo, T., & Sancisi, R. 2006, A&A, 447, 49
Begeman, K. 1987, PhD thesis, University of Groningen, NL
Begum, A., Chengalur, J. N., Karachentsev, I. D., Sharina, M. E., & Kaisin, S. S. 2008, MNRAS, 386, 1667
Bekki, K. 2008, MNRAS, 388, L10
Bekki, K., Couch, W. J., & Drinkwater, M. J. 2001, ApJL, 552, L105
Bell, E. F. & de Jong, R. S. 2001, ApJ, 550, 212
Bender, R., Burstein, D., & Faber, S. M. 1992, ApJ, 399, 462
Bershady, M. A., Martinsson, T. P. K., Verheijen, M. A. W., et al. 2011, ApJL, 739, L47
Bershady, M. A., Verheijen, M. A. W., Swaters, R. A., et al. 2010, ApJ, 716, 198
Binggeli, B. 1994, in European Southern Observatory Conference and Workshop Proceedings, Vol. 49, European Southern Observatory Conference and Workshop Proceedings, ed. G. Meylan & P. Prugniel, 13
Binggeli, B. & Cameron, L. M. 1991, A&A, 252, 27
Binney, J. & Tremaine, S. 1994, Galactic Dynamics, 1st edn. (Princeton, USA: Princeton University Press)
Birnboim, Y. & Dekel, A. 2003, MNRAS, 345, 349
Bosma, A. 1978, PhD thesis, PhD Thesis, Groningen Univ., (1978)
Bothun, G., Impey, C., & McGaugh, S. 1997, PASP, 109, 745
Bournaud, F., Elmegreen, B. G., & Elmegreen, D. M. 2007, ApJ, 670, 237
Bournaud, F., Elmegreen, B. G., & Martig, M. 2009, ApJL, 707, L1
Brinks, E. & Klein, U. 1988, MNRAS, 231, 63P
Brook, C. B., Governato, F., Roškar, R., et al. 2011, MNRAS, 415, 1051
Brosch, N., Almoznino, E., & Hoffman, G. L. 1998, A&A, 331, 873
Brüns, R. C. & Kroupa, P. 2012, A&A, 547, A65
Cairós, L. M., Vílchez, J. M., González Pérez, J. N., Iglesias-Páramo, J., & Caon, N. 2001, ApJS, 133, 321
Cannon, J. M., McClure-Griffiths, N. M., Skillman, E. D., & Côté, S. 2004, ApJ, 607, 274
Cannon, J. M., Most, H. P., Skillman, E. D., et al. 2011, ApJ, 735, 36
Caon, N., Cairós, L. M., Aguerri, J. A. L., & Muñoz-Tuñón, C. 2005, ApJS, 157, 218
Casertano, S. 1983, MNRAS, 203, 735
Cayatte, V., van Gorkom, J. H., Balkowski, C., & Kotanyi, C. 1990, AJ, 100, 604
Cignoni, M. & Tosi, M. 2010, Advances in Astronomy, 2010
Ciotti, L. 1991, A&A, 249, 99
Ciotti, L. & Bertin, G. 1999, A&A, 352, 447

Courteau, S., Cappellari, M., de Jong, R. S., et al. 2013, ArXiv e-prints
Cox, A. L., Sparke, L. S., Watson, A. M., & van Moorsel, G. 2001, AJ, 121, 692
Dalcanton, J. J., Williams, B. F., Seth, A. C., et al. 2009, ApJS, 183, 67
de Blok, W. J. G. & McGaugh, S. S. 1996, ApJL, 469, L89
de Blok, W. J. G., McGaugh, S. S., & Rubin, V. C. 2001, AJ, 122, 2396
de Blok, W. J. G., McGaugh, S. S., & van der Hulst, J. M. 1996, MNRAS, 283, 18
de Boer, T. J. L., Tolstoy, E., Hill, V., et al. 2012, A&A, 544, A73
de Vaucouleurs, G. 1948, Annales d'Astrophysique, 11, 247
de Vaucouleurs, G. 1959, Handbuch der Physik, 53, 275
Dekel, A. & Silk, J. 1986, ApJ, 303, 39
Dellenbusch, K. E., Gallagher, III, J. S., & Knezek, P. M. 2007, ApJL, 655, L29
Dellenbusch, K. E., Gallagher, III, J. S., Knezek, P. M., & Noble, A. G. 2008, AJ, 135, 326
Dolphin, A. E. 2002, MNRAS, 332, 91
Doublier, V., Caulet, A., & Comte, G. 1999, A&AS, 138, 213
Drinkwater, M. J., Jones, J. B., Gregg, M. D., & Phillipps, S. 2000, PASA, 17, 227
Ekta, B., Pustilnik, S. A., & Chengalur, J. N. 2009, MNRAS, 397, 963
Elmegreen, B. G., Zhang, H.-X., & Hunter, D. A. 2012, ApJ, 747, 105
Elmegreen, D. M., Elmegreen, B. G., Marcus, M. T., et al. 2009, ApJ, 701, 306
Elson, E. C., de Blok, W. J. G., & Kraan-Korteweg, R. C. 2010, MNRAS, 404, 2061
Elson, E. C., de Blok, W. J. G., & Kraan-Korteweg, R. C. 2013, MNRAS, 429, 2550
Fall, S. M. & Efstathiou, G. 1980, MNRAS, 193, 189
Famaey, B. & McGaugh, S. S. 2012, Living Reviews in Relativity, 15, 10
Fellhauer, M. & Kroupa, P. 2002, MNRAS, 330, 642
Ferguson, H. C. & Binggeli, B. 1994, A&ARv, 6, 67
Ferrara, A. & Tolstoy, E. 2000, MNRAS, 313, 291
Ferrarese, L., Côté, P., Jordán, A., et al. 2006, ApJS, 164, 334
Förster Schreiber, N. M., Genzel, R., Bouché, N., et al. 2009, ApJ, 706, 1364
Förster Schreiber, N. M., Genzel, R., Lehnert, M. D., et al. 2006, ApJ, 645, 1062
Freeman, K. C. 1970, ApJ, 160, 811
Frenk, C. S. & White, S. D. M. 2012, Annalen der Physik, 524, 507
Gallagher, III, J. S. & Hunter, D. A. 1987, AJ, 94, 43
Gatto, A., Fraternali, F., Read, J. I., et al. 2013, ArXiv e-prints
Gavazzi, G., Donati, A., Cucciati, O., et al. 2005, A&A, 430, 411
Genzel, R., Burkert, A., Bouché, N., et al. 2008, ApJ, 687, 59
Gil de Paz, A. & Madore, B. F. 2005, ApJS, 156, 345
Gil de Paz, A., Madore, B. F., & Pevunova, O. 2003, ApJS, 147, 29
Governato, F., Brook, C., Mayer, L., et al. 2010, Nature, 463, 203

Governato, F., Zolotov, A., Pontzen, A., et al. 2012, MNRAS, 422, 1231
Graham, A. W. & Guzmán, R. 2003, AJ, 125, 2936
Gunn, J. E. & Gott, III, J. R. 1972, ApJ, 176, 1
Hilker, M., Infante, L., Vieira, G., Kissler-Patig, M., & Richtler, T. 1999, A&AS, 134, 75
Hoffman, G. L., Brosch, N., Salpeter, E. E., & Carle, N. J. 2003, AJ, 126, 2774
Hubble, E. 1926, Contributions from the Mount Wilson Observatory / Carnegie Institution of Washington, 324, 1
Hubble, E. P. 1927, The Observatory, 50, 276
Hunter, D. A. & Elmegreen, B. G. 2004, AJ, 128, 2170
Hunter, D. A., Elmegreen, B. G., & van Woerden, H. 2001, ApJ, 556, 773
Hunter, D. A., Ficut-Vicas, D., Ashley, T., et al. 2012, AJ, 144, 134
Hunter, D. A., van Woerden, H., & Gallagher, J. S. 1999, AJ, 118, 2184
Hunter, D. A., van Woerden, H., & Gallagher, III, J. S. 1996, ApJS, 107, 739
Hunter, D. A., Wilcots, E. M., van Woerden, H., Gallagher, J. S., & Kohle, S. 1998, ApJL, 495, L47
Hurley-Keller, D., Mateo, M., & Nemec, J. 1998, AJ, 115, 1840
Izotov, Y. I. & Thuan, T. X. 1999, ApJ, 511, 639
Izotov, Y. I. & Thuan, T. X. 2004, ApJ, 616, 768
Jerjen, H. & Binggeli, B. 1997, in Astronomical Society of the Pacific Conference Series, Vol. 116, The Nature of Elliptical Galaxies; 2nd Stromlo Symposium, ed. M. Arnaboldi, G. S. Da Costa, & P. Saha, 239
Johnson, M., Hunter, D. A., Oh, S.-H., et al. 2012, AJ, 144, 152
Jore, K. P. 1997, PhD thesis, CORNELL UNIVERSITY
Kauffmann, G., White, S. D. M., & Guiderdoni, B. 1993, MNRAS, 264, 201
Kennicutt, R. C. & Evans, N. J. 2012, ARA&A, 50, 531
Kent, S. M. 1987, AJ, 93, 816
Kereš, D., Katz, N., Weinberg, D. H., & Davé, R. 2005, MNRAS, 363, 2
Kobulnicky, H. A. & Skillman, E. D. 2008, AJ, 135, 527
Komatsu, E., Dunkley, J., Nolta, M. R., et al. 2009, ApJS, 180, 330
Kormendy, J. 1985, ApJ, 295, 73
Kormendy, J. & Bender, R. 2012, ApJS, 198, 2
Kormendy, J., Fisher, D. B., Cornell, M. E., & Bender, R. 2009, ApJS, 182, 216
Kravtsov, A. 2010, Advances in Astronomy, 2010
López-Sánchez, Á. R., Koribalski, B. S., van Eymeren, J., et al. 2012, MNRAS, 419, 1051
Lundmark, K. 1926, Arkiv for Matematik, Astronomi och Fysik, 19, B8
Lundmark, K. 1927, Nova Acta Regiae Soc. Sci. Upsaliensis Ser. V, 1
Mac Low, M.-M. & Ferrara, A. 1999, ApJ, 513, 142
Marlowe, A. T., Meurer, G. R., & Heckman, T. M. 1999, ApJ, 522, 183
Martinsson, T. P. K., Verheijen, M. A. W., Westfall, K. B., et al. 2013, A&A, 557, A131
Mateo, M. L. 1998, ARA&A, 36, 435

Matthews, L. D. & Uson, J. M. 2008, AJ, 135, 291
Mayer, L., Mastropietro, C., Wadsley, J., Stadel, J., & Moore, B. 2006, MNRAS, 369, 1021
McGaugh, S. S. 2005, ApJ, 632, 859
McGaugh, S. S. 2012, AJ, 143, 40
McGaugh, S. S., Schombert, J. M., Bothun, G. D., & de Blok, W. J. G. 2000, ApJL, 533, L99
McQuinn, K. B. W., Skillman, E. D., Cannon, J. M., et al. 2010a, ApJ, 721, 297
McQuinn, K. B. W., Skillman, E. D., Cannon, J. M., et al. 2010b, ApJ, 724, 49
McQuinn, K. B. W., Skillman, E. D., Dalcanton, J. J., et al. 2012, ApJ, 759, 77
Meurer, G. R., Carignan, C., Beaulieu, S. F., & Freeman, K. C. 1996, AJ, 111, 1551
Meurer, G. R., Staveley-Smith, L., & Killeen, N. E. B. 1998, MNRAS, 300, 705
Micheva, G., Östlin, G., Bergvall, N., et al. 2013, MNRAS, 431, 102
Milgrom, M. 1983, ApJ, 270, 371
Moore, B., Lake, G., & Katz, N. 1998, ApJ, 495, 139
Most, H. P., Cannon, J. M., Salzer, J. J., et al. 2013, AJ, 145, 150
Navarro, J. F., Frenk, C. S., & White, S. D. M. 1996, ApJ, 462, 563
Noeske, K. G., Iglesias-Páramo, J., Vílchez, J. M., Papaderos, P., & Fricke, K. J. 2001, A&A, 371, 806
Noordermeer, E., van der Hulst, J. M., Sancisi, R., Swaters, R. A., & van Albada, T. S. 2005, A&A, 442, 137
Oh, S.-H., de Blok, W. J. G., Brinks, E., Walter, F., & Kennicutt, Jr., R. C. 2011, AJ, 141, 193
Okamoto, T., Frenk, C. S., Jenkins, A., & Theuns, T. 2010, MNRAS, 406, 208
Ostriker, J. P. & Peebles, P. J. E. 1973, ApJ, 186, 467
Ott, J., Stilp, A. M., Warren, S. R., et al. 2012, AJ, 144, 123
Palunas, P. & Williams, T. B. 2000, AJ, 120, 2884
Papaderos, P., Izotov, Y. I., Thuan, T. X., et al. 2002, A&A, 393, 461
Papaderos, P., Loose, H.-H., Fricke, K. J., & Thuan, T. X. 1996a, A&A, 314, 59
Papaderos, P., Loose, H.-H., Thuan, T. X., & Fricke, K. J. 1996b, A&AS, 120, 207
Penny, S. J., Forbes, D. A., & Conselice, C. J. 2012, MNRAS, 422, 885
Planck Collaboration. 2013, ArXiv e-prints
Pustilnik, S. A., Brinks, E., Thuan, T. X., Lipovetsky, V. A., & Izotov, Y. I. 2001a, AJ, 121, 1413
Pustilnik, S. A., Kniazev, A. Y., Lipovetsky, V. A., & Ugryumov, A. V. 2001b, A&A, 373, 24
Putman, M. E., Bureau, M., Mould, J. R., Staveley-Smith, L., & Freeman, K. C. 1998, AJ, 115, 2345
Ramya, S., Kantharia, N. G., & Prabhu, T. P. 2011, ApJ, 728, 124

Salzer, J. J., Rosenberg, J. L., Weisstein, E. W., Mazzarella, J. M., & Bothun, G. D. 2002, AJ, 124, 191
Sancisi, R. 2004, in IAU Symposium, Vol. 220, Dark Matter in Galaxies, ed. S. Ryder, D. Pisano, M. Walker, & K. Freeman, 233
Sancisi, R., Fraternali, F., Oosterloo, T., & van der Hulst, T. 2008, A&ARv, 15, 189
Sandage, A. & Binggeli, B. 1984, AJ, 89, 919
Sandage, A., Binggeli, B., & Tammann, G. A. 1985, AJ, 90, 1759
Sandage, A. & Hoffman, G. L. 1991, ApJL, 379, L45
Sanders, R. H. 2010, The Dark Matter Problem: A Historical Perspective
Sawala, T., Frenk, C. S., Crain, R. A., et al. 2013, MNRAS, 431, 1366
Schaye, J., Dalla Vecchia, C., Booth, C. M., et al. 2010, MNRAS, 402, 1536
Searle, L. & Sargent, W. L. W. 1972, ApJ, 173, 25
Serra, P., Oosterloo, T., Morganti, R., et al. 2012, MNRAS, 422, 1835
Sérsic, J. L. 1963, Boletin de la Asociacion Argentina de Astronomia La Plata Argentina, 6, 41
Silk, J., Wyse, R. F. G., & Shields, G. A. 1987, ApJL, 322, L59
Simpson, C. E. & Gottesman, S. T. 2000, AJ, 120, 2975
Simpson, C. E., Hunter, D. A., Nordgren, T. E., et al. 2011, AJ, 142, 82
Skillman, E. D., Côté, S., & Miller, B. W. 2003, AJ, 125, 593
Springel, V. & Hernquist, L. 2003, MNRAS, 339, 289
Stil, J. M. & Israel, F. P. 2002, A&A, 392, 473
Stringer, M. J., Bower, R. G., Cole, S., Frenk, C. S., & Theuns, T. 2012, MNRAS, 423, 1596
Swaters, R. A., Sancisi, R., van Albada, T. S., & van der Hulst, J. M. 2009, A&A, 493, 871
Swaters, R. A., Sancisi, R., van Albada, T. S., & van der Hulst, J. M. 2011, ApJ, 729, 118
Swaters, R. A., van Albada, T. S., van der Hulst, J. M., & Sancisi, R. 2002, A&A, 390, 829
Tammann, G. A. 1994, in European Southern Observatory Conference and Workshop Proceedings, Vol. 49, European Southern Observatory Conference and Workshop Proceedings, ed. G. Meylan & P. Prugniel, 3
Taylor, C. L., Brinks, E., Grashuis, R. M., & Skillman, E. D. 1995, ApJS, 99, 427
Taylor, C. L., Brinks, E., Pogge, R. W., & Skillman, E. D. 1994, AJ, 107, 971
Taylor, C. L., Kobulnicky, H. A., & Skillman, E. D. 1998, in Magellanic Clouds and Other Dwarf Galaxies, ed. T. Richtler & J. M. Braun, 205–208
Tegmark, M., Blanton, M. R., Strauss, M. A., et al. 2004, ApJ, 606, 702
Telles, E. & Maddox, S. 2000, MNRAS, 311, 307
Terlevich, R., Melnick, J., Masegosa, J., Moles, M., & Copetti, M. V. F. 1991, A&AS, 91, 285
Thacker, R. J. & Couchman, H. M. P. 2001, ApJL, 555, L17

Thuan, T. X., Hibbard, J. E., & Lévrier, F. 2004, AJ, 128, 617
Tolstoy, E., Hill, V., & Tosi, M. 2009, ARA&A, 47, 371
Tosi, M. 2004, Memorie della Societá Astronomica Italiana, 75, 103
Tosi, M., Greggio, L., Marconi, G., & Focardi, P. 1991, AJ, 102, 951
Tully, R. B. & Verheijen, M. A. W. 1997, ApJ, 484, 145
van Albada, T. S., Bahcall, J. N., Begeman, K., & Sancisi, R. 1985, ApJ, 295, 305
van Albada, T. S. & Sancisi, R. 1986, Royal Society of London Philosophical Transactions Series A, 320, 447
van der Kruit, P. C. & Freeman, K. C. 2011, ARA&A, 49, 301
van Eymeren, J., Marcelin, M., Koribalski, B., et al. 2009a, A&A, 493, 511
van Eymeren, J., Marcelin, M., Koribalski, B. S., et al. 2009b, A&A, 505, 105
van Zee, L., Salzer, J. J., & Skillman, E. D. 2001, AJ, 122, 121
van Zee, L., Skillman, E. D., & Salzer, J. J. 1998a, AJ, 116, 1186
van Zee, L., Skillman, E. D., & Salzer, J. J. 1998b, AJ, 116, 1186
van Zee, L., Westpfahl, D., Haynes, M. P., & Salzer, J. J. 1998c, AJ, 115, 1000
Verheijen, M. A. W. 2001, ApJ, 563, 694
Verheijen, M. A. W. & Sancisi, R. 2001, A&A, 370, 765
Viallefond, F. & Thuan, T. X. 1983, ApJ, 269, 444
Vogelsberger, M., Genel, S., Sijacki, D., et al. 2013, ArXiv e-prints
Walter, F., Brinks, E., de Blok, W. J. G., et al. 2008, AJ, 136, 2563
Walter, F., Brinks, E., Duric, N., & Klein, U. 1997, AJ, 113, 2031
Warren, S. R., Weisz, D. R., Skillman, E. D., et al. 2011, ApJ, 738, 10
Weisz, D. R., Dalcanton, J. J., Williams, B. F., et al. 2011, ApJ, 739, 5
White, S. D. M. & Frenk, C. S. 1991, ApJ, 379, 52
White, S. D. M. & Rees, M. J. 1978, MNRAS, 183, 341
Wilcots, E. M. & Miller, B. W. 1998, AJ, 116, 2363
Willman, B., Blanton, M. R., West, A. A., et al. 2005, AJ, 129, 2692
Wirth, A. & Gallagher, III, J. S. 1984, ApJ, 282, 85
Wolf, J., Martinez, G. D., Bullock, J. S., et al. 2010, MNRAS, 406, 1220
Zucker, D. B., Belokurov, V., Evans, N. W., et al. 2006a, ApJL, 650, L41
Zucker, D. B., Belokurov, V., Evans, N. W., et al. 2006b, ApJL, 643, L103
Zwicky, F. & Zwicky, M. A. 1971, Catalogue of selected compact galaxies and of post-eruptive galaxies

Chapter 2

Dynamics of starbursting dwarf galaxies. I Zw 18

— **Federico Lelli, Marc Verheijen, Filippo Fraternali, and Renzo Sancisi** —

Astronomy & Astrophysics, 2012, 537, A72

Abstract

I Zw 18 is a prototype blue compact dwarf (BCD) galaxy, characterized by a strong starburst and extremely low metallicity ($Z \simeq 0.02\ Z_{\odot}$). It has long been considered a candidate young galaxy in the Local Universe, but recent studies have found that it contains old stars. We analysed archival VLA observations of the 21 cm line and found that the H I associated to the starburst region forms a compact, rapidly-rotating disk. The H I column densities are very high, up to $\sim 50 - 100\ M_{\odot}\ \mathrm{pc}^{-2}$ ($\sim 0.6 - 1.2\ \times 10^{22}$ atoms cm^{-2}). The rotation curve is flat with a steep rise in the inner parts, indicating that there is a strong central concentration of mass. Mass models with a dark matter halo show that baryons may dominate the gravitational potential in the inner regions. A radial inflow/outflow motion of $\sim$15 km s^{-1} is also present. I Zw 18 appears to be structurally different from typical dwarf irregulars in terms of its gas distribution, stellar distribution, and dynamics. It may be considered as a "miniature" high-surface-brightness disk galaxy. These dynamical properties must be tightly related to the starburst. They also shed new light on the question of the descendants of BCDs. There is also extended H I emission towards the outlying stellar complex I Zw 18 C and a $\sim$13.5 kpc H I tail. An interaction/merger between gas-rich dwarfs is the most likely explanation of the starburst.

2.1 Introduction

Blue compact dwarfs (BCDs) are low-mass galaxies that are experiencing a starburst. They are usually characterized by small physical sizes (∼2-3 kpc), low metallicities ($0.2 \lesssim Z/Z_{\odot} \lesssim 0.02$), and relatively large amounts of gas ($M_{\rm HI}/L_{\rm B} \gtrsim 1$). The question has arisen as to whether they are young galaxies undergoing their first burst of star formation (Searle & Sargent 1972), but several studies based on surface brightness and colour profiles (e.g. Gil de Paz & Madore 2005), as well as colour-magnitude diagrams of resolved stellar populations (e.g. Tosi 2009) have demonstrated that BCDs also contain old stars, with ages >2-3 Gyr. The star-formation histories of the nearby BCDs, as derived using colour-magnitude diagrams (e.g. Tosi 2009), show that the starburst is a short-lived phenomenon, typically sustained for a few 100 Myr (e.g. McQuinn et al. 2010). Thus, BCDs are *transition-type dwarfs*, but it is unclear whether there are evolutionary connections with dwarf irregulars (Irrs) and/or spheroidals (Sphs) (e.g. Papaderos et al. 1996; van Zee et al. 2001). In addition, the mechanisms that trigger, sustain, and quench the starburst activity are not understood.

Various studies of the H I distribution and kinematics (e.g. van Zee et al. 1998a, 2001) have highlighted two striking properties of BCDs: i) they have strong concentrations of H I within the starburst region near the galaxy centre; ii) they usually have steep central velocity gradients. Both properties are *not* observed in more quiescent Irrs (e.g. Swaters et al. 2002). This suggests that there is a close connection between the starburst, the compact distribution of baryons (gas and stars), and the H I kinematics. The nature of the steep velocity gradients is unclear and two main interpretations are possible: i) rapid rotation (e.g. van Zee et al. 2001), and ii) gaseous inflows/outflows (e.g. Kobulnicky & Skillman 2008; Cannon et al. 2004). Rapid rotation in the inner regions could imply that there is a strong concentration of mass that may be either luminous or dark. Gaseous inflows/outflows might be linked to fuelling processes and/or feedback mechanisms.

On larger scales, BCDs usually have extended and diffuse H I structures, which may form reservoirs for fueling the starburst. In general, two different kinds of structures are observed: i) extended H I disks in regular rotation, e.g. NGC 2915 (Elson et al. 2010) and NGC 2366 (Oh et al. 2008); ii) complex filamentary structures, e.g. II Zw 40 (van Zee et al. 1998a) and NGC 5253 (Kobulnicky & Skillman 2008). The study of these extended H I structures can provide key information about the triggering mechanism (external or internal processes), the properties of the progenitor galaxies (gas-rich Irrs or gas-poor Sphs), and the possible presence of massive gas inflows/outflows.

We present an H I study of I Zw 18, the BCD prototype (e.g. Zwicky 1966; Searle & Sargent 1972), which is one of the most metal-poor galaxies known (12+log(O/H)≃7.2, Izotov & Thuan 1999) and has long been considered a candidate young galaxy in the Local Universe, formed within the past 0.5 Gyr

Table 2.1 – VLA observing parameters

Project	Array	Observing Dates	ToS	Calibrators
AC0710	A	8, 9, 14, 18, 19, 28 Nov. & 4, 6 Dec. 2004	33.3 h	0834+555, 1331+305, 0542+498
AZ0074	B	26 Oct. & 3, 15 Dec. 1995	15.5 h	0834+555, 1331+305, 0542+498, 0137+331
AP264	C	27 Aug. 1993	6.6 h	0834+555, 1331+305
AP264	D	22 Dec. 1993	2.3 h	0834+555, 1331+305

(e.g. Papaderos et al. 2002; Izotov & Thuan 2004). However, Aloisi et al. (2007), using HST observations, detected stars older than 1-2 Gyr and ruled out the possibility that I Zw 18 is a truly primordial galaxy (as suggested by e.g. Aloisi et al. 1999; Östlin & Mouhcine 2005). The intense star-formation activity started only ∼20 Myr ago (e.g. Aloisi et al. 1999). Two key questions remain open: What triggered the starburst? Why is the metallicity so low?

Previous H I studies (Viallefond et al. 1987; van Zee et al. 1998b) showed that I Zw 18 is characterized by a strong central concentration of H I and a steep velocity gradient, as is typical of BCDs. In addition, the optical galaxy is surrounded by an extended H I envelope that was described by van Zee et al. (1998b) as "a fragmenting H I cloud in the early stages of galaxy evolution".

We analysed archival H I data to i) investigate the relation between the gas distribution and the starburst activity; ii) clarify the nature of the velocity gradient; and iii) study the structure, kinematics, and origin of the extended gas.

2.2 Data reduction & analysis

We analysed public H I data taken from the VLA archive. The observations were carried out between 1993 and 2004, using the VLA in all four configurations (see Table 2.1). Data from the B, C, and D configurations were presented by van Zee et al. (1998b). In this new analysis, we also included data taken in 2004 with the high-resolution A-array configuration. The correlator was used in 2AD mode, with a total bandwidth of 0.8 MHz (∼165 km s^{-1}). An on-line Hanning taper was applied to the data, producing 127 spectral line channels with a width of 6.3 kHz (∼1.3 km s^{-1}).

The raw UV data were interactively flagged, calibrated, and combined using the AIPS package and following standard VLA procedures. The UV data were mapped using a robust weighting technique (Briggs 1995) and various Gaussian baseline tapers to attenuate the longest baselines. We built three datacubes with different spatial resolutions by using different combinations of the robust parameter $\Re$ and the taper FWHM (see Table 2.2). After various trials, we chose the combinations that minimize sidelobes and wings in the beam profiles.

Table 2.2 – H I Datacubes

Resolution	$\Re$	Taper (kλ)	Synth. beam (asec×asec)	P.A. (°)	Smooth. beam (asec×asec)	ΔV (km/s)	Rms noise (mJy/beam)
Low	0	10	14.6×14.4	32.7	20×20	5.2	0.40
Intermediate	0	60	3.3×2.9	89.3	5×5	5.2	0.26
High	-1	150	1.5×1.4	-76.3	2×2	10.4	0.16

After the Fourier transform, the datacubes were analysed using the Groningen Imaging Processing SYstem (GIPSY) (van der Hulst et al. 1992). Continuum maps were constructed by averaging line-free channels. Owing to the narrow bandwidth of the observations, a few line-free channels were available and the resulting continuum-subtracted datacubes displayed correlated noise in the spectral direction. Thus, we constructed a continuum map by using a mask, defining the area of H I emission in every channel and averaging, for each spatial pixel, all the channels without any H I signal. The masks were constructed by smoothing the datacubes both in velocity (by a factor 4) and spatially (by a factor $\sim$3, i.e. at $45''$, $10''$, and $5''$ for the low, intermediate, and high resolution data, respectively) and clipping at $2.5\sigma_s$ (where σ_s is the noise in the smoothed cubes). The masks were inspected channel by channel and any remaining noise peaks were blotted out.

The use of a mask for the continuum subtraction may have the disadvantage that the noise is no longer uniform across the channel maps, as a different number of channels is used at every pixel to build the continuum map. Thus, we built signal-to-noise ratio (S/N) maps for every channel (similarly to Verheijen & Sancisi 2001) and calculated a pseudo-1σ contour by averaging the values for the pixels with $0.75<S/N<1.25$. The resulting pseudo-1σ level is close to that obtained by calculating the noise in a box without signal, suggesting that the noise is still almost uniform.

The channel maps were cleaned (Högbom 1974) down to 0.5σ, using the masks to define the search areas for the clean-components, which were then restored with a Gaussian beam of the same FWHM as the antenna pattern. In order to improve the S/N, the cubes were smoothed in velocity to a resolution of 5.2 km s^{-1} (10.4 km s^{-1} for the high-resolution data) and spatially to $20''$, $5''$, and $2''$ for the low, intermediate, and high resolution data, respectively. Table 2.2 summarizes the properties of the cubes.

Total H I maps were constructed by summing the signal inside the clean-masks. A pseudo-3σ contour was calculated following Verheijen & Sancisi (2001). Velocity fields were derived by fitting a Gaussian function to the H I line profiles. Fitted Gaussians with a peak intensity less than 2.5σ and a FWHM smaller than 5.2 km s^{-1} were discarded; the remaining noise in the velocity fields (i.e. signal outside the pseudo-3σ contour of the total H I maps) was blotted out. The H I line profiles are quite broad and asymmetric, thus the velocity fields must be considered as only a rough indication of the global kinematics.

Our kinematical analysis is based on position-velocity diagrams (Sect. 2.3) and on three-dimensional (3D) models of the observations (Sect. 2.4.1).

2.3 H I distribution and kinematics

We describe the overall H I structure of I Zw 18. We adopt the standard nomenclature introduced by Davidson et al. (1989). The main body is designated as I Zw 18 A (Fig. 2.2, top-right) and is characterized by two starburst regions: one to the north-west (NW) and one to the south-east (SE). The light concentrations denoted by Davidson et al. (1989) as B, D, and E are background galaxies. The stellar complex to the NW is named I Zw 18 C or C-component. We assume a distance of 18.2 Mpc, as derived from the tip of the red giant branch (Aloisi et al. 2007) and confirmed by observations of Cepheids (Fiorentino et al. 2010).

We use data at three different resolutions (see Table 2.2) to probe different spatial scales and H I column densities.

2.3.1 The low-resolution view

The low-resolution data (with FWHM = $20''$ ∼1.8 kpc and 3σ column density sensitivity $N_{\rm H\,I}(3\sigma) \simeq 4 \times 10^{18}$ atoms cm^{-2} per channel) illustrate the large-scale overall structure of I Zw 18.

Figure 2.1 (top) shows the channel maps, superimposed with two isophotes of a B-band image (from Gil de Paz et al. 2003). The central H I emission presents a velocity gradient at a position angle P.A.≃140°-150°. At velocities from ∼750 to ∼720 km s^{-1}, extended emission also appears to the south.

Figure 2.2 (top-left) shows the integrated H I map, superimposed on a V-band HST image (from Aloisi et al. 2007). I Zw 18 A is associated with a strong concentration of gas, while diffuse emission extends beyond the optical galaxy, covering an angular size of ∼$3'.5$ (∼18.5 kpc). The H I gas to the south of I Zw 18 A displays a tail-like morphology that extends over ∼$2'.5$ (∼13.5 kpc).

Figure 2.2 (middle-left) shows the velocity field. The main body (I Zw 18 A) is associated with the central velocity gradient. The southern "tail" does not seem to be kinematically connected to the SE region of I Zw 18 A, as the gas velocity changes abruptly from ∼790 km s^{-1} to ∼720 km s^{-1}. Moreover, at the junction between I Zw 18 A and the "tail", the H I line profiles are double peaked, suggesting that there are two distinct components, which are possibly well-separated in space but projected on the same location on the sky.

Figure 2.2 (bottom-left) shows a position-velocity (PV) diagram, obtained from the $20''$ datacube following the "tail" (the dashed line overlaid on the velocity field). The central velocity gradient (associated with I Zw 18 A) is very steep and there is a spatial broadening towards the NW direction between ∼700 and ∼780 km s^{-1}. The gas to the south forms a coherent kinematical structure

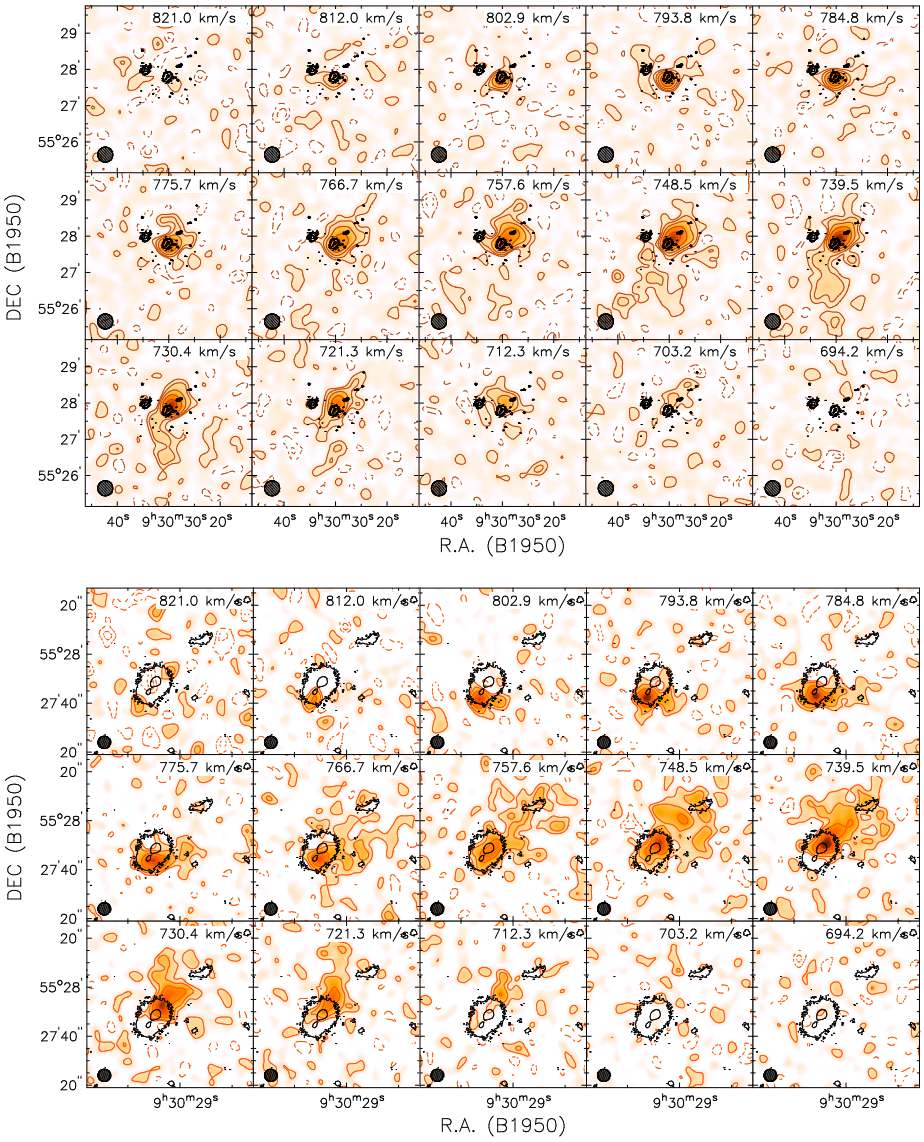

Figure 2.1 – Channel maps at a resolution of 20″ (*top*) and 5″ (*bottom*). Red-solid contours are at 1.5, 3, 6, 12, 24 × σ. Red-dashed contours are at -3, -1.5 × σ. Black contours show two isophotes of a B-band image (from Gil de Paz et al. 2003); the object to the north-east (R.A. = 9h 30m 34s, DEC = 55° 28″) is a foreground star.

at velocities between ∼710 and ∼760 km s^{-1}. Strikingly, the broadened part of the PV-diagram and the "tail" are almost at the same velocities, suggesting

that they may be physically connected. This hypothesis is investigated further in Sect. 2.5.

2.3.2 The intermediate-resolution view

The intermediate-resolution data (FWHM = $5''$ $\simeq$ 440 pc and $N_{\rm H\,I}(3\sigma)$ $\simeq$ 4×10^{19} atoms cm^{-2} per channel) illustrate the H I emission associated with I Zw 18 A and I Zw 18 C, and their possible connections.

Figure 2.1 (bottom) shows the channel maps, superimposed with two isophotes of a B-band image. The H I emission to the NW is spatially resolved but still visible, whereas the southern "tail" is completely resolved out, indicating the diffuse nature of this gas. Between ∼770 and ∼740 km s^{-1}, there are H I clumps near the C-component. Their association with I Zw 18 C is very likely, because the H I clumps are at the same velocities as the Hα emission ($V_{\rm sys,\,H\alpha}$[C] = 751 ± 5 km s^{-1}, Dufour et al. 1996).

Figure 2.2 (top-right) shows the integrated H I map, overlaid on a V-band HST image. The main body is characterized by two H I peaks, roughly corresponding to the NW and SE starburst regions. With respect to I Zw 18 A, the H I is more extended to the north-west, in the direction of I Zw 18 C.

Figure 2.2 (middle-right) shows the velocity field, while Figure 2.2 (bottom-right) shows a PV-diagram obtained by following the dashed line superimposed on the velocity field. The steep velocity gradient is aligned approximately along the two H I peaks. The H I emission to the NW shows a shallow velocity gradient from I Zw 18 A to I Zw 18 C and seems to connect the two stellar bodies. This connection is also visible in Hα at velocities similar to those observed in H I (Dufour & Hester 1990; Dufour et al. 1996). Along I Zw 18 A, the Hα velocity gradient, instead, shows a "wiggly" behaviour that is not observed in H I. This may be caused by an Hα superbubble (see Martin 1996 and Sect. 2.5.2). In addition, there is H I emission to the west of the main body, that shows a velocity gradient and seems to have an Hα counterpart (see Sect. 2.5.2).

2.3.3 The high-resolution view

The high-resolution data (FWHM = $2''$ $\simeq$ 180 pc and $N_{\rm H\,I}(3\sigma)$ $\simeq$ 2×10^{20} atoms cm^{-2} per channel) show in detail the H I emission associated with the NW and SE starburst regions.

Figure 2.3 shows the total H I map in grayscale (left) and in contours overlaid on a Hα image (middle). The two H I peaks are spatially resolved. The H I clump to the SE coincides with a complex of H II regions and has a strong peak, where the H I column density reaches ∼100 M$_\odot$ pc^{-2} (∼ 1.2×10^{22} atoms cm^2). In-between the two clumps, an H I hole is associated with a strong H II region, suggesting that the neutral gas has been consumed, ionized, and/or blown out by young stars. The H I clump to the NW coincides with a Hα shell, which surrounds the bulk of the young stars (see Fig. 1 of Cannon et al. 2002).

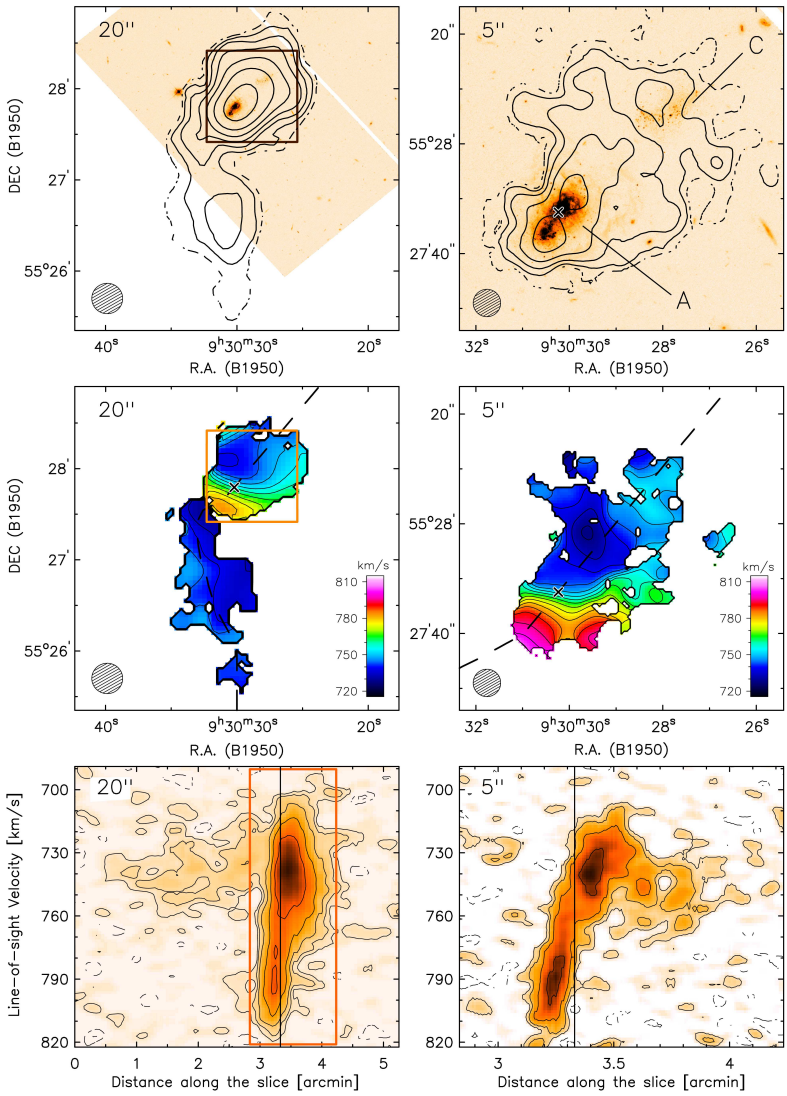

Figure 2.2 – *Top*: integrated H I maps at a resolution of 20″ (*left*) and 5″ (*right*), superimposed on a HST image (from Aloisi et al. 2007). The box in the left panel shows the area covered by the right panel. The dashed line corresponds to the pseudo-1.5σ density contour. In the map at 20″, contours are at 0.25 (dashed), 0.5, 1, 2, 4, 8, 16 $\times$ 10^{20} atoms cm^{-2}. In the map at 5″, contours are at 3 (dashed), 6, 12, 24, 48 $\times$ 10^{20} atoms cm^{-2}. The circle shows the beam size. *Middle*: velocity fields at a resolution of 20″ (*left*) and 5″ (*right*). The box in the left panel shows the area covered by the right panel. Contours range from 722.4 to 805.6 km s^{-1}, with steps of 5.2 km s^{-1}. The circle shows the beam size. The dashed line shows the path followed to obtain the position-velocity diagram. *Bottom*: position-velocity diagrams at a resolution of 20″ (*left*) and 5″ (*right*). Contours are at -1.5 (dashed), 1.5, 3, 6, 12, 24 $\times$ σ. The box in the left panel shows the region covered by the right panel. The vertical line corresponds to the cross in the velocity fields.

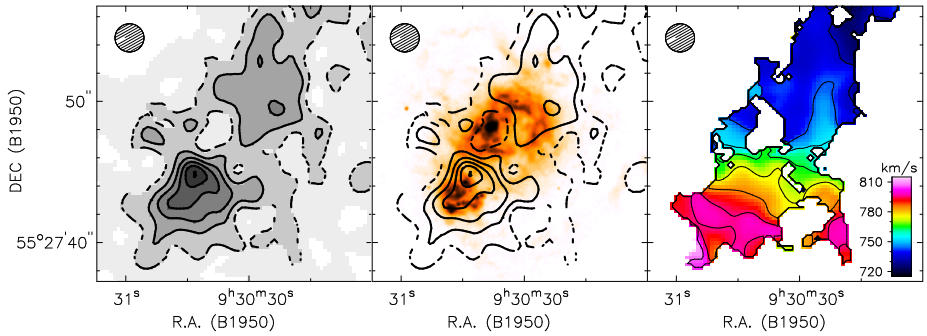

Figure 2.3 – *Left:* integrated H I map at 2″ resolution. Countours are at 3 (dashed), 6, 9, 12, 15×10^{21} atoms cm^{-2}. *Middle:* Hα image (Cannon et al. 2002) overlaid with the integrated H I map at 2″ resolution. *Right:* velocity field at 2″ resolution. Contours range from 722.4 to 805.6 km s^{-1} with steps of 10.4 km s^{-1}. The circle shows the beam size.

This shell is probably connected to the high-velocity Hα emission detected by Dufour et al. (1996) and Martin (1996) at $\pm$200 km s^{-1} with respect to the systemic velocity.

The velocity field at 2″ resolution is shown in Fig. 2.3 (right). This velocity field is very uncertain because of the clumpy H I distribution, the asymmetric line profiles, and the low S/N of the data at this high angular resolution. However, it shows a clear velocity gradient from the SE to the NW region, as already observed at lower spatial resolution. The H I depression is in the approaching NW side of the galaxy.

2.4 Dynamics of I Zw 18 A

In Sect. 2.3, we described the overall structure of I Zw 18. Two important findings need to be explained: i) the steep velocity gradient associated with I Zw 18 A; ii) the extended H I emission to the south and to the north-west of the galaxy. In this section, we focus on the dynamics of I Zw 18 A, while in Sect. 2.5 we study the large-scale gas emission.

2.4.1 Kinematical models

There is some controversy in the literature about the interpretation of the velocity gradient of I Zw 18 A. Viallefond et al. (1987), Petrosian et al. (1997), and van Zee et al. (1998b) analysed velocity fields and interpreted the gradient as rotation, whereas Skillman & Kennicutt (1993) and Dufour et al. (1996) obtained long-slit spectroscopy and argued that the gradient may result from the merger of two (or more) gaseous clouds. The velocity gradient is along the optical major axis of the galaxy (Fig. 2.4) and the velocity field displays a

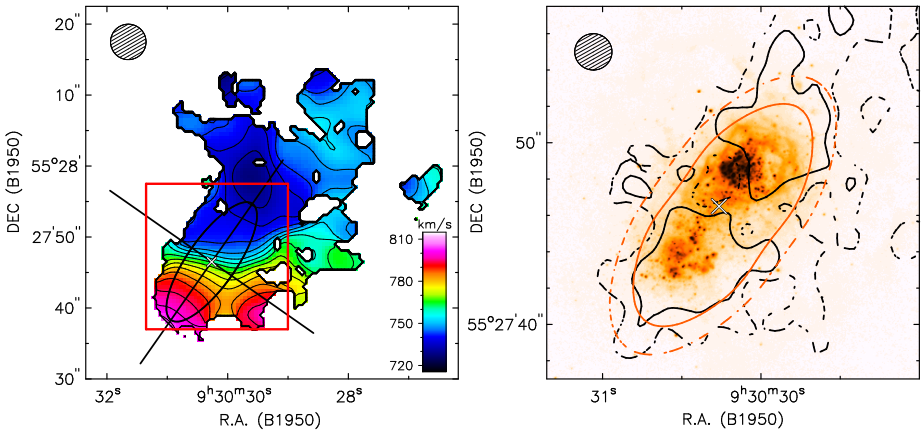

Figure 2.4 – *Left*: velocity field at 5″ resolution. The ellipse shows the modelled disk. The centre, and both the major and the minor axes are shown. The box shows the area covered by the right panel. The circle shows the beam. Countours are the same as in Fig. 2.2. *Right*: HST image superimposed with the observed H I map at 2″ (black) and the H I map obtained from a 3D model with $i = 70°$ and $z_0 = 100$ pc (red). Countours are at 3 (dashed) and 6 (solid) $\times$ 10^{21} atoms cm^{-2}. The cross marks the centre and the circle shows the beam.

pattern that is typical of rotation: this strongly suggests that there is a rotating disk. Here we present 3D kinematical models that demonstrate that the H I disk is differentially rotating and has a global inflow/outflow motion.

The disk is modelled by a set of gas rings with fixed values of centre, systemic velocity, position angle, inclination, surface density, thickness, velocity dispersion, and rotation velocity. The centre, the systemic velocity, and the position angle were estimated by eye using both optical and H I data (see table 2.3). The centre is between the NW and the SE starburst regions (see Fig. 2.4, right). For the radial distribution, we used the H I surface density profile derived from the total H I map at 2″ resolution by azimuthally averaging over ellipses (Fig. 2.6, top). For the vertical distribution, we assumed an exponential law $\exp(-z/z_0)$. We built a set of models with different values for the inclination i, the scale height z_0, and the velocity dispersion $\sigma_{\rm H\,I}$, assuming that each of these parameters is constant with radius. The inclination and the scale height are constrained by the observed H I map; their values are slightly degenerate but do not strongly affect the final result; we assumed that $i = 70°$ and $z_0 = 100$ pc (see Fig. 2.4, right). The mean velocity dispersion is constrained by the shape of different PV-diagrams and values larger than $\sim$10 km s^{-1} are ruled out; we assumed $\sigma_{\rm H\,I} = 7.5$ km s^{-1}. A thickness of 100 pc and a H I velocity dispersion of 7.5 km s^{-1} are typical values for a H I disk.

The actual H I distribution of I Zw 18 A is clearly not axisymmetric (see Fig. 2.2). Thus, once we had fixed the structural and geometrical parameters

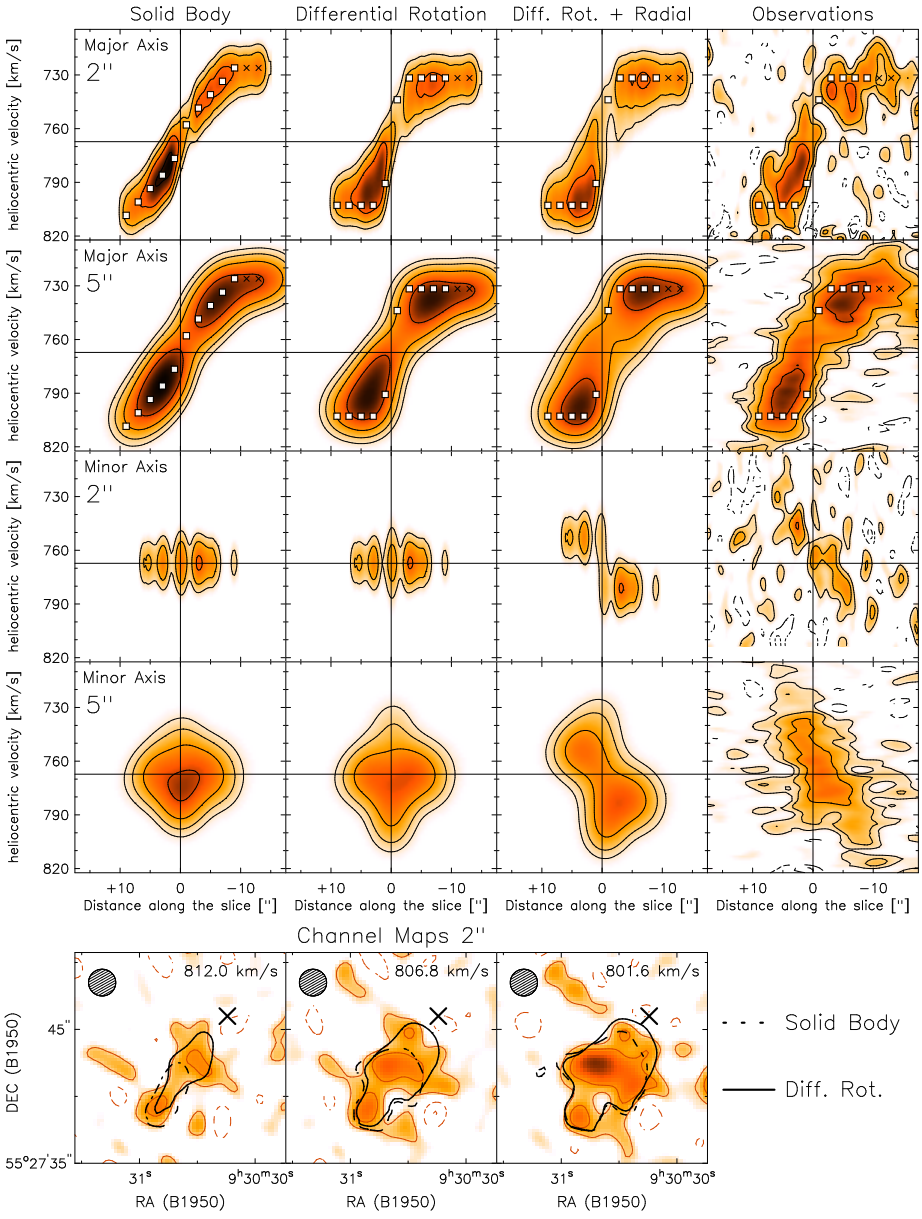

Figure 2.5 – Comparison between different 3D kinematical models and the observations. *Top*: Position-velocity diagrams at a resolution of both 2″ and 5″. The slices are taken along the major and minor axes, as indicated in Fig. 2.4 (left). Contours are at -1.5 (dashed), 1.5, 3, 6, 12 × σ. *Bottom*: Channels maps at 2″ resolution (red contours) superimposed with two models: differential rotation (black-solid contours) and solid body rotation (black-dashed contours). Contours are at 2σ. The cross marks the galaxy centre. The circle shows the beam size. See text for details.

Table 2.3 – Properties of I Zw 18.

Parameter	I Zw 18 A	I Zw 18 C
α (B1950)	$09^{\rm h}30^{\rm m}30.3^{\rm s} \pm 0.1^{\rm s}$	$09^{\rm h}30^{\rm m}27.9^{\rm s} \pm 0.2^{\rm s}$
δ (B1950)	$55^\circ 27' 47'' \pm 1''$	$55^\circ 28' 06'' \pm 2''$
$V_{\rm sys}$ (km s^{-1})	767 ± 4	751 ± 5
Position Angle ($^\circ$)	145 ± 5	-
Inclination Angle ($^\circ$)	70 ± 4	-
$V_{\rm rot}$ (km s^{-1})	38 ± 4.4	-
$L_{\rm B}$ (10^7 L$_\odot$)	13.9	1.1
$L_{\rm R}$ (10^7 L$_\odot$)	5.8	0.4
$M_{\rm H\,I}$ (10^8 M$_\odot$)	1.0	$\lesssim$1.2
$M_{\rm dyn}$ (10^8 M$_\odot$)	3 ± 1	-

Notes. Optical luminosities were calculated using the apparent magnitudes from Papaderos et al. (2002), the distance from Aloisi et al. (2007) and the solar absolute magnitudes from Binney & Merrifield (1998). The H I mass of I Zw 18 C refers to the extended emission described in Sect. 2.5, although only part of this gas may be physically associated with the C-component. The southern "tail" accounts for $\sim 0.5 \times 10^8$ M$_\odot$.

of the disk, we built models with axisymmetric kinematics but a clumpy H I distribution, i.e. the surface density varies with position as in the observed H I map. The procedure is as follows: we built a disk model with a uniform density distribution (fixing z_0, $\sigma_{\rm H\,I}$ and the rotation curve), projected it on the sky, and then renormalized the H I line profiles at every spatial position to reproduce the H I density distribution observed at $2''$ resolution. For the rotation curve, we tried two extreme cases: solid body (slowly rising rotation curve) and differential (steeply rising and flat rotation curve).

Figure 2.5 (top) shows PV-diagrams obtained from both different models and observations at a resolution of $2''$ and $5''$. The slices are taken along the major and minor axes, as indicated in Fig. 2.4 (left). The velocity gradient along the major axis is grossly reproduced by all the models. This demonstrates that: i) a rotating disk is a good representation of the data; ii) the asymmetry between the NW and the SE region is mostly caused by the clumpy H I distribution. Moreover, it is possible to discriminate between solid body and differential rotation. The observed PV-diagram along the major axis indicates that there is H I emission close to the galaxy centre ($R < 5''$) at high rotational velocities ($\sim$810 and $\sim$730 km s^{-1}). The solid body model does not reproduce this emission, as the gas in the inner radii is mostly concentrated near the systemic velocity. The differentially rotating model, instead, correctly reproduces the high-velocity gas. This is clearly illustrated by the channel maps at $2''$ resolution at receding velocities (Fig. 2.5, bottom): the solid body model (dashed line) is not extended enough towards the galaxy centre, whereas the differentially rotating model (solid line) provides a good match of the observations. The approaching NW side of the galaxy is not reproduced as well as the receding SE side, perhaps because the NW starburst region is more active than the SE

one (Contreras Ramos et al. 2011). Nonetheless, on this side, a differentially rotating disk is also preferable to a solid body one.

A simple rotating disk (independently of the assumed rotation curve) cannot reproduce the observed PV-diagrams along the minor axis (Fig. 2.5, top), because of the kinematic asymmetry and the presence of H I emission at velocities forbidden by circular motions. This effect is also visible in the velocity field at 5″ resolution (Fig. 2.4, left): the kinematic minor axis, defined by the contours close to the systemic velocity, is not orthogonal to the kinematic major axis. This is usually attributed to radial motions (e.g. Fraternali et al. 2002). Alternatively, the non-orthogonality between the minor and major axes may be due to a bar-like or oval distortion (e.g. Bosma 1978), although the optical images of I Zw 18 provide no evidence of these strong distortions. We improved the differentially rotating model by adding a global radial motion of 15 km s^{-1}. The resulting model reproduces the H I emission at forbidden velocities. The model, however, cannot reproduce all the details present in the observed PV-diagram. The non-circular motions are not uniform across the disk and small variations (of the order of 3-4 km s^{-1}) could account for the observed discrepancies. It is impossible to discriminate between inflow and outflow, as it is unclear which side of the disk is the nearest to the observer. Vertical motions with roughly the same speed as the radial ones may also be present. Non-circular motions in excess of 20 km s^{-1} are ruled out, confirming that the disk kinematics is dominated by rotation.

The rotation curve used to build our best model was not derived from a standard tilted-ring fit to the velocity field (Begeman 1987), but by building 3D models by trial-and-error. The uncertainties in the rotation velocities are difficult to quantify, but we conservatively estimated them by assigning an error equal to $\Delta V/2.35 = 4.4$ km s^{-1}, where ΔV is the velocity resolution of the 2″ datacube. The first point of the rotation curve is the most uncertain, as the velocity dispersion in the inner ring may be larger than the mean value of 7.5 km s^{-1}. For example, if $\sigma_{\rm H\,I}$ were 10 km s^{-1} larger than the mean value, the rotation velocity would decrease by $\sim$5 km s^{-1}. Following Meurer et al. (1996), we calculated the asymmetric drift correction, which is smaller than the errors.

2.4.2 Mass models

In Sect. 2.4.1, we showed that I Zw 18 A has a rotating H I disk. The rotation curve is uncertain, but has an inner steep rise and an outer flat part, which indicate that there is a strong central concentration of mass that may be either luminous or dark. Using this rotation curve, we built mass models to estimate the relative contributions of luminous and dark matter to the gravitational potential, following Begeman (1987).

The contribution of the gaseous disk was computed using the surface density profile derived from the total H I map at 2″ resolution (Fig. 2.6, top), multiplied by a factor of 1.33 to take into account the presence of Helium. The possible

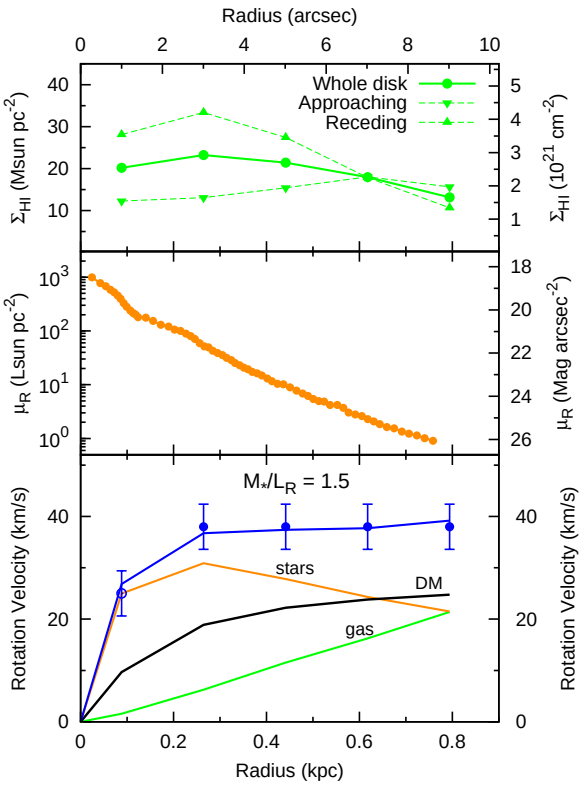

Figure 2.6 – *Top*: H I surface density profile (inclination corrected), derived by ellipse averaging over the entire disk (dots) and over the approaching and receding sides separately (down-triangles and up-triangles, respectively). *Middle:* *R*-band surface brightness profile (from Papaderos et al. 2002). *Bottom:* "maximum disk" decomposition of the rotation curve. Dots and circles show the observed curve. Lines show the contributions of the gas, stars, and dark matter and the resulting rotation curve.

gravitational effect of the H I components *outside* the disk (i.e. the "tail" to the south and the extensions to the north-west and to the west) was not taken into account. Molecular gas was not explicitly considered in the mass model because its amount is very uncertain (Leroy et al. 2007). However, if molecules are distributed in a similar way to the stars, their contribution is reflected as an increase in the stellar mass-to-light ratio (M_*/L). In agreement with the models in Sect. 2.4.1, we assumed an exponential vertical distribution with $z_0 = 100$ pc.

The contribution of the stars was computed using the *R*-band surface brightness profile from Papaderos et al. (2002) (Fig. 2.6, middle), which was derived from an HST image after subtracting the nebular emission (dominated by the Hα line). The colour profiles of Papaderos et al. (2002) (their Fig. 11) show that, after subtracting the nebular emission, the colour of I Zw 18 A is almost constant with radius. Thus, it makes sense to use a constant value of M_*/L_R. We assumed a stellar disk with a vertical density distribution given by $\rho(z) = \mathrm{sech}^2(z/z_0)$ (van der Kruit & Searle 1981), with $z_0 = 100$ pc.

For the dark matter distribution, we assumed a pseudo-isothermal halo described by the equation

$$\rho_{\rm ISO}(r) = \frac{\rho_0}{1 + (r/r_{\rm c})^2}, \tag{2.1}$$

where the central density ρ_0 and the core radius $r_{\rm c}$ are both free parameters of the mass models.

Figure 2.6 (bottom) shows the "maximum disk" decomposition of the rotation curve. The resulting stellar mass-to-light ratio is $M_*/L_{\rm R} \simeq 1.5$. In the maximum disk hypothesis, the baryons dominate the gravitational potential in the inner regions of the galaxy, while the dark matter halo dominates in the outer parts. The parameters of the halo are uncertain because the sampling of the rotation curve is quite course. The halo shown in Fig. 2.6 (bottom) has $\rho_0 = 833 \times 10^{-3}$ M$_\odot$ pc^{-3} and $r_{\rm c} = 0.13$ kpc.

A $M_*/L_{\rm R} \simeq 1.5$ implies a stellar mass of $\sim 9{\times}10^7$ M$_\odot$. According to Aloisi et al. (1999), the starburst started $\sim$20 Myr ago with a star-formation rate (SFR) of $6{\times}10^{-2}$ M$_\odot$ yr^{-1}, giving a mass in *young stars* of $\sim 10^6$ M$_\odot$[1]. Thus, the newly formed stars and the concentration of H I cannot explain the steep rise in the rotation curve, implying that the mass concentration consists of either *old* stars, molecules, or dark matter. Old stars were detected by Aloisi et al. (2007), and their total mass can be constrained by deriving the galaxy star-formation history from color-magnitude diagrams. The maximum-disk value requires a mean SFR of $\sim 7{\times}10^{-3}$ M$_\odot$ yr^{-1} over the past 13 Gyr, that cannot be ruled out. For the molecules, the upper limit to the H_2 mass within $\sim$400 pc is $\sim 7 \times 10^5$ M$_\odot$ (Leroy et al. 2007)[2], using a Galactic CO-to-H_2 conversion factor ($X_{\rm CO}$). However, Leroy et al. (2007) argued that, in I Zw 18, $X_{\rm CO}$ may be 10^{-2} times the Galactic value. The same result is found by extrapolating the relation between $X_{\rm CO}$ and metallicity by Boselli et al. (2002) down to the metallicity of I Zw 18. Thus, the H_2 mass within $\sim$400 pc may be dynamically important and be as high as $\sim 7{\times}10^7$ M$_\odot$.

We also used MOdified Newtonian Dynamics (MOND) (Milgrom 1983; Sanders & McGaugh 2002) to fit the rotation curve. We assumed that $a_0 = 1.21 \times 10^{-8}$ cm s^{-2} (Begeman et al. 1991) and the distance $D = 18.2$ Mpc (Aloisi et al. 2007), thus the only free parameter is $M_*/L_{\rm R}$. Using MOND, acceptable fits are possible for $M_*/L_{\rm R} = 1.5$ using the "standard" interpolation function (Milgrom 1983) and $M_*/L_{\rm R} = 1$ using the "simple" one (Famaey & Binney 2005).

Following McGaugh (2011), we check the position of I Zw 18 A on the baryonic Tully-Fisher relation. The galaxy follows the correlation within the observed scatter.

[1] Aloisi et al. (1999) assumed a distance of 10 Mpc. With the new value of 18.2 Mpc, the starburst parameters slightly change, but the mass in young stars remains almost the same (F. Annibali, priv. comm.).

[2] We rescaled the original values to a distance of 18.2 Mpc.

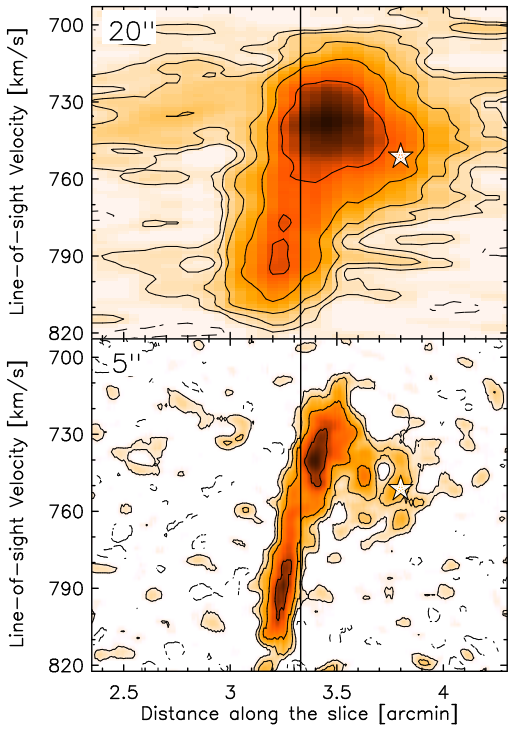

Figure 2.7 – Position-velocity diagrams at a resolution of 20″ (*top*) and 5″ (*bottom*). They are derived following the path shown in Fig. 2.2. Countours are at -1.5 (dashed), 1.5, 3, 6, 12, 24 σ. The star indicates the Hα systemic velocity and spatial position of I Zw 18 C.

2.5 The extended emission

In this section we study the extended H I emission. This may provide some clues to the mechanism that triggered the starburst. In addition, we compare the large-scale H I and Hα emission to investigate the possible presence of outflows.

2.5.1 The C-component and the H I tail

In Sect. 2.3.1, we reported two puzzling results (see Fig. 2.2, left): i) an H I "tail" at line-of-sight velocities of 710-760 km s^{-1} extending to the south of I Zw 18 A and kinematically disconnected from the south-east side of the central rotating disk; ii) a broadening of the H I emission in the PV-diagram at almost the same velocities (700-780 km s^{-1}) to the north-west (in the direction of I Zw 18 C). This is clearly shown in Fig. 2.7, where the PV-diagrams at resolutions of 20″ and 5″ (with different column density sensitivities) are plotted on the same scale.

To study these components and their possible connection in more detail, we subtracted the compact H I disk of I Zw 18 A from the surrounding extended H I emission. We used the high-resolution data to define the emission from the disk

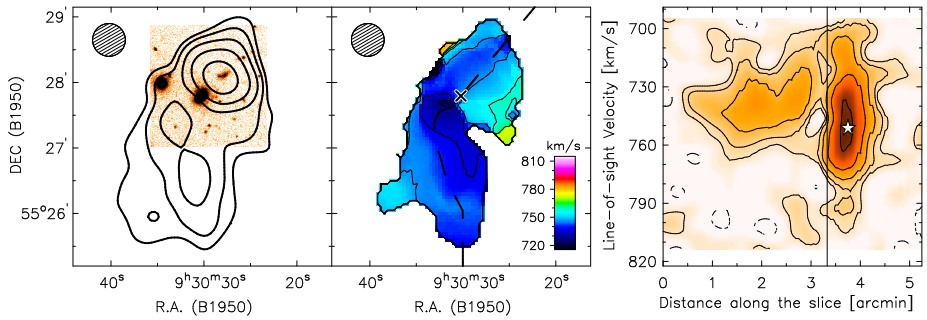

Figure 2.8 – The H I emission at 30″ resolution, after the subtraction of the main body. *Left*: *B*-band image overlaid with the total H I map. Countours are at 2.4, 4.8, 9.6, 19.2 × 10^{19} atoms cm^{-2}. *Middle*: Velocity field. Contours range from 735.8 to 767 km s^{-1} with steps of 10.4 km s^{-1}. The cross shows the position of I Zw 18 A. The dashed line shows the path followed to obtain the position-velocity diagram. *Right*: Position-velocity diagram. Countours are at -1.5 (dashed), 1.5, 3, 6, 12 σ, where $\sigma = 0.3$ mJy/beam. The vertical line corresponds to the cross in the velocity field. The star shows the Hα systemic velocity and the spatial position of I Zw 18 C.

and subtracted this emission from the low-resolution datacube[3]. Subsequently, we smoothed the residual datacube to both 30″ and 10.4 km s^{-1} and used it to obtain: i) a total H I map by summing the channels in the velocity range ∼700-780 km s^{-1}; ii) a velocity field by estimating an intensity-weighted mean velocity; iii) a PV-diagram by following the tail (dashed line in Fig. 2.8).

Figure 2.8 shows the results of the subtraction. Interestingly, extended H I emission is centered on I Zw 18 C (left panel) and forms a coherent kinematical structure with velocities ranging between ∼700 and 800 km s^{-1} (right panel). The physical association of the C-component with this surrounding H I emission is likely because the Hα systemic velocity of I Zw 18 C is ∼751±5 km s^{-1} (Dufour et al. 1996) (see star in Fig. 2.8, right).

The southern H I tail seems to be connected in both space and velocity to the H I structure around I Zw 18 C, as shown by the velocity field (Fig. 2.8, middle). The connection may be either behind or in front of I Zw 18 A. Possible interpretations of the extended H I emission are discussed in Sect. 2.6.1.

[3] Technically, we built a mask containing only the H I signal from the disk and cleaned the datacube at 1.5″ × 1.4″ resolution down to 1σ, using the mask to define the search areas. We restored the clean-components on a blank cube, using a Gaussian beam of 20″. The resulting "clean-component" cube contains only the emission from the disk, but at the desired resolution of 20″. Finally, the "clean-component" cube was subtracted channel by channel from the 20″ datacube.

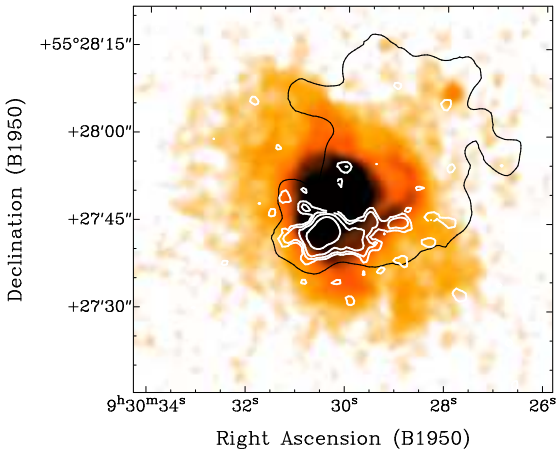

Figure 2.9 – Hα image (Gil de Paz et al. 2003) superimposed with the H I emission. White contours show the H I emission at 2.8″ × 3.3″ resolution, integrated across the velocity range 800-770 km s^{-1}, and correspond to 5, 10, 20, 40 × 10^{20} atoms cm^{-2}. The black line shows the pseudo-3σ contour of the total H I map at 5″ resolution.

2.5.2 The connection between the H I and Hα emission

In Sect. 2.3.3, we pointed out the relative H I and Hα distributions in the inner regions of I Zw 18 A. Here we compare the distribution and kinematics of neutral and ionized gas on larger scales.

Figure 2.9 shows an Hα image (from Gil de Paz et al. 2003) superimposed with the H I emission (black and white contours). The Hα emission extends well beyond the stellar body and is almost perpendicular to the H I disk, suggesting that it traces an outflow. This interpretation agrees with that of Martin (1996), who used Hα long-slit spectroscopy and detected a bipolar superbubble expanding with velocities of ±60 km s^{-1} out to ∼2 kpc from I Zw 18 A. The H I to the north-east of the main body (see black contour) seems to border the Hα emission and is almost at the same velocity, suggesting that part of the diffuse H I may be associated with the outflow.

The Hα emission also presents a prominent arc to the west of I Zw 18 A. This feature was first identified by Dufour & Hester (1990) and interpreted as a radiation-bound ionization front driven into the ISM. Petrosian et al. (1997), instead, argued that the Hα arc also contains stellar emission and suggested that it is a structure with stars that are able to ionize the gas "in situ". The H I to the west of I Zw 18 A is associated with the Hα arc. To show this, we summed the channel maps at 2.8″ × 3.3″ resolution in the velocity range 800-770 km s^{-1} (see Fig. 2.9, white contours). Moreover, the Hα velocity field of Petrosian et al. (1997) shows a gradient along the arc similar to the one observed in Fig. 2.2 (middle-right), confirming the physical association between H I and Hα. The hypothesis of a radiation-bound ionization front is difficult to reconcile with the presence along the Hα arc of a high-density (∼10^{21} atoms cm^{-2}) neutral gas.

2.6 Discussion

2.6.1 Observational evidence & interpretation

This H I study of I Zw 18 has shown that:

- I Zw 18 A has a compact rotating disk with very high H I densities. The rotation curve is flat with a steep inner rise, indicating that there is a strong concentration of mass. A global inflow/outflow motion is also present.
- I Zw 18 C is located in the direction of the major axis of I Zw 18 A and is almost at the same velocities as its approaching side. Gas emission with a smooth velocity gradient connects the two stellar bodies. I Zw 18 C appears to be at the centre of a diffuse H I structure.
- An H I tail extends to the south of I Zw 18 A out to ∼13.5 kpc. The tail has a coherent kinematical structure and seems to be connected with the H I emission to the north-west.

Studies of the resolved stellar populations (Aloisi et al. 2007; Contreras Ramos et al. 2011) have shown that: i) the two starburst regions in I Zw 18 A (NW and SE) are embedded in a common envelope of old stars with ages >1 Gyr; ii) I Zw 18 A and I Zw 18 C are two completely separate stellar bodies and there are no stars between them; iii) I Zw 18 C also contains both old (>1 Gyr) and young (∼10 Myr) stars, but its current star formation rate (SFR) is lower than that of I Zw 18 A.

For the interpretation, we consider first the hypothesis of an interaction/merger of two (or more) gas-rich dwarfs. It is well-known that interactions/mergers can produce tidal tails (e.g. Toomre & Toomre 1972). In addition, numerical simulations (e.g. Hibbard & Mihos 1995) suggest that mergers can lead to gas inflows, produce strong gas concentrations, and trigger intense star-formation. Thus, an interaction/merger may provide an explanation of: i) the concentration of H I, ii) the ongoing starburst, and iii) the southern H I tail. The C-component may be either a "relic" of the interaction or a dwarf galaxy that is interacting/merging with I Zw 18 A. The two objects are at a projected distance of ∼2.2 kpc, the difference between their systemic velocities is ∼12 km s^{-1}, and are connected by H I emission with a smooth velocity gradient. The ratio of the R-band luminosities of I Zw 18 A to I Zw 18 C is ∼14, thus this would be classified as a minor merger. The merger hypothesis may also explain the extremely low metallicity, as we now discuss.

Bekki (2008) argued that BCDs with low nebular metallicity are the results of mergers between gas-rich dwarfs with extended H I disks. According to his simulations, the central starburst is fuelled with metal-poor gas transferred from the outer regions of the extended disks, where the star formation and the chemical enrichment were inefficient owing to the low H I densities. Our

results are consistent with this picture, as the C-component is surrounded by an extended H I structure, that does not have a stellar counterpart and has probably not been efficiently enriched by SN explosions. Therefore, this H I structure may provide "fresh" unprocessed gas into the starburst regions of I Zw 18 A. A similar mechanism of metal dilution was proposed by Ekta & Chengalur (2010) to explain why I Zw 18 and the other extremely metal-deficient BCDs are outliers of the mass-metallicity relation.

The extended H I emission, including the tail, has been considered above as supporting evidence of a merger, but might this instead be the result of a blowout from the starburst? The Hα observations of I Zw 18, indeed, suggest that there is an outflow (Sect. 2.5.2). In addition, numerical simulations predict that starbursting dwarfs undergo massive outflows because they have a shallow gravitational potential (e.g. Mac Low & Ferrara 1999). The rate of the outflowing gas $dM_{\rm out}/dt$ can be roughly estimated as

$$\frac{dM_{\rm out}}{dt} = \frac{2 \times \varepsilon \times {\rm SNR} \times \overline{E_{\rm SN}}}{V_{\rm esc}^2}, \tag{2.2}$$

where SNR is the rate of supernovae (SN), $\overline{E_{\rm SN}}$ is the mean energy of a SN, $V_{\rm esc}$ is the escape velocity, and ε is the efficiency of the SN feedback. Thus, $M_{\rm out} = dM_{\rm out}/dt \times \Delta T$, where ΔT is the duration of the starburst. Assuming that $\overline{E_{\rm SN}} = 1.2 \times 10^{51}$ erg, $V_{\rm esc} = \sqrt{2} \times V_{\rm rot}$, $\varepsilon = 0.15$, $\Delta T = 20$ Myr (Aloisi et al. 1999), and SNR $= 0.01 \times$ SFR with SFR $= 0.06$ M$_\odot$ yr^{-1} (Aloisi et al. 1999), we find that $M_{\rm out} \simeq 5 - 8 \times 10^7$ M$_\odot$. The total mass of the extended gas is $\sim 1.6 \times 10^8$ M$_\odot$ (corrected for the presence of He). Thus, a massive outflow may explain *all* the diffuse gas if only slightly higher values of SFR, ΔT, and ε are assumed. Since the extended H I emission is entirely at approaching velocities, any outflow should be highly asymmetric and confined.

Finally, we would also like to mention the hypothesis of a "fragmenting H I cloud in the early stages of galaxy evolution", which was suggested by van Zee et al. (1998b). This picture can explain the extremely low metallicity of I Zw 18, but is in contrast to the results of Aloisi et al. (2007), who concluded that I Zw 18 has old stars and is not a young galaxy in formation. Alternatively, I Zw 18 A and I Zw 18 C may be old stellar systems that are accreting cold gas from the inter-galactic medium and are now forming new stars. This may be in line with some simulations of dwarf galaxy formation (e.g. Kereš et al. 2005; Dekel & Birnboim 2006).

2.6.2 Comparison with other dwarf galaxies

The evolution of BCDs is still not understood. In particular, it is unclear what objects can be identified as their progenitors and descendants (Papaderos et al. 1996; van Zee et al. 2001). It is useful, therefore, to compare their properties with those of other types of dwarf galaxies.

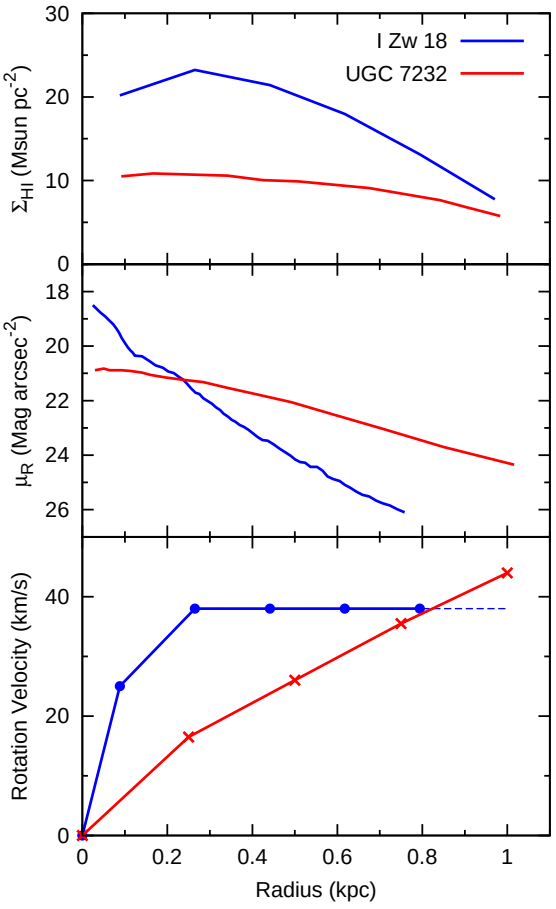

Figure 2.10 – Comparison between I Zw 18 A (blue line) and a typical dwarf irregular UGC 7232 (red line), selected from the sample of Swaters et al. (2009). *Top:* H I surface density profile. *Middle:* *R*-band surface brightness profile. *Bottom*: H I rotation curve.

In Fig. 2.10, we compare I Zw 18 A with a typical dwarf irregular (UGC 7232) taken from the sample of Swaters et al. (2009). The H I observations of these two objects have almost the same linear resolution (∼200 pc), making it possible to compare H I surface densities and velocity gradients. The two galaxies have approximately the same H I size and the same rotation velocity at the last measured point, thus they have roughly the same dynamical mass. However, their structural properties are very different:

1. The azimuthally-averaged H I surface densities of I Zw 18 A are a factor of ∼2 higher than those of UGC 7232 (Fig 2.10, top). In addition, the H I distribution of I Zw 18 A is clumpy with H I column densities as high as ∼50-100 $M_\odot$ pc^{-2} (Fig. 2.3).

2. The stellar component of I Zw 18 A is much more compact than that of UGC 7232 (Fig. 2.10, middle).

3. The rotation curves have a completely different shape (Fig. 2.10, bottom). UGC 7232 has a slowly-rising rotation curve indicating a smooth mass distribution, whereas I Zw 18 A has a flat rotation curve with an inner steep rise, indicating that there is a strong concentration of mass.

In Section 2.4.2, we showed that the central mass concentration cannot be explained by the newly formed stars and/or by the concentration of HI, but can be identified with the old stars and/or dark matter. As to the molecules, their amount is highly uncertain and it is unclear whether they are dynamically important or not. The now uncovered concentration of mass is unique among dwarf irregular galaxies and must be tightly linked to the starburst. Furthermore, this result sheds new light on the question of the evolution of BCDs and their descendants. It is clear that, unless a significant redistribution of mass takes place, a steeply rising rotation curve, as found for I Zw 18, would be the distinctive signature that would make the descendants recognizable.

For other BCDs, it is known that their underlying stellar component, which consists of *old stars*, is generally more compact than common Irrs and Sphs (e.g. Papaderos et al. 1996; Gil de Paz & Madore 2005). In particular, the old stellar component of the majority of BCDs has a typical central surface brightness $\mu_0 \simeq 21$ mag arcsec^{-2} in the B-band (e.g. Gil de Paz & Madore 2005), that is similar to those of high surface brightness (HSB) disk galaxies (e.g. van der Kruit & Freeman 2011). If the distribution of mass is strongly coupled to the distribution of light (Sancisi 2004), we expect BCDs to show a dynamical behaviour similar to HSB spiral galaxies, i.e. steeply-rising rotation curves that can be described under the maximum disk hypothesis. This seems to be the case for I Zw 18 A. In all these respects, I Zw 18 A resembles a "miniature" HSB disk galaxy. There are already indications that BCDs may have "steeper rotation curves than similar luminosity, low surface brightness dwarf galaxies" (van Zee et al. 2001), but a detailed dynamical study is needed to derive reliable rotation curves and determine the relative contributions of gas, stars, and dark matter to the gravitational potential.

2.7 Conclusions

We have analysed H I observations of the blue compact dwarf galaxy I Zw 18. Our main results can be summarized as follows:

1. The H I gas associated with the starburst region (I Zw 18 A) is in a compact, rotating disk. The H I column densities are very high, up to $\sim 50 - 100$ M$_\odot$ pc^{-2} ($\sim 0.6 - 1.2 \times 10^{22}$ atoms cm^{-2}).

2. The disk has a flat rotation curve with an inner steep rise. This indicates that there is a strong concentration of mass that may be either luminous

or dark. Baryons may dominate the gravitational potential in the inner regions.

3. The disk has a radial inflow/outflow motion of $\sim$15 km s^{-1}.
4. The stellar concentration to the north-west (I Zw 18 C) is surrounded by extended H I emission, which is smoothly connected with I Zw 18 A.
5. An H I tail extends to the south of I Zw 18 A out to $\sim$13.5 kpc. It has a coherent kinematical structure and seems to be connected to the H I emission to the north-west.

I Zw 18 A appears structurally different from a typical dwarf irregular in terms of H I distribution, stellar distribution, and dynamics. In particular, it has a strong central concentration of mass. It may be considered as a "miniature" HSB disk galaxy. The H I concentration and the dynamical properties must be tightly linked to the starburst. They are also crucial to address the question of the progenitors/descendants of BCDs.

The mechanism that triggered the starburst is most likely to have been an interaction/merger between gas-rich dwarf galaxies.

Acknowledgements

We thank F. Annibali, G. Fiorentino, and M. Tosi for helpful discussions about the stellar populations of BCDs and for providing the HST image of I Zw 18. We are grateful to J. van Gorkom for stimulating discussions. We also thank J. Cannon for kindly making his HST images available to us.

References

Aloisi, A., Clementini, G., Tosi, M., et al. 2007, ApJL, 667, L151
Aloisi, A., Tosi, M., & Greggio, L. 1999, AJ, 118, 302
Begeman, K., Broeils, A., & Sanders, R. 1991, MNRAS, 249, 523
Begeman, K. G. 1987, PhD thesis, , Kapteyn Institute, (1987)
Bekki, K. 2008, MNRAS, 388, L10
Binney, J. & Merrifield, M. 1998, Galactic astronomy, ed. Binney, J. & Merrifield, M.
Boselli, A., Lequeux, J., & Gavazzi, G. 2002, A&A, 384, 33
Bosma, A. 1978, PhD thesis, PhD Thesis, Groningen Univ., (1978)
Briggs, D. S. 1995, in Bulletin of the American Astronomical Society, Vol. 27, Bulletin of the American Astronomical Society, 1444–+
Cannon, J. M., McClure-Griffiths, N. M., Skillman, E. D., & Côté, S. 2004, ApJ, 607, 274
Cannon, J. M., Skillman, E. D., Garnett, D. R., & Dufour, R. J. 2002, ApJ, 565, 931
Contreras Ramos, R., Annibali, F., Fiorentino, G., et al. 2011, ApJ, 739, 74
Davidson, K., Kinman, T. D., & Friedman, S. D. 1989, AJ, 97, 1591
Dekel, A. & Birnboim, Y. 2006, MNRAS, 368, 2
Dufour, R. J., Esteban, C., & Castaneda, H. O. 1996, ApJL, 471, L87+
Dufour, R. J. & Hester, J. J. 1990, ApJ, 350, 149
Ekta, B. & Chengalur, J. N. 2010, MNRAS, 406, 1238
Elson, E. C., de Blok, W. J. G., & Kraan-Korteweg, R. C. 2010, MNRAS, 404, 2061
Famaey, B. & Binney, J. 2005, MNRAS, 363, 603
Fiorentino, G., Contreras Ramos, R., Clementini, G., et al. 2010, ApJ, 711, 808
Fraternali, F., van Moorsel, G., Sancisi, R., & Oosterloo, T. 2002, AJ, 123, 3124
Gil de Paz, A. & Madore, B. F. 2005, ApJS, 156, 345
Gil de Paz, A., Madore, B. F., & Pevunova, O. 2003, ApJS, 147, 29
Hibbard, J. E. & Mihos, J. C. 1995, AJ, 110, 140
Högbom, J. A. 1974, A&AS, 15, 417
Izotov, Y. I. & Thuan, T. X. 1999, ApJ, 511, 639
Izotov, Y. I. & Thuan, T. X. 2004, ApJ, 616, 768
Kereš, D., Katz, N., Weinberg, D. H., & Davé, R. 2005, MNRAS, 363, 2
Kobulnicky, H. A. & Skillman, E. D. 2008, AJ, 135, 527
Leroy, A., Cannon, J., Walter, F., Bolatto, A., & Weiss, A. 2007, ApJ, 663, 990
Mac Low, M. & Ferrara, A. 1999, ApJ, 513, 142
Martin, C. L. 1996, ApJ, 465, 680
McGaugh, S. S. 2011, Physical Review Letters, 106, 121303
McQuinn, K. B. W., Skillman, E. D., Cannon, J. M., et al. 2010, ApJ, 721, 297
Meurer, G. R., Carignan, C., Beaulieu, S. F., & Freeman, K. C. 1996, AJ, 111, 1551
Milgrom, M. 1983, MNRAS, 270, 365

Oh, S., de Blok, W. J. G., Walter, F., Brinks, E., & Kennicutt, R. C. 2008, AJ, 136, 2761
Östlin, G. & Mouhcine, M. 2005, A&A, 433, 797
Papaderos, P., Izotov, Y. I., Thuan, T. X., et al. 2002, A&A, 393, 461
Papaderos, P., Loose, H., Fricke, K. J., & Thuan, T. X. 1996, A&A, 314, 59
Petrosian, A. R., Boulesteix, J., Comte, G., Kunth, D., & Lecoarer, E. 1997, A&A, 318, 390
Sancisi, R. 2004, in IAU Symposium, Vol. 220, Dark Matter in Galaxies, ed. S. Ryder, D. Pisano, M. Walker, & K. Freeman, 233–+
Sanders, R. H. & McGaugh, S. S. 2002, ARA&A, 40, 263
Searle, L. & Sargent, W. L. W. 1972, ApJ, 173, 25
Skillman, E. D. & Kennicutt, Jr., R. C. 1993, ApJ, 411, 655
Swaters, R. A., Sancisi, R., van Albada, T. S., & van der Hulst, J. M. 2009, A&A, 493, 871
Swaters, R. A., van Albada, T. S., van der Hulst, J. M., & Sancisi, R. 2002, A&A, 390, 829
Toomre, A. & Toomre, J. 1972, ApJ, 178, 623
Tosi, M. 2009, in IAU Symposium, Vol. 258, IAU Symposium, ed. E. E. Mamajek, D. R. Soderblom, & R. F. G. Wyse, 61–72
van der Hulst, J., Terlouw, J., Begeman, K., Zwitser, W., & Roelfsema, P. 1992, in ASP Conf. Ser. 25, ed. D. M. Worall, C. Biemesderfer, & J. Barnes, San Francisco: ASP, 131
van der Kruit, P. C. & Freeman, K. C. 2011, ARA&A, 49, 301
van der Kruit, P. C. & Searle, L. 1981, A&A, 95, 105
van Zee, L., Salzer, J. J., & Skillman, E. D. 2001, AJ, 122, 121
van Zee, L., Skillman, E. D., & Salzer, J. J. 1998a, AJ, 116, 1186
van Zee, L., Westpfahl, D., Haynes, M. P., & Salzer, J. J. 1998b, AJ, 115, 1000
Verheijen, M. & Sancisi, R. 2001, A&A, 370, 765
Viallefond, F., Lequeux, J., & Comte, G. 1987, in Starbursts and Galaxy Evolution, ed. T. X. Thuan, T. Montmerle, & J. Tran Thanh van, 139–143
Zwicky, F. 1966, ApJ, 143, 192

Chapter 3

Dynamics of starbursting dwarf galaxies. II. UGC 4483

— **Federico Lelli, Marc Verheijen, Filippo Fraternali, and Renzo Sancisi** —

Astronomy & Astrophysics, 2012, 544, A145

Abstract

UGC 4483 is a nearby Blue Compact Dwarf (BCD) galaxy. HST observations have resolved the galaxy into single stars and this has led to the derivation of its star formation history and to a direct estimate of its stellar mass. We have analysed archival VLA observations of the 21 cm line and found that UGC 4483 has a steeply-rising rotation curve which flattens in the outer parts at a velocity of $\sim$20 km s^{-1}. Radial motions of $\sim$5 km s^{-1} may also be present. As far as we know, UGC 4483 is the lowest-mass galaxy with a differentially rotating H I disk. The steep rise of the rotation curve indicates that there is a strong central concentration of mass. We have built mass models using the HST information on the stellar mass to break the disk-halo degeneracy: old stars contribute $\sim$50% of the observed rotation velocity at 2.2 disk scale-lengths. Baryons (gas and stars) constitute an important fraction of the total dynamical mass. These are striking differences with respect to typical dwarf irregular galaxies (Irrs), which usually have slowly-rising rotation curves and are thought to be entirely dominated by dark matter. BCDs appear to be different from non-starbursting Irrs in terms of their H I and stellar distributions and their internal dynamics. To their high central surface brightnesses and high central H I densities correspond strong central rotation-velocity gradients. This implies that the starburst is closely related with the gravitational potential and the concentration of gas. We discuss the implications of our results on the properties of the progenitors/descendants of BCDs.

3.1 Introduction

The mechanisms that trigger strong bursts of star formation in galaxies are poorly understood. In the Local Universe, starburst activity is mostly observed in low-mass galaxies, which are usually classified as blue compact dwarfs (BCDs) (e.g. Gil de Paz et al. 2003), amorphous dwarfs (e.g. Gallagher & Hunter 1987), or H II galaxies (e.g. Taylor et al. 1995). Hereafter, we will refer to any starbursting dwarf galaxy as a BCD. Several studies (e.g. Gil de Paz & Madore 2005; Tosi 2009, and references therein) have shown that BCDs are *not* young galaxies undergoing their first burst of star formation (as suggested by Searle & Sargent 1972), as they also contain old stellar populations with ages >2-3 Gyr. In particular, HST has made it possible to resolve nearby BCDs into single stars and to derive colour-magnitude diagrams deep enough to provide the following information: i) accurate distances of the galaxies, ii) a direct estimate of their total stellar mass, and iii) their star formation history (SFH) (e.g. Tosi 2009). These SFHs show that the starburst is a short-lived phenomenon, typically sustained for a few 100 Myr (McQuinn et al. 2010a). Thus, BCDs are *transition-type dwarfs* but the nature of their progenitors and descendants remains unclear. In particular, it is not known whether there are evolutionary connections with dwarf irregulars (Irrs) and/or spheroidals (Sphs) (e.g. Papaderos et al. 1996; van Zee et al. 2001).

There are striking differences between BCDs and other types of dwarf galaxies: i) the old stellar component of BCDs generally has a smaller scale-length and higher central surface brightness than Irrs and Sphs (e.g. Papaderos et al. 1996; Gil de Paz & Madore 2005); ii) BCDs have strong concentrations of H I within the starburst region, where the column densities are typically 2-3 times higher than in Irrs (e.g. van Zee et al. 1998, 2001); iii) BCDs have steep central velocity gradients that are not observed in Irrs (e.g. van Zee et al. 1998, 2001). The steep velocity gradients may signify a steeply-rising rotation curve (van Zee et al. 2001; Lelli et al. 2012), high velocity dispersion, or non-circular motions (e.g. Elson et al. 2011b). Detailed studies of the gas kinematics are needed to determine the inner shape of the rotation curve. In Chapter 2 (Lelli et al. 2012), we studied the BCD prototype I Zw 18, and found that it has a flat rotation curve with a steep rise in the inner parts, indicating that there is a high central concentration of mass. Such a mass concentration is not observed in typical Irrs. This points to a close connection between the starburst and the gravitational potential. It is also clear that a BCD like I Zw 18 cannot evolve into a typical Irr at the end of the starburst, unless the central concentration of mass is removed. It is important, therefore, to investigate whether all BCDs have steeply-rising rotation curves, and to determine the relative contributions of gas, stars, and dark matter to the gravitational potential.

We present a detailed study of the gas kinematics of UGC 4483, a starbursting dwarf galaxy located in the M81 group and resolved into individual stars by HST (Dolphin et al. 2001; Izotov & Thuan 2002). UGC 4483 is

Table 3.1 – Properties of UGC 4483.

α (J2000)	$08^{\rm h}37^{\rm m}3.1^{\rm s} \pm 0.5^{\rm s}$
δ (J2000)	$69^\circ 46' 31'' \pm 2''$
Distance (Mpc)	3.2 ± 0.2
$V_{\rm sys}$ (km s^{-1})	158 ± 2
Position Angle ($^\circ$)	0 ± 5
Inclination Angle ($^\circ$)	58 ± 3
$V_{\rm rot}$ (km s^{-1})	19 ± 2
$M_{\rm dyn}$ (10^7 $M_\odot$)	16 ± 3
M_* (10^7 $M_\odot$)	1.0 ± 0.3
$M_{\rm H\,I}$ (10^7 $M_\odot$)	2.5 ± 0.3
$L_{\rm B}$ (10^7 $L_\odot$)	1.4
$L_{\rm R}$ (10^7 $L_\odot$)	0.9

Notes. Luminosities were calculated using the apparent magnitudes from Gil de Paz et al. (2003), the distance from Dolphin et al. (2001), and the solar absolute magnitudes from Binney & Merrifield (1998). The stellar mass was calculated integrating the SFH from McQuinn et al. (2010a) and assuming a gas recycling efficiency of 30%. The dynamical mass was calculated taking into account the pressure-support.

extremely metal-poor (12+log(O/H)$\simeq$7.5, see Skillman et al. 1994 and van Zee & Haynes 2006) and may be classified as a "cometary" BCD, as its high-surface-brightness starburst region is located at the edge of an elongated low-surface-brightness stellar body (see Fig. 3.1, top-left). Previous H I studies (Lo et al. 1993; van Zee et al. 1998) showed that the galaxy has an extended H I disk, with a strong H I concentration near the starburst region and a steep central velocity gradient, but the H I kinematics was not studied in detail. We analysed archival VLA data and were able to derive a rotation curve, which we used to investigate the distributions of luminous and dark matter in this galaxy.

3.2 Data reduction & analysis

We analysed H I data taken from the VLA archive. The observations have been carried out with the B and C arrays, and are described in van Zee et al. (1998). The correlator was used in 2AD mode, with a total bandwidth of 1.56 MHz ($\sim$330 km s^{-1}). An on-line Hanning taper was applied to the data, producing 127 spectral line channels with a width of 12.3 kHz ($\sim$2.6 km s^{-1}).

We interactively flagged, calibrated, and combined the raw UV data using the AIPS package and following standard VLA procedures. The UV data were mapped using a robust weighting technique (Briggs 1995) and a Gaussian baseline taper to attenuate the longest baselines. After various trials, we chose a robust parameter of -1 and a taper FWHM of 40 kλ; these parameters minimize sidelobes and wings in the beam profile and lead to a datacube with an angular resolution of $5.7'' \times 4.5''$.

After the Fourier transform, the data analysis was continued using the Groningen Imaging Processing SYstem (GIPSY) (van der Hulst et al. 1992). A

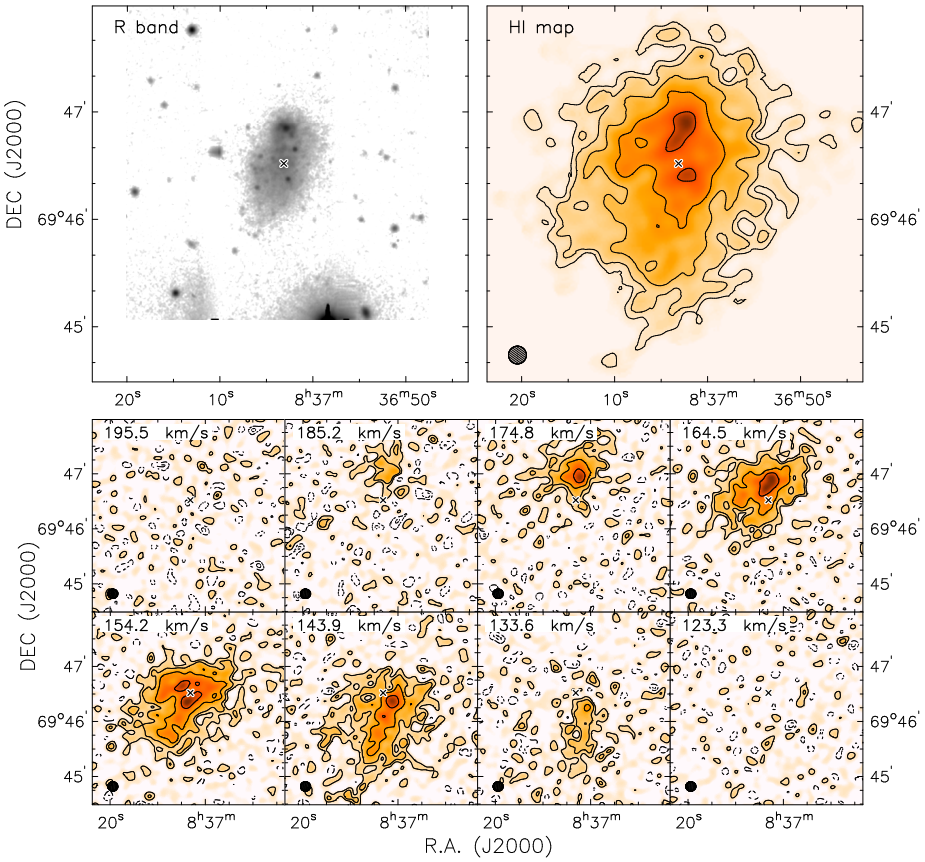

Figure 3.1 – *Top-Left:* *R*-band image (from Gil de Paz et al. 2003). *Top-Right:* total H I map at 10″ resolution. The contour values are 1.7, 3.4, 6.8, 13.6, 27.2 × 10^{20} atoms cm^{-2}. *Bottom:* channel maps at 10″ resolution. Contours are at 1.5, 3, 6, 12, 24 × σ, where σ=0.66 mJy/beam ($\sim$2×10^{19} atoms cm^{-2}). In each panel, the cross and the circle show the galaxy centre and the beam size, respectively.

continuum map was constructed by averaging line-free channels, and subtracted from the datacube. The channel maps were cleaned (Högbom 1974) down to 0.3σ, using a mask to define the search areas for the clean-components that were then restored with a Gaussian beam of the same FWHM as the antenna pattern. The mask was constructed by smoothing the datacube both in velocity (to 10.4 km s^{-1}) and spatially (to 20″) and clipping at $\sim$3σ_s (where σ_s is the rms noise in the smoothed cube). In order to improve the S/N, the cleaned datacube was smoothed in velocity to a resolution of 5.2 km s^{-1} and spatially to 10″, providing a 3σ column density sensitivity of 6×10^{19} atoms cm^{-2} per 2.6 km s^{-1}-wide channel.

A total H I map was constructed by summing the signal inside the clean-mask; a pseudo-3σ contour was calculated following Verheijen & Sancisi (2001). A velocity field was derived by fitting a Gaussian function to the H I line profiles. Fitted Gaussians with a peak intensity less than 3σ and a FWHM smaller than 5.2 km s^{-1} were discarded. The H I line profiles are quite broad and asymmetric, thus the velocity field derived from the Gaussian fitting provides only an overall description of the galaxy kinematics. Our kinematical analysis is based on three-dimensional (3D) models of the observations (Sect. 3.3.2) and not merely on the two-dimensional (2D) velocity field.

3.3 Results

3.3.1 H I distribution and kinematics

Figure 3.1 shows the total H I map of UGC 4483 at a resolution of 10″ (top-right) and a R-band image at the same scale (top-left). The H I distribution is lopsided and closely resembles the optical morphology. There is a strong H I concentration near the starburst region to the North. At 5.7″ × 4.5″ resolution (∼80 pc), the peak column densities are ∼5×10^{21} atoms cm^{-2} (∼40 $M_\odot$ pc^{-2}, same as found by van Zee et al. 1998).

The H I kinematics of UGC 4483 is illustrated in Fig. 3.1 (bottom) and Fig. 3.2 (top). The H I emission shows a velocity gradient along a position angle P.A.∼0°, which roughly corresponds to the optical major axis of the galaxy, suggesting that there is a rotating H I disk. The velocity field indicates large-scale differential rotation. It also shows, however, large-scale asymmetries. In the next section, we derive the rotation curve of UGC 4483 and discuss possible non-circular motions.

3.3.2 Rotation curve and non-circular motions

Rotation curves of disk galaxies are usually derived by fitting a tilted-ring model to a velocity field (e.g. Begeman 1987). In the case of UGC 4483, there are severe limitations because of the asymmetries in the velocity field. Van Zee et al. (1998) modeled the velocity field of UGC 4483 and obtained a rough estimate of the dynamical mass. We derived a rotation curve using the following approach. As a first step, we fit a tilted-ring model to the velocity field to obtain an initial estimate of the rotation curve. Then, this rotation curve was used as input to build a 3D kinematic model and subsequently corrected by trial and error to produce a model-cube that matches the observations.

When fitting a tilted-ring model to the velocity field, we used a ring width of 10″ (1 beam), thus the points of the rotation curve are nearly independent. The points of the velocity field were weighted by $\cos^2(\theta)$, where θ is the azimuthal angle in the plane of the galaxy. We kept the centre (x_0, y_0) and the inclination

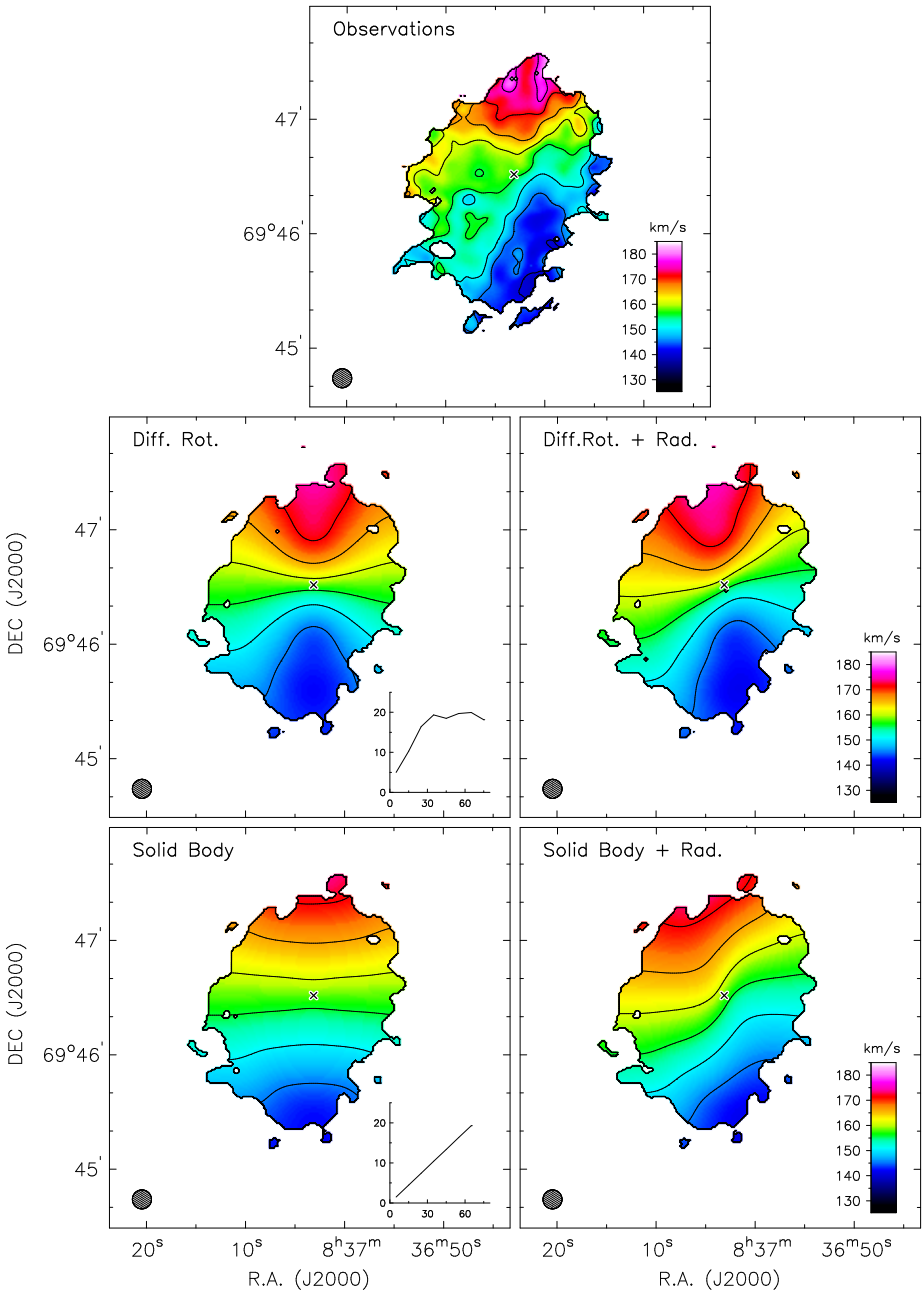

Figure 3.2 – Velocity fields derived from different 3D kinematic models and the observations. The rotation curve used to build the models is shown in the inset on the left (x-axis: radius in arcsec, y-axis: rotation velocity in km s^{-1}). Contours range from 140 to 181.6 km s^{-1}, with steps of 5.2 km s^{-1}. The circles show the beam size (10″). See Sect. 3.3.2 for details.

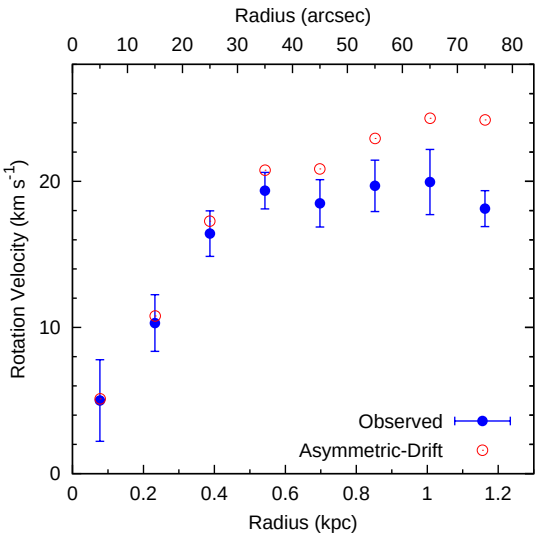

Figure 3.3 – Observed H I rotation curve (blue-filled circles) and asymmetric-drift-corrected rotation curve (red-open circles).

i fixed, using the values derived from the optical image by fitting ellipses to the outermost isophotes (see Table 3.1). An inclination of 58° is formally a lower limit, because the stellar component may be thick; if the disk is assumed to be 5° more edge-on, the rotation velocities would decrease by only ∼5%. We also fixed the P.A. assuming the value of 0° suggested by the H I morphology (Fig. 3.1, top), which is consistent with the optical P.A. ($\simeq -10°$) within the uncertainties. As a first step, we determined the systemic velocity $V_{\rm sys}$, by taking the mean value over all the rings. Then, we fixed $V_{\rm sys}$ and determined the rotation velocity $V_{\rm rot}$ and the radial velocity $V_{\rm rad}$ for each ring. The rotation curve has an amplitude of ∼18-20 km s^{-1} (Fig. 3.3), while the radial velocities are ∼4-5 km s^{-1}.

As a final step in the derivation of the rotation curve, we built 3D kinematic models, similarly to Swaters et al. (2009) and Lelli et al. (2010, 2012). The disk kinematics is assumed to be axisymmetric, while the H I distribution is clumpy, i.e. the surface density varies with position as in the observed H I map. The procedure is as follows: i) a disk with *uniform* surface density and constant thickness is constructed by fixing the velocity dispersion $\sigma_{\rm H\,I}$, the rotation velocity $V_{\rm rot}$ and the radial velocity $V_{\rm rad}$ at every radius; ii) the disk is projected on the sky using the geometrical parameters (x_0, y_0), $V_{\rm sys}$, P.A., and i and a model-cube is created; iii) the model-cube is convolved with the observational beam; and iv) the H I line profiles are rescaled to reproduce the observed H I map, i.e. the flux density is recovered at every spatial pixel. For the geometrical parameters, we used the values in Table 3.1. For the vertical distribution, we assumed an exponential-law $\exp(-z/z_0)$ with z_0=100 pc. We also assumed that $\sigma_{\rm H\,I}$=8 km s^{-1} over the entire disk; a mean velocity dispersion

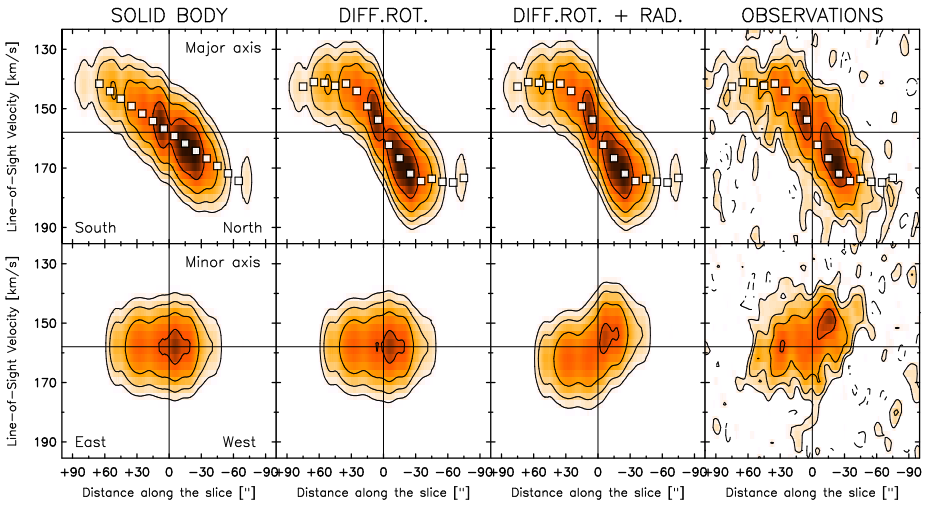

Figure 3.4 – Position-velocity diagrams derived for different 3D kinematic models and from the observations. The slices are taken along the major and minor axes. Contours are at 1.5, 3, 6, 12 × σ, where σ=0.66 mJy/beam. Squares show the rotation curve used to build the models. See Sect. 3.3.2 for details.

higher than 10 km s^{-1} can be ruled out by comparing the shape of position-velocity (PV) diagrams obtained from the models and the observations. The values of z_0 and $\sigma_{\rm H\,I}$ are slightly degenerate, but do not significantly affect the final results. For the rotation curve, we used the rotation velocities obtained by fitting the velocity field, then we corrected them by trial and error to obtain a model-cube that matches the observations. We find a good match by increasing the first four points by ∼3 km s^{-1}. This rotation curve is shown in Fig. 3.3. The comparison between models and observations has been done using velocity fields (see Fig. 3.2) and PV-diagrams (see Fig. 3.4), Note that the model velocity fields were derived from the model-cubes and, therefore, include the effects of spatial and spectral resolution, velocity dispersion, and possible non-circular motions. Because in our models we initially assumed a uniform H I disk, some aspects of the effects of beam-smearing are not fully included if the H I distribution varies rapidly on small scales. However, we used PV-diagrams at the full resolution (5.″7×4.″5) and compared them with those at 10″ to check that beam-smearing effects do not significantly affect our rotation curve.

Figure 3.3 (filled-circles) shows that UGC 4483 has a steeply-rising rotation curve that flattens in the outer parts at a velocity of ∼18-20 km s^{-1}. This is a striking difference with respect to Irrs of similar mass, as they usually have a slowly-rising rotation curve close to a solid body. As far as we know, UGC 4483 is the lowest-mass galaxy with a differentially rotating H I disk. To further test the validity of this result, we built 3D kinematic models assuming

a solid-body rotation curve and compared them with the differentially-rotating disk-model and with the observations. The results are shown in Fig. 3.2 and Fig. 3.4. It is clear that a flat rotation curve provides a better match of the observations than a solid-body one, as the iso-velocity contours of the observed velocity field display a curvature that is typical of differential rotation. The same conclusions are reached by comparing PV-diagrams obtained from the models and the observations along the major axis (Fig. 3.4, top). The observed PV-diagram shows a "flattening" on the southern-approaching side of the disk, that is reproduced only by a differentially rotating disk. On the northern-receding side, the "flattening" is less clear as the disk is less extended, but a differentially rotating disk is still preferable than a solid body one.

A simple rotating disk, however, cannot reproduce the asymmetries present in the observed velocity field. In particular, the kinematic minor axis, defined by the contours close to the systemic velocity, is not orthogonal to the major axis. This may be due either to radial motions (e.g. Fraternali et al. 2002) or to an oval distortion of the gravitational potential (e.g. Bosma 1978). These asymmetries can be seen also in the PV-diagram taken along the *geometrical* minor axis, i.e. in the direction perpendicular to the major axis (Fig 3.4, bottom). Thus, we improved our models by adding a constant radial component of $\sim$5 km s^{-1}, which is also indicated by the tilted-ring fit to the velocity field. A model with solid-body rotation plus radial motions is still not acceptable (Fig. 3.2, bottom-right), whereas a model with differential rotation plus radial motions reproduces most of the features in the data (Fig. 3.2, middle-right and Fig. 3.4, bottom).

The errors on the rotation curve have been estimated as $\sigma^2_{\rm rot} = \sigma^2_{\rm fit} + \sigma^2_{\rm asym}$, where $\sigma^2_{\rm fit}$ is the formal error given by the tilted-ring fit and $\sigma^2_{\rm asym}$ is an additional uncertainty due to the asymmetries between the approaching and receding sides, that is estimated as $\sigma_{\rm asym} = (V_{\rm rot,app} - V_{\rm rot,rec})/4$ (Swaters et al. 2009). We point out that the observed H I line profiles are quite broad and, therefore, it is very difficult to trace the rotation curve in the innermost parts. We compared models that have an inner solid-body rise and flatten at different radii and estimated that the rotation curve must flatten between $\sim$0.3 and $\sim$0.6 kpc, giving an inner rotation-velocity gradient between $\sim$35 and $\sim$65 km s^{-1} kpc^{-1}. We adopted an intermediate value for the rotation-velocity gradient.

In UGC 4483 the H I velocity dispersion $\sigma_{\rm H\,I}$ is only a factor $\sim$2-3 smaller than the observed rotation velocity $V_{\rm rot}$. Thus, in order to trace the gravitational potential, the rotation curve has to be corrected for pressure support. We calculated the asymmetric-drift correction following Meurer et al. (1996). We assumed that the H I disk has constant scale-height and velocity dispersion, and fitted the H I surface density profile (Fig. 3.7) with the Gaussian function $\Sigma_{\rm H\,I}\,(R) = \Sigma_0 \times \exp\left(-R^2/2s^2\right)$, obtaining $\Sigma_0 = 10.5\ M_\odot$ pc^{-2} and $s = 580$ pc. The circular velocity $V_{\rm circ}$, corrected for asymmetric-drift, is thus given by $V^2_{\rm circ} = V^2_{\rm rot} + \sigma^2_{\rm H\,I}(R^2/s^2)$. Using the 3D models, we can constrain the mean velocity dispersion between $\sim$6 and $\sim$10 km s^{-1}. We assumed the intermediate

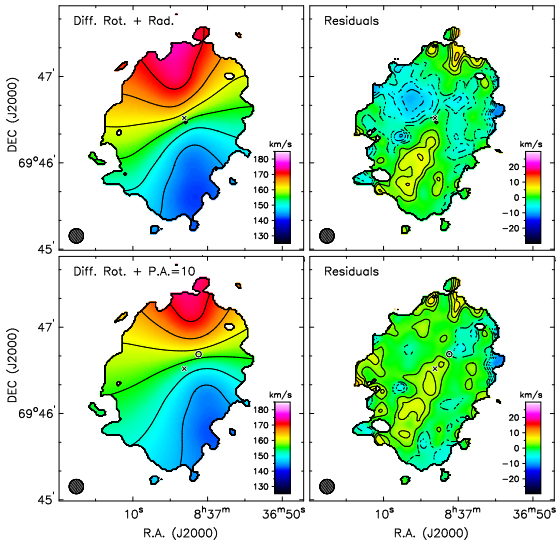

Figure 3.5 – *Left*: Velocity fields derived from disk-models with different geometrical parameters: optical centre (cross), P.A.=0°, and radial motions of ∼5 km s^{-1} (top panel, same as Fig. 3.2 middle-right); shifted dynamical centre (circle), P.A.=10°, and no radial motions (bottom panel). Contours are the same as in Fig. 3.2. *Right:* differences between the observed and the model velocity fields. Contours are at ±2, ±4, ±6, ±8 km s^{-1}. The filled circle shows the beam.

value of 8 km s^{-1}. The asymmetric-drift correction is significant only in the outer parts (see Fig. 3.3). Depending on the assumed value of $\sigma_{\rm H\,I}$, the correction at the last measured points may be between ∼2 and ∼8 km s^{-1}, giving a dynamical mass between about 1 and 2 $\times 10^8$ $M_\odot$.

In the above analysis, we used the centre and the P.A. derived from the stellar and H I morphologies. However, the differences between the observed and the best-model velocity fields (Fig. 3.5, top-right) show a systematic pattern that may point to a different location of the dynamical centre (cf. Warner et al. 1973, their Fig. 8). Thus, we built further models by changing the position of the centre and found that a shift of ∼14″ (∼220 pc) towards the North-West reduces the pattern significantly. Moreover, a disk-model with an off-set centre and a P.A.≃10° can reproduce the observed velocity field without radial motions (Fig. 3.5, bottom). However, these values for the centre and the P.A. are in marked contrast with the observed stellar and H I morphologies. In particular, the distribution of the old stars (which constitute an important fraction of the dynamical mass in the inner parts, see Sect. 3.3.3) is remarkably symmetric and consistent with the centre and P.A. previously adopted (see Fig. 6 of Dolphin et al. 2001 and Fig. 9 of Izotov & Thuan 2002). Thus, in the following, we keep the dynamical centre coincident with the optical one. This has no significant effects on the derived rotation curve.

3.3.3 Mass models

In Sect. 3.3.2, we showed that UGC 4483 has a steeply-rising and flat rotation curve, indicating that there is a strong central concentration of mass.

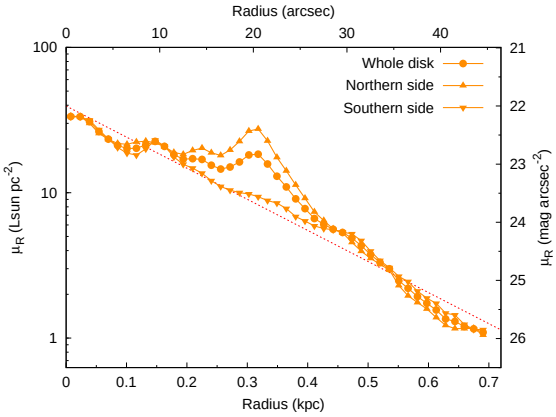

Figure 3.6 – R-band surface brightness profiles, derived separately for the northern (up-triangles) and southern (down-triangles) sides and for the entire galaxy (dots). The profiles are not corrected for internal extinction and inclination. The red-dotted line shows an exponential fit to the southern profile, giving $\mu_0 = 22.0$ mag arcsec^{-2} ($\sim 40\ L\odot$ pc^{-2}) and $R_{\rm d} = 13.1'' \pm 0.1''$ (~ 203 pc).

To determine the relative contributions of luminous and dark matter to the gravitational potential, we built mass models following Begeman (1987).

The gravitational contribution of the stars was calculated using a new approach: we estimated the stellar mass-to-light ratio M_*/L using the HST results on the resolved stellar populations. Surface brightness profiles were derived from a sky-subtracted R-band image (Fig. 3.1, top-left), azimuthally averaging over a set of ellipses defined by (x_0, y_0), i, and P.A (see Table 3.1). The sky-background was determined by masking the sources in the field and fitting a 2D polynomial to the masked image. The surface brightness profiles were not corrected for internal extinction, as UGC 4483 is extremely metal-poor (Skillman et al. 1994) and the dust content is likely to be low, but were corrected for Galactic extinction assuming $A_{\rm R} = 0.09$ (Schlegel et al. 1998). Figure 3.6 shows the surface brightness profiles derived for the entire galaxy and for the southern (approaching) and northern (receding) halves separately. At $R \simeq 20''$, the northern side of the galaxy is $\sim$1 mag brighter than the southern one, owing to the recent starburst. Dolphin et al. (2001) and Izotov & Thuan (2002) resolved UGC 4483 into single stars and showed that the young stellar populations are mostly concentrated to the North. The mass in young stars, however, constitutes only $\sim$10% of the total stellar mass: the SFH derived by McQuinn et al. (2010a) (modelling the color-magnitude diagram) implies that the stellar mass formed in the last 500 Myr is $\sim 0.15\times10^7\ M_\odot$, whereas the stellar mass formed more than 500 Myr ago is $\sim 1.31\times10^7\ M_\odot$. Thus, to calculate the gravitational contribution of the stars, we used the southern surface brightness profile, as it provides a better approximation of the stellar mass surface density. Assuming that $30\% \pm 10\%$ of the gas is returned to the inter stellar medium by supernovae and stellar winds, the total stellar mass is $(1.0 \pm 0.3) \times 10^7\ M_\odot$ (cf. McQuinn et al. 2010b), giving a stellar mass-to-light ratio $M_*/L_{\rm R} = 1.1 \pm 0.3$. The southern surface brightness profile can be fitted by an exponential-law with $\mu_0 = 22.0 \pm 0.1$ mag arcsec^{-2} ($\sim 40\ L_\odot$ pc^{-2}) and

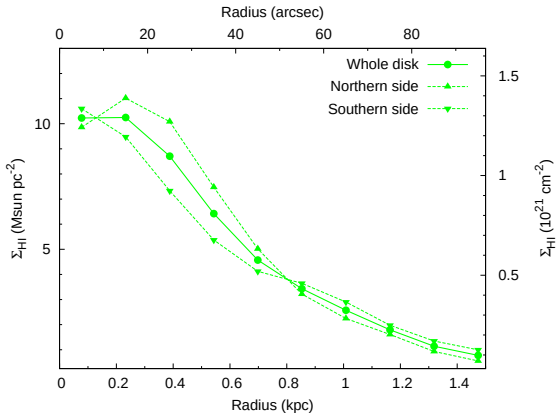

Figure 3.7 – H I surface density profiles (inclination corrected), derived separately for the northern (up-triangles) and southern (down-triangles) sides and for the entire galaxy (dots).

$R_{\rm d} = 13.1'' \pm 0.1''$ (~ 203 pc). We assumed that the stars are located in a disk with vertical density distribution given by $\rho(z) = {\rm sech}^2(z/z_0)$ (van der Kruit & Searle 1981) with $z_0 \simeq 0.5 R_{\rm d} \simeq 100$ pc.

The gravitational contribution of the gaseous disk was calculated using the azimuthally-averaged H I surface density profile, which was derived from the total H I map. Figure 3.7 shows the H I density profiles derived by azimuthally-averaging over the entire galaxy and over the southern (approaching) and northern (receding) sides separately. There is a difference of the order of $\sim$2-3 $M_\odot$ pc^{-2} between the two halves, that has a small effect on the resulting gravitational contribution. In agreement with the models in Sect. 3.3.2, we assumed an exponential vertical distribution with $z_0 = 100$ pc. The mass of the H I disk was calculated from the total H I flux (see Table 3.1) and multiplied by a factor of 1.33 to take into account the presence of Helium. Molecular gas was not explicitly considered in the mass model because its amount is unknown.

For the dark matter distribution, we assumed a pseudo-isothermal halo described by the equation

$$\rho_{\rm ISO}(r) = \frac{\rho_0}{1 + (r/r_{\rm c})^2}, \tag{3.1}$$

where the central density ρ_0 and the core radius $r_{\rm c}$ are both free parameters of the mass model.

Figure 3.8 (left) shows the rotation curve decomposition assuming that $M_*/L_{\rm R}$=1.1, as is found by integrating the galaxy SFH (McQuinn et al. 2010a,b). The gravitational contribution of the stars V_* is $\sim$50% of the circular velocity $V_{\rm circ}$ at $R_{\rm peak} = 2.2 R_{\rm d} \simeq 450$ pc. The parameters of the halo are $\rho_0 = (101 \pm 20) \times 10^{-3}$ $M_\odot$ pc^{-3} and $r_{\rm c} = 0.34 \pm 0.05$ kpc. These values are comparable with those found by Swaters et al. (2011) for a sample of 18 Irrs (assuming that $M_*/L_{\rm R}$=1); the halo of UGC 4483, however, is one with the smallest core radius and highest central density. As discussed at the end

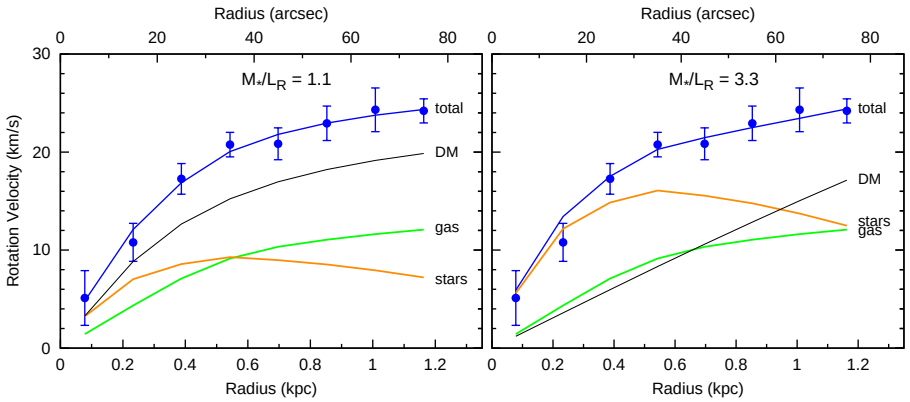

Figure 3.8 – Rotation curve decompositions with the $M_*/L_{\rm R}$ (= 1.1) obtained from the study of the resolved stellar populations (*left*) and with the $M_*/L_{\rm R}$ (= 3.3) from the maximum-disk solution (*right*). Dots show the observed rotation curve. Lines show the gravitational contribution of the gas, stars, and dark matter and the resulting rotation curve.

of Sect 3.3.1, we applied the asymmetric-drift correction assuming a constant velocity dispersion $\sigma_{\rm H\,I} = 8$ km s^{-1}. Different values of $\sigma_{\rm H\,I}$ would change the circular velocity at large radii and, thus, give slightly different values for the dark matter halo. In particular, considering that $\sigma_{\rm H\,I}$ may be between 6 and 8 km s^{-1}, the dynamical mass within the last measured point of the rotation curve may be between 1 and 2 $\times 10^8$ $M_\odot$ and the baryon fraction between $\sim$43% and $\sim$22%, respectively. In any case, baryons (gas and stars) constitute a relevant fraction of the total mass.

A stellar disk is defined to be maximum if $F_* = V_*/V_{\rm circ} = 0.85 \pm 0.10$ at $R_{\rm peak}$ (Sackett 1997; Bershady et al. 2011). In our case $F_* = 0.5 \pm 0.1$; the error takes into account the uncertainties on the stellar mass, the gas-recycling efficiency and the rotation velocity. This is in line with the results of the DiskMass survey (Bershady et al. 2011), that have measured the stellar velocity dispersion in a sample of spiral galaxies and found that stellar disks typically have $F_* \simeq 0.5$. We point out that the colour-magnitude diagrams of the resolved stellar populations provide the most direct method to quantify stellar masses, as the results depend only slightly on the assumed evolutionary tracks, metallicity, and sampling of the SFH (e.g. Annibali et al. 2003). The initial mass function (IMF), instead, may have a stronger effect: McQuinn et al. (2010a) assumed a single-slope Salpeter from 0.1 to 100 $M_\odot$ and a binary fraction of 35%. If the Chabrier and/or Kroupa IMFs are assumed, the stellar mass would systematically decrease by, respectively, $\sim$25% and $\sim$30% and the gas-recycling efficiency may go up to $\sim$50%, further decreasing the stellar mass.

We note that the molecular gas component has been neglected so far. UGC 4483 is undetected in the CO line with an upper limit of 0.195 K km s^{-1}

within the inner 55″ (∼800 pc) (Taylor et al. 1998). We extrapolated the relation between the CO-to-H_2 conversion factor and metallicity from Boselli et al. (2002) down to the metallicity of UGC 4483, and obtained a corresponding upper limit on the H_2 mass of $M_{H_2} \lesssim 10^7\ M_\odot$. Alternatively, we estimated the H_2 mass from the empirical relation between SFR and molecular mass, as determined by Leroy et al. (2008), although this relation may not apply to starburst galaxies. Assuming that SFR = 0.01 $M_\odot$ yr^{-1} (McQuinn et al. 2010a), we derived $M_{H_2} \simeq 1.9 \times 10^7\ M_\odot$. Both estimates indicate that the molecular gas may be dynamically important and comparable in mass to the stellar component, implying a full maximum-disk situation, as we now discuss.

Figure 3.8 (right) shows the maximum-disk solution (Sancisi & van Albada 1987). The stellar contribution can explain the inner parts of the rotation curve if $M_*/L_R \simeq 3.3$, i.e. if the stellar mass is ∼3 times higher than obtained from the study of the resolved stellar populations. This mass may be provided by molecules, if they are distributed in a way similar to the stars. We also find a good fit by fixing $M_*/L_R = 1.1$ and scaling the H I contribution by a factor of ∼5, similarly to the results of Hoekstra et al. 2001 for other gas-rich galaxies. These results suggest that the distribution of the dynamical mass is closely coupled to that of the baryonic mass (see e.g. Sancisi 2004 and Swaters et al. 2011). We also checked the position of UGC 4483 on the baryonic Tully-Fisher relation and found that it follows the correlation within the observed scatter (cf. McGaugh 2011).

Finally, we considered the predictions of the MOdified Newtonian Dynamics (MOND) (Milgrom 1983, see Famaey & McGaugh 2011 for a review). Using UGC 4483, we can test MOND without any free parameter, as the value of M_*/L is provided by the colour-magnitude diagram of the resolved stellar populations and the distance is well determined from the tip of the red giant branch (Dolphin et al. 2001; Izotov & Thuan 2002). We found that MOND systematically over-predicts the observed rotation curve by ∼5-6 km s^{-1}. The discrepancy does not strongly depend on the assumed M_*/L, as it is mainly driven by the atomic gas content, and it would further increase if molecules are also considered in the mass model. However, the discrepancy disappears if the inclination of the H I disk is assumed to be ∼43° instead of 58° (as is derived from the optical image). This possibility cannot be ruled out by the present observations, because it is not possible to determine i neither from the total H I map (as the H I distribution is strongly lopsided) nor from the velocity field.

3.4 Discussion

In Sect. 3.3.2, we showed that UGC 4483 has a steeply-rising rotation curve that flattens in the outer parts at a velocity of ∼18-20 km s^{-1}. As far as we know, this is the lowest-mass galaxy with a differentially rotating H I disk. The steep rise of the rotation curve points to a strong central concentration of mass,

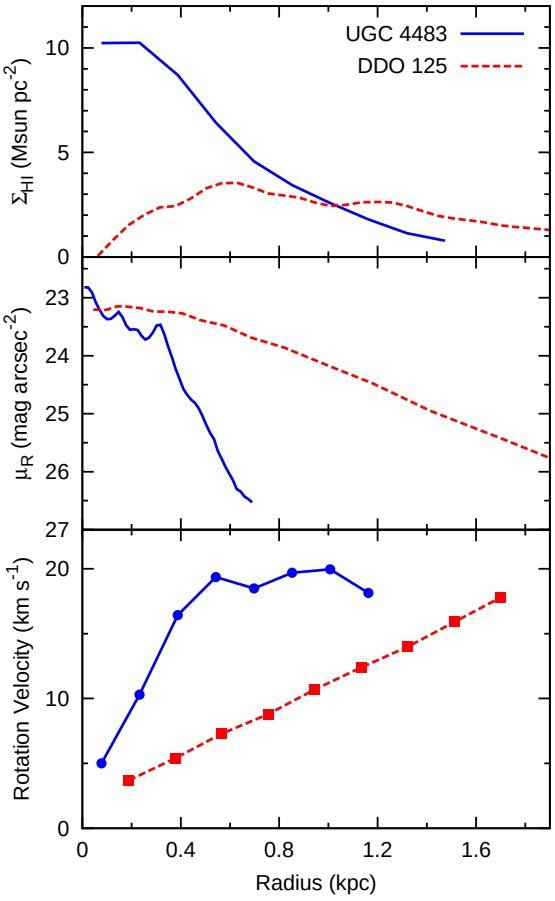

Figure 3.9 – Comparison between UGC 4483 (blue line) and the dwarf irregular galaxy DDO 125 (UGC 7577) (red line). *Top:* H I surface density profiles. *Middle:* *R*-band surface brightness profiles, corrected for the inclination assuming that the disk is transparent and using the ellipticity from Swaters & Balcells (2002). *Bottom:* H I rotation curves (not corrected for asymmetric drift).

which seems to be a characterizing property of BCDs. Indeed, similar results have been found also for other BCDs, e.g. I Zw 18 (Lelli et al. 2012), NGC 2537 (Matthews & Uson 2008), and NGC 1705 (Meurer et al. 1998). The steeply-rising and flat rotation curves of these BCDs are remarkable, as Irrs typically have slowly-rising rotation curves (e.g. Swaters et al. 2009). The terms "steeply-rising" and "slowly-rising" are referred to rotation-velocity gradients measured in physical units (km s^{-1} kpc^{-1}) that can be directly related to the dynamical mass surface densities in $M_\odot$ pc^{-2}. If these gradients are expressed in terms of disk scale-lengths, rotation curves of Irrs rise as steep as those of spiral galaxies (e.g. Swaters et al. 2009).

In Lelli et al. (2012) (Fig. 10), we have illustrated the dynamical difference between the BCD-prototype I Zw 18 and a typical Irr of the same mass. Similarly, Fig. 3.9 compares UGC 4483 with the dwarf irregular DDO 125 (UGC 7577, from Swaters et al. 2009). Assuming that DDO 125 is at a distance

of 2.6 Mpc (Jacobs et al. 2009; Dalcanton et al. 2009), the H I observations of Swaters et al. (2009) have a linear resolution of ∼180 pc, similar to our linear resolution for UGC 4483 (∼155 pc), making it possible to compare H I surface densities and velocity gradients. The two galaxies have approximately the same rotation velocity at the last measured point (∼20 km s^{-1}) and dynamical mass (∼1-2×10^8 $M_\odot$), but their structural properties are very different: i) the H I surface densities of UGC 4483 are ∼3-4 times higher than those of DDO 125 in the inner regions (top); ii) the stellar component of UGC 4483 is much more compact than that of DDO 125 (middle); iii) the rotation curve of UGC 4483 has a steeper rise than the one of DDO 125 and flattens in the outer parts. These structural and dynamical differences between BCDs and typical Irrs must be the key to understand the starburst phenomenon in BCDs. They also shed new light on the question of the progenitors and descendants of BCDs, as we now discuss.

In Section 3.3.3, we showed that the central mass concentration of UGC 4483 cannot be explained by the newly formed stars or by the concentration of H I. Old stars, although not sufficient to account for the inner rise of the rotation curve, constitute an important fraction of the mass in the inner parts. Similarly, the central mass concentration of I Zw 18 may be due to old stars and/or dark matter (unfortunately, the HST observations of I Zw 18 do not provide a direct estimate of the mass in old stars, see Contreras Ramos et al. 2011). For both galaxies, the gravitational contribution of molecules is very uncertain and it is unclear whether they are dynamically important or not. These results imply that either the progenitors of these BCDs are unusually compact, gas-rich dwarfs, or there must be a mechanism that leads to a concentration of gas, old stars, and/or dark matter, eventually causing the starburst. This mechanism may be external (interactions/mergers) and/or internal (torques from massive star-forming "clumps", see Elmegreen et al. 2012). It is also clear that, unless a redistribution of mass takes place, the descendants of BCDs must be compact dwarfs. Compact Irrs do exist and have the following properties: i) high-surface-brightness exponential profiles (see e.g. UGC 7690 and UGC 8550 in Swaters & Balcells 2002) or low-surface-brightness exponential profiles with an inner light concentration (see e.g. UGC 6628 and UGC 12632 in Swaters & Balcells 2002), and ii) steeply-rising and flat rotation curves (see the same galaxies in Swaters et al. 2009). The evolutionary links outlined here are in line with the results of e.g. Papaderos et al. (1996) and Gil de Paz & Madore (2005), which are based on surface photometry of large galaxy samples and indicate that the old stellar component of BCDs generally has higher central surface brightness and smaller scale-length than typical Irrs and Sphs. We present here two plots that compare the structural and dynamical properties of BCDs and Irrs.

In order to compare the *dynamics* of BCDs and Irrs, we use the inner circular-velocity gradient $d_{\rm R}V(0) \simeq V_{\rm circ}/R$ as an estimate of central concentration of mass (see also Chapter 5 and Chapter 7). This is calculated at

$R = R_{\rm d}$ (along the solid-body portion of the rotation curve), where $R_{\rm d}$ is the galaxy scale-length in the R-band. In Fig. 3.10, $V_{\rm circ}(R_{\rm d})/R_{\rm d}$ is plotted versus the central disk surface brightness μ_0 (left) and the peak H I column density $\Sigma_{\rm H\,I,\,peak}$ (right) for a sample of both BCDs and Irrs. The BCDs are UGC 4483, I Zw 18, NGC 1705, and NGC 6789. For I Zw 18, we used the R-band structural parameters from Papaderos et al. (2002), the rotation curve from Lelli et al. (2012), and a distance of 18.2 Mpc (Aloisi et al. 2007). For NGC 1705, we used the R-band structural parameters from Gil de Paz & Madore (2005), the rotation curve from Meurer et al. (1998) named "model DD" (see their Fig. 10), and a distance of 5.1 Mpc (Tosi et al. 2001). For NGC 6789, we used the R-band structural parameters and the rotation curve from Chapter 4, and a distance of 3.6 Mpc (Drozdovsky et al. 2001). The Irrs were taken from the sample of Swaters et al. (2009), by selecting objects that have high-quality rotation curves ($q \leq 2$, see Swaters et al. 2009) and $V_{\rm rot} < 70$ km s^{-1} at the last measured point. For $\Sigma_{\rm H\,I,\,peak}$, we used the peak value of the azimuthally-averaged H I density profile. The value of $\Sigma_{\rm H\,I,\,peak}$ depends on the linear resolution of the H I observations, but we checked that this does not strongly bias our analysis as the trend in Fig. 3.10 does not significantly change if one considers only galaxies with linear resolution $\lesssim$500 pc. We also point out that BCDs usually have clumpy H I distributions and locally the H I column densities can reach even higher values, up to 40-50 $M_\odot$ pc^{-2}, much higher than in Irrs.

The two diagrams in Fig. 3.10 show a clear trend: galaxies with a high circular-velocity gradient have also high central surface brightness (left) and high peak H I surface density (right). The BCDs are in the upper parts of these distributions: they have $V_{\rm circ}(R_{\rm d})/R_{\rm d} \gtrsim 40$ km s^{-1} kpc^{-1} whereas Irrs typically have $V_{\rm circ}(R_{\rm d})/R_{\rm d} < 40$ km s^{-1} kpc^{-1}. However, some Irrs (UGC 3966, UGC 8550, UGC 7232, and UGC 7690) have inner circular-velocity gradients comparable to those of BCDs and thus, in this respect, are dynamically similar to BCDs. These objects have peak H I column densities much smaller than those found in I Zw 18 and NGC 1705 (Fig. 3.10, right) and are candidate progenitors/descendants of BCDs. It would be interesting to study the SFHs of these compact Irrs and investigate if they experienced a starburst in the recent past.

Finally, we have seen that the asymmetries in the velocity field of UGC 4483 can be described as a global radial motion of 5 km s^{-1}. Radial motions have been found in two other BCDs: NGC 2915 (Elson et al. 2011a,b) and I Zw 18 (Lelli et al. 2012). Elson et al. (2011a) assumed that the spiral arms in the H I disk of NGC 2915 are trailing and concluded that the radial motions are an outflow. For I Zw 18 and UGC 4483, it is not possible to discriminate between inflow and outflow, as it is not known which side of the disk is the near one. For both galaxies, we calculated the timescales associated with the radial motions ($\simeq R_{\rm H\,I}/V_{\rm rad}$) and found that they are of the same order of magnitude of the orbital times ($\simeq 2\pi R_{\rm H\,I}/V_{\rm rot}$). This suggests that any outflow or inflow must be

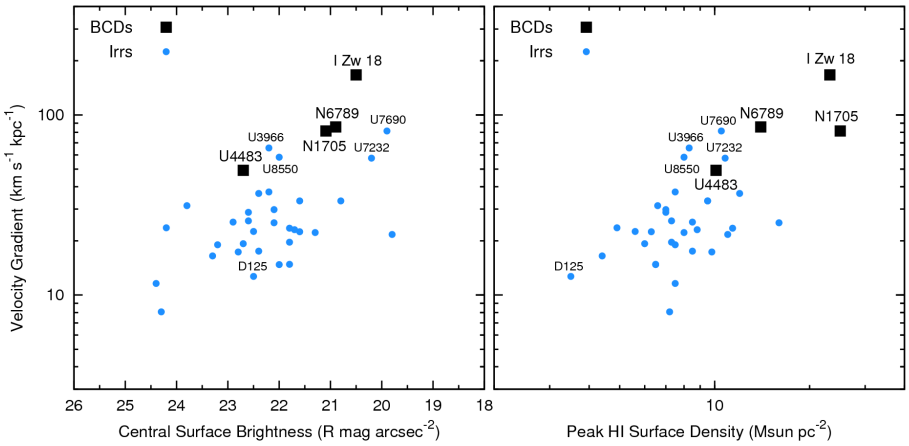

Figure 3.10 – Comparison between the properties of BCDs (squares) and Irrs (dots). The Irrs are taken from Swaters et al. (2009), selecting the objects with high-quality rotation curves and $V_{\rm rot} < 70$ km s^{-1} at the last measured point. The BCDs are UGC 4483 (this work), I Zw 18 (Lelli et al. 2012), NGC 6789 (Chapter 4), and NGC 1705 (Meurer et al. 1998). Some galaxies are labelled according to their UGC number. *Left:* R-band central surface brightness (inclination corrected) versus the inner circular-velocity gradient $d_R V(0) \simeq V_{\rm circ}(R_{\rm d})/R_{\rm d}$, where $R_{\rm d}$ is the optical scale-length. *Right:* peak H I surface density $\Sigma_{\rm H\,I,\,peak}$ versus $V_{\rm circ}(R_{\rm d})/R_{\rm d}$. $\Sigma_{\rm H\,I,\,peak}$ is derived from the azimuthally-averaged H I surface density profiles. See Sect. 3.4 for details.

very recent and possibly associated with the most recent burst of star-formation (∼10-20 Myr, see McQuinn et al. 2010a for UGC 4483 and Aloisi et al. 1999 for I Zw 18). If the radial motions were an outflow, its kinetic energy would correspond to only ∼1% of the energy released by supernovae.

3.5 Conclusions

We analysed archival H I observations of the blue compact dwarf galaxy UGC 4483 and built model datacubes to investigate its gas kinematics. Our main results can be summarized as follows:

1. UGC 4483 has a steeply-rising rotation curve that flattens in the outer parts at a velocity of ∼20 km s^{-1}. This is, to our knowledge, the lowest-mass galaxy with a differentially rotating H I disk. Radial motions of ∼5 km s^{-1} may also be present.

2. The steep rise of the rotation curve indicates that there is a strong central concentration of mass. Mass models with a dark matter halo show that *old* stars contribute ∼50% of the observed rotation speed at 2.2 disk scale-lengths. Baryons (gas and stars) constitute an important fraction

of the total dynamical mass. These conclusions are based on the stellar mass obtained from the color-magnitude diagram of the resolved stellar populations.

3. The maximum-disk solution requires a stellar mass 3 times higher than observed, that could be provided by molecules. A good solution is also found by scaling the H I contribution by a factor of ∼5. These results suggest that the distribution of the dynamical mass is closely coupled to that of the baryons.

UGC 4483, together with other BCDs like I Zw 18 and NGC 1705, appears structurally different from typical Irrs in terms of H I distribution, stellar distribution, and dynamics. In particular, a central concentration of mass (gas, stars, and dark matter) seems to be a characterizing property of BCDs. This implies that the starburst is closely related with the gravitational potential and the H I concentration. Our results also suggest that the progenitors/descendants of BCDs must be compact dwarf galaxies, unless a redistribution of mass (both luminous and dark) takes place before/after the starbursting phase.

Acknowledgements

We thank Rob Swaters for stimulating comments. We are grateful to F. Annibali and M. Tosi for helpful discussions about the stellar populations of BCDs. We thank the ISSI (Bern) for support of the team “Defining the full life-cycle of dwarf galaxy evolution: the Local Universe as a template”.

References

Aloisi, A., Clementini, G., Tosi, M., et al. 2007, ApJL, 667, L151
Aloisi, A., Tosi, M., & Greggio, L. 1999, AJ, 118, 302
Annibali, F., Greggio, L., Tosi, M., Aloisi, A., & Leitherer, C. 2003, AJ, 126, 2752
Begeman, K. G. 1987, PhD thesis, , Kapteyn Institute, (1987)
Bershady, M. A., Martinsson, T. P. K., Verheijen, M. A. W., et al. 2011, ApJL, 739, L47
Binney, J. & Merrifield, M. 1998, Galactic astronomy, ed. Binney, J. & Merrifield, M.
Boselli, A., Lequeux, J., & Gavazzi, G. 2002, A&A, 384, 33
Bosma, A. 1978, PhD thesis, PhD Thesis, Groningen Univ., (1978)
Briggs, D. S. 1995, in Bulletin of the American Astronomical Society, Vol. 27, Bulletin of the American Astronomical Society, 1444–+
Contreras Ramos, R., Annibali, F., Fiorentino, G., et al. 2011, ApJ, 739, 74
Dalcanton, J. J., Williams, B. F., Seth, A. C., et al. 2009, ApJS, 183, 67
Dolphin, A. E., Makarova, L., Karachentsev, I. D., et al. 2001, MNRAS, 324, 249
Drozdovsky, I. O., Schulte-Ladbeck, R. E., Hopp, U., Crone, M. M., & Greggio, L. 2001, ApJL, 551, L135
Elmegreen, B. G., Zhang, H.-X., & Hunter, D. A. 2012, ApJ, 747, 105
Elson, E. C., de Blok, W. J. G., & Kraan-Korteweg, R. C. 2011a, MNRAS, 411, 200
Elson, E. C., de Blok, W. J. G., & Kraan-Korteweg, R. C. 2011b, MNRAS, 415, 323
Famaey, B. & McGaugh, S. 2011, ArXiv e-prints
Fraternali, F., van Moorsel, G., Sancisi, R., & Oosterloo, T. 2002, AJ, 123, 3124
Gallagher, III, J. S. & Hunter, D. A. 1987, AJ, 94, 43
Gil de Paz, A. & Madore, B. F. 2005, ApJS, 156, 345
Gil de Paz, A., Madore, B. F., & Pevunova, O. 2003, ApJS, 147, 29
Hoekstra, H., van Albada, T. S., & Sancisi, R. 2001, MNRAS, 323, 453
Högbom, J. A. 1974, A&AS, 15, 417
Izotov, Y. I. & Thuan, T. X. 2002, ApJ, 567, 875
Jacobs, B. A., Rizzi, L., Tully, R. B., et al. 2009, AJ, 138, 332
Lelli, F., Fraternali, F., & Sancisi, R. 2010, A&A, 516, A11+
Lelli, F., Verheijen, M., Fraternali, F., & Sancisi, R. 2012, A&A, 537, A72
Leroy, A. K., Walter, F., Brinks, E., et al. 2008, AJ, 136, 2782
Lo, K. Y., Sargent, W. L. W., & Young, K. 1993, AJ, 106, 507
Matthews, L. D. & Uson, J. M. 2008, AJ, 135, 291
McGaugh, S. S. 2011, Physical Review Letters, 106, 121303
McQuinn, K. B. W., Skillman, E. D., Cannon, J. M., et al. 2010a, ApJ, 721, 297
McQuinn, K. B. W., Skillman, E. D., Cannon, J. M., et al. 2010b, ApJ, 724, 49

Meurer, G. R., Carignan, C., Beaulieu, S. F., & Freeman, K. C. 1996, AJ, 111, 1551
Meurer, G. R., Staveley-Smith, L., & Killeen, N. E. B. 1998, MNRAS, 300, 705
Milgrom, M. 1983, MNRAS, 270, 365
Papaderos, P., Izotov, Y. I., Thuan, T. X., et al. 2002, A&A, 393, 461
Papaderos, P., Loose, H., Fricke, K. J., & Thuan, T. X. 1996, A&A, 314, 59
Sackett, P. D. 1997, ApJ, 483, 103
Sancisi, R. 2004, in IAU Symposium, Vol. 220, Dark Matter in Galaxies, ed. S. Ryder, D. Pisano, M. Walker, & K. Freeman, 233–+
Sancisi, R. & van Albada, T. S. 1987, in IAU Symposium, Vol. 117, Dark matter in the universe, ed. J. Kormendy & G. R. Knapp, 67–80
Schlegel, D. J., Finkbeiner, D. P., & Davis, M. 1998, ApJ, 500, 525
Searle, L. & Sargent, W. L. W. 1972, ApJ, 173, 25
Skillman, E. D., Televich, R. J., Kennicutt, Jr., R. C., Garnett, D. R., & Terlevich, E. 1994, ApJ, 431, 172
Swaters, R. A. & Balcells, M. 2002, A&A, 390, 863
Swaters, R. A., Sancisi, R., van Albada, T. S., & van der Hulst, J. M. 2009, A&A, 493, 871
Swaters, R. A., Sancisi, R., van Albada, T. S., & van der Hulst, J. M. 2011, ApJ, 729, 118
Taylor, C. L., Brinks, E., Grashuis, R. M., & Skillman, E. D. 1995, ApJS, 99, 427
Taylor, C. L., Kobulnicky, H. A., & Skillman, E. D. 1998, AJ, 116, 2746
Tosi, M. 2009, in IAU Symposium, Vol. 258, IAU Symposium, ed. E. E. Mamajek, D. R. Soderblom, & R. F. G. Wyse, 61–72
Tosi, M., Sabbi, E., Bellazzini, M., et al. 2001, AJ, 122, 1271
van der Hulst, J., Terlouw, J., Begeman, K., Zwitser, W., & Roelfsema, P. 1992, in ASP Conf. Ser. 25, ed. D. M. Worall, C. Biemesderfer, & J. Barnes, San Francisco: ASP, 131
van der Kruit, P. C. & Searle, L. 1981, A&A, 95, 105
van Zee, L. & Haynes, M. P. 2006, ApJ, 636, 214
van Zee, L., Salzer, J. J., & Skillman, E. D. 2001, AJ, 122, 121
van Zee, L., Skillman, E. D., & Salzer, J. J. 1998, AJ, 116, 1186
Verheijen, M. & Sancisi, R. 2001, A&A, 370, 765
Warner, P. J., Wright, M. C. H., & Baldwin, J. E. 1973, MNRAS, 163, 163

Chapter 4

Dynamics of starbursting dwarf galaxies. III. A HI study of 18 nearby objects

— **Federico Lelli, Marc Verheijen, and Filippo Fraternali** —

Submitted to Astronomy & Astrophysics

Abstract

We investigate the dynamics of starbursting dwarf galaxies, using both new and archival H I observations. We consider 18 nearby galaxies that have been resolved into single stars by HST observations, providing their star formation history and total stellar mass. We find that 9 objects have a regularly-rotating H I disk, 7 objects have a kinematically-disturbed H I disk, and 2 objects show unsettled H I distributions. Two galaxies (NGC 5253 and UGC 6456) show a velocity gradient along the minor axis of the H I disk, that we interpret as strong radial motions. For galaxies with a regularly-rotating disk, we derive rotation curves, while for galaxies with a kinematically-disturbed disk we estimate the rotation velocities in their outer parts. We derive baryonic fractions within about 3 optical scale-lengths and find that, on average, baryons constitute at least 30% of the total mass. Despite the star-formation having injected $\sim 10^{56}$ ergs in the ISM in the last $\sim$500 Myr, these starbursting dwarfs have both baryonic and gas fractions similar to those of typical dwarf irregulars, suggesting that they did not eject a large amount of gas out of their potential wells.

4.1 Introduction

Starburst activity is thought to strongly affect the evolution of dwarf galaxies. Both observations and theoretical models suggest that massive star-formation can alter the morphology and kinematics of the gas in dwarf galaxies (e.g. Mac Low & Ferrara 1999; Cannon et al. 2011), as well as their chemical properties (e.g. Recchi et al. 2004; Romano et al. 2006). Moreover, models of galaxy formation in a Λ cold dark matter (ΛCDM) cosmology require strong feedback from star-formation to explain several observational facts, such as i) the existence of bulgeless disk galaxies by removing low-angular-momentum gas from the galaxy center (e.g. Governato et al. 2010; Brook et al. 2011); ii) the "cored" DM profiles of dwarfs by flattening the presumed central "cusps" (e.g. Oh et al. 2011a; Governato et al. 2012); iii) the slope of the baryonic Tully-Fisher relation by reducing the baryonic fraction in galaxies (e.g. McGaugh 2012; Stringer et al. 2012), and iv) the number density of low-luminosity galaxies by suppressing star-formation in low-mass DM haloes (e.g. Okamoto et al. 2010; Sawala et al. 2013). Detailed dynamical studies of nearby starbursting dwarfs are necessary to determine the actual efficiency of these processes.

Starbursting dwarfs can be identified by i) their blue colors and high surface brightness, such as the Blue Compact Dwarfs (BCDs) (e.g. Gil de Paz et al. 2003); ii) their strong emission-lines, such as the H II-galaxies (e.g. Terlevich et al. 1991; Taylor et al. 1995); and iii) their peculiar morphologies, such as the "amorphous dwarfs" (e.g. Gallagher & Hunter 1987; Marlowe et al. 1999). Hereafter, we will refer to any starbursting dwarf as a BCD.

To date, detailed studies of the H I kinematics of BCDs have been focused either on individual galaxies (e.g. Viallefond & Thuan 1983; Hunter et al. 1996; Wilcots & Miller 1998; Matthews & Uson 2008), or on small galaxy samples with 4-5 objects (e.g. van Zee et al. 1998, 2001; Thuan et al. 2004; Ramya et al. 2011). These studies showed that some BCDs have regularly-rotating H I disks (e.g. van Zee et al. 1998, 2001), whereas other ones have complex H I kinematics (e.g. Cannon et al. 2004; Kobulnicky & Skillman 2008). The relative fraction of BCDs with ordered/disturbed H I kinematics remains unclear, as well as the possible relation between the gas kinematics and the starburst. The DM content of starbursting dwarfs is also poorly constrained. Elson et al. (2010, 2013) argued that the BCDs NGC 1705 and NGC 2915 are dominated by DM at all radii (see also Meurer et al. 1996, 1998). On the contrary, Walter et al. (1997) and Johnson et al. (2012) studied the starbursting dwarfs II Zw 33 and NGC 1569, respectively, and concluded that there is no need for DM to explain their inner kinematics.

To clarify these issues, we considered a sample of 18 starbursting dwarfs, for which we collected both new and archival H I observations. We selected objects that have been resolved into single stars by the *Hubble Space Telescope* (HST), providing a direct estimate of the recent star-formation history (SFH) and of the total stellar mass (e.g. Annibali et al. 2003). The latter information

Table 4.1 – Galaxy Sample

Name	Alternative Name	Dist (Mpc)	M_* (10^7 $M_\odot$)	M_R	M_*/L_R ($M_\odot/L_\odot$)	b	SFR_p ($10^{-3} M_\odot$ yr^{-1})	t_p (Myr)	12+log(O/H)	Ref.
NGC 625	ESO 297-G005	3.9±0.4	26±10	-17.25±0.24	>0.6	3.0±0.1	86±20	820±180	8.08±0.12	a, g, l
NGC 1569	UGC 3056	3.4±0.2	70±7	-17.14±0.25	1.7±0.2	21±1	240±10	40±10	8.19±0.02	a, h, m
NGC 1705	ESO 158-G013	5.1±0.6	>20	-16.35±0.26	>1	∼6	314±78	∼3	8.21±0.05	b, i, l
NGC 2366	UGC 3851	3.2±0.4	26±3	-16.64±0.27	1.0±0.1	5.6±0.4	160±10	450±50	7.91±0.05	a, h, l
NGC 4068	UGC 7047	4.3±0.1	22±3	-15.67±0.05	2.0±0.3	4.7±0.3	42±3	360±40	...	a, h
NGC 4163	UGC 7199	3.0±0.1	10±3	-14.81±0.10	2.0±0.6	2.9±0.6	12±3	450±50	7.56±0.14	a, h, l
NGC 4214	UGC 7278	2.7±0.2	>28	-17.77±0.24	>0.4	3.1±0.9	130±40	450±50	8.22±0.05	a, h, l
NGC 4449	UGC 7592	4.2±0.5	210±35	-18.88±0.26	1.0±0.2	6.0±0.5	970±70	5±3	8.26±0.09	a, h, l
NGC 5253	Haro 10	3.5±0.4	154±21	-17.61±0.27	2.4±0.3	9.0±0.9	400±40	450±50	8.12±0.05	a, g, k
NGC 6789	UGC 11425	3.6±0.2	7±2	-15.09±0.14	1.1±0.3	3.8±1.3	15±5	565±65	...	a, i
UGC 4483	...	3.2±0.2	1.0±0.2	-12.97±0.19	1.1±0.3	14±3	11±2	565±65	7.56±0.03	a, i, l
UGC 6456	VII Zw 403	4.3±0.1	5±2	-14.41±0.05	1.5±0.6	7.6±1.1	23±3	16±8	7.69±0.01	a, j, n
UGC 6541	Mrk 178	4.2±0.2	>0.8	-14.61±0.10	>0.2	∼3	∼3	...	7.82±0.06	c, j, l
UGC 9128	DDO 187	2.2±0.1	1.3±0.2	-12.82±0.12	1.6±0.2	6.3±1.4	5±1	150±50	7.75±0.05	a, h, l
UGCA 290	Arp 211	6.7±0.4	>1.0	-14.09±0.18	>0.4	∼3	42±15	∼15	...	d, i
I Zw 18	Mrk 116	18.2±1.4	>1.7	-14.99±0.26	>0.3	∼30	∼100	∼10	7.20±0.01	e, j, k
I Zw 36	Mrk 209	5.9±0.5	>0.8	-14.88±0.23	>0.1	∼7	∼25	...	7.77±0.01	f, i, k
SBS 1415+437	...	13.6±1.4	17±3	-15.90±0.25	1.3±0.2	12±2	150±10	450±50	7.62±0.03	a, i, o

Notes. Distances are derived from the TRGB. Stellar masses are calculated integrating the SFH and assuming i) a gas-recycling efficiency of 30%, and ii) a Salpeter IMF from 0.1 to 100 $M_\odot$. The birthrate parameter b is defined as $b = SFR_p/\overline{SFR}_{0-6}$, where SFR_p is the peak SFR over the past 1 Gyr and $\overline{SFR}_{0-6}$ is the mean SFR over the past 6 Gyr (see McQuinn et al. 2010b). t_p is the look-back time at SFR_p. The last column provides references for the HST studies of the resolved stellar populations, the integrated photometry, and the ionized gas metallicity, respectively.

References. (a) McQuinn et al. (2010a); (b) Annibali et al. (2003); (c) Schulte-Ladbeck et al. (2000); (d) Crone et al. (2002); (e) Annibali et al. (2013); (f) Schulte-Ladbeck et al. (2001); (g) Lauberts & Valentijn (1989); (h) Swaters & Balcells (2002); (i) Gil de Paz et al. (2003); (j) Papaderos et al. (2002); (k) Izotov & Thuan (1999); (l) Berg et al. (2012); (m) Kobulnicky & Skillman (1997); (n) Thuan & Izotov (2005); (o) Guseva et al. (2003).

allows us to break the "disk-halo degeneracy" (van Albada & Sancisi 1986) and to estimate baryonic fractions. In Chapter 2 (Lelli et al. 2012a) and Chapter 3 (Lelli et al. 2012b), we presented our results for two show-case galaxies: I Zw 18 and UGC 4483. For both objects, we showed that i) the H I gas forms a compact, rotating disk, ii) the rotation curve rises steeply in the inner parts and flattens in the outer regions, and iii) old stars and atomic gas are dynamically important, as they constitute at least $\sim 20-30\%$ of the total dynamical mass within the last measured point of the rotation curve. Here we present a dynamical study for the remaining 16 objects.

4.2 The sample

Table 4.1 summarizes the main properties of our sample of starbursting dwarfs. For these 18 galaxies, the studies of the resolved stellar populations provide i) the galaxy distance from the tip of the red giant branch (TRGB), ii) the spatial distribution of the different stellar populations, iii) the recent SFH (ages $\lesssim$1 Gyr) by modelling the color-magnitude diagrams (CMDs), iv) the energy produced during the burst by supernovae and stellar winds, and v) the stellar mass in young and old stars. For 13 objects, we adopt the SFHs derived by McQuinn et al. (2010a) using archival HST images. The remaining 5 objects (I Zw 18, I Zw 36, NGC 1705, UGC 6541, and UGCA 290) have not been studied by McQuinn et al. (2010a) because the HST observations have a relatively-shallow photometric dept ($\lesssim$1 mag below the TRGB). We use the SFHs derived by other authors (Annibali et al. 2003, 2013; Crone et al. 2002; Schulte-Ladbeck et al. 2000, 2001), although they are more uncertain due to the limited photometric dept. Note that all these 18 objects are well-defined starburst galaxies, as their star-formation rates (SFRs) show an increase in the recent SFH by a factor $\gtrsim 3$ with respect to the past, average SFR. The sample covers a broad range in luminosities ($-19 \lesssim M_{\rm R} \lesssim -13$), stellar masses ($10^7 \lesssim M_*/M_\odot \lesssim 10^9$), and metallicities ($0.3 \lesssim Z/Z_\odot \lesssim 0.03$).

For all these galaxies, we collected both new and archival H I data. We obtained new H I observations for SBS 1415+437 and UGCA 290 using the *Jansky Very Large Array* (VLA, during its upgrade period), and of NGC 6789 using the *Westerbork Synthesis Radio Telescope* (WSRT). We analysed raw data from the VLA archive for I Zw 18 (Lelli et al. 2012a), UGC 4483 (Lelli et al. 2012b), UGC 6456 and NGC 625 (this work). The H I datacubes of NGC 1705 (Elson et al. 2013) and NGC 5253 (López-Sánchez et al. 2012) were kindly provided by Ed Elson and Angel R. López-Sánchez, respectively. For the remaining 9 galaxies, we used H I cubes from 3 public surveys: WHISP (Swaters et al. 2002), THINGS (Walter et al. 2008), and LITTLE-THINGS (Hunter et al. 2012). For 4 galaxies (NGC 2366, NGC 4163, NGC 4214, and UGC 9128), H I cubes are available from both WHISP and THINGS/LITTLE-

THINGS; we used the VLA data as they have higher spatial resolution than the WSRT observations.

4.3 Data Reduction & Analysis

4.3.1 H I data

In the following, we outline the main steps of the H I data analysis. We first describe the new 21-cm line observations and the data reduction. For the latter, we followed procedures similar to Lelli et al. (2012a,b) and refer to these papers for further details. For the existing H I datacubes, we refer to the original papers (see Table 4.B.1). Finally, we describe the derivation of total H I maps and velocity fields.

NGC 6789 was observed in May 2011 with the WSRT in a standard 12 hour session. The correlator was used in dual-polarization mode, with a total bandwidth of 10 MHz and 1024 spectral channels, providing a velocity resolution of $\sim$2.5 km s^{-1}. SBS 1415+437 and UGCA 290 were observed with the B, C, and D arrays of the VLA between March 2011 and April 2012. The correlator was used in dual-polarization WIDAR mode with a total bandwidth of 2.0 MHz and 256 spectral line channels, providing a velocity resolution of $\sim$1.9 km s^{-1}. Between 20 Sept. 2011 and 3 Dec. 2011, the VLA correlator back-end, by mistake, integrated only for 1 sec per record, thus the D-array observations have a time on source of only $\sim$16 mins instead of the expected 2 hours. The new H I observations are summarized in Table 4.2. We also reduced archival VLA observations of NGC 625 and UGC 6456.

The raw UV data were flagged, calibrated, and combined using the AIPS package and following standard procedures. We Fourier-transformed the UV data using a robust weighting technique (Briggs 1995). After various trials, we chose the value of the robust parameter $\Re$ (either -1, -0.5, or 0) that minimizes sidelobes and wings in the beam profile. After the Fourier transform, we continued the data analysis using the Groningen Imaging Processing SYstem (GIPSY) (van der Hulst et al. 1992). The channel maps were continuum-subtracted using line-free channels and then cleaned (Högbom 1974) down to 0.3σ using a mask to define the search areas.

A detailed study of the H I kinematics requires a combination of spatial resolution, spectral resolution, and sensitivity that varies from object to object, depending both on the quality of the H I observations and on the intrinsic properties of the galaxy (e.g. angular size, rotation velocity, mean H I column density). We used the following approach. For every galaxy, we first analysed the H I datacube at the highest spatial and spectral resolutions available. This cube is typically obtained using $\Re \simeq 0$ and has relatively-low column density sensitivity, but the synthesized beam profile is close to a Gaussian and does *not* have the broad wings that are typical for natural-weighted UV-data. Then,

Table 4.2 – New 21 cm-line observations

Galaxy	Array	Project	Observing Dates	ToS	Calibrators
UGCA 290	VLA/B	10C-200	12, 26, 28 Mar. 2011	7.6 h	3C286, 1227+365
	VLA/C	12A-246	25, 27, 28 Apr. 2012	4.6 h	3C286, 1227+365
	VLA/D	11B-075	2, 13 Nov. 2011	0.28 h	2C295, 1227+365
SBS 1415+345	VLA/B	10C-200	4, 27 Mar. & 8 Apr. 2011	7.6 h	3C286, 1400+621
	VLA/C	12A-246	26, 28, 30 Apr. 2012	4.6 h	3C286, 1400+621
	VLA/D	11B-075	6, 9 Oct. 2011	0.28 h	3C295, 1400+621
NGC 6789	WSRT	R11A007	20 May. 2011	12 h	3C286, 3C48

we smoothed the cube both in the image plane and in velocity using various Gaussian tapers, until we found the optimal compromise between resolution and sensitivity. The properties of both original and final datacubes are summarized in Appendix 4.B (Table 4.B.1). The spatial and spectral resolutions range between $5''$ to $30''$ and 5 to 10 km s^{-1}, respectively.

Total H I maps were obtained by summing the masked channel maps. The masks were constructed by first smoothing the datacubes in the image plane to $30''$ or $60''$ (depending on the angular extent of the galaxy) and in velocity to $\sim$10 or $\sim$20 km s^{-1} (depending on the H I line-width of the galaxy), and subsequently clipping the channel maps at $3\sigma_s$ (σ_s is the rms noise in the smoothed cube). A pseudo-3σ contour in the H I map was calculated following Verheijen & Sancisi (2001). The H I datacube of NGC 1569 is strongly affected by Galactic emission that we have interactively blotted out; the resulting H I map is rather uncertain. Velocity fields (VF) were derived by fitting a Gaussian function to the H I line profiles. Fitted Gaussians with a peak intensity less than 3σ were discarded. For most galaxies, the H I line profiles are very broad and asymmetric, thus the VFs provide only a rough description of the galaxy kinematics. As a consequence, our kinematical analysis is mostly based on channel maps, Position-Velocity (PV) diagrams, and 3-dimensional (3D) disk models.

4.3.2 Optical data

In order to compare the relative H I and stellar distributions of the BCDs, we collected optical images via the NASA/IPAC Extra-galactic Database (NED[1]). When available, we used R-band images, otherwise we used V-band ones. The images come from the following studies: Kuchinski et al. (2000), Gil de Paz et al. (2003), Taylor et al. (2005), Hunter & Elmegreen (2006), and Meurer et al. (2006). In I Zw 18, the nebular emission line dominates the optical morphology, thus we have also used the Hα-subtracted, R-band image from Papaderos et al. (2002).

[1]The NASA/IPAC Extragalactic Database is operated by the Jet Propulsion Laboratory, California Institute of Technology, under contract with the National Aeronautics and Space Administration.

The images were analysed as follows. We determined the sky level by masking the sources in the frame and fitting a 2D polynomial to the masked image. Then, we created sky-subtracted images and isophotal maps, using the calibration parameters provided in the original papers. To improve the signal-to-noise ratio in the outer regions, the isophotal maps were pixel-averaged with a 3×3 box; this preserves the resolution of the images as the pixel sizes were typically 3-4 times smaller than the seeing.

The images were interactively fitted with ellipses to determine the optical center ($\alpha_{\rm opt}, \beta_{\rm opt}$), position angle ($\rm PA_{opt}$), and ellipticity $\epsilon_{\rm opt}$. Foreground stars and scattered light in the frames were masked out by hand. Since the inner isophotes of BCDs are usually irregular due to the starburst, we estimated ($\alpha_{\rm opt}, \beta_{\rm opt}$), $\rm PA_{opt}$, and $\epsilon_{\rm opt}$ by taking the mean value over the outer isophotes. We also estimated the optical inclination $i_{\rm opt}$ using the formula

$$\cos^2(i_{\rm opt}) = \frac{(1-\epsilon_{\rm opt})^2 - q_0^2}{1-q_0^2} \tag{4.1}$$

where q_0 is the intrinsic thickness of an oblate stellar disk. We assumed $q_0 = 0.3$, as indicated by statistical studies of the ellipticities of dwarf galaxies (Binggeli & Popescu 1995; Sánchez-Janssen et al. 2010). The orientation parameters of different isopthotes often show relatively-large variations with radii, that we used to estimate the uncertainties in $\rm PA_{opt}$ and $i_{\rm opt}$ ($\sim$2° to $\sim$6°, except for NGC 4214 that is very close to face-on). The resulting orientation parameters are provided in Appendix 4.B (Table 4.B.2). The sky-subtracted images and isophotal maps are presented in Appendix 4.C.

For 11 galaxies in our sample, Swaters & Balcells (2002) and Papaderos et al. (2002) derived R-band luminosity profiles that were used to estimate the scale length $R_{\rm d}$ and the central surface brightness μ_0 of the old stellar component by fitting an exponential-law to their outer parts. For the remaining 7 objects, we derived luminosity profiles both for the whole galaxy and for the approaching/receding sides separately, by azimuthally-averaging the R-band images over concentric ellipses. We did not correct the profiles for internal extinction, as BCDs are usually metal-poor (see Table 4.1) and the dust content is expected to be low. Finally, we estimated the central surface brightness μ_0 and scale-length $R_{\rm d}$ of the old stellar component by fitting an exponential-law to the side of the disk that is least affected by the starburst (as in Lelli et al. 2012b for UGC 4483).

4.4 H I distribution and kinematics

In the following, we discuss the distribution and kinematics of the high-column-density gas associated with the stellar component of BCDs. In Appendix 4.A we discuss individual galaxies in detail and compare our results to previous studies,

Table 4.3 – Structural properties of the H I disk.

Name	$M_{\rm H\,I}$ ($10^7 M_\odot$)	$R_{\rm H\,I}$ (kpc)	$R_{\rm opt}$ (kpc)	$R_{\rm H\,I}/R_{\rm opt}$	Ref.
Galaxies with a regularly-rotating H I *disk*					
NGC 1705	11.1±2.9	2.1	1.5	1.4	a
NGC 2366	62±17	6.8	4.4	1.5	b
NGC 4068	14.9±1.6	3.1	1.8	1.7	b
NGC 4214	43±8	5.5	2.2	2.5	b
NGC 6789	1.8±0.3	1.0	0.7	1.4	a
UGC 4483	2.9±0.5	1.4	0.6	2.3	a
I Zw 18	21±3	3.3	0.5	6.6	c
I Zw 36	6.7±1.3	1.9	0.9	2.1	a
SBS 1415+437	20.1±4.6	4.3	2.4	1.8	a
Galaxies with a kinematically-disturbed H I *disk*					
NGC 625	9.7±2.2	2.6	3.3	0.8	a
NGC 1569	29.1±4.5	3.9	3.0	1.3	b
NGC 4163	1.5±0.2	1.1	1.0	1.1	b
NGC 4449	300±77	8.9	3.3	2.7	b
NGC 5253	13.8±3.4	3.1	2.1	1.5	a
UGC 6456	4.5±0.5	1.8	1.2	1.5	c
UGC 9128	1.3±0.2	0.9	0.6	1.5	b
Galaxies with unsettled H I *distribution*					
UGC 6541	1.2±0.2	...	0.9	...	c
UGCA 290	1.4±0.2	...	0.9	...	a

Notes. The H I radius $R_{\rm H\,I}$ is defined as the radius where the H I surface density profile reaches 1 $M_\odot$ pc^{-2}. The optical radius $R_{\rm opt}$ is defined as 3.2 $R_{\rm d}$, where $R_{\rm d}$ is the exponential scale-length. The last column provides references for $R_{\rm d}$.

References. a) this work, b) Swaters & Balcells (2002), c) Papaderos et al. (2002).

while in Appendix 4.C we present an atlas with optical images, isophotal maps, total H I maps, H I surface density profiles, H I velocity fields, and PV-diagrams.

Based on the H I morphology and kinematics, we classify starbursting dwarfs into three main families:

- *BCDs with a regularly-rotating* H I *disk* (∼50%).
  The PV-diagram along the H I major axis shows a regular velocity gradient (see Fig. 4.1, left). The VF displays a pattern that is typical of a rotating disk, although minor asymmetries caused by non-circular motions may be present. In some cases, the kinematical center and PA may not coincide with the optical ones. For these galaxies, we derive rotation curves (see Sect. 4.5).

- *BCDs with a kinematically-disturbed* H I *disk* (∼40%).
  The H I distribution resembles a disk, but the PV-diagrams and the VF are irregular and asymmetric (see Fig. 4.1, center). For these galaxies, it is not possible to derive a reliable rotation curve, but we obtain rough estimates of the kinematical parameters and of the rotation velocity in the outer parts (see Sect. 4.6).

- *BCDs with unsettled* H I *distributions* ($\sim$10%).
  Both the H I distribution and kinematics are irregular and asymmetric (see Fig. 4.1, right), and they are inconsistent with a rotating disk.

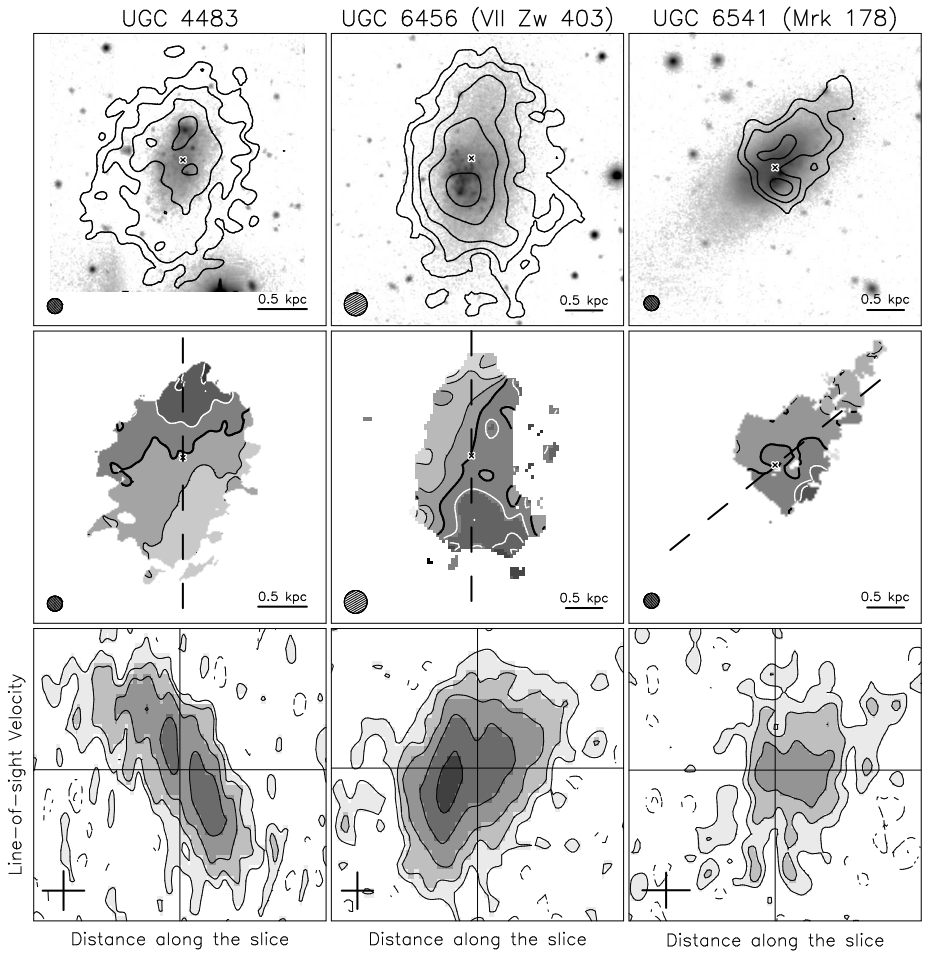

Figure 4.1 – Examples of BCDs with different H I distribution and kinematics: UGC 4483 (*left*) has a regularly-rotating H I disk, UGC 6456 (*center*) has a kinematically-disturbed H I disk, and UGC 6456 (*right*) has an unsettled H I distribution. *Top*: optical image superimposed with the total H I map (contours). The cross shows the optical center; the circle shows the H I beam. *Middle:* H I velocity field. Light and dark shading indicate approaching and receding velocities, respectively. The thick, black line shows the systemic velocity. The dashed-line indicates the H I major axis. The cross and the circle are the same as in the top panel. *Bottom:* position-velocity diagrams taken along the major axis. The cross corresponds to 0.5 kpc $\times$ 10 km s^{-1}. The horizontal and vertical lines indicate the systemic velocity and the galaxy center, respectively.

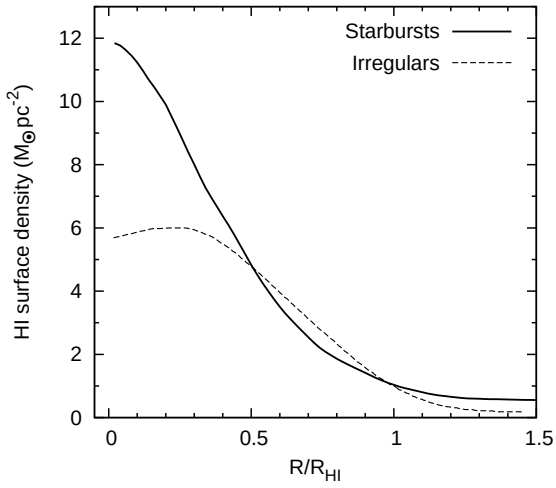

Figure 4.2 – Average H I surface density profile for starbursting dwarfs (solid line) and for typical irregulars (dashed line, from Swaters et al. 2002).

For the 16 galaxies with a H I disk, we derived H I surface density profiles by azimuthally-averaging the H I maps over ellipses with a width of 1 beam-size. We assumed the orientation parameters defined by the H I kinematics (see Table 4.B.2). Following Swaters et al. (2002), we calculated i) the H I radius $R_{\rm H\,I}$, defined as the radius where the H I surface density profile (corrected for inclination) reaches 1 $M_\odot$ pc^{-2}, and ii) the optical radius $R_{\rm opt}$, defined as 3.2 scale-lengths $R_{\rm d}$. The latter definition allows us to compare the sizes of galaxies with different central surface brightnesses: for an exponential disk with $\mu_0(B) = 21.65$ mag arcsec^{-2} (Freeman 1970), $R_{\rm opt} = 3.2R_{\rm d}$ corresponds to the isophotal radius R_{25}. In our sample of BCDs, the ratio $R_{\rm H\,I}/R_{\rm opt}$ ranges from $\sim$1 to $\sim$3 (see Table 4.3), which is typical for gas-rich spirals and irregulars (Irrs) (e.g. Verheijen & Sancisi 2001). The only exception is I Zw 18 with $R_{\rm H\,I}/R_{\rm opt} \simeq 6.6$, as the H I distribution extends towards a secondary stellar body (see Appendix 4.C and Lelli et al. 2012a). Excluding I Zw 18, the mean value of $R_{\rm H\,I}/R_{\rm opt}$ is 1.7$\pm$0.5, in close agreement with the values found by Swaters et al. (2002) for 73 gas-rich dwarfs (1.8$\pm$0.8) and by Broeils & Rhee (1997) for 108 gas-rich spirals (1.7$\pm$0.5).

Previous H I studies have shown that BCDs have centrally-concentrated H I distributions with higher surface densities than typical Irrs (Taylor et al. 1994; van Zee et al. 1998, 2001; Simpson & Gottesman 2000). We confirm this result for a larger sample of galaxies. In Fig. 4.2, we compare the mean H I surface density profile of late-type dwarfs obtained by Swaters et al. (2002) (averaging over 73 objects) with the mean H I surface density profile of our starbursting dwarfs (averaging over the 16 objects with a H I disk). Note that the sample of Swaters et al. (2002) contains a few BCDs that are also part of our sample, but it is fully dominated by typical, non-starbursting Irrs. Fig. 4.2 shows that BCDs, on average, have central H I surface densities a factor $\sim$2 higher than typical

Irrs. In several cases, the central, azimuthally-averaged H I surface densities can be as high as $\sim$20 $M_\odot$ pc^{-2} (see e.g. NGC 1569 and NGC 1705 in Appendix 4.C). The actual peak H I column densities can reach even higher values, up to $\sim$50-100 $M_\odot$ pc^{-2} in I Zw 18 at a linear resolution of $\sim$200 pc (Lelli et al. 2012a).

When comparing the H I surface densities of different galaxies, a possible concern is the different linear resolutions (in kpc) of the 21-cm line observations. The 16 H I cubes used here have linear resolutions ranging from $\sim$0.2 to $\sim$0.7 kpc (see Table 4.B.1), while the 73 cubes used by Swaters et al. (2002) have linear resolutions ranging from $\sim$0.4 to $\sim$2 kpc (apart for 13 cases where the linear resolution is $\gtrsim$2 kpc). To quantify the effect of beam smearing, we derived H I surface density profiles by smoothing our data to 30″ (as in Swaters et al. 2002), and checked that the distribution of the ratio $R_{\rm H\,I}$/beam-size is comparable for the two samples. We found that the *azimuthally-averaged* H I surface density of BCDs decreases by only $\sim$20% in the inner parts. Thus, we conclude that the difference between the mean H I surface density profile of BCDs and Irrs is not due to observational effects.

Finally, we compare the overall H I kinematics of BCDs and typical Irrs. A detailed comparison between the rotation curves of BCDs and Irrs is presented in Chapter 5. Gas-rich dwarfs generally have regularly-rotating H I disks. For example, Swaters et al. (2009) studied the H I kinematics of 69 late-type dwarfs and could derive rotation curves for 62 objects ($\sim$90%). In contrast, for our sample of 18 starbursting dwarfs, rotation curves could be derived for only 50% of the galaxies, as the other objects have either a kinematically-disturbed H I disk or an unsettled H I distribution. This suggests that complex H I kinematics are much more common in BCDs than in typical Irrs. This may be related to the starburst trigger (e.g. interactions/mergers or disk instabilities) and/or be a consequence of feedback from supernovae (SN) and stellar winds.

4.5 Galaxies with a regularly-rotating H I disk

4.5.1 Derivation of the rotation curves

Nine galaxies in our sample (50%) have a regularly-rotating H I disk: NGC 1705, NGC 2366, NGC 4068, NGC 4214, NGC 6789, UGC 4483, I Zw 18, I Zw 36, and SBS 1415+437. For these objects, we derived rotation curves following a procedure similar to Swaters et al. (2009). As a first step, we obtained initial estimates of the geometrical parameters and of the rotation curve by fitting a tilted-ring model to the VF (Begeman 1987). These initial estimates were then used as input to build a 3D kinematic model, which was subsequently corrected by trial and error to obtain a model-cube that matches the observations. The model-cubes take into account the spatial and spectral resolution of the observations, the observed gas distribution, the velocity dispersion, the disk

thickness, and possibly non-circular motions. For I Zw 18 and UGC 4483, the derivation of the rotation curve is described in detail in Lelli et al. (2012a,b). In the following, we briefly describe the derivation of the rotation curves for the remaining galaxies.

The VF was fitted with a tilted-ring model using a ring width of one beam and weighting every point by $\cos^2(\theta)$, where θ is the azimuthal angle in the plane of the galaxy from the major axis. The parameters of the fit are the kinematical center $(\alpha_{\rm kin}, \delta_{\rm kin})$, the systemic velocity $V_{\rm sys}$, the position angle $\rm PA_{kin}$, the inclination $i_{\rm kin}$, and the rotation velocity $V_{\rm rot}$. We first left all the parameters free, and determined $(\alpha_{\rm kin}, \delta_{\rm kin})$ and $V_{\rm sys}$ by taking the average value within the innermost rings. Then, we fixed $(\alpha_{\rm kin}, \delta_{\rm kin})$ and $V_{\rm sys}$, and determined $\rm PA_{kin}$ and $i_{\rm kin}$. Finally, we determined $V_{\rm rot}$ at every radius, keeping all the other parameters fixed. The errors on $V_{\rm rot}$ have been estimated by considering the differences in the rotation curves derived from the approaching and receding sides separately (see e.g. Lelli et al. 2012b).

The 3D disk models were built assuming that the H I kinematics is axisymmetric while the H I distribution is clumpy, i.e. the surface density varies with position as in the observed H I map (see Lelli et al. 2012a,b for details). We also assumed that i) the velocity dispersion $\sigma_{\rm H\,I}$ is constant with radius, and ii) the H I disk has an exponential vertical distribution with a constant scale-height z_0 of ~ 100 pc. The actual value of z_0 does not affect our results, since kinematic models with different scale-heights (up to 1 kpc) show no significant differences in their channel maps and PV-diagrams. For the mean velocity dispersion $\sigma_{\rm H\,I}$, we estimated values between 8 and 12 km s^{-1} (see Table 4.4) by comparing several PV-diagrams obtained from models and observations; values higher than 12 km s^{-1} are generally ruled out. An exception is NGC 4214, which seems to have $\sigma_{\rm H\,I} \simeq 15$ km s^{-1} for $R \lesssim 1'$.

Figs. 4.3, 4.4, and 4.5 compare PV-diagrams obtained from both the observations and the models along the disk major axis. We generally found a good agreement between models and observations when increasing the values of $V_{\rm rot}$ derived with the tilted-ring fit to the VF by $\sim$2 to 3 km s^{-1} at the innermost radii. Exceptions are NGC 4214 and SBS 1415+437, as their inner velocity-points require a correction of $\sim$10 km s^{-1} due to severe beam-smearing effects. For NGC 1705, the corrections to the velocity-points are even larger ($\sim$20 to 30 km s^{-1}) because the H I disk appears close to edge-on in the outer parts and, thus, the VF provides only a poor representation of the rotation velocities. We also used PV-diagrams at the full resolution (see Table 4.B.1) to further check that beam-smearing effects do not significantly affect our rotation curves. In two cases (NGC 4068 and SBS 1415+437), the 3D disk models also suggest that the position of the kinematical center should be shifted by about one beam with respect to the results of the tilted-ring fit to the VF.

The observed PV-diagram of NGC 2366 shows H I emission close to the systemic velocity that cannot be reproduced by our disk model (see Fig. 4.3).

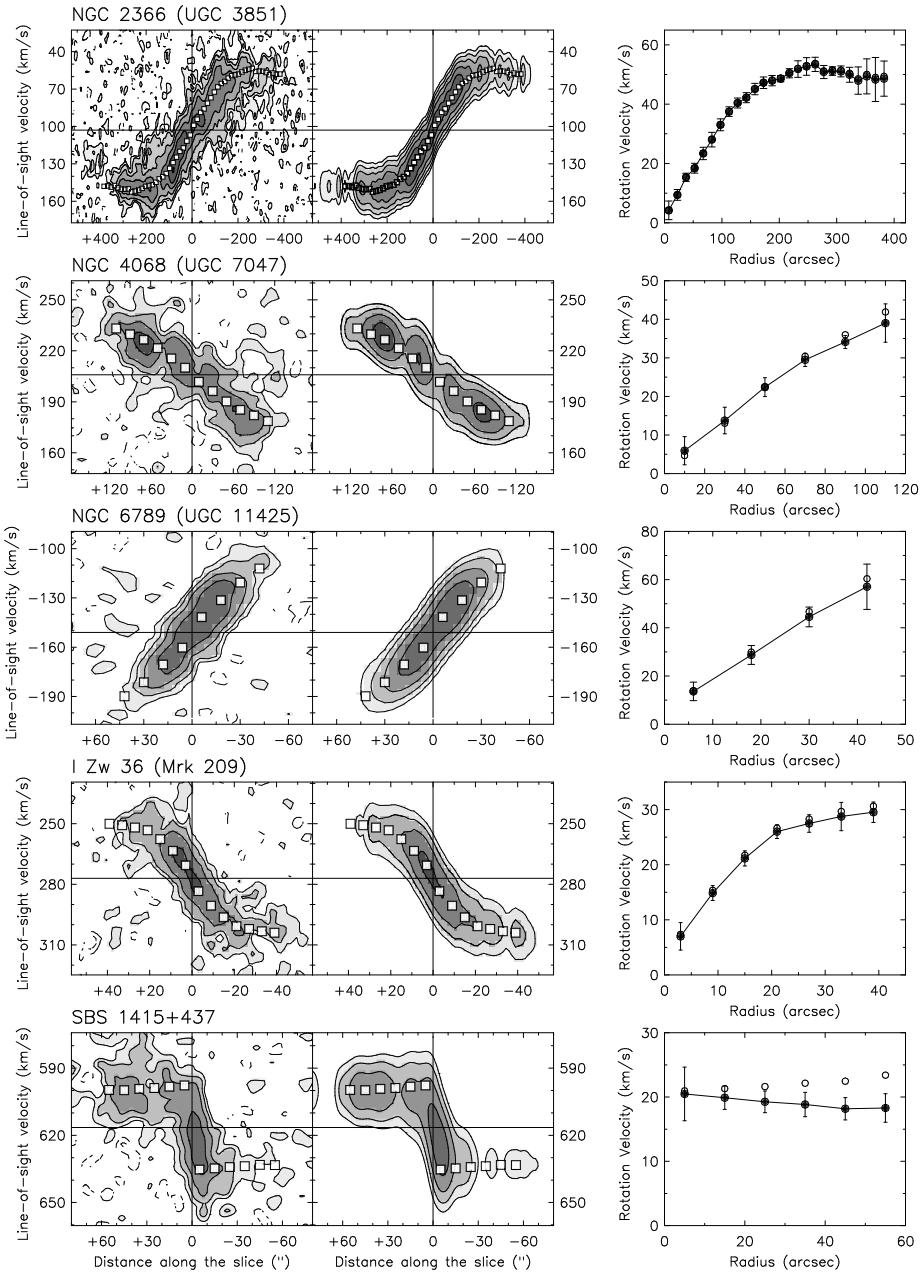

Figure 4.3 – Kinematical analysis of five BCDs with a regularly-rotating H I disk. *Left*: PV-diagrams obtained along the disk major axis from the observed cube and the model-cube. Contours are at -1.5 (dashed), 1.5, 3, 6, 12 σ. The squares show the rotation curve used to build the models, projected along the line of sight. *Right:* observed rotation curve (filled circles) and asymmetric-drift-corrected rotation curve (open circles). See Sect. 4.5 for details.

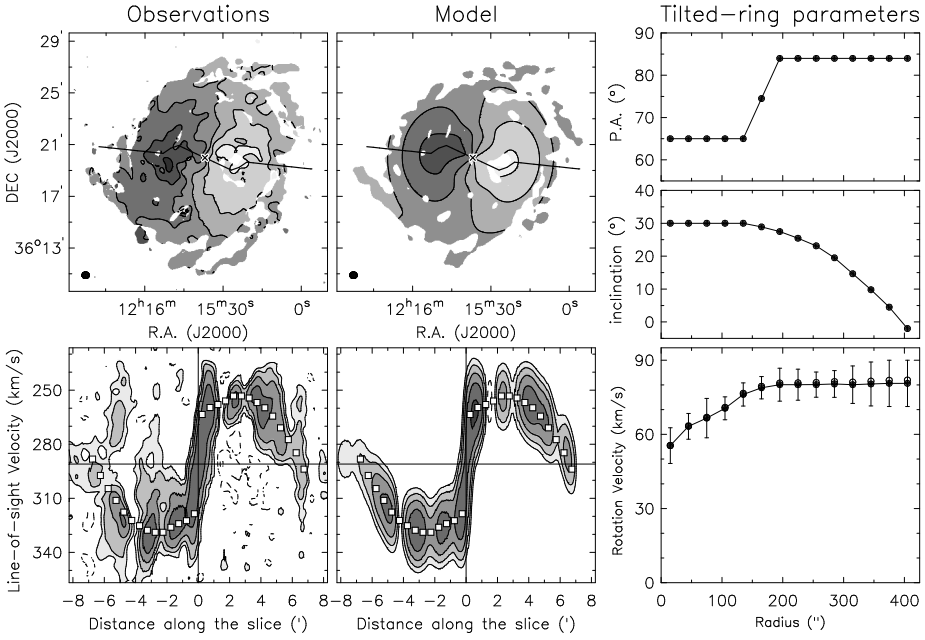

Figure 4.4 – The warped galaxy NGC 4214. *Left*: velocity fields (*top*) and PV-diagrams (*bottom*) obtained from the observed cube and the model-cube. In the velocity fields, the contours range from 257 to 337 km s^{-1} with steps of 16 km s^{-1}; the thick line shows the line of nodes; the circle to the bottom-left shows the beam. In the PV-diagrams, the contours are at -1.5 (dashed), 1.5, 3, 6, 12 σ; the squares show the rotation curve projected along the line of sight. *Right:* tilted-ring parameters for the disk model. The open circles show the asymmetric-drift-corrected rotation curve. See Sect. 4.5 for details.

This is likely due to extra-planar H I emission that is rotating at a lower velocity than the disk (a so-called "lagging H I halo", see e.g. Fraternali et al. 2002), as it is observed in several nearby spiral galaxies (e.g. Sancisi et al. 2008). The modelling of a lagging H I halo is beyond the scope of this paper.

The galaxies NGC 4214 and NGC 1705 deserve special attention, as their H I disks are close to face-on in the inner parts and strongly warped in the outer parts. A tilted-ring fit to the VF, therefore, poses severe limitations when determining the dependence of $\mathrm{PA_{kin}}$ and i_{kin} on radius (cf. Begeman 1987). We built a series of disk models assuming different types of warps. In the following, we discuss only our best models (shown in Figs. 4.4 and 4.5). For both galaxies, the warp is slightly asymmetric between the approaching and receding sides of the disk, and the actual dependence of i_{kin} on radius remains uncertain.

For NGC 4214, we found that $\mathrm{PA_{kin}} \simeq 65°$ and $i_{\mathrm{kin}} \simeq 30°$ for $R \lesssim 3'$, in agreement with the optical values within the uncertainties, while at larger radii $\mathrm{PA_{kin}} \simeq 84°$ and i_{kin} gradually decrease (see Fig. 4.4, right panels). This model

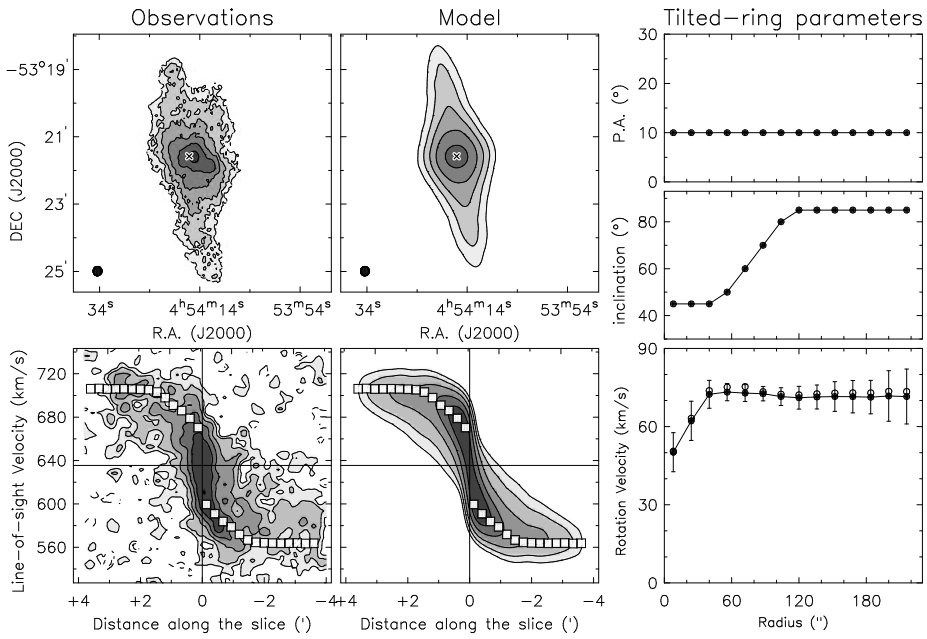

Figure 4.5 – The warped galaxy NGC 1705. *Left*: total H I map at $\sim$16″ resolution (*top*) and PV-diagrams at 20″ resolution (*bottom*) obtained from the observed cube and the model-cube. In the total H I map, contours are at 1.1, 2.2, 4.4, 8.8, 17.6 $\times 10^{20}$ atoms cm^{-2}; the circle to the bottom-left shows the beam. In the PV-diagrams, the contours are at -1.5 (dashed), 1.5, 3, 6, 12, 24 σ; the squares show the rotation curve projected along the line of sight. *Right:* tilted-ring parameters for the disk model. The open circles show the asymmetric-drift-corrected rotation curve. See Sect. 4.5 for details.

provides a good match to the observed VF and PV-diagram taken along the line of nodes (see Fig. 4.4, left panels); minor discrepancies ($\sim$20 km s^{-1}) are observed, possibly due to non-circular motions caused by the inner stellar bar and/or streaming motions along the prominent H I spiral arms (see the H I map in Appendix 4.C).

The H I disk of NGC 1705 appears highly inclined in the outer parts, thus the VF does not provide useful information regarding the dependence of $i_{\rm kin}$ on radius. For this galaxy, we built 3D models using an *axisymmetric* H I distribution in each ring, and determined the values of $i_{\rm kin}$ by comparing total H I maps and PV-diagrams obtained from the observed cube and the model-cubes. Similarly to Elson et al. (2013), we found that PA$_{\rm kin} \simeq 10°$ while $i_{\rm kin}$ abruptly changes at $R \simeq 1.5'$ (see Fig. 4.5, right panels). We adopted, however, a higher value of $i_{\rm kin}$ in the outer parts than Elson et al. (2013) (85° instead of 65°). This is necessary to reproduce the tails of H I emission towards $V_{\rm sys}$ that are clearly visible in PV-diagrams at 20″ resolution (see Fig. 4.5, bottom-

Table 4.4 – Parameters for the asymmetric-drift correction

Galaxy	Funct.	$\Sigma_{0,\mathrm{H\,I}}$ ($\mathrm{M_\odot\ pc^{-2}}$)	$R_{0,\mathrm{H\,I}}$ (kpc)	s (kpc)	$\sigma_{\mathrm{H\,I}}$ ($\mathrm{km\ s^{-1}}$)
NGC 1705 ($R < 80''$)	Exp	24.0	0.7	...	12
NGC 1705 ($R > 80''$)	Exp	1.5	2.8	...	12
NGC 2366	Gauss	9.1	0.8	6.31	10
NGC 4068	Gauss	9.0	1.0	0.92	8
NGC 4214	Exp	13.6	2.5	...	10
NGC 6789	Gauss	16.4	0.0	0.37	8
I Zw 36	Exp	11.9	0.7	...	9
SBS 1415+357	Exp	11.8	1.4	...	9

panels). To fully reproduce these broad H I profiles, especially the H I emission in the "forbidden" quadrants of the PV-diagram, we also had to include radial motions of $\sim$15 km s^{-1} (cf. with NGC 2915, Elson et al. 2011). As a consequence of the high value of i_{kin} in the outer parts, the thickness of the H I disk must be $\sim$ 500 pc in order to reproduce the observed total H I map (see Fig. 4.5, top-panels).

4.5.2 Asymmetric-drift correction

For several galaxies in our sample, the observed rotation velocity V_{rot} is only a factor $\sim$2 or 3 larger than the H I velocity dispersion $\sigma_{\mathrm{H\,I}}$. In order to trace the underlying mass distribution, the observed rotation curves have to be corrected for pressure support. We calculated the asymmetric-drift correction following Meurer et al. (1996). We assumed that i) the H I kinematics is axisymmetric, ii) the H I velocity dispersion is isotropic, iii) the velocity dispersion and the scale-height of the H I disk are constant with radius, and iv) the H I surface density profile can be approximated either by an exponential function $\Sigma_{0,\mathrm{H\,I}} \times \exp(-R/R_{0,\mathrm{H\,I}})$ or by a Gaussian function $\Sigma_{0,\mathrm{H\,I}} \times \exp[-(R-R_{0,\mathrm{H\,I}})^2/(2s^2)]$. The circular velocity V_{circ}, corrected for asymmetric-drift, is thus given by

$$V_{\mathrm{circ}} = \sqrt{V_{\mathrm{rot}}^2 + \sigma_{\mathrm{H\,I}}^2\,(R/R_{0,\mathrm{H\,I}})} \tag{4.2}$$

in the case of an exponential surface density profile, and by

$$V_{\mathrm{circ}} = \sqrt{V_{\mathrm{rot}}^2 + \sigma_{\mathrm{H\,I}}^2\,R(R-R_{0,\mathrm{H\,I}})/s^2} \tag{4.3}$$

in the case of a Gaussian surface density profile. For NGC 1705, the first assumption is *not* valid because the H I disk is strongly warped with an abrupt change of the inclination by $\sim$40° (see Fig. 4.5), thus we calculated the asymmetric-drift correction separately for the inner, face-on disk and for the outer, edge-on disk.

Table 4.4 provides the values of $\sigma_{\mathrm{H\,I}}$, derived by building 3D disk models, and the parameters for the exponential/Gaussian functions, obtained by fitting the

observed H I surface density profiles. For NGC 1705, we fitted the H I surface density profile with 2 different exponential functions for the inner face-on disk and the outer edge-on disk. The open-circles in Figs. 4.3, 4.4, and 4.5 (right panels) show the asymmetric-drift-corrected rotation curves. The correction is generally smaller than the error bars, except for SBS 1415+437 that is rotating at only ∼20 km s^{-1} (see also UGC 4483 in Lelli et al. 2012b).

4.5.3 Non-circular motions

The PV-diagrams in Figs. 4.3, 4.4, and 4.5 clearly show that the H I kinematics of these galaxies is dominated by rotation. In several cases, however, a simple rotating-disk model cannot reproduce all the features of the observed cube. In Lelli et al. (2012a,b), we showed that the H I disk of I Zw 18 and UGC 4483 likely have radial motions of ∼15 and ∼5 km s^{-1}, respectively. We did not find such regular radial motions in the 7 BCDs analysed here, with the possible exception of NGC 1705 that shows double-peaked H I profiles near the center and may have radial motions of ∼15 km s^{-1}. Several galaxies, however, do show kinematically-anomalous components that deviate from the main rotation pattern of the disk. We briefly discuss 3 interesting cases: NGC 1705, NGC 2366, and NGC 4214.

NGC 1705 has a H I "spur" to the North-West (see Meurer et al. 1998; Elson et al. 2013), that may be interpreted as an H I outflow associated with the Hα wind (Meurer et al. 1992). The VF of NGC 2366 shows a strong distortion to the North-West (see Appendix 4.C), that Oh et al. (2008) interpreted as non-circular motions of ∼ 20 km s^{-1} (see their Figure 3). Finally, NGC 4214 shows non-circular motions of ∼20 to ∼50 km s^{-1} (corrected for i) that are visible in several PV-diagrams taken across the disk (not shown here, but some kinematically-anomalous gas can be seen in the bottom panels of Fig. 4.4); these non-circular motions are likely associated with the H I spiral arms and/or the inner stellar bar.

4.6 Galaxies with a kinematically-disturbed H I disk

Seven galaxies in our sample have a kinematically-disturbed H I disk: NGC 625, NGC 1569, NGC 4163, NGC 4449, NGC 5253, UGC 6456, and UGC 9128. For these objects, we used channels maps and PV-diagrams to estimate $(\alpha_{\rm kin}, \delta_{\rm kin})$, $V_{\rm sys}$, PA$_{\rm kin}$, and the rotation velocity in the outer parts. For the inclination, we assumed the optical value. The values of the kinematic parameters have been tested by building 3D disk models with constant $V_{\rm rot}$. These models cannot reproduce the observations in details, but indicate that the observed H I kinematics are consistent with a rotating disk. The resulting values for the kinematic parameters are rather uncertain.

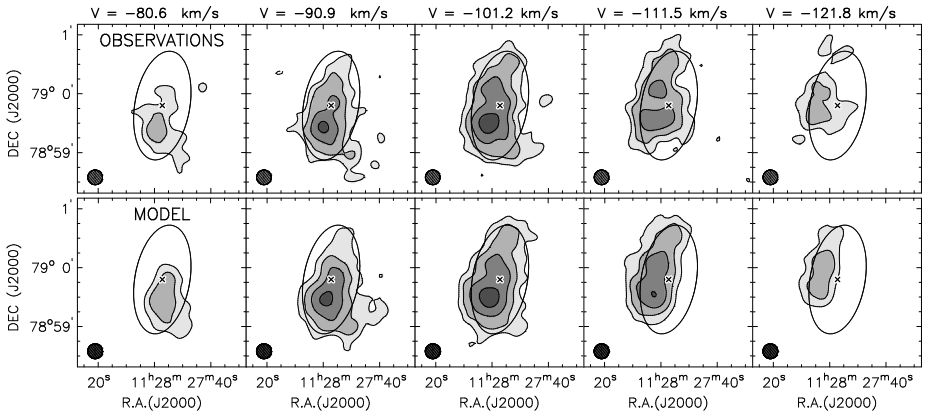

Figure 4.6 – Channel maps for UGC 6456 (VII Zw 403). *Top*: observations. *Bottom*: a 3D disk model with $V_{\rm rot} \simeq V_{\rm rad} \simeq \sigma_{\rm H\,I} \simeq 10$ km s^{-1}. Contours are at 3, 6, 12, 24 σ. The cross shows the optical centre. The ellipse corresponds to the R-band isophote at 25 mag arcsec^{-2}.

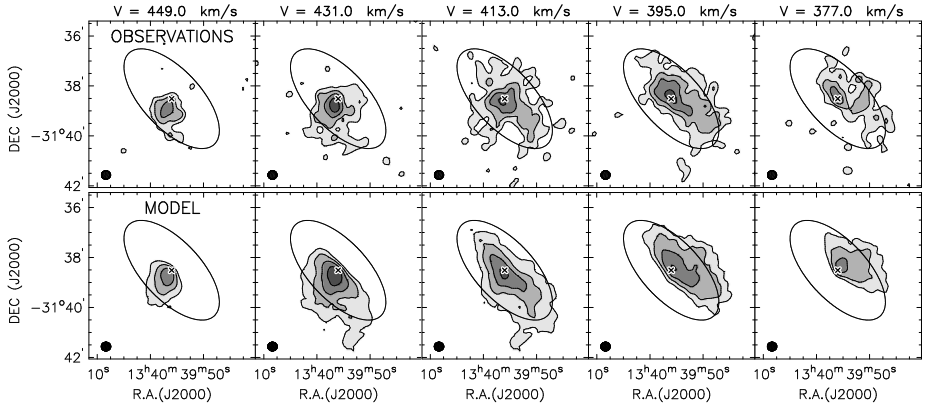

Figure 4.7 – Channel maps for NGC 5253. Contours are at 3, 6, 12, 24 σ. *Top*: observations. *Bottom*: a 3D disk model with $V_{\rm rot} = 0$, $V_{\rm rad} = 25$, and $\sigma_{\rm H\,I} = 15$ km s^{-1}. The cross shows the optical centre. The ellipse corresponds to the R-band isophote at 24 mag arcsec^{-2}.

Two galaxies (NGC 5253 and UGC 6456) show a regular velocity gradient approximately along the H I minor axis (see the VFs in Appendix 4.C). Velocity gradients along the H I minor axis have been observed also in other BCDs and interpreted as unusual rotation around the major axis (e.g. Thuan et al. 2004; Bravo-Alfaro et al. 2004). This peculiar kinematic behaviour, however, can also be interpeted as a H I disk with strong *radial* motions (e.g. López-Sánchez et al. 2012). We built 3D disk models assuming the PA suggested by the total H I map (consistent with the optical value within the errors) and tried different

combinations of circular and radial motions. Our best-models are shown in Figs 4.6 and 4.7. For UGC 6456, the H I emission can be reproduced by a combination of circular and radial motions ($V_{\rm rot} \simeq V_{\rm rad} \simeq 10$ km s^{-1}, see Fig. 4.6). The case of NGC 5253 is even more extreme, as the radial component is $\sim$25 km s^{-1} while the rotation is constrained to be $\lesssim$5 km s^{-1} (see Fig. 4.7). In our opinion, strong radial motions are a more likely interpretation than rotation around the major axis, since gas inflows/outflows are expected in starburst galaxies.

For UGC 6456, it is not possible to discriminate between inflow and outflow, as it is unknown which side of the disk is nearest to the observer. For NGC 5253, instead, shadowing of the X-ray emission suggests that the southern side of the disk is the nearest one (Ott et al. 2005a), implying that the radial motion is an inflow. For both galaxies, the inflow timescale $t_{\rm in} = R_{\rm H\,I}/V_{\rm rad}$ is $\sim$100-200 Myr, thus comparable with the starburst duration (see McQuinn et al. 2010b). We also calculated the gas inflow rates $\dot{M}_{\rm in} = 1.33\,M_{\rm H\,I}/t_{\rm in}$ (the factor 1.33 takes into account the contribution of Helium) and found that they are about 1 order of magnitude higher than the current SFRs (from McQuinn et al. 2010a): for NGC 5253 $\dot{M}_{\rm in} \simeq 1.5$ M$_\odot$ yr^{-1} and SFR$\simeq$0.16 M$_\odot$ yr^{-1}, while for UGC 6456 $\dot{M}_{\rm in} \simeq 0.3$ M$_\odot$ yr^{-1} and SFR$\simeq$0.02 M$_\odot$ yr^{-1}. Similar results can be derived for I Zw 18 and UGC 4483, which show a global radial motion superimposed on a regularly-rotating H I disk (Lelli et al. 2012a,b): for I Zw 18 $\dot{M}_{\rm in} \simeq 1$ M$_\odot$ yr^{-1} and SFR$\simeq$0.1 M$_\odot$ yr^{-1}, while for UGC 4483 $\dot{M}_{\rm in} \simeq 0.1$ M$_\odot$ yr^{-1} and SFR$\simeq$0.01 M$_\odot$ yr^{-1}. If the hypothesis of a radial inflow is correct, these results would imply that only $\sim$10% of the inflowing gas is converted into stars, in line with several estimates of the star-formation efficiencies in dwarf galaxies (e.g. Leroy et al. 2008).

4.7 Mass models

4.7.1 Preliminary considerations

In Sect. 4.5 we derived rotation curves for 9 BCDs with a regularly-rotating H I disk, while in Sect. 4.6 we estimated the outer rotation velocities of 7 BCDs with a kinematically-disturbed H I disk. In several cases, we found that the values for the kinematical center, PA, and i do not coincide with the optical ones (see Table 4.B.2). Non-circular motions are also present in the H I disks of several galaxies. This raises the question as to whether the H I disks are in a fully-stable configuration and the observed rotation velocities are suitable to investigate the mass distributions in these galaxies.

In Fig. 4.8, we consider the location of the starbursting dwarfs in our sample on the baryonic Tully-Fisher relation (BTFR, McGaugh et al. 2000). We exclude UGC 6456 and NGC 5253 as their H I kinematics seems to be dominated by radial motions (Figs. 4.6 and 4.7), and UGCA 290 and UGC 6541 as they

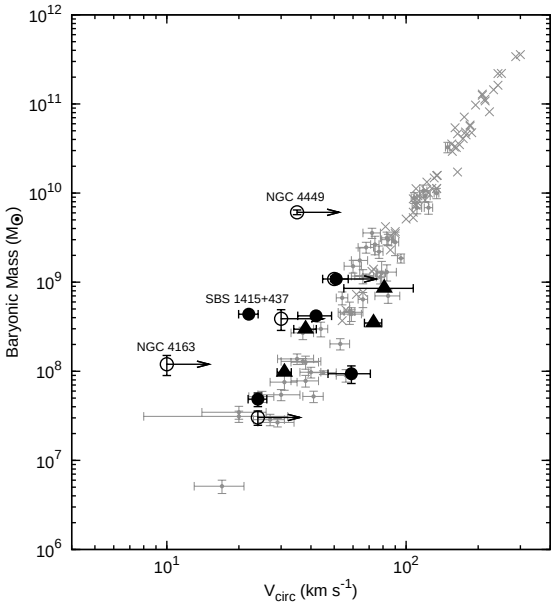

Figure 4.8 – The location of star-bursting dwarfs on the baryonic Tully-Fisher relation. Grey-crosses indicate star-dominated galaxies from McGaugh (2005), while grey-dots indicate gas-dominated galaxies from McGaugh (2011). Filled and open symbols indicate, respectively, BCDs with a regularly-rotating H I disk and BCDs with a kinematically-disturbed H I disk. For the latter ones, the circular velocity may be underestimated. The triangles indicate galaxies for which the baryonic mass is a lower limit. Galaxies that significantly deviate from the relation are labelled.

have unsettled H I distributions. We use data from McGaugh (2005) for star-dominated galaxies (grey crosses) and McGaugh (2012) for gas-dominated ones (grey dots). Most BCDs with a regularly-rotating H I disk have flat rotation curves in the outer parts (Figs. 4.3, 4.4, and 4.5), thus we use the mean value of $V_{\rm circ}$ along the flat part (Verheijen 2001). In 2 cases (NGC 4068 and NGC 6789), however, the rotation curve does not reach the flat part, thus we use the maximum observed value of $V_{\rm circ}$. One would expect these galaxies to deviate from the BTFR if $V_{\rm circ}$ keeps rising after the last measured point. For BCDs with a kinematically-disturbed H I disk, our estimates of $V_{\rm circ}$ are considered as lower limits in Fig. 4.8 because i) they may not correspond to the flat part of the rotation curve, and ii) they have not been corrected for pressure support. As in McGaugh (2005, 2012), the total baryonic mass is calculated as $M_* + 1.33 M_{\rm H\,I}$; the possible contributions of molecular and ionized gas are neglected. Note that McGaugh (2005, 2012) estimated M_* using integrated colors and synthetic stellar population models, while our estimate of M_* is based on the HST studies of the resolved stellar populations.

Fig. 4.8 shows that both BCDs with a regularly-rotating H I disk (filled symbols) and BCDs with a kinematically-disturbed H I disk (open symbols) follow the BTFR within the uncertainties, except for NGC 4163, NGC 4449, and SBS 1415+437. Thus, for the majority of galaxies in our sample, the observed rotation velocity is a reasonable proxy for the total dynamical mass. The 3 objects that strongly deviate from the BTFR may be unusual for the following reasons. NGC 4163 has a disturbed H I distribution with tails and plumes;

it is unclear whether the observed velocity gradient (of only ∼10 km s^{-1}) is really due to rotation. NGC 4449 is characterized by two counter-rotating gas systems (see VF in Appendix 4.C and Hunter et al. 1999); we estimated the rotation velocity of the *inner* H I disk, that possibly does not correspond to the asymptotic velocity along the flat part of the rotation curve. It is unclear whether the *outer* gas system forms a rotating disk; intriguingly, its inferred circular-velocity would be consistent with the BTFR. Finally, SBS 1415+437 has a kinematic center that is strongly off-set (∼800 pc) with respect to the optical center and to the centroid of the H I distribution; the lopsided H I morphology and kinematics may be explained by a pattern of elliptical orbits viewed almost edge-on (cf. Baldwin et al. 1980). A detailed investigation of these models is beyond the scope of this paper, but it is clear that the observed rotation curve might not be a reliable tracer of the dynamical mass.

Considering the uncertainties involved, we proceed as follows. In Sect. 4.7.2 we estimate global baryonic fractions within $R_{\rm opt}$ for the 14 objects in Fig. 4.8, while in Sect. 4.7.3 we build detailed mass models for 4 galaxies with a regularly-rotating disk (NGC 2366, NGC 6789, NGC 4068, and UGC 4483). In Lelli et al. (2012a,b), we presented similar mass models for I Zw 18 and UGC 4483, respectively. For I Zw 18, the stellar mass from the HST studies is very uncertain, thus we built mass models assuming a maximum-disk. For UGC 4483, instead, we used the HST information on the stellar mass to break the "disk-halo degeneracy" (van Albada & Sancisi 1986); here we extend our previous analysis on UGC 4483 by making different assumptions about the IMF and including the gravitational contribution of molecules. We do not decompose the rotation curves of NGC 1705, I Zw 36, and SBS 1415+437 because the optical and kinematical centers show a strong off-set ($\gtrsim$ 1 disk scale-length), thus it is not possible to calculate the gravitational contributions of stars, gas, and DM using a common dynamical center. We also exclude NGC 4214 because the H I disk is close to face-on and strongly warped.

4.7.2 Baryonic fractions

As we mentioned in Sect. 4.2, the HST studies of the resolved stellar populations provide a direct estimate of the total stellar mass of a galaxy. For 7 objects, however, these stellar masses are *lower limits* because either the HST field of view covers only a small portion of the galaxy (NGC 1705, NGC 4214, and NGC 625), or the ancient SFH (>1 Gyr) is uncertain due to the limited photometric depth (I Zw 18 and UGCA 290), or both (I Zw 36 and UGC 6541). Moreover, the values of M_* depend on the assumed IMF and on the mass returned to the ISM by stellar ejecta. The stellar masses in Table 4.1 are calculated assuming a Salpeter IMF from 0.1 to 100 $M_\odot$ and a gas-recycling efficiency of 30%; a Kroupa IMF would give stellar masses lower by a factor of 1.6 (McQuinn et al. 2012). In Appendix 4.B (Table 4.B.3), we provide three different estimates for the baryonic mass within $R_{\rm opt}$ (in order of increasing

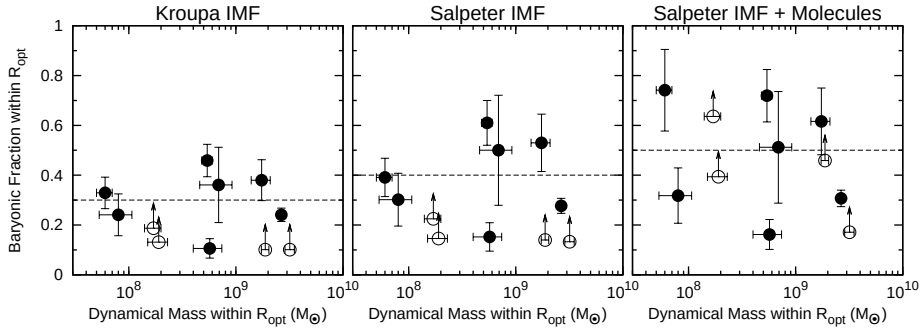

Figure 4.9 – Baryonic fractions $f_{\rm bar} = M_{\rm bar}/M_{\rm dyn}$ versus $M_{\rm dyn}$ calculated within the optical radius $R_{\rm opt}$. The open circles indicate lower limits for $f_{\rm bar}$. See Sect. 4.7.2 for details.

mass): i) $M_{\rm bar}^{\rm Kr} = M_*^{\rm Kr} + 1.33\,M_{\rm H\,I}(R_{\rm opt})$, where $M_*^{\rm Kr}$ is the stellar mass assuming a Kroupa IMF and $M_{\rm H\,I}(R_{\rm opt})$ is the H I mass within $R_{\rm opt}$; ii) $M_{\rm bar}^{\rm Sal} = M_*^{\rm Sal} + 1.33\,M_{\rm H\,I}(R_{\rm opt})$, where $M_*^{\rm Sal}$ is the stellar mass assuming a Salpeter IMF; and iii) $M_{\rm bar}^{\rm mol} = M_*^{\rm Sal} + 1.33\,M_{\rm H\,I}(R_{\rm opt}) + M_{\rm mol}$, where we also include an indirect estimate of the molecular mass $M_{\rm mol}$.

The molecular content of dwarf galaxies is very uncertain as they usually have low metallicities and the CO-line, which traces the molecular hydrogen, is often undetected (e.g. Taylor et al. 1998). Moreover, even when the CO-line is detected, the conversion factor from CO luminosity to H_2 mass is poorly constrained, as it may differ from the Milky-Way value and vary with metallicity and/or other physical conditions (e.g. Boselli et al. 2002). Thus, we chose to indirectly estimate the molecular mass by using the correlation between SFR surface density $\Sigma_{\rm SFR}$ and H_2 surface density $\Sigma_{\rm H_2}$ (e.g. Bigiel et al. 2008). In particular, we use Eq. 28 of Leroy et al. (2008), which assumes that the star-formation efficiency in dwarf galaxies is the same as in spirals (but see also Roychowdhury et al. 2011). This equation can be written as:

$$M_{\rm H_2}[M_\odot] = 1.9 \times 10^9\,{\rm SFR}[{\rm M_\odot yr^{-1}}]. \tag{4.4}$$

We use the average SFR over the last ∼10 Myr as obtained by the HST studies, and assume a systematic uncertainty of 30% on $M_{\rm H_2}$. The real uncertainty, however, may be larger as starbursting dwarfs may deviate from the $\Sigma_{\rm H_2} - \Sigma_{\rm SFR}$ relation.

We used the 3 different estimates of the total baryonic mass to calculate baryonic fractions $f_{\rm bar} = M_{\rm bar}/M_{\rm dyn}$ within $R_{\rm opt}$ (see Table 4.B.3). The dynamical mass is calculated assuming a spherical mass distribution and using the asymmetric-drift-corrected circular velocities. The 3 galaxies that deviate from the BTFR (NGC 4163, NGC 4449, and SBS 1415+437) have unphysically-large baryonic fractions ($f_{\rm bar} \gtrsim 1$), further suggesting that the observed circular velocities are not adequate to trace the total dynamical mass. For the remaining

11 objects, we plot $f_{\rm bar}$ against $M_{\rm dyn}$ in Fig. 4.9. We find no clear trend with $M_{\rm dyn}$ or with other physical parameters such as M_*, $M_{\rm H\,I}$, $\rm SFR_p$, and $t_{\rm p}$ (see Table 4.1). The mean baryonic fractions within the stellar component are relatively high: ∼0.3 for a Kroupa IMF, ∼0.4 for a Salpeter IMF, and ∼0.5 for a Salpeter IMF plus molecules. Old stars (with ages >1 Gyr) generally provide the major contribution to these baryonic fractions, except for a few cases where either the atomic gas dominates (NGC 2366) or the molecular gas may be very important (NGC 1705 and UGC 4483, see Table 4.B.3).

4.7.3 Rotation curve decompositions

In this section, we decompose the rotation curves of 4 galaxies (NGC 2366, NGC 4068, NGC 6789, and UGC 4483), which have a regularly-rotating H I disk centered on the stellar component. We follow standard procedures described by Begeman (1987). Similarly to Sect. 4.7.2, we compute 3 different mass models which assume i) a Kroupa IMF, ii) a Salpeter IMF, and iii) a Salpeter IMF plus the molecular mass inferred by Eq. 4.4. These mass models are shown in Fig. 4.10.

The gravitational contribution of the atomic gas was calculated using the H I surface density profiles and scaled to the total atomic gas mass as $\sqrt{1.33 M_{\rm H\,I}}$. In agreement with the models in Sect. 4.5.1, we assume that the gaseous disk has an exponential vertical density distribution with a scale height of 100 pc.

The gravitational contribution of the stellar component $V_*(R)$ was calculated using R-band surface brightness profiles and assuming that the stars are located in a disk with a vertical density distribution given by $\rm sech^2(z/z0)$ (van der Kruit & Searle 1981) with $z_0 = 0.3 R_{\rm d}$. If one assumes that $z_0/R_{\rm d} = 0.2$ or 0.4, $V_*(R)$ would change only by a few percent in the inner parts ($R \lesssim R_{\rm opt}$). The amplitude of V_* was scaled to the total stellar mass as $\sqrt{M_*}$ (assuming either a Kroupa or a Salpeter IMF). This is equivalent to using a stellar mass-to-light ratio that is constant with radius (see Table 4.1).

To include the possible contribution of molecular gas, we simply assume that molecules are distributed in the same way as the stars and thus scale the amplitude of V_* by $\sqrt{M_*^{\rm Sal} + M_{\rm mol}}$. We also tried to estimate the shape of the molecular gas contribution $V_{\rm mol}$ using Hα and 24μm images (from Dale et al. 2009 and Gil de Paz et al. 2003). These images show very clumpy and asymmetric distributions, that are completely dominated by strong star-forming regions and shell-like structures. We thus prefer to include the molecular gas contribution in $V_*(R)$.

For the DM distribution, we assume a pseudo-isothermal halo described by equation

$$\rho_{\rm ISO}(r) = \frac{\rho_0}{1 + (r/r_{\rm c})^2}, \tag{4.5}$$

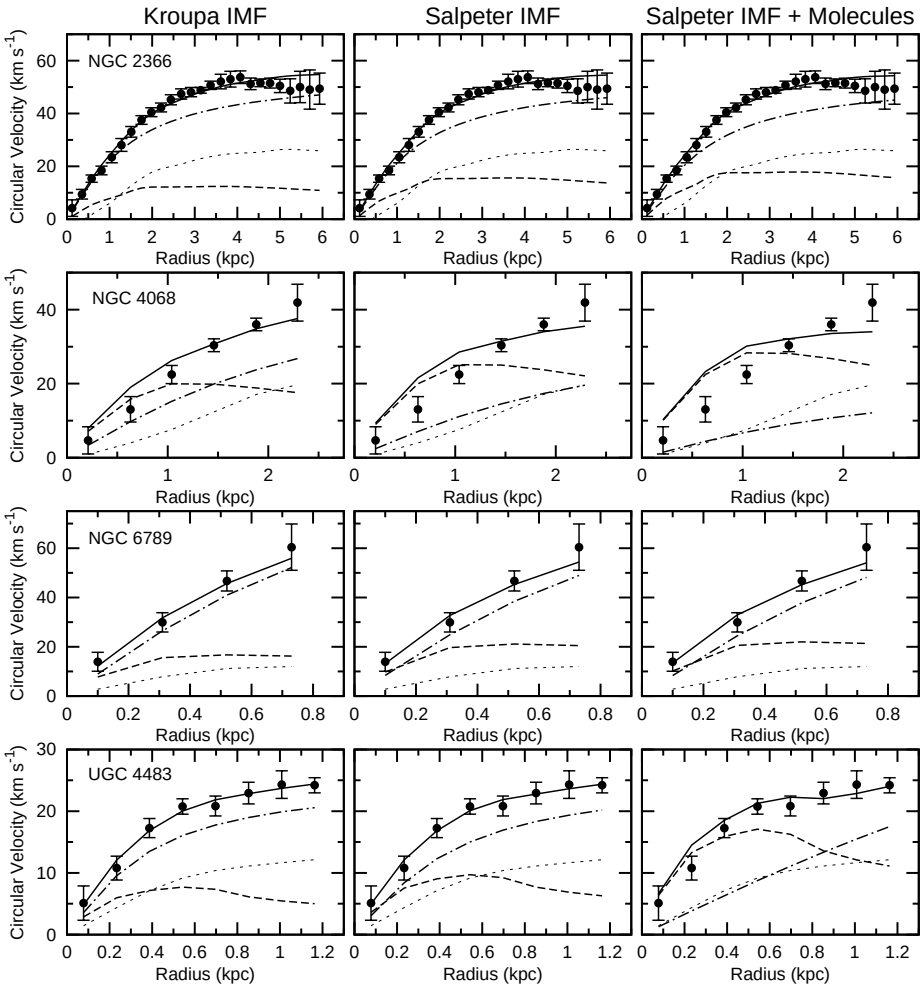

Figure 4.10 – Rotation curve decompositions. Dots show the observed rotation curve (corrected for asymmetric-drift). Long-dashed, short-dashed, and dot-dashed lines show the gravitational contribution due to stars, atomic gas, and dark matter, while the solid line shows the resulting total contribution to the rotation curve. See Sect. 4.7.3 for details.

where the central density ρ_0 and the core radius r_c are the free parameters of the mass model. This is motivated by the fact that observed rotation curves of low-mass galaxies are well-reproduced by cored DM density profiles (e.g. Gentile et al. 2005; Oh et al. 2011b). Since the H I rotation curves are not well-sampled (except for NGC 2366), the parameters of the DM halo cannot be determined with high accuracy. In particular, for NGC 6789 and NGC 4068, the core radius is completely unconstrained, thus we assumed $r_c = R_{opt}$. Given these

Table 4.5 – Results of the rotation curve decompositions.

Galaxy	$F_{\rm bar}(2.2\,R_{\rm d})$			ρ_0 (10^{-3} M$_\odot$ pc^{-3})			$r_{\rm c}$ (kpc)		
	Kroupa	Sal.	Sal.+ Mol.	Kroupa	Sal.	Sal.+ Mol.	Kroupa	Sal.	Sal.+ Mol.
NGC 2366	0.5	0.6	0.6	37	34	31	1.2	1.3	1.3
NGC 4068	0.9	1.2	1.3	14	7	3	*1.8*	*1.8*	*1.8*
NGC 6789	0.4	0.5	0.5	450	397	384	*0.7*	*0.7*	*0.7*
UGC 4483	0.6	0.7	0.9	122	87	15	0.3	0.4	2.0

uncertainties, we did not explore other DM density profiles than the pseudo-isothermal one.

A baryonic disk is usually defined to be maximum if $F_{\rm bar} = V_{\rm bar}/V_{\rm circ} = 0.85 \pm 0.10$ at 2.2 disk scale lenghts (Sackett 1997; Bershady et al. 2011), where $V_{\rm bar}$ is the contribution to the rotation curve given by the baryons. The BCDs in Fig. 4.10 have $F_{\rm bar} \simeq 0.4$ to 0.6, except for NGC 4068 that has $F_{\rm bar} \simeq 0.9$ for a Kroupa IMF and $F_{\rm bar} > 1$ for a Salpeter IMF (see Table 4.5). The latter result may suggest that a Salpeter IMF implies an unphysical, over-maximal disk for NGC 4068; however, if one assumes a nearly-spherical stellar body with a scale-height of ∼600 pc, a Salpeter IMF would give acceptable results with $F_{\rm bar} \lesssim 1$. The sub-maximal disks of NGC 2366, NGC 6789, and UGC 4483 are in line with the results of the DiskMass survey (e.g. Bershady et al. 2011; Westfall et al. 2011; Martinsson 2011), who measured the stellar velocity dispersions of a sample of spiral galaxies and found that $F_{\rm bar} \simeq 0.5$. Note, however, that baryons are still dynamically significant, as $F_{\rm bar} \simeq 0.4$ to 0.6 correspond to baryonic fractions $f_{\rm bar} = M_{\rm bar}/M_{\rm dyn} \simeq 0.2$ to 0.4 within 2.2 $R_{\rm d}$, in line with the results in Sect. 4.7.2.

4.8 Discussion

4.8.1 Comparison with other dwarf galaxies

In Sect. 4.4, we compared the H I distribution and kinematics of BCDs and Irrs. In agreement with previous studies (e.g. van Zee et al. 1998, 2001), we found that BCDs have central H I densities a factor of ∼2 higher than typical Irrs. The average extent of the H I disk with respect to the stellar component, instead, is similar for BCDs, Irrs, and spirals ($R_{\rm H\,I}/R_{\rm opt} \simeq 1.7$ with $R_{\rm opt}$ defined as 3.2 exponential scale-lengths $R_{\rm d}$). We also found that complex H I kinematics are much more common in BCDs (∼50%) than in typical Irrs (∼10%), likely due to the effects of stellar feedback and/or of the triggering mechanism (interactions/mergers or disk instabilities). In Chapter 5, we present a comparison between the rotation curves of BCDs and those of Irrs, and discuss the link between the starburst, the gas concentration, and the gravitational potential (see also Lelli et al. 2012a,b). Here we compare the baryonic fractions of BCDs with those of gas-rich Irrs and gas-poor spheroidals (Sphs).

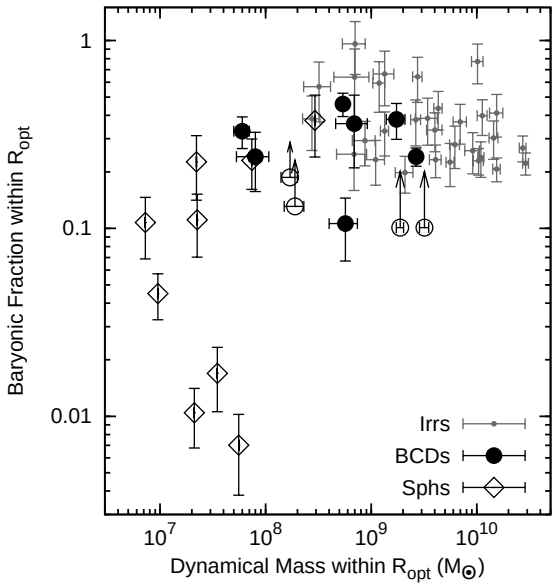

Figure 4.11 – Comparison between the baryonic fractions of BCDs (open and filled circles, same as Fig. 4.9, left panel), Irrs (grey dots), and Sphs (open diamonds). The data for Irrs and Sphs are taken from Swaters et al. (2009) and Wolf et al. (2010), respectively.

For gas-rich Irrs, maximum-disk decompositions of H I rotation curves usually result in high values of the stellar mass-to-light ratio, up to ∼15 in the R-band (e.g. Swaters et al. 2011). These high values of $M_*/L_{\rm R}$ are difficult to explain using stellar population synthesis models (e.g. Zibetti et al. 2009), suggesting that Irrs are dominated by DM at all radii. The detailed baryonic fractions of Irrs, however, remain uncertain because they depend on the assumed value of $M_*/L_{\rm R}$. For the BCDs in our sample, instead, we can directly calculate the values of $M_*/L_{\rm R}$ using the stellar masses from the HST studies of the resolved stellar populations. Assuming a Salpeter IMF from 0.1 to 100 $M_\odot$ and a gas-recycling efficiency of 30%, we find that the mean value of $M_*/L_{\rm R}$ is ∼1.5 (see Table 4.1). Photometric studies of BCDs (e.g. Papaderos et al. 1996) suggest that the starburst typically increases the total luminosity by a factor of ∼2, whereas studies of the SFHs (e.g. McQuinn et al. 2010b) indicate that the burst produces only a small fraction of the total stellar mass (∼10%). Thus, it is reasonable to assume that Irrs have, on average, $M_*/L_{\rm R} \simeq 3$ for a Salpeter IMF and $M_*/L_{\rm R} \simeq 2$ for a Kroupa IMF.

Similarly to Sect. 4.7.2, we calculated the baryonic fractions of 30 gas-rich dwarfs using the R-band luminosities, H I surface density profiles, and H I rotation curves from Swaters et al. (2002, 2009), and assuming $M_*/L_{\rm R} = 2$. We considered only galaxies with $i > 30°$ and high-quality rotation curves ($q > 2$, see Swaters et al. 2009), that are traced out to ∼3 $R_{\rm d}$ and have $V_{\rm rot} < 100$ km s^{-1} at the last measured point. We also calculated the baryonic fractions of several gas-poor dwarfs using the V-band luminosities and dynamical masses from Wolf et al. (2010), and assuming $M_*/L_{\rm V} = 2.0$. For the nearby Sphs Sculptor and

Fornax, the stellar masses from de Boer et al. (2012a,b) imply, respectively, $M_*/L_V \simeq 2.2$ and $M_*/L_V \simeq 1.7$ (assuming a Kroupa IMF and a gas-recycling efficiency of 30%). We considered only 9 Sphs that have accurate estimates of the stellar velocity dispersion: the 8 "classical" satellites of the Milky Way (Carina, Draco, Fornax, Leo I, Leo II, Sculptor, Sextans, and Ursa Minor) and NGC 185, which is a satellite of M 31. For these Sphs, the baryonic fractions are computed at the 3D deprojected half-light radius $r_{1/2}$ (for an exponential density profile $r_{1/2} \simeq 2.2R_d$, see Wolf et al. 2010), thus they may be slightly overestimated with respect to those of Irrs and BCDs (computed at 3.2 R_d), since the DM contribution is expected to increase at larger radii.

Figure 4.11 shows that starbursting dwarfs (open and filled circles) have baryonic fraction comparable with those of typical Irrs (grey dots) and of some Sphs (open diamonds). The Sphs with extremely-low baryonic fractions ($f_{bar} < 0.1$) are Carina, Draco, Sextans and Ursa Minor, that are very close to the Milky Way and may have suffered from environmental effects (e.g. Mayer et al. 2006; Gatto et al. 2013). We conclude that the baryonic content of BCDs is similar to that of other types of dwarf galaxies, except for some low-luminosity satellities of the Milky Way.

4.8.2 Stellar feedback and outflows

Simulations of galaxy formation in a ΛCDM cosmology require massive gas ouflows to reproduce the observed stellar and DM properties of gas-rich and gas-poor dwarfs at $z \simeq 0$ (e.g. Governato et al. 2010; Oh et al. 2011a; Sawala et al. 2012). In the 18 BCDs considered here, the starburst is a relatively-recent ($\lesssim$1 Gyr) and on-going phenomenon (see e.g. McQuinn et al. 2010a), thus one may expect these galaxies to eject significant amounts of gas out of their low potential wells at the present epoch. We computed atomic gas fractions $f_{gas} = 1.33\, M_{H\,I}/M_{dyn}$ within R_{opt} for the 11 BCDs with accurate estimates of M_{dyn} (see Sect. 4.7.1) and for the 30 Irrs considered in Sect. 4.8.1 (from Swaters et al. 2009). Fig. 4.12 (left panel) shows that both Irrs and BCDs have relatively-high gas fractions ($0.1 \lesssim f_{gas} \lesssim 0.3$), and only a few objects show gas fractions $\lesssim 5\%$. Moreover, the gas fractions of BCDs are similar to those of Irrs. This suggests that either i) BCDs did *not* expell a large amount of gas out of their potential well, or ii) their gas fractions were much higher at the beginning of the starburst, or iii) the gas expelled has been replenished by gas inflows. These 3 hypothesis are discussed in the following.

The possibility that massive gas inflows replenish the presumed outflowing gas seems unlikely, as we found evidence for radial motions in only 4 galaxies (see Sect. 4.6 and Lelli et al. 2012a,b). We do not know the direction of these radial motions, but if we interpret them as inflows, the inferred gas accretion rates would be *only* ∼1 order of magnitude higher than the current SFRs and, thus, consistent with a typical efficiency of ∼10% in converting gas into stars. Moreover, it is likely that these radial motions are recent and short-lived

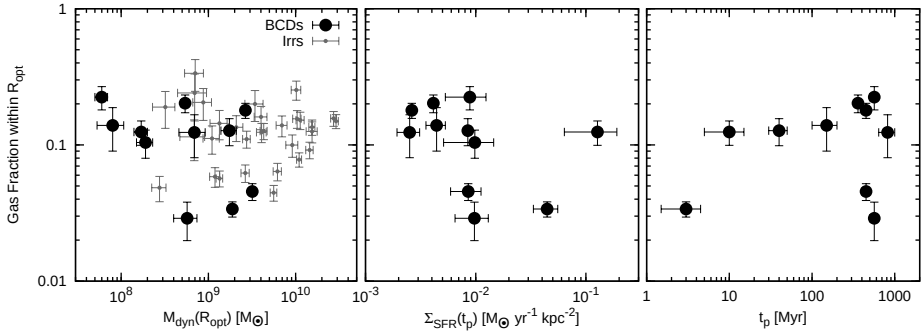

Figure 4.12 – *Left*: the atomic gas fractions $f_{\rm gas} = 1.33\,M_{\rm H\,I}/M_{\rm dyn}$ versus $M_{\rm dyn}$ calculated within the optical radius $R_{\rm opt}$. Large, black dots and small, grey dots indicate BCDs (this work) and Irrs (Swaters et al. 2009), respectively. *Middle*: $f_{\rm gas}$ versus the SFR surface density $\Sigma_{\rm SFR}(t_{\rm p}) = {\rm SFR_p}/(\pi R_{\rm opt}^2)$ where $\rm SFR_p$ is the peak SFR over the last 1 Gyr (see Table 4.1). *Right*: $f_{\rm gas}$ versus the look-back time $t_{\rm p}$ at $\rm SFR_p$.

phenomena, as their typical timescales are comparable with the orbital times (Lelli et al. 2012b). For the other BCDs with a regularly-rotating disk, any radial motion must be $\lesssim 5$ km s^{-1}, which gives us a firm upper-limit to the mean gas inflow rate of $\sim$0.3 $M_\odot$ yr^{-1}. This seems adequate to feed the current star-formation and build up the central concentration of gas observed in BCDs (see Fig. 4.2), but leave little room for massive gas outflows.

In Fig. 4.12 (middle panel), we plot $f_{\rm gas}$ versus the SFR surface density $\Sigma_{\rm SFR}(t_{\rm p}) = {\rm SFR_p}/(\pi R_{\rm opt}^2)$, where $\rm SFR_p$ is the peak SFR over the past 1 Gyr (see Table 4.1). The SFHs of 5 galaxies (NGC 2366, NGC 4068, UGC 4483, UGC 9128, and SBS 1415+437) show two distinct peaks with similar SFRs (consistent within 1σ). Here we consider the older peak as this is the one that formed more stars, given that the SFR is averaged over a larger time-bin (typically a factor of $\sim$4, see McQuinn et al. 2010a). One may expect that BCDs with higher values of $\Sigma_{\rm SFR}(t_{\rm p})$ expell a higher fraction of gas out of their potential well and, thus, might have lower values of $f_{\rm gas}$. This is *not* observed for the 11 objects considered here. However, in some BCDs the starburst started only $\sim$10 Myr ago whereas in other ones it started more than $\sim$500 Myr ago (see e.g. McQuinn et al. 2010a). In Fig. 4.12 (right panel), we also plot $f_{\rm gas}$ versus the look-back time $t_{\rm p}$ at $\rm SFR_p$, which can be considered as the typical "age" of the starburst. There is also no clear correlation between these two quantities. Similarly, we found no clear correlation between $f_{\rm gas}$ and the product $\Sigma_{\rm SFR} \times t_{\rm p}$ or other parameters that quantify the relative strength of the burst, such as $\rm SFR_p/\mathit{M}_{dyn}$, $\rm SFR_p/\mathit{M}_*$, and the birthrate parameter b (see Table 4.1). The lack of *any* significant trend between $f_{\rm gas}$ and the starburst properties suggests that BCDs did *not* eject a large quantity of gas out of their potential wells.

To further investigate the possible effects of outflows, we estimated the gas masses that might have been expelled from the potential wells of BCDs by using

Table 4.6 – Ouflowing gas masses from Eq. 4.7.

Galaxy	$\log(E_{\rm burst})$ (erg)	$M_{\rm out}^{\rm max}$ (10^6 M$_\odot$)	$< \dot{M}_{\rm out}^{\rm max} >$ (M$_\odot$ yr^{-1})	$M_{\rm out}^{\rm max}/M_{\rm gas}$
NGC 625	56.0	11.2±1.9	0.025	0.09
NGC 1569	56.6	16.0±1.6	0.036	0.04
NGC 2366	56.5	12.2±0.5	0.027	0.01
NGC 4068	56.0	7.8±0.4	0.017	0.04
NGC 4214	56.7	8.1±0.4	0.010	0.01
NGC 6789	55.5	0.9±0.1	0.002	0.04
UGC 4483	55.4	5.7±0.5	0.007	0.14
UGC 9128	55.5	5.5±0.9	0.004	0.32

Notes. The burst energies are taken from McQuinn et al. (2010b). $M_{\rm out}^{\rm max}$ is calculated assuming a feedback efficiency $\xi \times \eta \simeq 2 \times 10^{-3}$. See Sect. 4.8.2 for details.

i) the escape velocities derived from the H I kinematics, ii) the burst energies derived from the observed SFHs, and iii) the feedback efficiencies derived by Mac Low & Ferrara (1999) and Ferrara & Tolstoy (2000) using both analytical calculations and high-resolution hydrodynamical simulations. Adopting Eq. 28 of Ferrara & Tolstoy (2000), the mass-loss rate $\dot{M}_{\rm out}$ due to stellar feedback is given by

$$\dot{M}_{\rm out} = 2\,\xi\,\eta\,E\,\gamma/V_{\rm out}^2 \tag{4.6}$$

where η and ξ are parameters related to the feedback efficiency, E is the energy produced by supernovae and stellar winds, γ is the energy production rate, and $V_{\rm out}^2$ is the velocity of the outflowing gas that must be higher than the escape velocity $V_{\rm esc}$. The parameter η represents the fraction of injected energy that is converted into kinetic energy; for radiative bubbles $\eta \lesssim 0.03$ (Koo & McKee 1992; Ferrara & Tolstoy 2000). Since part of the kinetic energy accelerates material in the equatorial plane of the bubble, the parameter ξ corresponds to the fraction of gas that is expelled from the galaxy almost perpendicular to the disk. Using hydrodynamical simulations, Mac Low & Ferrara (1999) found that ξ is usually $\lesssim$7%. Following Ferrara & Tolstoy (2000), we here assume that $\eta = 0.03$ and $\xi = 0.07$, but we warn that the actual values of these parameters are uncertain. Maximum mass-loss rates occur when $V_{\rm out} = V_{\rm esc}$. Assuming that $V_{\rm esc}$ does not significantly change during the burst, the maximum mass that can be expelled from the galaxy is given by

$$M_{\rm out}^{\rm max} = \int_{t_i}^{t_f} \dot{M}_{\rm out} dt = 2\,\xi\,\eta\,V_{\rm esc}^{-2} \int_{t_i}^{t_f} E\,\gamma dt = 2\,\xi\,\eta\,V_{\rm esc}^{-2}\,E_{\rm burst} \tag{4.7}$$

where t_i and t_f are the initial and final times of the burst, and $E_{\rm burst}$ is the total energy created during the burst. In Table 4.6, we list $M_{\rm out}^{\rm max}$ for 7 galaxies in our sample that have both good estimates of $E_{\rm burst}$ and $V_{\rm esc}$. We adopt the values of $E_{\rm burst}$ calculated by McQuinn et al. (2010b) using the observed SFHs

and the evolutionary synthesis code STARBURST99, which can simulate the energy produced by supernovae and stellar winds for a given SFR. We calculate $V_{\rm esc}$ as $\sqrt{2}V_{\rm circ}$ at the optical radius. Table 4.6 shows that, for $\eta \times \xi \simeq 2 \times 10^{-3}$, $M_{\rm out}^{\rm max}$ is very small, less than 10% of the current atomic gas mass. Exceptions are UGC 4483 and UGC 9128, which are among the lowest mass galaxies in our sample, with rotation velocities of only ∼20 km s^{-1}. Only if one assumes that $\eta \times \xi$ is a few times 10^{-2}, the starbursting dwarfs in our sample could have expelled a gas mass comparable to the current, atomic gas mass.

Relatively-low values of $M_{\rm out}/M_{\rm gas}$ are in line with the results of both optical and X-ray observations. Studies of the Hα kinematics have shown that galactic winds are common in BCDs, but the velocities of the Hα gas are usually smaller than the escape velocities (Martin 1996, 1998; van Eymeren et al. 2009a,b, 2010), implying that the ionized gas is gravitationally-bound to the galaxy. Similar results have been found by studies of the Na D absorption doublet (Schwartz & Martin 2004). X-ray observations have revealed that several starbursting dwarfs have a diffuse coronae of hot gas at $T \simeq 10^6$ K, which are likely due to outflows but have low masses, ∼1% of the current H I mass (Ott et al. 2005a,b). The observational evidence, therefore, suggests that galactic winds are common in nearby dwarf galaxies, but they do not expell a significant fraction of the gas mass out of the potential well.

4.9 Summary and conclusions

We presented a systematic study of the H I content of 18 starbursting dwarf galaxies, using both new and archival observations. We selected only nearby galaxies that have been resolved into single stars by HST, thus providing information on their total stellar masses. According to their H I distribution and kinematics, we classified starbursting dwarfs into 3 main families: i) galaxies with a regularly-rotating H I disk (∼50%), ii) galaxies with a kinematically-disturbed H I disk (∼40%), and iii) galaxies with unsettled H I distributions (∼10%). For galaxies with a regularly-rotating H I disk, we derived rotation curves by building 3D kinematic models. For galaxies with a kinematically-disturbed H I disk, we obtained estimates of the rotation velocities in the outer parts. Our main results can be summarized as follows:

1. We firmly establish that the H I surface density profiles of starbursting dwarfs are different from those of typical Irrs. On average, starbursting dwarfs have central H I densities a factor of ∼2 higher than typical Irrs.

2. The average ratio of the H I radius to the optical radius (defined as 3.2 exponential scale-lengths) is 1.7±0.5, similar to the values found for gas-rich spiral and irregular galaxies.

3. Disturbed H I kinematics are much more common in starbursting dwarfs (∼50%) than in typical Irrs (∼10%, see Swaters et al. 2009). This may be

related either to the starburst trigger (interactions/mergers and/or disk instabilities) or to stellar feedback.

4. Two galaxies (NGC 5253 and UGC 6456) show a velocity gradient along the H I minor axis. We modelled the H I emission by a disk dominated by *radial* motions and derived inflow/outflow timescales of ∼100-200 Myr. For NGC 5253, the radial motions appear to be an inflow and would imply a gas accreation rate ∼1 order of magnitude higher than the current SFR.

5. For 11 galaxies with accurate estimates of the circular velocities, we calculated the baryonic fraction $f_{\rm bar}$ within the optical radius, using the stellar masses from the HST studies of the resolved stellar populations. We found that, on average, $f_{\rm bar} \simeq 0.3$ for a Kroupa IMF and $f_{\rm bar} \simeq 0.4$ for a Salpeter IMF. If molecular gas is also taken into account, the mean baryonic fraction may increase up to ∼0.5.

6. For 4 galaxies with a regularly-rotating H I disk centered on the stellar component, we decomposed the rotation curves into mass components. We found that baryons (both stars and gas) are generally not sufficient to explain the inner rise of the rotation curve, although they constitute $\sim 20 - 40\%$ of the total mass at ∼2.2 exponential scale-lengths.

7. Despite the star-formation having injected $\sim 10^{56}$ ergs into the ISM in the last ∼500 Myr (McQuinn et al. 2010b), these starbursting dwarfs have gas fractions comparable with those of typical Irrs. This suggests that *either* starbursting dwarfs do not expell a large amount of gas out of their potential wells, *or* their gas fractions must have been much higher at the beginning of the burst. The lack of any correlation between the observed gas fractions and the starburst properties favors the former scenario.

Acknowledgements

We are grateful to Renzo Sancisi for sharing insights and ideas that fueled this work. We thank Eline Tolstoy for stimulating discussions. We also thank Ed Elson and Angel R. López-Sánchez for providing us with the H I datacubes of NGC 1705 and NGC 5253, respectively, and Polychronis Papaderos for the Hα-subtracted HST image of I Zw 18. We finally thank the members of the WHISP, THINGS, and LITTLE-THINGS projects for having made the H I datacubes publicly available. FL acknowledges the Ubbo Emmius bursary program of the University of Groningen and the Leids Kerkhoven-Bosscha Fund. FF acknowledges financial support from PRIN MIUR 2010-2011, project "The Chemical and Dynamical Evolution of the Milky Way and Local Group Galaxies", prot. 2010LY5N2T.

Appendix 4.A Notes on individual galaxies

Galaxies with a regularly-rotating H I disk

NGC 1705 has a strongly warped H I disk. Our rotation curve rises more steeply than those of Meurer et al. (1998) and Elson et al. (2013) because we applied a beam-smearing correction to the inner velocity-points using 3D disk models (see Fig. 4.5). Meurer et al. (1998) and Elson et al. (2013) decomposed their rotation curves into mass components and found that DM dominates the gravitational potential at all radii. We did *not* build a detailed mass model because the optical and kinematic centers differ by ∼550 pc, while PA_{opt} and PA_{kin} differ by ∼45°.
NGC 2366 has an extended H I disk with a strong kinematic distortion to the North-West (see its velocity field in Appendix 4.C). Our rotation curve is in overall agreement with previous results (Hunter et al. 2001; Thuan et al. 2004; Oh et al. 2008; Swaters et al. 2009; van Eymeren et al. 2009a), but we do not confirm the declining part of the rotation curve found by Hunter et al. (2001) and van Eymeren et al. (2009a) at $R \gtrsim 5'$. This latter result appears to be caused by an anomalous H I cloud that lies at $V_{l.o.s} \simeq 130$ km s^{-1} along the major axis (∼ 7′ from the galaxy center to the North, see the PV-diagram in Fig. 4.3 and Appendix 4.C).
NGC 4068 has a H I distribution characterized by a central depression and several shell-like structures. The H I kinematics is slightly lopsided. Our rotation curve agrees with the one of Swaters et al. (2009) within the errors.
NGC 4214 has a H I disk with multiple spiral arms. Intriguingly, the optical and H I spiral arms wind in opposite directions (clockwise and counter-clockwise, respectively). The H I disk is close to face-on and strongly warped, thus the rotation curve is uncertain. In the inner parts, our rotation curve rises more steeply than the one derived by Swaters et al. (2009); the difference seems to be due to a different choice of the dynamical center (see the PV-diagram in Swaters et al. 2009).
NGC 6789 has a compact H I disk that extends out to only ∼3.5 optical scale-lenghts. The inclination is uncertain: we derived $i = 43° \pm 7°$ using 3D disk models.
UGC 4483 has been studied in Lelli et al. (2012b).
I Zw 18 has been studied in Lelli et al. (2012a).
I Zw 36 has an extended and asymmetric H I distribution (see Ashley et al. 2013), but in the central parts the H I forms a compact, rotating disk. The optical and kinematic centers are offset by ∼12″ (∼340 kpc), while PA_{opt} and PA_{kin} differs by ∼36°.
SBS 1415+437 is a prototype "cometary" BCD, as the starburst region is located at the edge of an elongated stellar body. Remarkably, the kinematic center does not coincide with the optical one but with the starburst region to the South (see Appendix 4.C; the object at R.A.≃$14^h\ 17^m\ 00^s$ and Dec.≃43° 29′

45″ is a foreground star). The lopsided H I distribution and kinematics may be due to a pattern of elliptical orbits centered on the starburst region (cf. Baldwin et al. 1980).

Galaxies with a kinematically-disturbed H I disk

NGC 625 has been previously studied by Côté et al. (2000) and Cannon et al. (2004). Côté et al. (2000) suggested that the complex H I kinematics is due to an interaction/merger, whereas Cannon et al. (2004) argued that it is best described by a gaseous outflow superimposed on a rotating disk. We find it difficult to distinguish between these two possibilities. It is clear, however, that the galaxy has a inner, rotating disk with $V_{\rm rot} \simeq 30$ km s^{-1} (see PV-diagram in Appendix 4.C).

NGC 1569 has been previously studied by Stil & Israel (2002) and Johnson et al. (2012). Both studies derived a rotation curve by fitting the H I velocity field with a tilted-ring model. The PV-diagram along the major axis, however, does not show any sign of rotation in the inner parts (R$\lesssim$1′, see Appendix 4.C). Moreover, the H I line-profiles are very broad and asymmetric, likely due to strong non-circular motions. For these reasons, we restrict our analysis to the rotation velocity in the outer parts ($\sim$50 km s^{-1}).

NGC 4163 shows a very small velocity gradient of $\sim$10 km s^{-1}. The complex H I kinematics may be due to the low $V_{\rm rot}/\sigma_{\rm H\,I}$ ratio. The PA of the stellar body and of the H I disk significantly differ by $\sim$40°.

NGC 4449 has been previously studied by Hunter et al. (1998, 1999), who found that the H I distribution forms 2 counter-rotating systems. For the inner H I disk, we find a rotation velocity of $\sim$35 km s^{-1}. It is unclear whether the outer gas system is really a counter-rotating disk or is formed by two or three H I tails wrapping around the inner disk (similarly to I Zw 18, see Lelli et al. 2012a).

NGC 5253 has been previously studied by Kobulnicky & Skillman (2008) and López-Sánchez et al. (2012), who discussed the possibility of gas inflows/outflows along the minor axis of the galaxy. The data are, indeed, consistent with a H I disk with $V_{\rm rot} < 5$ km s^{-1} and $V_{\rm rad} \simeq 25$ km s^{-1} (see Fig. 4.7). Shadowing of the X-ray emission indicates that the southern side of the galaxy is the nearest one to the observer (Ott et al. 2005a), suggesting that the radial motions are an inflow.

UGC 6456 has been previously studied by Thuan et al. (2004) and Simpson et al. (2011). Simpson et al. (2011) derived a rotation curve using low-resolution (C+D array) observations. They assumed different values of the PA for the approaching and receding sides, which would imply an unusual, asymmetric warp starting within the stellar component (see their Fig. 13). Our 3D models show that the H I kinematics may be simply explained by a disk with $V_{\rm rot} \simeq V_{\rm rad} \simeq \sigma_{\rm H\,I} \simeq 10$ km s^{-1} (see Fig 4.6).

UGC 9128 has a H I disk that rotates at $\sim$25 km s^{-1}, but the VF is very

irregular and the H I line profiles are broad and asymmetric, possibly due to non-circular motions. The optical and kinematic PA differ by $\sim$30°.

Galaxies with unsettled H I distribution

UGC 6541 has a very asymmetric H I distribution. Gas emission is detected only in the northern half of the galaxy. This may be the remnant of a disrupted disk.
UGCA 290 has a H I distribution that is offset with respect to the stellar component. The kinematics is irregular and dominated by a few distinct H I clouds.

Appendix 4.B Tables

Properties of the H I datacubes

Column (1) gives the galaxy name, following the ordering NGC, UGC, UGCA, Zwicky, SBS.
Column (2) gives the radio interferometer used for the 21cm-line observations.
Column (3), (4), and (5) give the spatial and spectral resolutions of the original cube. This cube is typically obtained using a Robust parameter $\Re \simeq 0$.
Column (6), (7), and (8) give the spatial and spectral resolutions of the cube after Gaussian smoothing.
Column (9) gives the noise in the final cube.
Column (10) provides the reference for the original cube.

Optical and H I orientation parameters

Column (1) gives the galaxy name.
Column (2), (3), (4), (5) and (6) give the optical center, ellipticity, inclination, and position angle. These values are derived by interactively fitting ellipses to the outer isophotes. The inclination is calculated assuming an oblate spheroid with intrinsic thickness $q_0 = 0.3$.
Column (7), (8), (9), (10) and (11) give the kinematical center, systemic velocity, inclination, and position angle. These values are derived using H I velocity fields, channel maps, PV-diagrams, and building 3D disk models.
Column (12) gives the projected offset between the optical and kinematical centers. This is calculated as $\sqrt{(\alpha_{\rm opt} - \alpha_{\rm kin})^2 - (\delta_{\rm opt} - \delta_{\rm kin})^2}$, assuming the galaxy distance given in Table 4.1. The error is estimated as FWHM/2.35, where FWHM is the beam of the smoothed H I datacube (see Table 4.B.1). Projected distances smaller than FWHM/2.35 are assumed to be zero.

Structural and dynamical properties

Column (1) gives the galaxy name.
Column (2) gives the stellar mass. This is calculated by integrating the galaxy SFH and assuming a gas-recycling efficiency of 30%. The SFHs were derived by fitting the CMDs of the resolved stellar populations and assuming a Salpeter IMF from 0.1 to 100 $M_\odot$.
Column (3) gives the molecular mass. This is indirectly estimated using Eq. 4.4, which assumes that the star-formation efficiency in dwarfs is the same as in spirals.
Column (4) gives the H I mass $M_{\rm H\,I}$ within $R_{\rm opt}$.
Column (5), (6), and (7) give the baryonic mass within $R_{\rm opt}$ assuming, respectively, a Kroupa IMF, a Salpeter IMF, and a Salpeter IMF plus the possible contribution of molecules.

Column (8) gives the circular velocity at $R_{\rm opt}$.
Column (9) gives the dynamical mass within $R_{\rm opt}$ calculated as $M_{\rm dyn} = V_{\rm circ}^2 \times R_{\rm opt}/G$.
Column (10), (11), and (12) gives the baryonic fraction within $R_{\rm opt}$ assuming, respectively, a Kroupa IMF, a Salpeter IMF, and a Salpeter IMF plus molecules. *Italics* indicate unphysical values >1.

Table 4.B.1 – Properties of the H I datacubes.

Name	Telescope	Original Beam		Original ΔV	Final Beam		Final ΔV	Rms Noise	Source
		(asec×asec)	(pc×pc)	(km s^{-1})	(asec×asec)	(pc×pc)	(km s^{-1})	(mJy/beam)	
(1)	(2)	(3)	(4)	(5)	(6)	(7)	(8)	(9)	(10)
NGC 625	VLA	18.9×11.7	357×221	2.6	30.0×30.0	567×567	5.2	1.80	a
NGC 1569	VLA	5.8×5.0	96×82	2.6	10.0×10.0	165×165	5.2	0.46	b
NGC 1705	ATCA	16.7×14.5	413×358	4.0	16.7×14.5	413×358	7.0	0.40	c
NGC 2366	VLA	6.9×5.9	107×91	2.6	15.0×15.0	233×233	5.2	0.66	b
NGC 4068	WSRT	14.8×11.5	308×240	2.5	20.0×20.0	417×417	6.1	2.00	d
NGC 4163	VLA	9.7×5.9	141×86	1.3	10.0×10.0	145×145	5.2	0.43	b
NGC 4214	VLA	7.6×6.4	99×84	1.3	30.0×30.0	393×393	5.2	2.20	b
NGC 4449	VLA	13.7×12.5	279×254	5.2	20.0×20.0	407×407	10.4	0.80	e
NGC 5253	ATCA	13.6×7.5	231×127	4.0	20.0×20.0	339×339	9.0	0.95	f
NGC 6789	WSRT	13.7×12.7	239×222	2.5	13.7×12.7	239×222	6.1	0.75	a
UGC 4483	VLA	5.7×4.5	88×70	2.6	10.0×10.0	155×155	5.2	0.66	g
UGC 6456	VLA	5.7×4.8	119×100	2.6	15.0×15.0	313×313	5.2	0.90	a
UGC 6541	VLA	6.2×5.5	126×112	1.3	10.0×10.0	204×204	5.2	0.44	b
UGC 9128	VLA	6.2×5.5	66×59	2.6	15.0×15.0	160×160	5.2	0.80	b
UGCA 290	VLA	5.4×4.2	175×136	1.9	10.0×10.0	325×325	4.9	0.56	a
I Zw 18	VLA	1.5×1.4	132×123	1.3	5.0×5.0	441×441	5.2	0.16	h
I Zw 36	VLA	6.8×5.5	194×157	2.6	6.8×5.5	194×157	5.2	0.34	b
SBS 1415+437	VLA	4.6×4.3	303×283	1.9	10.0×10.0	659×659	4.9	0.60	a

References. (a) This work; (b) Hunter et al. (2012); (c) Elson et al. (2013); (d) Swaters et al. (2002); (e) Walter et al. (2008); (f) López-Sánchez et al. (2012); (g) Lelli et al. (2012b); (h) Lelli et al. (2012a).

Table 4.B.2 – Optical and H I orientation parameters.

Name	RA_{opt} (J2000)	Dec_{opt} (J2000)	ϵ_{opt}	i_{opt} (°)	PA_{opt} (°)	RA_{kin} (J2000)	Dec_{kin} (J2000)	V_{sys} (km s^{-1})	i_{kin} (°)	PA_{kin} (°)	Δc (pc)
(1)	(2)	(3)	(4)	(5)	(6)	(7)	(8)	(9)	(10)	(11)	(12)
Galaxies with a regularly-rotating H I *disk*											
NGC 1705	04 54 13.9	-53 21 25	0.28	47±2	55±3	04 54 16.1	-53 21 35	635±2	45:85	10±5	552±164
NGC 2366	07 28 51.9	+69 12 34	0.66	80±2	29±4	07 28 53.3	+69 12 43	103±1	68±5	42±2	150±99
NGC 4068	12 04 02.7	+52 35 28	0.38	56±4	31±4	12 04 03.0	+52 35 30	206±2	44±6	24±3	0
NGC 4214	12 15 38.8	+36 19 39	0.09	26±5	40±20	12 15 36.9	+36 19 59	291±1	30:−1	65:84	393±167
NGC 6789	19 16 41.9	+63 58 17	0.15	34±2	86±4	19 16 41.9	+63 58 17	-151±2	43±7	82±5	0
UGC 4483	08 37 03.4	+69 46 31	0.47	63±3	-13±5	08 37 03.4	+69 46 31	158±2	58±3	0±5	0
I Zw 18	09 34 02.0	+55 14 25	0.50	65±5	135±1	09 34 02.0	+55 14 25	767±4	70±4	145±5	0
I Zw 36	12 26 16.8	+48 29 39	0.30	49±2	80±3	12 26 18.0	+48 29 41	277±2	67±3	44±3	340±74
SBS 1415+437	14 17 02.1	+43 30 19	0.66	80±3	30±5	14 17 01.7	+43 30 07	616±2	66±3	23±3	824±280
Galaxies with a kinematically-disturbed H I *disk*											
NGC 625	01 35 04.3	-41 26 15	0.64	78±2	94±1	01 35 06.3	-41 26 17	398±6	...	120±10	0
NGC 1569	04 30 49.0	+64 50 53	0.54	69±2	118±3	04 30 51.9	+64 50 56	-80±10	...	115±10	310±70
NGC 4163	12 12 09.0	+36 10 11	0.30	49±2	14±2	12 12 09.0	+36 10 16	158±4	...	-25±10	72±62
NGC 4449	12 28 10.8	+44 05 37	0.40	57±3	55±3	12 28 11.3	+44 05 58	210±5	...	60±5	444±173
NGC 5253	13 39 56.0	-31 38 31	0.53	68±2	43±2	13 39 56.0	-31 38 31	410±10	...	40±5	0
UGC 6456	11 27 57.2	+78 59 48	0.50	65±5	-10±5	11 27 58.8	+78 59 51	-102±4	...	0±5	0
UGC 9128	14 15 56.8	+23 03 22	0.28	47±6	33±6	14 15 57.6	+23 03 08	150±4	...	0±10	181±68
Galaxies with unsettled H I *distribution*											
UGC 6541	11 33 28.9	+49 14 22	0.50	65±4	129±2	...	...	250±2	...	...	...
UGCA 290	12 37 22.1	+38 44 41	0.50	65±3	47±3	...	...	468±5	...	...	...

Table 4.B.3 – Mass budget within the optical radius $R_{\rm opt}$.

Name	$M_*^{\rm Sal}$	$M_{\rm mol}$	$M_{\rm H\,I}(R_{\rm opt})$	$M_{\rm bar}^{\rm Kr}$	$M_{\rm bar}^{\rm Sal}$	$M_{\rm bar}^{\rm mol}$	$V_{\rm circ}$	$M_{\rm dyn}(R_{\rm opt})$	$f_{\rm bar}^{\rm Kr}$	$f_{\rm bar}^{\rm Sal}$	$f_{\rm bar}^{\rm mol}$
	(10^7 M$_\odot$)						(km s^{-1})	(10^7 M$_\odot$)			
(1)	(2)	(3)	(4)	(5)	(6)	(7)	(8)	(9)	(10)	(11)	(12)
Galaxies with a regularly-rotating H I *disk*											
NGC 1705	>20	60±18	4.8±0.5	>19	>26	>86	73±3	188±15	>0.10	>0.14	>0.46
NGC 2366	26±3	8±2	36±4	64±5	74±6	82±6	51±2	266±21	0.24±0.03	0.28±0.03	0.31±0.03
NGC 4068	22±3	5.9±1.8	8.2±0.8	25±2	33±3	39±4	36±2	54±6	0.46±0.06	0.61±0.09	0.72±0.10
NGC 4214	>28	12±4	11±1	>32	>42	>54	79±4	319±32	>0.10	>0.13	>0.17
NGC 6789	7±2	0.6±0.2	1.2±0.1	6.0±1.3	8.6±2.0	9.2±2.0	59±9	57±17	0.11±0.04	0.15±0.06	0.16±0.06
UGC 4483	1.0±0.2	2.1±0.6	1.0±0.1	2.0±0.2	2.3±0.2	4.4±0.6	21±2	6±1	0.33±0.06	0.39±0.08	0.74±0.16
I Zw 18	>1.7	7±2	1.6±0.2	>3.2	>3.8	>11	38±4	17±3	>0.19	>0.22	>0.64
I Zw 36	>0.8	4.7±1.4	1.5±0.1	>2.5	>2.8	>7.5	30±3	19±4	>0.13	>0.15	>0.39
SBS 1415+437	17±3	7.6±2.3	6.8±0.7	20±2	26±3	34±4	22±2	27±5	0.73±0.16	0.97±0.21	*1.25±0.27*
Galaxies with a kinematically-disturbed H I *disk*											
NGC 625	26±10	0.8±0.2	6.4±0.6	25±6	34±10	35±10	30±5	69±23	0.36±0.15	0.50±0.22	0.51±0.22
NGC 1569	70±7	15±5	17±2	66±5	92±7	107±9	50±5	174±35	0.38±0.08	0.53±0.11	0.62±0.13
NGC 4163	10±3	1.0±0.3	1.1±0.1	8±2	11±3	12±3	10±4	2.3±1.9	*3.4±2.9*	*5.0±4.3*	*5.4±4.7*
NGC 4449	210±35	184±55	32±3	174±22	252±35	436±65	35±5	94±27	*1.8±0.6*	*2.7±0.9*	*4.6±1.5*
NGC 5253	154±21	31±9	6.8±0.7	106±13	163±21	194±23	<5	...	...	...	...
UGC 6456	5±2	4.3±1.3	2.6±0.3	6.6±1.3	8.5±2.0	13±2	10±5	...	...	...	...
UGC 9128	1.3±0.2	0.13±0.04	0.8±0.1	2.0±0.2	2.4±0.2	2.5±0.2	24±4	8.0±2.7	0.24±0.08	0.30±0.11	0.32±0.11
Galaxies with unsettled H I *distribution*											
UGC 6541	>0.8	0.6±0.2	1.2±0.1	>2.1	>2.4	>2.7	...	...	...	...	...
UGCA 290	>1	2.1±0.6	1.4±0.2	>2.5	>2.9	>4.9	...	...	...	...	...

Appendix 4.C Atlas

In the following, we present overview figures for the 18 starbursting dwarfs in our sample. For each galaxy, we show six panels including both optical and H I data.

Top-left: a sky-subtracted optical image in the R or V band. The cross shows the optical center.

Bottom-left: an isophotal map (black contours) overlaid with a set of concentric ellipses (white contours). The value of the outermost isophote $\mu_{\rm out}$ is given in the note; the isophotes increase in steps of 1 mag arcsec^{-2}. The orientation parameters for the ellipses ($\epsilon_{\rm opt}$ and PA$_{\rm opt}$) are given in Table 4.B.2. The cross shows the optical center. For I Zw 18, the isophotal map was derived from a R-band HST image after the subtraction of the Hα emission, as the nebular emission dominates the galaxy morphology (see Papaderos et al. 2002).

Top-middle: the total H I map. The contour levels are at 1, 2, 4, 8, ... $\times$ $N_{\rm H\,I}(3\sigma)$, where $N_{\rm H\,I}(3\sigma)$ is the pseudo-3σ contour, calculated following Verheijen & Sancisi (2001). The value of $N_{\rm H\,I}(3\sigma)$ is given in the note. The cross shows the optical center. The ellipse shows the beam.

Bottom-middle: the H I surface density profile, derived by azimuthally-averaging over the entire H I disk (black line) and over the approaching and receding sides separately (filled and open circles, respectively). In UGC 6541 and UGCA 290, H I emission is detected only on one side of the galaxy, thus the H I surface density profile was derived using the optical orientation parameters and averaging over a single side.

Top-right: the H I velocity field. Light and dark shading indicate approaching and receding velocities, respectively. The thick, black line shows the systemic velocity. The velocity interval between approaching (black) and receding (white) contours is given in the note. The cross shows the optical center, while the circle shows the kinematic center. The dashed line indicates the kinematic position angle. The ellipse shows the beam.

Bottom-right: Position-Velocity diagram taken through the kinematic center and along the kinematic major axis. Contours are at -3, -1.5 (dashed), 1.5, 3, 6, 12, ... $\times$ σ. The value of σ is given in Table 4.B.1. The vertical and horizontal lines show the kinematic center and the systemic velocity, respectively. For galaxies with a regularly-rotating H I disk, squares show the rotation curve as derived in Sect. 4.5.1, projected along the line of sight. For galaxies with a kinematically-disturbed H I disk, arrows show the estimated value of $V_{\rm rot}$, projected along the line of sight.

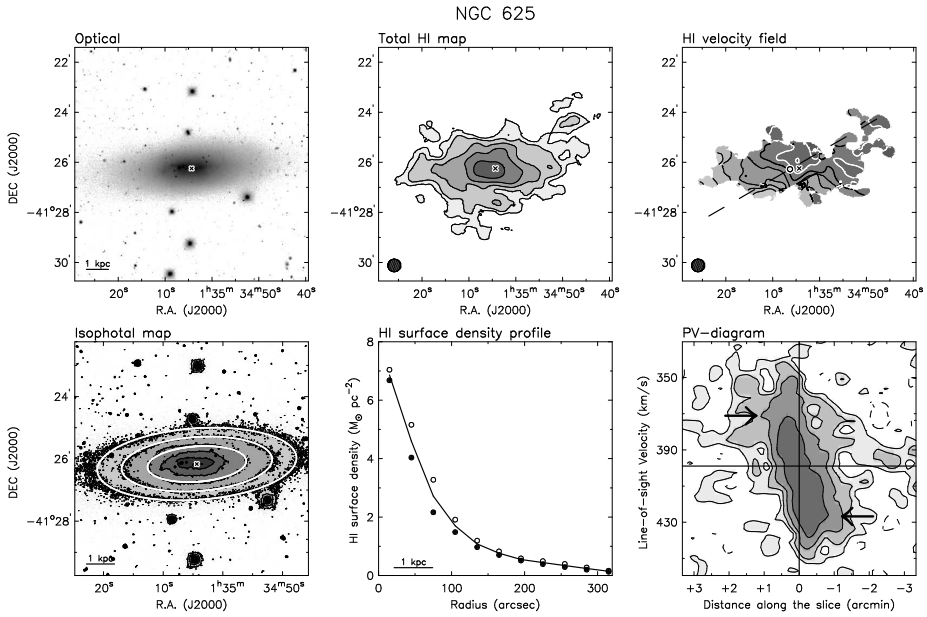

Figure C.1 – *Contours:* $\mu_{\rm out} = 24.5$ R mag arcsec^{-2}; $N_{\rm H\,I}(3\sigma) = 1.1 \times 10^{20}$ atoms cm^{-2}; $V_{\rm l.o.s} = 398 \pm 10$ km s^{-1}.

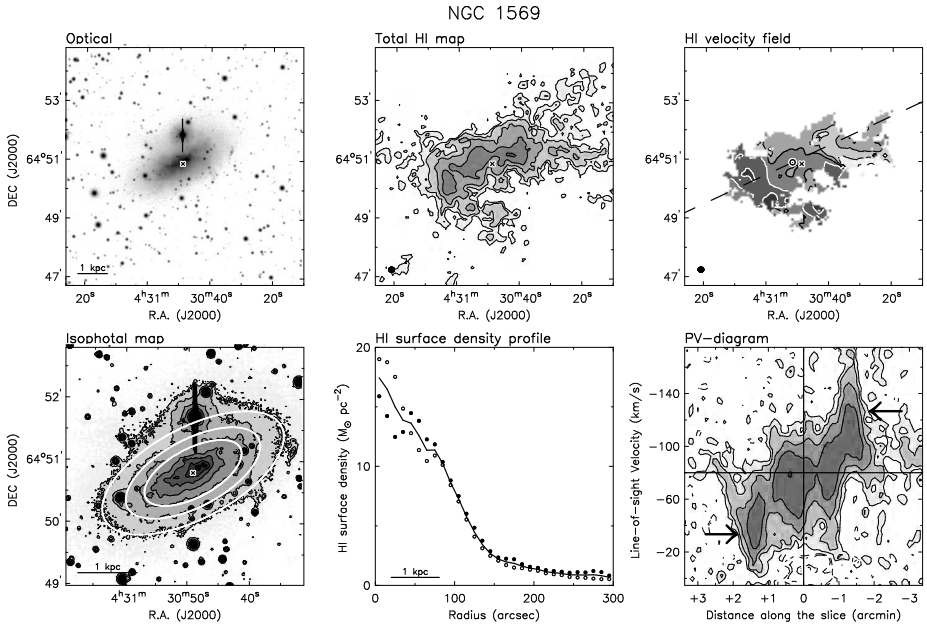

Figure C.2 – *Contours:* $\mu_{\rm out} = 24$ V mag arcsec^{-2}; $N_{\rm H\,I}(3\sigma) = 4.3 \times 10^{20}$ atoms cm^{-2}; $V_{\rm l.o.s} = -80 \pm 20$ km s^{-1}.

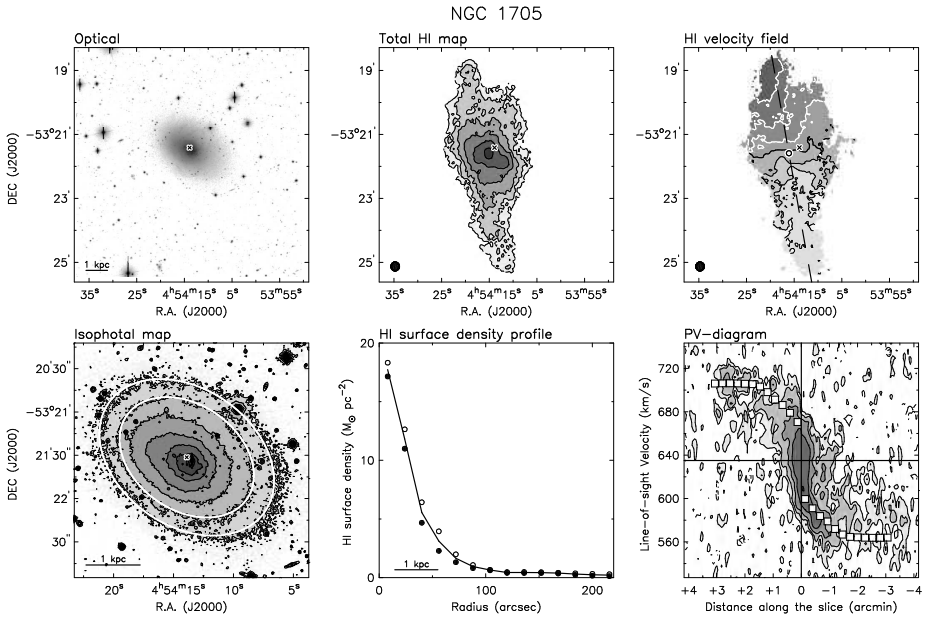

Figure C.3 – *Contours:* $\mu_{\rm out} = 25.5$ R mag arcsec^{-2}; $N_{\rm H\,I}\,(3\sigma) = 1.1 \times 10^{20}$ atoms cm^{-2}; $V_{\rm l.o.s} = 635 \pm 20$ km s^{-1}.

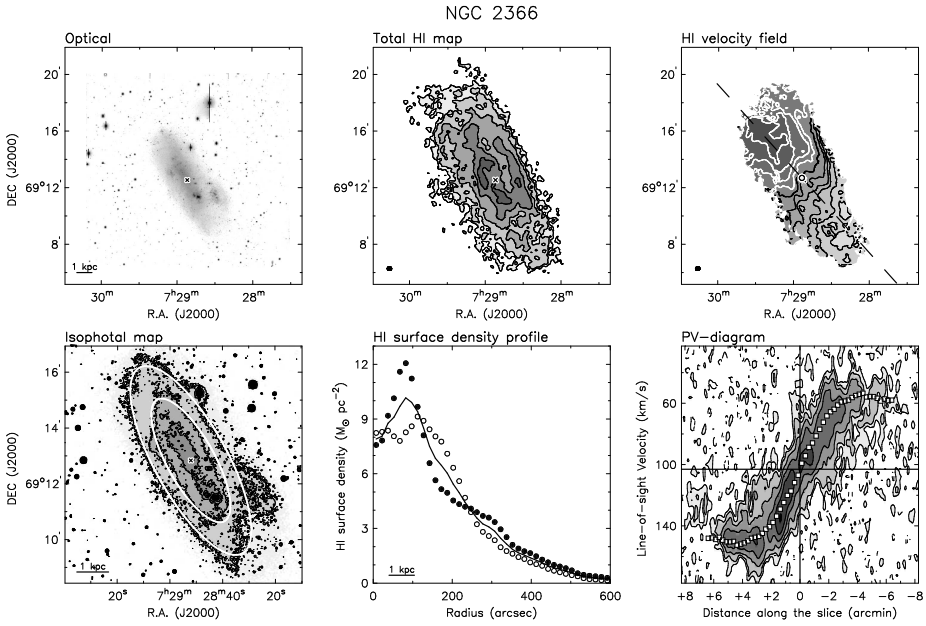

Figure C.4 – *Contours:* $\mu_{\rm out} = 24.5$ V mag arcsec^{-2}; $N_{\rm H\,I}\,(3\sigma) = 2.3 \times 10^{20}$ atoms cm^{-2}; $V_{\rm l.o.s} = 103 \pm 10$ km s^{-1}.

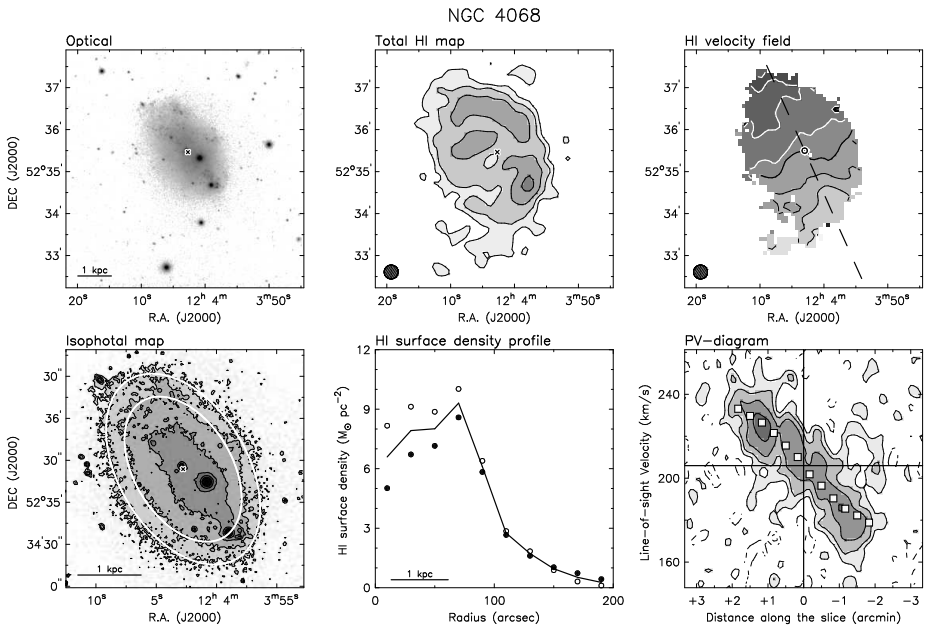

Figure C.5 – **Contours:** $\mu_{\rm out} = 24.5$ R mag arcsec^{-2}; $N_{\rm H\,I}\,(3\sigma) = 3.6 \times 10^{20}$ atoms cm^{-2}; $V_{\rm l.o.s} = 206 \pm 10$ km s^{-1}.

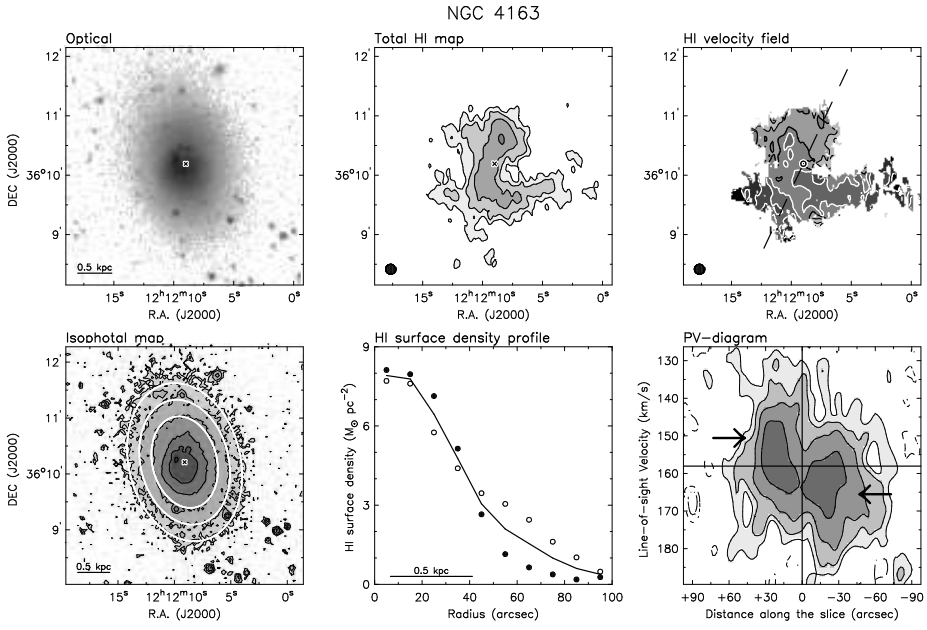

Figure C.6 – **Contours:** $\mu_{\rm out} = 26.5$ V mag arcsec^{-2}; $N_{\rm H\,I}\,(3\sigma) = 2.7 \times 10^{20}$ atoms cm^{-2}; $V_{\rm l.o.s} = 158 \pm 5$ km s^{-1}.

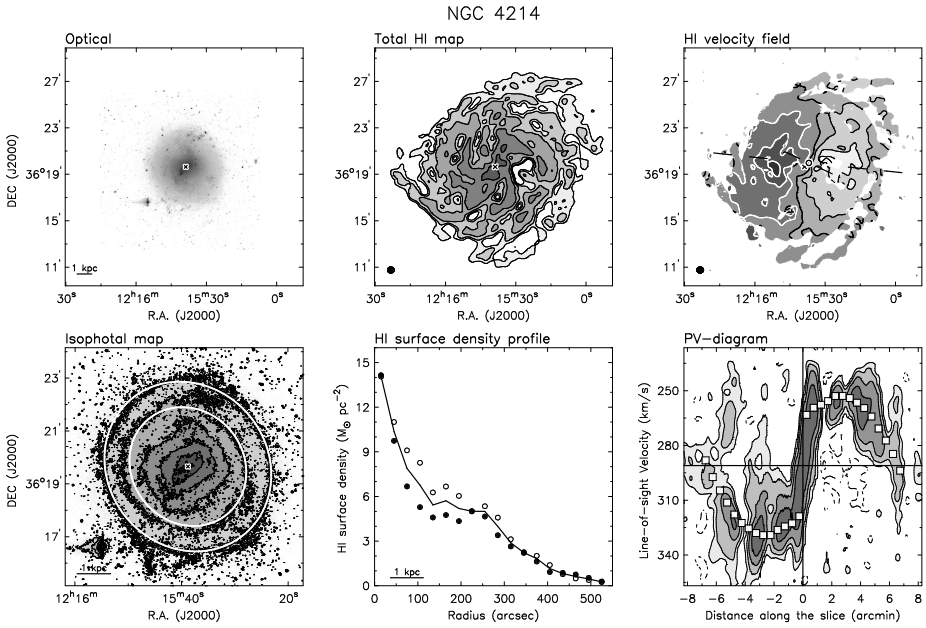

Figure C.7 – **Contours:** $\mu_{\rm out} = 24.5$ V mag arcsec^{-2}; $N_{\rm H\,I}(3\sigma) = 1.2 \times 10^{20}$ atoms cm^{-2}; $V_{\rm l.o.s} = 291 \pm 15$ km s^{-1}.

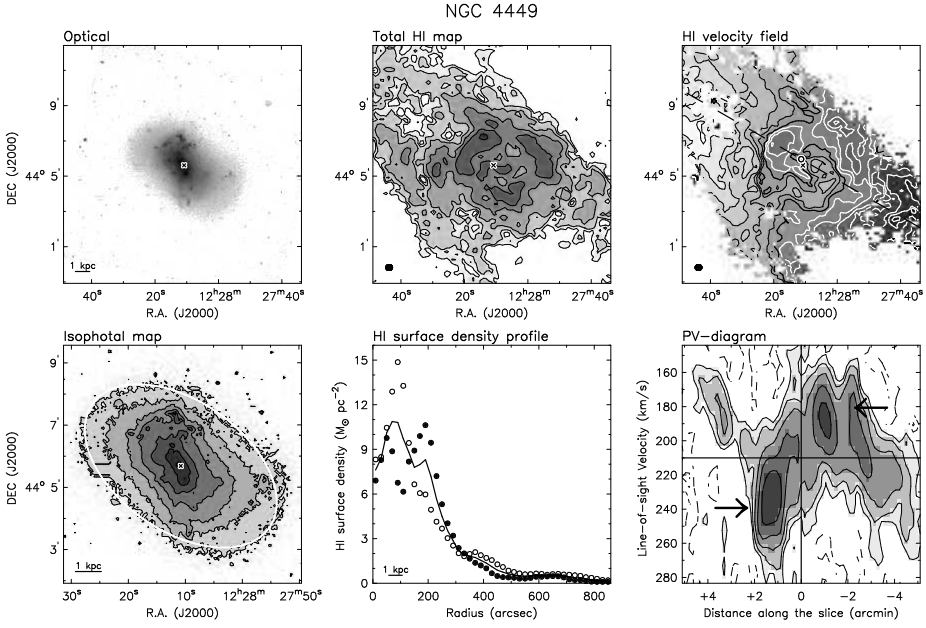

Figure C.8 – **Contours:** $\mu_{\rm out} = 25$ V mag arcsec^{-2}; $N_{\rm H\,I}(3\sigma) = 1.4 \times 10^{20}$ atoms cm^{-2}; $V_{\rm l.o.s} = 210 \pm 10$ km s^{-1}.

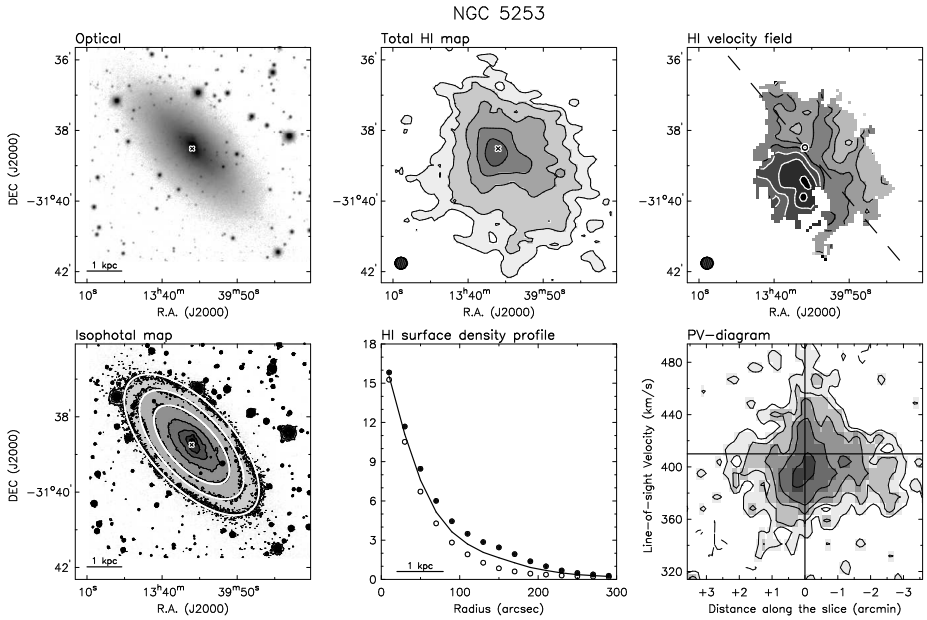

Figure C.9 – **Contours:** $\mu_{\rm out} = 24$ R mag arcsec^{-2}; $N_{\rm H\,I}\,(3\sigma) = 2.1 \times 10^{20}$ atoms cm^{-2}; $V_{\rm l.o.s} = 410 \pm 10$ km s^{-1}.

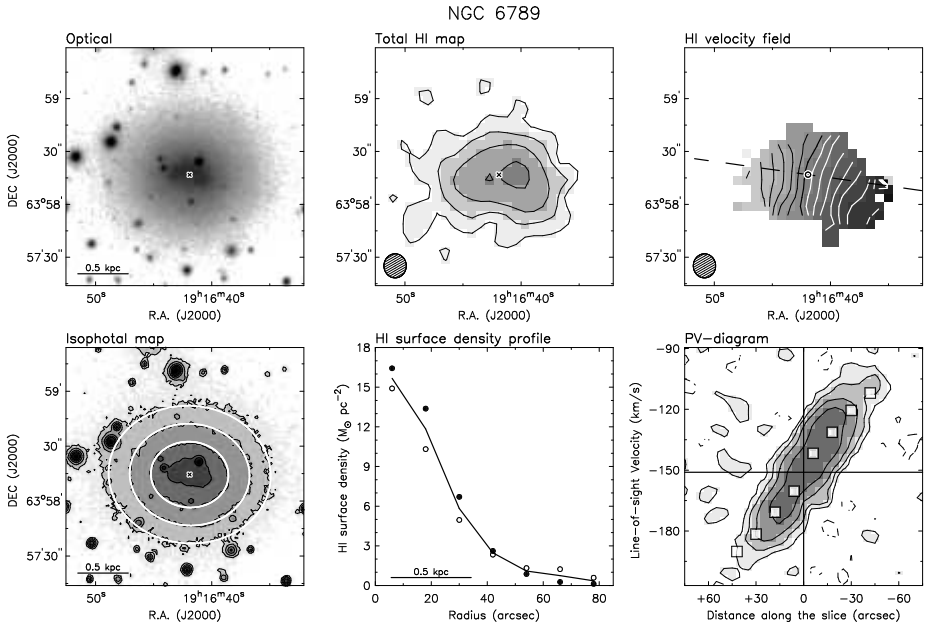

Figure C.10 – **Contours:** $\mu_{\rm out} = 24.5$ R mag arcsec^{-2}; $N_{\rm H\,I}\,(3\sigma) = 3.4 \times 10^{20}$ atoms cm^{-2}; $V_{\rm l.o.s} = -151 \pm 5$ km s^{-1}.

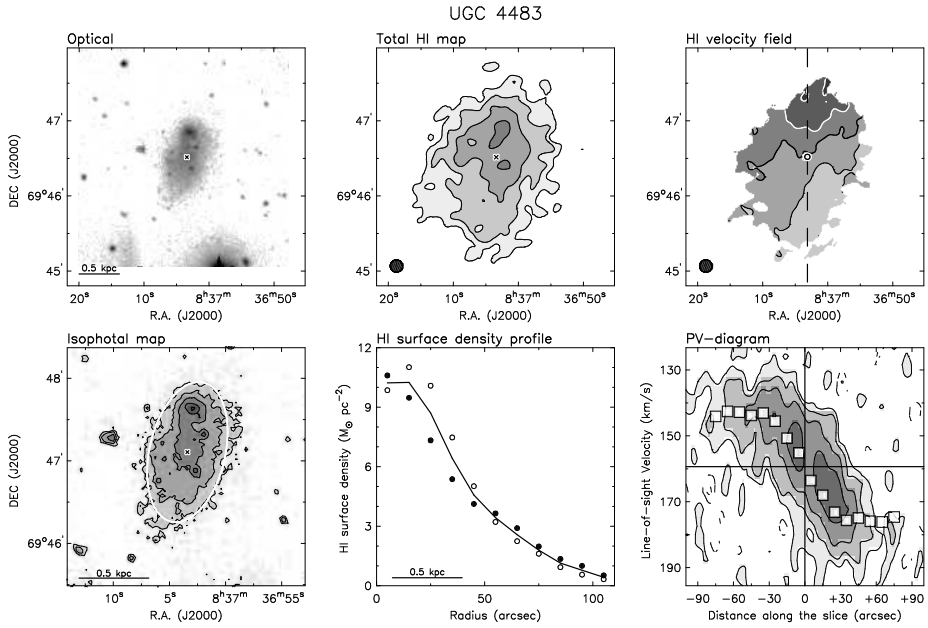

Figure C.11 – **Contours:** $\mu_{\rm out} = 25$ R mag arcsec^{-2}; $N_{\rm H\,I}\,(3\sigma) = 3.4 \times 10^{20}$ atoms cm^{-2}; $V_{\rm l.o.s} = 158 \pm 10$ km s^{-1}.

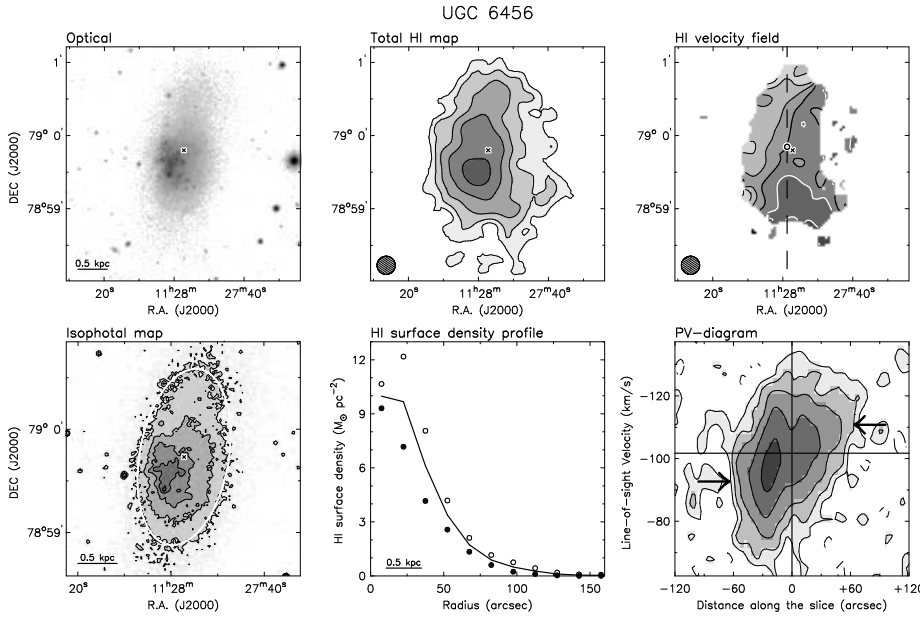

Figure C.12 – **Contours:** $\mu_{\rm out} = 25$ R mag arcsec^{-2}; $N_{\rm H\,I}\,(3\sigma) = 1.8 \times 10^{20}$ atoms cm^{-2}; $V_{\rm l.o.s} = -102 \pm 5$ km s^{-1}.

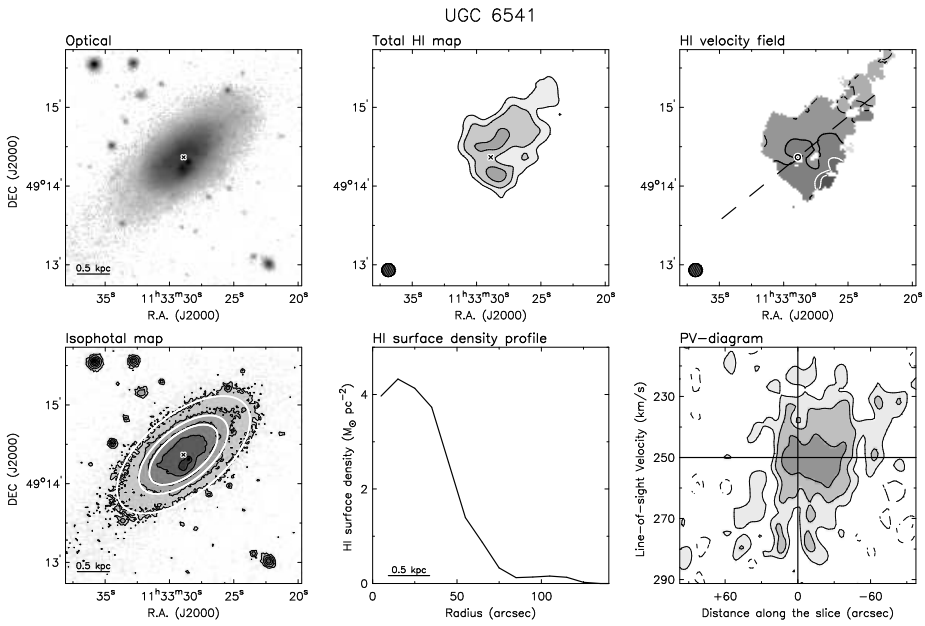

Figure C.13 – **Contours:** $\mu_{\rm out} = 25.5$ R mag arcsec^{-2}; $N_{\rm H\,I}\,(3\sigma) = 3.4 \times 10^{20}$ atoms cm^{-2}; $V_{\rm l.o.s} = 250 \pm 10$ km s^{-1}.

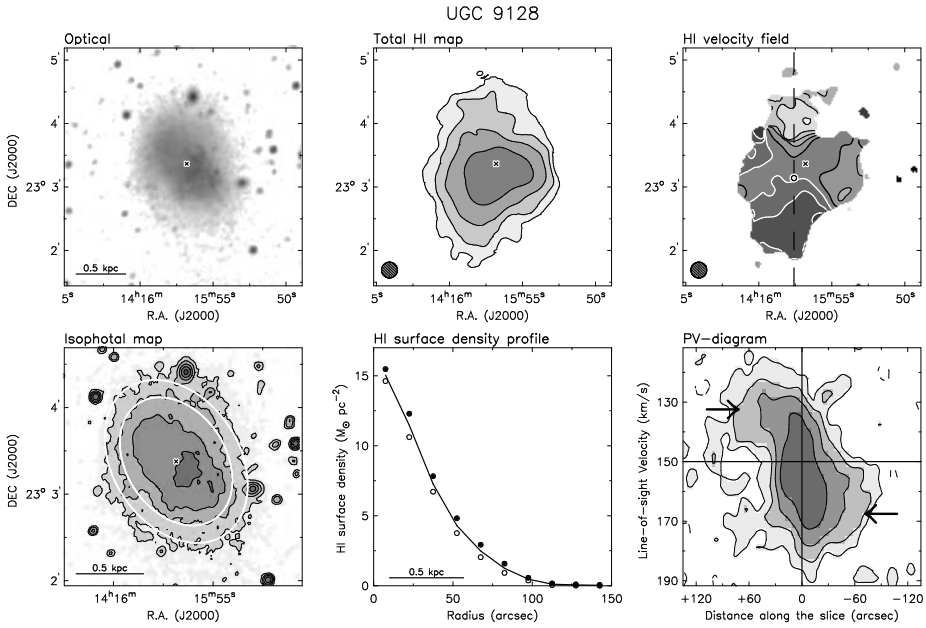

Figure C.14 – **Contours:** $\mu_{\rm out} = 26.5$ V mag arcsec^{-2}; $N_{\rm H\,I}\,(3\sigma) = 2.0 \times 10^{20}$ atoms cm^{-2}; $V_{\rm l.o.s} = 150 \pm 5$ km s^{-1}.

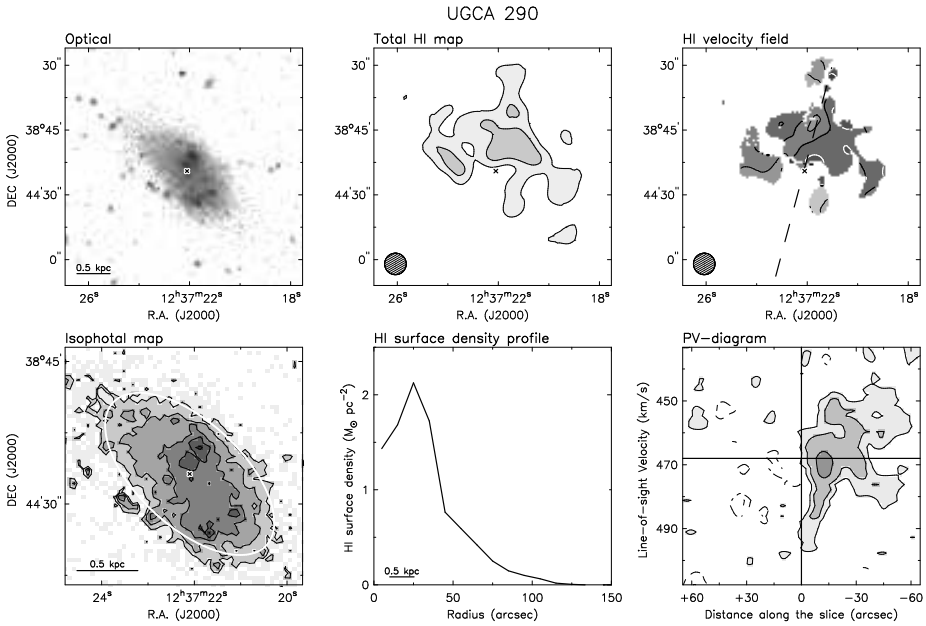

Figure C.15 – **Contours:** $\mu_{\rm out} = 25$ R mag arcsec^{-2}; $N_{\rm H\,I}\,(3\sigma) = 3.1 \times 10^{20}$ atoms cm^{-2}; $V_{\rm l.o.s} = 468 \pm 5$ km s^{-1}.

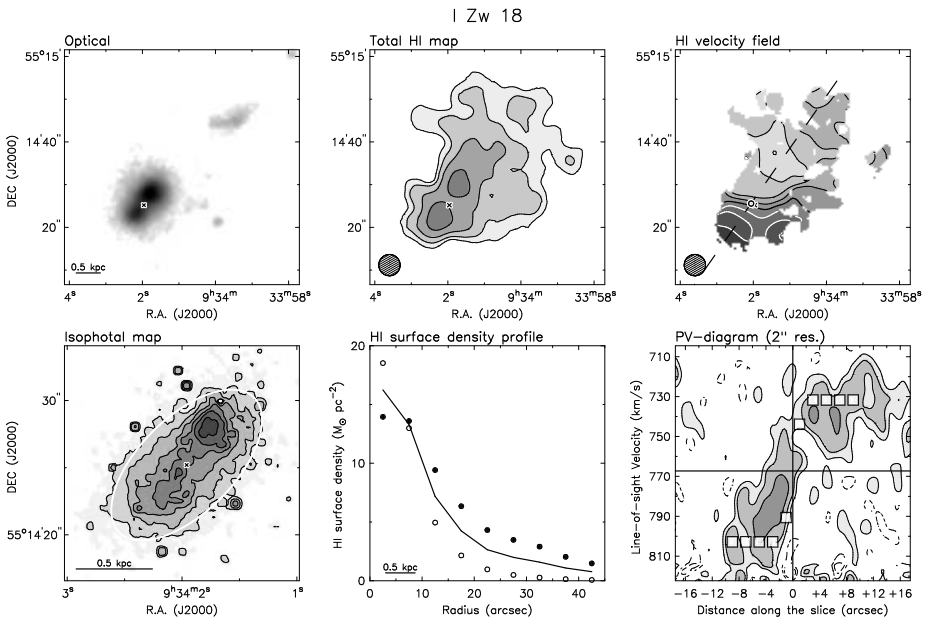

Figure C.16 – **Contours:** $\mu_{\rm out} = 24$ R mag arcsec^{-2}; $N_{\rm H\,I}\,(3\sigma) = 6.3 \times 10^{20}$ atoms cm^{-2}; $V_{\rm l.o.s} = 767 \pm 10$ km s^{-1}.

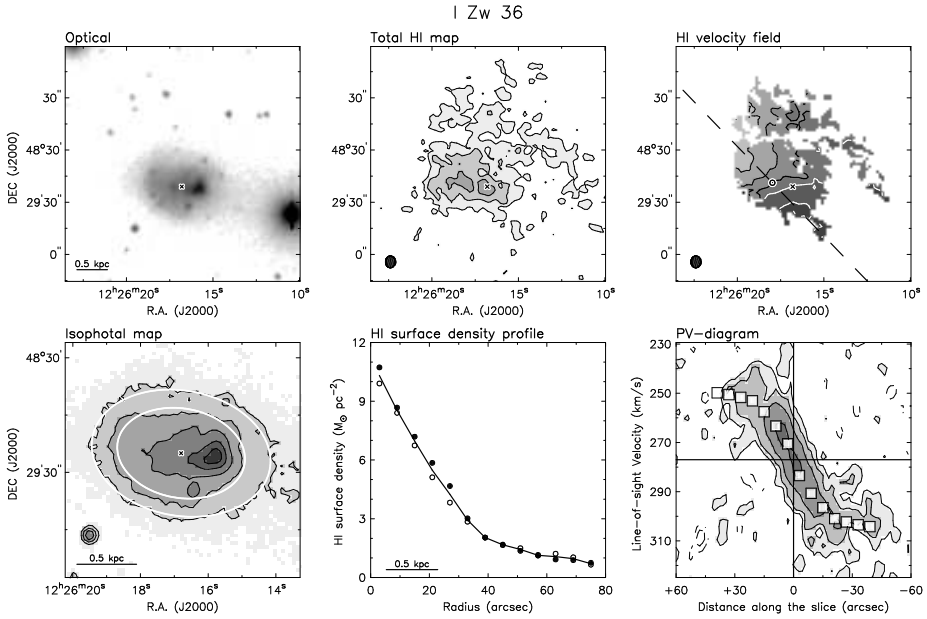

Figure C.17 – **Contours:** $\mu_{\rm out} = 24.5$ R mag arcsec^{-2}; $N_{\rm H\,I}\,(3\sigma) = 7.4 \times 10^{20}$ atoms cm^{-2}; $V_{\rm l.o.s} = 277 \pm 10$ km s^{-1}.

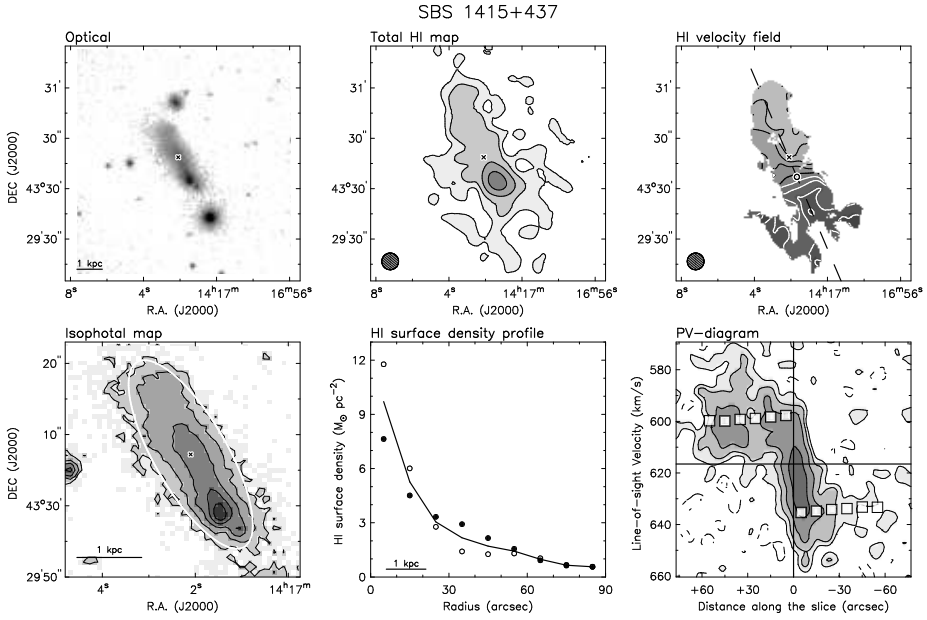

Figure C.18 – **Contours:** $\mu_{\rm out} = 24.5$ R mag arcsec^{-2}; $N_{\rm H\,I}\,(3\sigma) = 3.7 \times 10^{20}$ atoms cm^{-2}; $V_{\rm l.o.s} = 616 \pm 5$ km s^{-1}.

References

Annibali, F., Cignoni, M., Tosi, M., et al. 2013, ArXiv e-prints
Annibali, F., Greggio, L., Tosi, M., Aloisi, A., & Leitherer, C. 2003, AJ, 126, 2752
Ashley, T., Simpson, C. E., & Elmegreen, B. G. 2013, AJ, 146, 42
Baldwin, J. E., Lynden-Bell, D., & Sancisi, R. 1980, MNRAS, 193, 313
Begeman, K. G. 1987, PhD thesis, , Kapteyn Institute, (1987)
Berg, D. A., Skillman, E. D., Marble, A. R., et al. 2012, ApJ, 754, 98
Bershady, M. A., Martinsson, T. P. K., Verheijen, M. A. W., et al. 2011, ApJL, 739, L47
Bigiel, F., Leroy, A., Walter, F., et al. 2008, AJ, 136, 2846
Binggeli, B. & Popescu, C. C. 1995, A&A, 298, 63
Boselli, A., Lequeux, J., & Gavazzi, G. 2002, A&A, 384, 33
Bravo-Alfaro, H., Brinks, E., Baker, A. J., Walter, F., & Kunth, D. 2004, AJ, 127, 264
Briggs, D. S. 1995, in Bulletin of the American Astronomical Society, Vol. 27, Bulletin of the American Astronomical Society, 1444–+
Broeils, A. H. & Rhee, M.-H. 1997, A&A, 324, 877
Brook, C. B., Governato, F., Roškar, R., et al. 2011, MNRAS, 415, 1051
Cannon, J. M., McClure-Griffiths, N. M., Skillman, E. D., & Côté, S. 2004, ApJ, 607, 274
Cannon, J. M., Most, H. P., Skillman, E. D., et al. 2011, ApJ, 735, 36
Côté, S., Carignan, C., & Freeman, K. C. 2000, AJ, 120, 3027
Crone, M. M., Schulte-Ladbeck, R. E., Greggio, L., & Hopp, U. 2002, ApJ, 567, 258
Dale, D. A., Cohen, S. A., Johnson, L. C., et al. 2009, ApJ, 703, 517
de Boer, T. J. L., Tolstoy, E., Hill, V., et al. 2012a, A&A, 539, A103
de Boer, T. J. L., Tolstoy, E., Hill, V., et al. 2012b, A&A, 544, A73
Elson, E. C., de Blok, W. J. G., & Kraan-Korteweg, R. C. 2010, MNRAS, 404, 2061
Elson, E. C., de Blok, W. J. G., & Kraan-Korteweg, R. C. 2011, MNRAS, 415, 323
Elson, E. C., de Blok, W. J. G., & Kraan-Korteweg, R. C. 2013, MNRAS, 429, 2550
Ferrara, A. & Tolstoy, E. 2000, MNRAS, 313, 291
Fraternali, F., van Moorsel, G., Sancisi, R., & Oosterloo, T. 2002, AJ, 123, 3124
Freeman, K. C. 1970, ApJ, 160, 811
Gallagher, III, J. S. & Hunter, D. A. 1987, AJ, 94, 43
Gatto, A., Fraternali, F., Read, J. I., et al. 2013, MNRAS, 433, 2749
Gentile, G., Burkert, A., Salucci, P., Klein, U., & Walter, F. 2005, ApJL, 634, L145
Gil de Paz, A., Madore, B. F., & Pevunova, O. 2003, ApJS, 147, 29
Governato, F., Brook, C., Mayer, L., et al. 2010, Nature, 463, 203

Governato, F., Zolotov, A., Pontzen, A., et al. 2012, MNRAS, 422, 1231
Guseva, N. G., Papaderos, P., Izotov, Y. I., et al. 2003, A&A, 407, 105
Högbom, J. A. 1974, A&AS, 15, 417
Hunter, D. A. & Elmegreen, B. G. 2006, ApJS, 162, 49
Hunter, D. A., Elmegreen, B. G., & van Woerden, H. 2001, ApJ, 556, 773
Hunter, D. A., Ficut-Vicas, D., Ashley, T., et al. 2012, AJ, 144, 134
Hunter, D. A., van Woerden, H., & Gallagher, J. S. 1999, AJ, 118, 2184
Hunter, D. A., van Woerden, H., & Gallagher, III, J. S. 1996, ApJS, 107, 739
Hunter, D. A., Wilcots, E. M., van Woerden, H., Gallagher, J. S., & Kohle, S. 1998, ApJL, 495, L47
Izotov, Y. I. & Thuan, T. X. 1999, ApJ, 511, 639
Johnson, M., Hunter, D. A., Oh, S.-H., et al. 2012, AJ, 144, 152
Kobulnicky, H. A. & Skillman, E. D. 1997, ApJ, 489, 636
Kobulnicky, H. A. & Skillman, E. D. 2008, AJ, 135, 527
Koo, B.-C. & McKee, C. F. 1992, ApJ, 388, 93
Kuchinski, L. E., Freedman, W. L., Madore, B. F., et al. 2000, ApJS, 131, 441
Lauberts, A. & Valentijn, E. A. 1989, The surface photometry catalogue of the ESO-Uppsala galaxies
Lelli, F., Verheijen, M., Fraternali, F., & Sancisi, R. 2012a, A&A, 537, A72
Lelli, F., Verheijen, M., Fraternali, F., & Sancisi, R. 2012b, A&A, 544, A145
Leroy, A. K., Walter, F., Brinks, E., et al. 2008, AJ, 136, 2782
López-Sánchez, Á. R., Koribalski, B. S., van Eymeren, J., et al. 2012, MNRAS, 419, 1051
Mac Low, M. & Ferrara, A. 1999, ApJ, 513, 142
Marlowe, A. T., Meurer, G. R., & Heckman, T. M. 1999, ApJ, 522, 183
Martin, C. L. 1996, ApJ, 465, 680
Martin, C. L. 1998, ApJ, 506, 222
Martinsson, T. P. K. 2011, PhD thesis, University of Groningen
Matthews, L. D. & Uson, J. M. 2008, AJ, 135, 291
Mayer, L., Mastropietro, C., Wadsley, J., Stadel, J., & Moore, B. 2006, MNRAS, 369, 1021
McGaugh, S. S. 2005, ApJ, 632, 859
McGaugh, S. S. 2011, Physical Review Letters, 106, 121303
McGaugh, S. S. 2012, AJ, 143, 40
McGaugh, S. S., Schombert, J. M., Bothun, G. D., & de Blok, W. J. G. 2000, ApJL, 533, L99
McQuinn, K. B. W., Skillman, E. D., Cannon, J. M., et al. 2010a, ApJ, 721, 297
McQuinn, K. B. W., Skillman, E. D., Cannon, J. M., et al. 2010b, ApJ, 724, 49
McQuinn, K. B. W., Skillman, E. D., Dalcanton, J. J., et al. 2012, ApJ, 751, 127
Meurer, G. R., Carignan, C., Beaulieu, S. F., & Freeman, K. C. 1996, AJ, 111, 1551

Meurer, G. R., Freeman, K. C., Dopita, M. A., & Cacciari, C. 1992, AJ, 103, 60
Meurer, G. R., Hanish, D. J., Ferguson, H. C., et al. 2006, ApJS, 165, 307
Meurer, G. R., Staveley-Smith, L., & Killeen, N. E. B. 1998, MNRAS, 300, 705
Oh, S., de Blok, W. J. G., Walter, F., Brinks, E., & Kennicutt, R. C. 2008, AJ, 136, 2761
Oh, S.-H., Brook, C., Governato, F., et al. 2011a, AJ, 142, 24
Oh, S.-H., de Blok, W. J. G., Brinks, E., Walter, F., & Kennicutt, Jr., R. C. 2011b, AJ, 141, 193
Okamoto, T., Frenk, C. S., Jenkins, A., & Theuns, T. 2010, MNRAS, 406, 208
Ott, J., Walter, F., & Brinks, E. 2005a, MNRAS, 358, 1423
Ott, J., Walter, F., & Brinks, E. 2005b, MNRAS, 358, 1453
Papaderos, P., Izotov, Y. I., Thuan, T. X., et al. 2002, A&A, 393, 461
Papaderos, P., Loose, H., Fricke, K. J., & Thuan, T. X. 1996, A&A, 314, 59
Ramya, S., Kantharia, N. G., & Prabhu, T. P. 2011, ApJ, 728, 124
Recchi, S., Matteucci, F., D'Ercole, A., & Tosi, M. 2004, A&A, 426, 37
Romano, D., Tosi, M., & Matteucci, F. 2006, MNRAS, 365, 759
Roychowdhury, S., Chengalur, J. N., Kaisin, S. S., Begum, A., & Karachentsev, I. D. 2011, MNRAS, 414, L55
Sackett, P. D. 1997, ApJ, 483, 103
Sánchez-Janssen, R., Méndez-Abreu, J., & Aguerri, J. A. L. 2010, MNRAS, 406, L65
Sancisi, R., Fraternali, F., Oosterloo, T., & van der Hulst, T. 2008, A&ARv, 15, 189
Sawala, T., Frenk, C. S., Crain, R. A., et al. 2013, MNRAS, 431, 1366
Sawala, T., Scannapieco, C., & White, S. 2012, MNRAS, 420, 1714
Schulte-Ladbeck, R. E., Hopp, U., Greggio, L., & Crone, M. M. 2000, AJ, 120, 1713
Schulte-Ladbeck, R. E., Hopp, U., Greggio, L., Crone, M. M., & Drozdovsky, I. O. 2001, AJ, 121, 3007
Schwartz, C. M. & Martin, C. L. 2004, ApJ, 610, 201
Simpson, C. E. & Gottesman, S. T. 2000, AJ, 120, 2975
Simpson, C. E., Hunter, D. A., Nordgren, T. E., et al. 2011, AJ, 142, 82
Stil, J. M. & Israel, F. P. 2002, A&A, 392, 473
Stringer, M. J., Bower, R. G., Cole, S., Frenk, C. S., & Theuns, T. 2012, MNRAS, 423, 1596
Swaters, R. A. & Balcells, M. 2002, A&A, 390, 863
Swaters, R. A., Sancisi, R., van Albada, T. S., & van der Hulst, J. M. 2009, A&A, 493, 871
Swaters, R. A., Sancisi, R., van Albada, T. S., & van der Hulst, J. M. 2011, ApJ, 729, 118
Swaters, R. A., van Albada, T. S., van der Hulst, J. M., & Sancisi, R. 2002, A&A, 390, 829

Taylor, C. L., Brinks, E., Grashuis, R. M., & Skillman, E. D. 1995, ApJS, 99, 427
Taylor, C. L., Brinks, E., Pogge, R. W., & Skillman, E. D. 1994, AJ, 107, 971
Taylor, C. L., Kobulnicky, H. A., & Skillman, E. D. 1998, AJ, 116, 2746
Taylor, V. A., Jansen, R. A., Windhorst, R. A., Odewahn, S. C., & Hibbard, J. E. 2005, ApJ, 630, 784
Terlevich, R., Melnick, J., Masegosa, J., Moles, M., & Copetti, M. V. F. 1991, A&AS, 91, 285
Thuan, T. X., Hibbard, J. E., & Lévrier, F. 2004, AJ, 128, 617
Thuan, T. X. & Izotov, Y. I. 2005, ApJS, 161, 240
van Albada, T. S. & Sancisi, R. 1986, Royal Society of London Philosophical Transactions Series A, 320, 447
van der Hulst, J., Terlouw, J., Begeman, K., Zwitser, W., & Roelfsema, P. 1992, in ASP Conf. Ser. 25, ed. D. M. Worall, C. Biemesderfer, & J. Barnes, San Francisco: ASP, 131
van der Kruit, P. C. & Searle, L. 1981, A&A, 95, 105
van Eymeren, J., Koribalski, B. S., López-Sánchez, Á. R., Dettmar, R.-J., & Bomans, D. J. 2010, MNRAS, 407, 113
van Eymeren, J., Marcelin, M., Koribalski, B., et al. 2009a, A&A, 493, 511
van Eymeren, J., Marcelin, M., Koribalski, B. S., et al. 2009b, A&A, 505, 105
van Zee, L., Salzer, J. J., & Skillman, E. D. 2001, AJ, 122, 121
van Zee, L., Skillman, E. D., & Salzer, J. J. 1998, AJ, 116, 1186
Verheijen, M. & Sancisi, R. 2001, A&A, 370, 765
Verheijen, M. A. W. 2001, ApJ, 563, 694
Viallefond, F. & Thuan, T. X. 1983, ApJ, 269, 444
Walter, F., Brinks, E., de Blok, W. J. G., et al. 2008, AJ, 136, 2563
Walter, F., Brinks, E., Duric, N., & Klein, U. 1997, AJ, 113, 2031
Westfall, K. B., Bershady, M. A., Verheijen, M. A. W., et al. 2011, ApJ, 742, 18
Wilcots, E. M. & Miller, B. W. 1998, AJ, 116, 2363
Wolf, J., Martinez, G. D., Bullock, J. S., et al. 2010, MNRAS, 406, 1220
Zibetti, S., Charlot, S., & Rix, H.-W. 2009, MNRAS, 400, 1181

Chapter 5

Evolution of dwarf galaxies: a dynamical perspective

— **Federico Lelli, Filippo Fraternali, and Marc Verheijen** —

Submitted to Astronomy & Astrophysics

Abstract

For a rotating galaxy, the inner circular-velocity gradient $d_R V(0)$ provides a direct estimate of the central dynamical mass density, including gas, stars, and dark matter. We consider 60 low-mass galaxies with high-quality H I and/or stellar rotation curves (including starbursting dwarfs, irregulars, and spheroidals), and estimate $d_R V(0)$ as $V_{R_\mathrm{d}}/R_\mathrm{d}$, where R_d is the galaxy scale-length. For gas-rich dwarfs, we find that $V_{R_\mathrm{d}}/R_\mathrm{d}$ correlates with the central surface brightness μ_0, the mean atomic gas surface density Σ_gas, and the star formation rate surface density Σ_SFR. Starbursting galaxies, such as blue compact dwarfs (BCDs), generally have higher values of $V_{R_\mathrm{d}}/R_\mathrm{d}$ than dwarf irregulars, suggesting that the starburst is closely related to the inner shape of the potential well. There are, however, some "compact" irregulars with values of $V_{R_\mathrm{d}}/R_\mathrm{d}$ similar to BCDs. Unless a redistribution of mass takes place, BCDs must evolve into compact irregulars. Rotating spheroidals in the Virgo cluster follow the same correlation between $V_{R_\mathrm{d}}/R_\mathrm{d}$ and μ_0 as gas-rich dwarfs. They have values of $V_{R_\mathrm{d}}/R_\mathrm{d}$ comparable to those of BCDs and compact irregulars, pointing at evolutionary links between these types of dwarfs. Finally, we find that, similarly to spiral galaxies and massive starbursts, the star-formation activity in dwarfs can be parametrized as $\Sigma_\mathrm{SFR} = \epsilon\,\Sigma_\mathrm{gas}/\tau_\mathrm{orb}$, where τ_orb is the orbital time and $\epsilon \simeq 0.02$.

5.1 Introduction

Low-luminosity, dwarf galaxies are the most common systems in the Universe (e.g. Ferguson & Binggeli 1994). Despite numerous observational and theoretical studies, their formation and evolution is still not fully understood (e.g. Tolstoy et al. 2009; Mayer 2011; Kormendy & Bender 2012). Three main types of dwarfs exist in the nearby Universe: i) gas-poor dwarfs that are *not* currently forming stars, which are usually called spheroidals (Sphs) or dwarf ellipticals (dEs), hereafter we will refer to them as Sphs; ii) gas-rich dwarfs that are forming stars at a relatively-low rate, named irregulars (Irrs); and iii) starbursting dwarfs that are forming stars at an unusually high rate. The latter objects are often classified as amorphous dwarfs (based on optical morphology, e.g. Gallagher & Hunter 1987; Marlowe et al. 1999), H II-galaxies (based on emission-line spectroscopy, e.g. Terlevich et al. 1991), and/or blue compact dwarfs (BCDs, based on colors and surface brightness measurements, e.g. Gil de Paz et al. 2003). Hereafter, we will refer to any starbursting dwarf as a BCD. As we will show in Sect. 5.4.1, the term "BCD" captures a fundamental observational fact: the starburst activity (the *blue* color) occurs mainly in galaxies with a steep gravitational potential (i.e., a *compact* distribution of mass), providing that they have also a strong concentration of gas.

It is known that Sphs, Irrs, and BCDs follow the same correlations between the effective surface brightness $\mu_{\rm eff}$, the effective radius $R_{\rm eff}$, and the total magnitude M, pointing at evolutionary links between them (e.g. Kormendy 1985; Binggeli 1994; Tolstoy et al. 2009). In this respect, BCDs are particularly interesting as the burst durations are typically of the order of a few 100 Myr (McQuinn et al. 2010a), thus they must evolve into another type of dwarf as the starburst fades. The possibility of morphological transformations between low-mass galaxies is also suggested by the existence of "transition type" dwarfs, which have intermediate properties between Sphs and Irrs/BCDs (e.g. Sandage & Hoffman 1991; Mateo 1998; Dellenbusch et al. 2007, 2008).

Several photometric studies have shown that the underlying, old stellar component of BCDs typically has a smaller scale-length and a higher central surface brightness than Irrs and Sphs of the same luminosity, suggesting that the evolutionary links between BCDs and Irrs/Sphs are not straightforward (e.g. Papaderos et al. 1996; Gil de Paz & Madore 2005). However, it is generally difficult to obtain accurate structural parameters for starbursting dwarfs, as the galaxy morphology is extremely irregular and young stars may dominate the integrated light over much of the stellar body. Recently, Micheva et al. (2013) obtained deep optical and near-infrared photometry, and challenged the previous results, arguing that the structural parameters of the old stellar component of BCDs are consistent with those of Irrs and Sphs.

A different approach is to consider dynamical information that directly traces the distribution of mass, such as H I rotation curves (e.g. Lelli et al. 2012a,b). Using qualitative estimates of the rotation velocities, van Zee et al. (2001)

suggested that BCDs have steeper rotation curves than low surface brightness galaxies of similar luminosity (see also Meurer et al. 1998). In Chapter 3 (Lelli et al. 2012b), we considered a small sample of BCDs and Irrs with high-quality H I rotation curves, and measured the circular-velocity gradient $V_{R_\mathrm{d}}/R_\mathrm{d}$, where R_d is the exponential scale-length of the stellar body. We found that BCDs generally have higher values of $V_{R_\mathrm{d}}/R_\mathrm{d}$ than typical Irrs, implying that they have a higher central dynamical mass density (including gas, stars, and dark matter). BCDs also have higher central H I surface densities than Irrs (e.g. van Zee et al. 1998, 2001; Simpson & Gottesman 2000). This suggests that the starburst is closely related to the inner shape of the gravitational potential and to the central concentration of gas. This connection must be the key to understanding the mechanisms that trigger and drive the starburst in BCDs.

In this paper, we confirm the results of Lelli et al. (2012b) for a larger sample of BCDs and Irrs, and include star formation rate (SFR) indicators in the analysis. We also consider a sample of rotating Sphs. We use the dynamical information provided by $V_{R_\mathrm{d}}/R_\mathrm{d}$ to constrain the possible evolutionary links between dwarf galaxies.

5.2 The sample

We define a dwarf galaxy as an object with $V_\mathrm{flat} \leq 100$ km s^{-1}, where V_flat is the asymptotic velocity along the flat part of the rotation curve. For a pressure-supported system, V_flat can be estimated as $\sqrt{3}\sigma_\mathrm{obs}$ (McGaugh & Wolf 2010), where σ_obs is the observed velocity dispersion along the line of sight. According to the Tully-Fisher (TF) relation, $V_\mathrm{flat} \simeq 100$ km s^{-1} occurs at $M_\mathrm{B} \simeq -16.5$ mag (cf. Verheijen 2001), thus our definition of a dwarf galaxy qualitatively agrees with the standard one given by Tammann (1994), which is based on total luminosity and size. However, contrary to Tammann's criteria, our definition is directly related to the potential well of the galaxy and is not affected by the effects of recent star-formation, which can be serious for BCDs where the light is dominated by young stellar populations. The choice of 100 km s^{-1} is *not* arbitrary: in galaxies with $V_\mathrm{flat} \leq 100$ km s^{-1} bulges tend to disappear (e.g. Kormendy & Bender 2012) and some cosmological models predict that mass loss from supernova feedback may start to affect the baryonic content (e.g. Dekel & Silk 1986). Using the baryonic TF relation (e.g. McGaugh 2012), we estimate that galaxies with $V_\mathrm{flat} \leq 100$ km s^{-1} have a baryonic mass (stars and atomic gas) $M_\mathrm{bar} \lesssim 5 \times 10^9\ M_\odot$.

We built a sample of dwarf galaxies with high-quality rotation curves, retrieving optical and H I data from various sources. We included in our selection also galaxies with rotation curves that do not reach the flat part but have $V_\mathrm{last} < 100$ km s^{-1}, where V_last is the circular velocity at the last measured point. The dynamical masses of these objects are uncertain, as their rotation curves may continue to rise, but their total magnitudes are $\lesssim -18$ R mag ($\lesssim -17$

B mag), indicating that these galaxies are actual dwarfs. In the following, we describe our sub-samples of starbursting dwarfs (BCDs), typical star-forming dwarfs (Irrs), and gas-poor dwarfs (Sphs). We also clarify the nomenclature used throughout this paper.

5.2.1 Starbursting dwarfs

In Chapter 4, we built a sample of 18 starbursting dwarfs by considering objects that satisfy two criteria: i) they have been resolved into single stars by the *Hubble Space Telescope* (HST); and ii) their star formation histories (SFHs), as derived by modelling color-magnitude diagrams (e.g. McQuinn et al. 2010a), show an increase in the recent SFR by a factor $\gtrsim 3$ with respect to the average, past SFR. We consider here a sub-sample of 8 objects, for which high-quality H I rotation curves could be derived (see Chapter 4). For another object (SBS 1415+437), we could derive a rotation curve but this may not be a reliable tracer of the gravitational potential, as the galaxy strongly deviates from the baryonic TF relation (see Fig. 8 in Chapter 4), thus we exclude this object here. As we stressed in Sect. 5.1, we refer to any starbursting dwarf as a BCD.

We also added the well-studied BCD NGC 2915, which has been resolved into single stars by HST (Karachentsev et al. 2003), but its SFH has not yet been derived. NGC 2915 has a regularly-rotating H I disk (Elson et al. 2010), but the inner parts of the rotation curve are uncertain because of the presence of strong non-circular motions (Elson et al. 2011), thus we assigned a conservative error of 15 km s^{-1} to the inner points of the rotation curve.

The properties of our sample of 9 BCDs are given in Tables 5.B.1 and 5.B.2. For all these objects, the HST studies provide accurate distances using the tip of the red giant branch (TRGB) method.

5.2.2 Irregulars

We selected 37 Irrs from the sample of Swaters et al. (2009). We required that the galaxies have high-quality rotation curves ($q \leq 2$, see Swaters et al. 2009) and inclinations between 30° and 80°, thus the rotation velocities and the central surface brightnesses can be measured with small uncertainties. The rotation curves of these galaxies have been derived by Swaters et al. (2009) taking into account beam-smearing effects. We also added another 6 objects that meet our quality-criteria: UGC 6955 (DDO 105) and UGC 8320 (DDO 168) from Broeils (1992), UGC 6399 and UGC 6446 from Verheijen & Sancisi (2001), and the Local Group dwarfs WLM (Jackson et al. 2004) and NGC 6822 (Weldrake et al. 2003). These 43 galaxies are classified as Irr, Im, Sm, or Sd (de Vaucouleurs et al. 1991); for simplicity we refer to all of them as Irr.

It is possible that some of these Irrs may harbour a starburst and, thus, should be considered as BCDs. For example, the sample of Swaters et al. (2009) contains NGC 4214 (IBm), NGC 2366 (IBm), and NGC 4068 (Im), which are

part of our sample of starbursting dwarfs. Moreover, McQuinn et al. (2010a) studied the SFH of NGC 6822, a prototype Irr in the Local Group, and found that it may have experienced a recent starburst. However, since the HST field-of-view covers only ∼10% of the stellar body of NGC 6822 (McQuinn et al. 2012), the SFH is representative of a small fraction of the galaxy, thus we prefer to consider NGC 6822 as a typical Irr (see also Mateo 1998; Tolstoy et al. 2009). The sample of Swaters et al. (2009) also contains Holmberg II (UGC 4305), which is a well-studied starbursting dwarf (Weisz et al. 2008; McQuinn et al. 2010b). For this galaxy, the value of the inclination i is uncertain: Swaters et al. (2009) assumed $i = 40°$, Oh et al. (2011) derived $i = 49°$ from a tilted-ring fit to the velocity field and $i = 25°$ from the baryonic TF relation, whereas Gentile et al. (2012) constrained the outer value of i between 20° and 35° by building 3-dimensional disk models. Given these uncertainties, we chose to exclude Holmberg II.

Tables 5.B.3 and 5.B.4 provide the properties of our sample of 43 Irrs. Galaxy distances have been taken from the literature adopting the following distance indicators (in order of decreasing priority): Cepheids, TRGB, and TF relation.

5.2.3 Rotating spheroidals

The sample of gas-poor dwarfs is drawn from van Zee et al. (2004a,b), who used long-slit optical spectroscopy to derive stellar rotation curves and velocity dispersion profiles of 16 low-luminosity galaxies in the Virgo cluster. We selected only 8 objects that show a clear rotation-velocity gradient for $R \lesssim R_{\rm d}$. These galaxies have been classified as dEs by Binggeli et al. (1985). Following Kormendy et al. (2009), we refer to them as Sphs, since they are intrinsically different from bright elliptical galaxies and follow different scaling relations. We assume that the Virgo cluster is at a distance of 16.1±1.2 Mpc (Kelson et al. 2000).

Van Zee et al. (2004b) provide the rotation velocities projected along the line of sight. To trace the gravitational potential of the galaxy, these velocities must be corrected for inclination and pressure-support. To correct for inclination, we modelled the Sphs as thick disks (see Sect. 5.3.2). To correct for pressure-support, we calculated the asymmetric-drift correction (see Appendix 5.A). These 8 objects have $V_{\rm last} \leq 100$ km s^{-1} after applying the inclination and asymmetric-drift corrections, thus they fulfill our definition of a dwarf galaxy. The properties of our sample of rotating Sphs are given in Table 5.B.5.

5.3 Data Analysis

In Sect. 5.4, we will present several diagrams that compare the dynamical, structural, and star-formation properties of dwarf galaxies. Here we describe

the quantities that enter in those diagrams and provide details about the error budget.

5.3.1 The circular-velocity gradient

The key quantity here is the inner circular-velocity gradient

$$d_R V(0) = \lim_{R \to 0} \frac{dV_{\rm circ}(R)}{dR}, \tag{5.1}$$

where $V_{\rm circ}(R)$ is the circular velocity of a test particle orbiting at the galactocentric radius R (see also Lelli et al. 2013). For a spherical distribution of mass, $d_R V(0) = \sqrt{4/3\pi G\rho_0}$ where G is Newton's constant and ρ_0 is the central dynamical mass density (including gas, stars, and dark matter). Thus, for a given dynamical mass, $d_R V(0)$ provides, to a first approximation, a direct measure of the *inner steepness* of the potential well of a galaxy. The rotation curves of dwarf galaxies are typically described by a nearly solid-body part for $R \lesssim 2R_{\rm d}$ (where $R_{\rm d}$ is the exponential scale-length) and an outer flat part for $R \gtrsim 2R_{\rm d}$ (e.g. Swaters et al. 2009). Thus, we can estimate $d_R V(0)$ on the solid-body portion of the rotation curve as $V_{R_{\rm d}}/R_{\rm d}$, where $V_{R_{\rm d}} = V_{\rm circ}(R_{\rm d})$. If high-resolution rotation curves are available, it is possible to quantify $d_R V(0)$ using more sophisticated techniques such as a polynomial fit (Lelli et al. 2013); for bulgeless galaxies with a nearly-exponential luminosity profile, this would result in differences in $d_R V(0)$ within a factor of $\sim$2. For the purposes of this paper, a simple estimate of $d_R V(0)$ as $V_{R_{\rm d}}/R_{\rm d}$ is sufficiently accurate. We also note that, since we are considering the solid-body portion of the rotation curve, the exact value of $R_{\rm d}$ does not strongly affect the value of $d_R V(0) \simeq V_{R_{\rm d}}/R_{\rm d}$.

For gas-rich galaxies (BCDs and Irrs), $V_{\rm circ}(R)$ is directly provided by the H I rotation curve $v_{\rm rot}(R)$, as the asymmetric-drift correction to account for the pressure support is typically negligible in the inner galaxy regions (e.g. Swaters et al. 2009; Lelli et al. 2012b). For gas-poor galaxies (Sphs), instead, the stellar rotation curves must be corrected for pressure support. The asymmetric-drift correction is described in Appendix 5.A.

To estimate the error $\delta_{V/R}$ on $V_{R_{\rm d}}/R_{\rm d}$, we consider the following equation:

$$\frac{V_{\rm circ}}{R} = \frac{v_{\rm l.o.s}}{\sin(i)} \frac{1}{\alpha D}, \tag{5.2}$$

where $v_{\rm l.o.s}$ is the circular-velocity projected along the line of sight, i is the inclination, α is the angular scale-length (in radians), and D is the galaxy distance. The propagation of the errors gives

$$\delta^2_{V/R} = \left\{ \left[\frac{\delta_{v_{\rm l.o.s}}}{R\sin(i)} \right]^2 + \left[\frac{V_{\rm circ}}{R} \frac{\delta_i}{\tan(i)} \right]^2 + \left[\frac{V_{\rm circ}}{R} \frac{\delta_D}{D} \right]^2 \right\}_{R=R_{\rm d}} \tag{5.3}$$

where the error on α has been neglected. For $\delta_{v_{\rm l.o.s}}/\sin(i)$ we used the error on the rotation velocities given in the original papers; this includes the formal error given by a χ^2-minimization and an additional uncertainty due to the asymmetries between the approaching and the receding side of the galaxy (see e.g. Swaters et al. 2009). For δ_i we assumed a typical error of 3°, as δ_i is not provided in the original papers (except in a few cases, see Tables 5.B.1 and 5.B.3). Typically, δ_D gives a negligible contribution for galaxies with Cepheids and TRGB distances, whereas it dominates the error budget for galaxies with TF distances.

5.3.2 Structural parameters

We collected R-band apparent magnitudes $m_{\rm R}$, central surface brightnesses μ_0, and scale-lengths $R_{\rm d}$ from various sources. For the BCDs, we refer to Chapter 4. For the Irrs, the sources are Swaters & Balcells (2002) (40 galaxies), Tully et al. (1996) (UGC 6399 and UGC 6446), and Hunter & Elmegreen (2006) (WLM and NGC 6822, their V-band values have been converted to R-band assuming $V-R=0.5$). For the Sphs, the source is van Zee et al. (2004a). These authors derived the structural parameters μ_0 and $R_{\rm d}$ by fitting an exponential function to the outer parts of the surface brightness profiles. For BCDs, the resulting values of μ_0 and $R_{\rm d}$ are thought to be representative of the underlaying, old stellar component (e.g. Papaderos et al. 1996; Gil de Paz & Madore 2005).

We calculated absolute magnitudes $M_{\rm R}$ using our adopted distances, and estimated the errors considering the distance uncertainties only, hence $\delta_M = 5\log(e)\delta_D/D$. We corrected μ_0 for inclination i using the following equation:

$$\mu_0^i = \mu_0 - 2.5C\log[\cos(i)] \tag{5.4}$$

where C is a constant related to the internal extinction. Since dwarf galaxies typically have low metallicities (see Tables 5.B.2 and 5.B.4), the dust content is likely low. Hence, we assumed that they are optically-thin ($C=1$). The error $\delta_{\mu_0^i}$ on μ_0^i is given by:

$$\delta^2_{\mu^i} = \delta^2_{\mu_0} + [2.5\log(e)\tan(i)\delta_i]^2. \tag{5.5}$$

Since δ_{μ_0} is usually not provided in the original papers, we assumed that $\delta_{\mu_0} = 0.1$ mag. This conservative choice takes into account uncertainties on the photometric calibration, on the exponential fits, and on the fact that the surface brightness profiles of dwarf galaxies may have inner cores or cusps (see e.g. Swaters & Balcells 2002).

For BCDs and Irrs, the inclination was derived by fitting a tilted-ring model to the H I velocity field and/or by building model-cubes (see Chapter 4 and Swaters et al. 2009 for details). For Sphs, we estimated i from the observed ellipticities ε using the formula

$$\cos i^2 = \frac{(1-\varepsilon)^2 - q_0^2}{1-q_0^2}, \tag{5.6}$$

where q_0 is a constant that depends on the oblateness of the stellar distribution. We assumed $q_0 = 0.35$, as indicated by statistical studies of the observed ellipticities of dwarf galaxies (Lisker et al. 2007; Sánchez-Janssen et al. 2010). If one assumes that $q_0 = 0.2$, a typical value for the stellar disks of spiral galaxies (e.g. Holmberg 1950), the difference in i would be $\lesssim 3°$ for $\varepsilon \leq 0.35$ (within our assumed error δ_i) and $\lesssim 6°$ for $0.35 < \varepsilon < 0.55$ (within $2\delta_i$). In our sample of Sphs, there are no objects with $\varepsilon > 0.55$. Our results are listed in Tables 5.B.1, 5.B.3, and 5.B.5.

5.3.3 Gas and star formation properties

We collected information about the H I content, ionized-gas metallicity, and star formation for all the BCDs and Irrs in our sample. These are briefly described in the following.

We calculated H I masses using the standard formula

$$M_{\rm H\,I}\,[M_\odot] = 236 \times D\,[\rm Mpc]^2 \times S_{\rm H\,I}\,[\rm mJy\,km\,s^{-1}], \tag{5.7}$$

where $S_{\rm H\,I}$ is the observed H I flux from interferometric 21-cm line observations. The error $\delta_{M_{\rm H\,I}}$ on $M_{\rm H\,I}$ is given by:

$$\delta^2_{M_{\rm H\,I}} = (472\,D\,S_{\rm H\,I}\,\delta_D)^2 + (236\,D^2\,\delta_{S_{\rm H\,I}})^2. \tag{5.8}$$

Since the error on $S_{\rm H\,I}$ is usually not given in the original papers, we assumed $\delta_{S_{\rm H\,I}} = 0.1\,S_{\rm H\,I}$ (the typical calibration error of standard H I observations).

Following Swaters et al. (2002), we define the optical radius $R_{\rm opt} = 3.2R_{\rm d}$. $R_{\rm opt}$ is *not* an isophotal radius and, thus, allows us to compare the sizes of galaxies with different central surface brightnesses. For a HSB exponential disk with $\mu_0(B) = 21.65$ mag (Freeman 1970), $R_{\rm opt} = 3.2\ R_{\rm d}$ is equivalent to the usual isophotal radius R_{25}. We define $\overline{\Sigma}_{\rm H\,I}$ as the mean H I surface density within $R_{\rm opt}$. $\overline{\Sigma}_{\rm H\,I}$ is derived from the observed H I map using an elliptical aperture, and is corrected for i by multiplying the mean H I column density $\overline{N}_{\rm H\,I}$ by $\cos(i)$. We calculated $\overline{\Sigma}_{\rm H\,I}$ for our sample of BCDs, while Swaters et al. (2002) provide $\overline{\Sigma}_{\rm H\,I}$ for 38 Irrs. We point out that $\overline{\Sigma}_{\rm H\,I}$ is distance-independent and nearly unaffected by the linear resolution (in kpc) of the H I observations, as the galaxies in our sample are resolved within $R_{\rm opt}$. The error $\delta_{\overline{\Sigma}_{\rm H\,I}}$ on $\overline{\Sigma}_{\rm H\,I}$ is given by

$$\delta^2_{\overline{\Sigma}_{\rm H\,I}} = [\cos(i)\delta_{\overline{N}_{\rm H\,I}}]^2 + [\overline{N}_{\rm H\,I}\,\sin(i)\delta_i]^2 \tag{5.9}$$

where $\delta_{\overline{N}_{\rm H\,I}}$ is assumed to be 10% of $\overline{N}_{\rm H\,I}$.

We calculated SFRs using the Hα luminosities $L_{\rm H\alpha}$ from Kennicutt et al. (2008), scaled to our assumed distances, and the standard calibration from Kennicutt (1998a). This calibration assumes a Salpeter initial mass function (IMF) from 0.1 to 100 $\rm M_\odot$ and solar metallicity. The latter assumption is

clearly not valid for dwarf galaxies, which generally have sub-solar metallicities (see Tables 5.B.1 and 5.B.4). According to Lee et al. (2009), the ratio SFR/$L_{H\alpha}$ for a galaxy with $Z \simeq Z_{\odot}/5$ is a factor of ∼0.7 lower with respect to a galaxy with $Z = Z_{\odot}$, thus our SFRs may be slightly overestimated. Other common calibrations, which assume a Kroupa IMF and different stellar evolutionary models, would give SFRs that are lower by a factor of ∼0.68 (see Kennicutt & Evans 2012). Kennicutt et al. (2008) provides $L_{H\alpha}$ for 8 BCDs and 29 Irrs present in our sample. For the remaining BCD (I Zw 18), we used the Hα luminosity from Gil de Paz et al. (2003). For another 8 Irrs, we used the Hα SFRs calculated by James et al. (2004) (scaled to our assumed distances and uncorrected for internal extiction), who also used the Kennicutt (1998a) calibration. Besides the uncertainties on the absolute SFR calibration, the errors on the SFRs are of the order of $2\delta_D/D$.

We then calculated the SFR surface density $\Sigma_{\rm SFR} = {\rm SFR}/(\pi R^2_{\rm opt})$ and the ratio SFR/$M_{\rm bar}$, which is a baryonic version of the specific SFR (sSFR=SFR/M_*). The baryonic mass (stars and atomic gas) was estimated from the baryonic TF relation, calibrated by McGaugh (2012) as $M_{\rm bar}[M_{\odot}] = 47 \times V^4_{\rm circ}[{\rm km\,s^{-1}}]$ with an accuracy of ∼10%. For the 16 Irrs and 2 BCDs that do not reach the flat part of the rotation curve, this baryonic mass may be slightly underestimated. We also calculated two types of gas-depletion times: i) $\tau_{\rm global} = 1.33\,M_{\rm H\,I}/{\rm SFR}$, which considers the total atomic gas mass, and ii) $\tau_{\rm local} = 1.33\,\overline{\Sigma}_{\rm H\,I}/\Sigma_{\rm SFR}$, which considers only the atomic gas mass inside $R_{\rm opt}$. The factor 1.33 takes into account the contribution of Helium. Note that $\Sigma_{\rm SFR}$, $\tau_{\rm global}$, and $\tau_{\rm local}$ are distance independent; the errors depend on the accuracy of the H I and Hα flux calibrations (typically ∼10%) and on the SFR calibration. Since the SFRs may be *overestimated* up to a factor of ∼2 due to the assumptions on the IMF and metallicity, the gas depletion times may be slightly *underestimated*. Finally, we compiled Hα+[N II] equivalent widths (EW) and ionized-gas metallicities $12 + \log(O/H)$ from the literature. Our results are listed in Tables 5.B.2 and 5.B.4.

5.4 Results

5.4.1 Gas-rich dwarf galaxies

We start by comparing the dynamical properties of gas-rich, star-forming dwarfs (BCDs and Irrs). As discussed in Sect. 5.3.1, for a bulgeless galaxy with a nearly exponential luminosity profile, $V_{R_{\rm d}}/R_{\rm d}$ is a good proxy for the circular-velocity gradient $d_R V(0) \propto \sqrt{\rho_0}$, where ρ_0 is the central dynamical mass density (including gas, stars, and dark matter). In Fig. 5.1, $V_{R_{\rm d}}/R_{\rm d}$ is plotted versus the central surface brightness μ^i_0 (left) and the mean H I surface density $\overline{\Sigma}_{\rm H\,I}$ (right). $V_{R_{\rm d}}/R_{\rm d}$ correlates with both μ^i_0 and $\overline{\Sigma}_{\rm H\,I}$ (see also Lelli et al. 2012b, 2013). Gas-rich dwarfs with a high central dynamical mass density (high $V_{R_{\rm d}}/R_{\rm d}$)

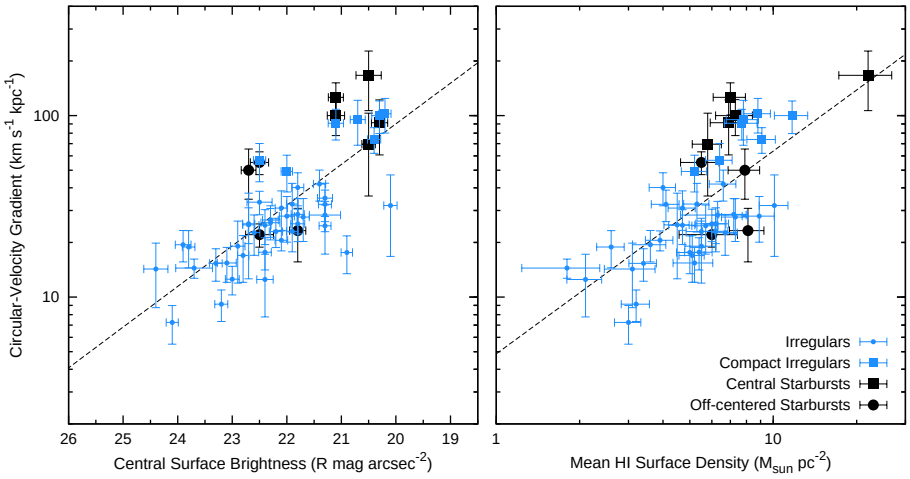

Figure 5.1 – *Left:* the circular-velocity gradient $V_{R_\mathrm{d}}/R_\mathrm{d}$ versus the R-band central surface brightness (inclination corrected). *Right:* $V_{R_\mathrm{d}}/R_\mathrm{d}$ versus the mean H I surface density within R_opt. The black dots and squares show, respectively, BCDs with a diffuse/off-centered starburst and BCDs with a centrally-concentrated starburst. The blue dots and squares show, respectively, typical Irrs and compact Irrs. The dashed lines show a linear-fit to the data. See Sect. 5.4.1 for details.

have also a high central surface brightness and a high H I surface density within the stellar body. To quantify the statistical significance of these relations, we calculated the Pearson's correlation coefficient ρ_cc, where $\rho_\mathrm{cc} = \pm 1$ for an ideal linear correlation/anticorrelation, while $\rho_\mathrm{cc} = 0$ if no correlation is present. We found that both correlations are highly significant: the $V_{R_\mathrm{d}}/R_\mathrm{d} - \mu_0^i$ diagram has $\rho_\mathrm{cc} \simeq -0.8$, while the $V_{R_\mathrm{d}}/R_\mathrm{d} - \overline{\Sigma}_\mathrm{H\,I}$ diagram has $\rho_\mathrm{cc} \simeq 0.7$. A linear, error-weighted fit to the data returns

$$\log(V_{R_\mathrm{d}}/R_\mathrm{d}) = (-0.22 \pm 0.03)\, \mu_0^i + (6.4 \pm 0.6), \tag{5.10}$$

and

$$\log(V_{R_\mathrm{d}}/R_\mathrm{d}) = (1.1 \pm 0.2)\, \log(\overline{\Sigma}_\mathrm{H\,I}) + (0.7 \pm 0.1). \tag{5.11}$$

The left panel of Fig. 5.1 is nearly equivalent to the lower part of the scaling relation described in Chapter 7 (Lelli et al. 2013), which holds for both irregular and spiral galaxies and extends for 2 orders of magnitude in $d_R V(0)$ and 4 orders of magnitude in surface brightness. The values of the slope and intersect in Eq. 5.10 are in close agreement with those found in Lelli et al. (2013) (-0.22 ± 0.02 and 6.3 ± 0.4, respectively).

The previous correlations are completely driven by the *local*, inner properties of the galaxies (μ_0^i and $\overline{\Sigma}_\mathrm{H\,I}$) and not by *global* properties, such as the total baryonic mass or the total dynamical mass. This is illustrated in Fig. 5.2

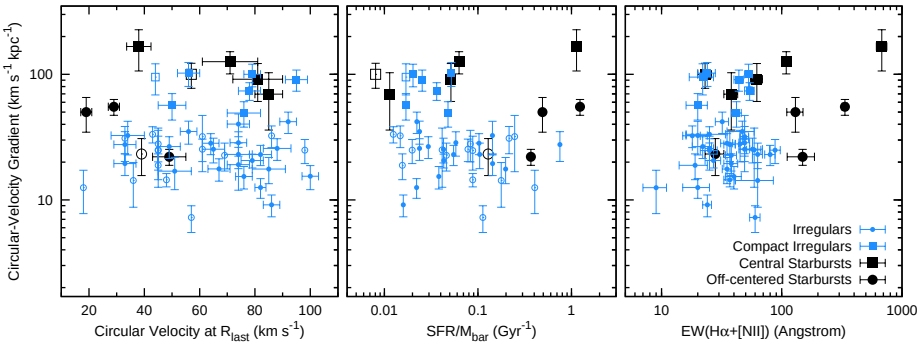

Figure 5.2 – *Left:* $V_{R_\mathrm{d}}/R_\mathrm{d}$ versus the circular velocity at the last measured point V_last. *Middle:* $V_{R_\mathrm{d}}/R_\mathrm{d}$ versus SFR/M_bar, where M_bar is estimated using the baryonic TF relation. *Right:* $V_{R_\mathrm{d}}/R_\mathrm{d}$ versus the Hα+[N II] equivalent width. Symbols are the same as in Fig. 5.1, except for the left and middle panels, where open symbols indicate galaxies with rotation curves that keep rising at V_last, thus their value of SFR/M_bar may be overestimated.

(left), where $V_{R_\mathrm{d}}/R_\mathrm{d}$ is plotted versus the circular-velocity at the last measured point V_last. Clearly, there is no correlation ($\rho_\mathrm{cc} \simeq 0.01$). Similarly, we found no correlation with the absolute magnitude M_R and with the dynamical mass (calculated at the last measured point). At every value of V_last (or M_R), one can find both high-surface-brightness (HSB) dwarfs with a steeply-rising rotation curve and low-surface-brightness (LSB) dwarfs with a slowly-rising rotation curve (cf. with Fig. 5.1, left). In particular, for a given V_last, BCDs typically have higher values of $V_{R_\mathrm{d}}/R_\mathrm{d}$ than the bulk of Irrs.

Fig. 5.1 clearly shows that BCDs are in the top-right part of the $V_{R_\mathrm{d}}/R_\mathrm{d} - \mu_0^i$ and $V_{R_\mathrm{d}}/R_\mathrm{d} - \overline{\Sigma}_\mathrm{H\,I}$ diagrams. This suggests that the starburst activity is closely linked to the inner shape of the potential well and to the central gas surface density. We can distinguish, however, between two types of BCDs: i) centrally-concentrated starbursts (NGC 1705, NGC 2915, NGC 4214, NGC 6789, and I Zw 18), and ii) diffuse and/or off-centered starbursts (NGC 2366, NGC 4068, UGC 4483, and I Zw 36). The former (black squares) have the highest values of $V_{R_\mathrm{d}}/R_\mathrm{d}$ and μ_0^i, whereas the latter (black dots) show moderate values of $V_{R_\mathrm{d}}/R_\mathrm{d}$ and μ_0^i. In particular, NGC 2366 and UGC 4483 are prototype "cometary" BCDs (e.g. Noeske et al. 2000), as the starburst region is located at the edge of an elongated LSB stellar body (see the Atlas in Chapter 4). I Zw 36 has an off-centered starburst region superimposed on an elliptical stellar body, and may be a "cometary-like" BCD observed close to face-on. Finally, NGC 4068 has several small star-forming regions spread over the entire stellar body. It is possible that BCDs with a diffuse/off-centered starburst are different from BCDs with a centrally-concentrated starburst in terms of their structure and dynamics. This may be related to different evolutionary histories and/or triggering mechanisms.

Several Irrs have circular-velocity gradients comparable to those of BCDs ($\gtrsim$ 45 km s^{-1} kpc^{-1}). These objects, shown by blue squares in Figs 5.1 and 5.2, are the following (the classification from de Vaucouleurs et al. 1991 is given): UGC 3711 (IBm), UGC 3966 (Im), UGC 5721 (SBd?), UGC 7232 (Im pec), UGC 7261 (SBdm), UGC 7690 (Im), and UGC 8490 (Sm). These galaxies have structural and dynamical properties more similar to BCDs than to typical Irrs. In particular, they have HSB exponential profiles with relatively-small scale-lengths ($\lesssim$1 kpc, see the right panel of Fig. 5.5) and strong concentrations of gas near the galaxy center (cf. Swaters & Balcells 2002). This suggests that either they are also starbursting dwarfs (and may be considered as BCDs) or they are progenitors/descendants of BCDs. Except for the barred galaxies UGC 3711 and UGC 7261, the surface brightness profiles of these Irrs do *not* show the central "light excess" that is typically observed in BCDs (cf. Swaters et al. 2002), thus it is likely that they are *not* experiencing a starburst at the present epoch. We will refer to them as compact Irrs. The study of the SFHs of these compact Irrs may be crucial to address their relation to BCDs.

5.4.2 Gravitational potential and starburst indicators

To clarify the relation between the gravitational potential and the star-formation, we plotted $V_{R_\mathrm{d}}/R_\mathrm{d}$ against several starburst indicators: the ratio SFR/M_bar (similar to sSFR=SFR/M_*), the equivalent width EW(Hα+[N II]), the SFR surface density Σ_SFR, and the gas depletion times t_local and t_global (see Sect. 5.3.3 for details). In the literature, there is no general agreement about which of these indicators best identifies a starburst galaxy.

The ratio SFR/M_bar quantifies the star-formation activity of a galaxy with respect to its baryonic mass (stars and atomic gas). This is comparable to SFR/M_*, which is often used for massive galaxies. We prefer to use SFR/M_bar for two reasons: i) we do not have a direct estimate of M_* for the Irrs, whereas we can estimate M_bar using the baryonic TF relation (see Sect. 5.3.3 for details), and ii) in some dwarf galaxies the atomic gas mass can be as high as the stellar mass, thus a LSB Irr that has been inefficiently forming stars during the Hubble time might have a relatively-high SFR/M_*-ratio but a low SFR/M_bar-ratio. The differences between SFR/M_bar and SFR/M_*, however, are typically within a factor of $\sim$2. Figure 5.2 (middle) shows that there is no correlation between $V_{R_\mathrm{d}}/R_\mathrm{d}$ and SFR/M_bar ($\rho_\mathrm{cc} \simeq -0.1$). Moreover, BCDs and Irrs can have similar values of SFR/M_bar, suggesting that this is not a good starburst indicator.

The EW(Hα) is thought to trace the stellar birthrate parameter b, defined as the ratio of the current SFR to the past, average SFR over the galaxy lifetime (e.g. Kennicutt 1998a). Lee et al. (2009) argued that an EW(Hα)$\gtrsim$ 100 Å corresponds to $b \gtrsim 2.5$ and, thus, indentifies a starburst. Fig. 5.2 (right) shows that there is no strong correlation between EW(Hα+[N II]) and $V_{R_\mathrm{d}}/R_\mathrm{d}$ ($\rho_\mathrm{cc} \simeq 0.3$). Most BCDs, as expected, have very high values of EW(Hα+[N II]), although some of them have EW(Hα+[N II])<100 Å. As pointed out by

McQuinn et al. (2010a), starbursts are events lasting for a few 100 Myr, whereas the Hα emission probes the star-formation activity over shorter timescales ($\lesssim$10 Myr), thus fluctuations in the SFH over a few Myr may explain why a EW(Hα) treshold misidentifies some BCDs.

The $\Sigma_{\rm SFR}$ normalizes the SFR by the area of the stellar body. Fig. 5.3 (left) shows that $V_{R_{\rm d}}/R_{\rm d}$ correlates with $\Sigma_{\rm SFR}$ ($\rho_{\rm cc} \simeq 0.8$). This suggests that there is a close link between the star-formation activity and the inner steepness of the potential well. A linear, error-weighted fit to the data returns

$$\log(V_{R_{\rm d}}/R_{\rm d}) = (0.36 \pm 0.04)\ \log(\Sigma_{\rm SFR}) + (2.6 \pm 0.1). \tag{5.12}$$

This correlation is expected from Fig. 5.1 (right) and the Kennicutt-Schmidt (KS) law (e.g. Kennicutt 1998b). By combining Eq. 5.11 and Eq. 5.12, indeed, one can obtain a KS type of relation, that considers the atomic gas only and has a slope of $\sim$3. This is in line with the results of Roychowdhury et al. (2009), who investigated the KS law in 23 extremly-faint dwarf galaxies ($M_{\rm B} \simeq -13$ mag) and found a slope of $\sim$2.5 by considering atomic gas only and UV-based SFRs. As expected, starbursting dwarfs are in the top-right part of the $V_{R_{\rm d}}/R_{\rm d} - \Sigma_{\rm SFR}$ diagram. In BCDs, the starburst typically increases the SFR by a factor of $\sim$5 to $\sim$10 (e.g. McQuinn et al. 2010a). NGC 6789, which is the only *known* post-starburst galaxy in our sample (see McQuinn et al. 2010a and Sect. 5.5.2), shows a large horizontal deviation with respect to the main relation ($\gtrsim$1 dex). Intriguingly, compact Irrs also have high values of $\Sigma_{\rm SFR}$, but they systematically lie on the left side of the linear-fit by $\sim$0.5 to $\sim$1 dex, thus they are consistent with being progenitors/descendants of BCDs. However, the overall, large scatter on the $V_{R_{\rm d}}/R_{\rm d} - \Sigma_{\rm SFR}$ relation prevents us from reaching any firm conclusion about the nature of compact Irrs and their link with BCDs.

We point out that $V_{R_{\rm d}}/R_{\rm d} = 2\pi/\tau_{\rm orb}$, where $\tau_{\rm orb}$ is the orbital time on the solid-body portion of the rotation curve. Kennicutt (1998b) found that, for spiral galaxies and massive starbursts, $\Sigma_{\rm SFR}$ also correlates with $\Sigma_{\rm gas}/\tau_{\rm orb}$, where $\tau_{\rm orb}$ was calculated at the outer edge of the optical disk (presumably along the flat part of the rotation curve) and $\Sigma_{\rm gas}$ includes both atomic and molecular gas. This correlation may be interpreted as the effect of spiral arms triggering the star-formation (e.g. Kennicutt 1998b). Fig. 5.3 (right) shows that a similar correlation (with $\rho_{\rm cc} \simeq 0.9$) holds also for gas-rich dwarfs, in which the effect of density waves clearly cannot be important. Here $\tau_{\rm orb}$ is calculated on the solid-body portion of the rotation curve, while $\Sigma_{\rm gas}$ includes the atomic gas component only, since the molecular content of low-metallicity, dwarf galaxies is very uncertain (e.g. Taylor et al. 1998; Leroy et al. 2008). As discussed by Kennicutt (1998b), one might expect a linear relation of the form:

$$\Sigma_{\rm SFR} = \epsilon\, \Sigma_{\rm gas}/\tau_{\rm orb} \tag{5.13}$$

where ϵ is the fraction of gas that is converted into stars during every orbit. For spiral galaxies and massive starbursts, Kennicutt (1998b) found that $\sim$10% of

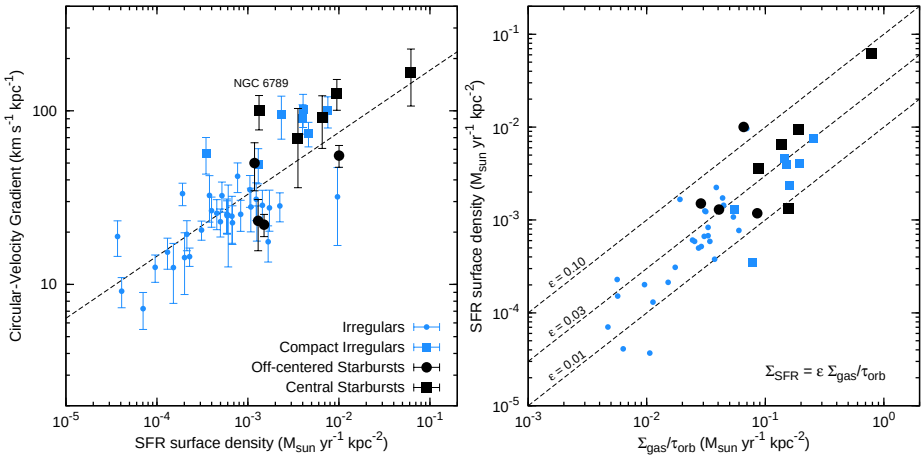

Figure 5.3 – *Left:* $V_{R_{\rm d}}/R_{\rm d}$ versus the SFR surface density $\Sigma_{\rm SFR}$. The dashed line shows a linear-fit to the data. The position of the post-starburst dwarf galaxy NGC 6789 is indicated. *Right:* $\Sigma_{\rm SFR}$ versus $\Sigma_{\rm gas}/\tau_{\rm orb}$, where $\Sigma_{\rm gas}$ considers the atomic gas only and $\tau_{\rm orb}$ is the orbital time on the solid-body portion of the rotation curve. The dashed lines show a linear relation for different value of ϵ. Symbols are the same as in Fig. 5.1.

the available gas (atomic plus molecular) is converted into stars during every orbit. The dashed lines in Fig. 5.3 (right) show fractions $\epsilon = 0.01$, 0.03, and 0.10. Most dwarf galaxies have $0.01 \lesssim \epsilon \lesssim 0.03$, but several BCDs seem to have $\gtrsim 0.03$, suggesting that they might be converting gas into stars more efficiently than other gas-rich dwarfs. However, metallicity and/or internal extinction may affect the relative values of $\Sigma_{\rm SFR}$ in different galaxies, thus it is unclear whether the differences in ϵ are real *or* due to the use of the same SFR calibration for all the galaxies, without considering the possible effects of internal extinction and metallicity.

Finally, $\tau_{\rm local}$ and $\tau_{\rm global}$ estimate the time that a galaxy will take to consume its gas reservoir, if it keeps forming stars at the current rate. $\tau_{\rm local}$ takes into account only the atomic gas within the stellar component, while $\tau_{\rm global}$ takes into account the total atomic gas. Since our SFRs may be slightly overestimated, the values of $\tau_{\rm local}$ and $\tau_{\rm global}$ may be underestimated by a factor of $\sim$2 (see Sect. 5.3.3). Several studies (e.g. van Zee 2001; Hunter & Elmegreen 2004) have shown that gas-rich dwarfs have long gas-depletion times ($>$ 10 Gyrs) and, thus, could keep forming stars for several Hubble times. In Fig. 5.4 (left), we show that $V_{R_{\rm d}}/R_{\rm d}$ correlates with $\tau_{\rm local}$ ($\rho_{\rm cc} \simeq -0.8$), as expected from Figs. 5.1 (right) and 5.3 (left). BCDs and compact Irrs typically have $\tau_{\rm local} \lesssim 5$ Gyr. A linear, error-weighted fit to the data yields

$$\log(V_{R_{\rm d}}/R_{\rm d}) = (-0.43 \pm 0.06)\ \log(\tau_{\rm local}) + (1.87 \pm 0.06). \qquad (5.14)$$

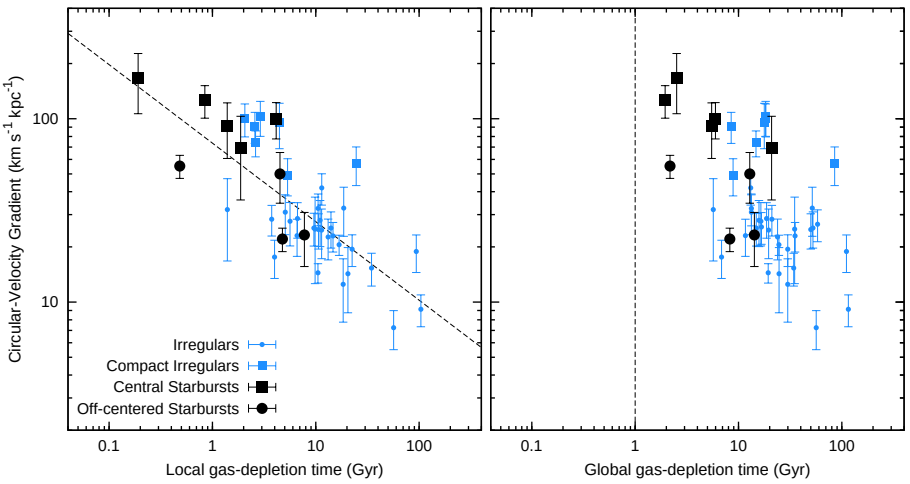

Figure 5.4 – *Left:* $V_{R_{\rm d}}/R_{\rm d}$ versus the local gas-depletion time, that takes into account the atomic gas mass within the $R_{\rm opt}$. The dashed line show a linear fit to the data. *Right:* $V_{R_{\rm d}}/R_{\rm d}$ versus the total gas-depletion time, that takes into account the total atomic gas mass. The dashed line shows the maximum duration of a typical starburst (∼1 Gyr). Symbols are the same as in Fig. 5.1.

Figure 5.4 (right), instead, shows that the relation between $V_{R_{\rm d}}/R_{\rm d}$ and $\tau_{\rm global}$ is less well defined ($\rho_{\rm cc} \simeq -0.6$). It also shows that $\tau_{\rm global}$ is significantly larger than $\tau_{\rm local}$, implying that Irrs and BCDs have massive gas reservoirs outside the stellar component. For most BCDs, both $\tau_{\rm local}$ and $\tau_{\rm global}$ are larger than the typical durations of the burst (few 100 Myr), implying that they do not consume their entire gas reservoir during the current event of intense star-formation. Burst durations can be estimated using the SFHs derived by fitting the color-magnitude diagrams of the resolved stellar populations (e.g. McQuinn et al. 2010a). In particular, the sample of McQuinn et al. (2010a) includes five "fossil" starbursting dwarfs, that allows us to estimate the *total* duration of the burst. If one defines the burst duration as the period when $b > 2$, Fig. 2 of McQuinn et al. (2010b) shows that the longest burst duration is ∼850 Myr in UGC 9128. McQuinn et al. (2010b) report slightly higher values as they use a less conservative definition of "burst duration". We assume a fiducial value of 1 Gyr as the maximum duration of a starburst; this is indicated in Fig. 5.4 by a verical dashed-line. All the BCDs in our sample have $\tau_{\rm global} > 1$ Gyr, and most of them also have $\tau_{\rm local} > 1$ Gyr.

5.4.3 Gas-poor dwarf galaxies

We now compare the structural and dynamical properties of gas-rich dwarfs with those of rotating Sphs in the Virgo cluster (van Zee et al. 2004a,b). The

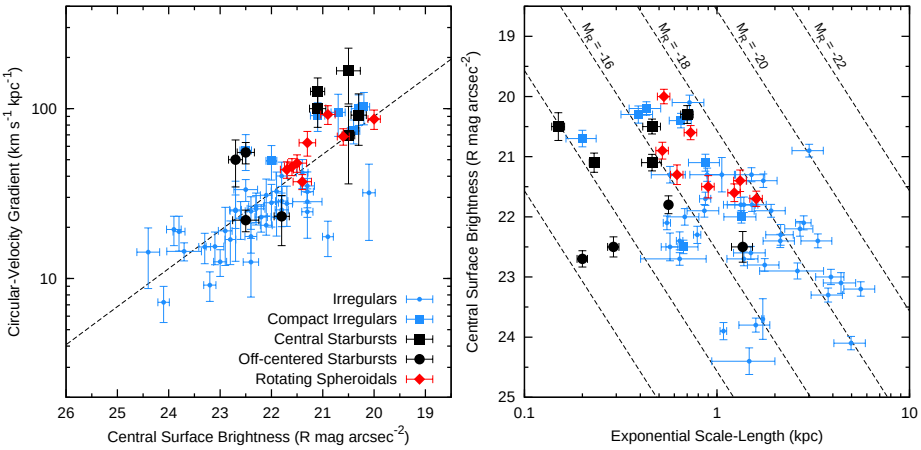

Figure 5.5 – *Left:* $V_{R_\mathrm{d}}/R_\mathrm{d}$ versus μ_0^i including rotating Sphs in the Virgo cluster (red diamonds). The other symbols are the same as in Fig. 5.1. The dashed line shows a linear fit to the Irr and BCD data (same as in Fig. 5.1). The stellar rotation velocities have been corrected for asymmetric drift (see Appendix 5.A). *Right*: R_d against μ_0^i. The dashed lines correspond to exponential profiles with a fixed total magnitude (-22, -20, -18, -16, -14, and -12 R mag).

stellar rotation velocities have been corrected for pressure-support as described in Appendix 5.A.

Figure 5.5 (left) shows that rotating Sphs follow the same correlation between $V_{R_\mathrm{d}}/R_\mathrm{d}$ and μ_0^i defined by Irrs and BCDs. Moreover, these rotating Sphs have values of $V_{R_\mathrm{d}}/R_\mathrm{d}$ and μ_0^i comparable with those of BCDs and compact Irrs. In Fig. 5.5 (right), we plot R_d against μ_0^i; the dashed lines correspond to exponential profiles with a fixed total magnitude. The rotating Sphs have total R-band magnitudes in the range $-16 \lesssim M_\mathrm{R} \lesssim -18$, comparable to the Irrs considered here. In general, for a given M_R, the values of μ_0^i and R_d of rotating Sphs are, respectively, higher and smaller than those of typical Irrs, but comparable with those of some BCDs and compact Irrs. Therefore, the structural and dynamical properties of rotating Sphs in the Virgo cluster appear similar to those of BCDs and compact Irrs in the field and nearby groups.

Since our sample of gas-poor dwarfs is relatively small, it is unclear whether rotating Sphs are necessarily more compact than typical Irrs, or whether this is the result of selection effects. It is clear, however, that a close link between the central dynamical mass density ($V_{R_\mathrm{d}}/R_\mathrm{d}$) and the stellar surface density (μ_0^i) is present in any kind of rotating galaxy (see also Lelli et al. 2013).

5.5 Discussion

5.5.1 The relation between gravitational potential, gas surface density, and starburst activity

In Sect. 5.3.1 we estimated the circular-velocity gradient $d_R V(0) \simeq V_{R_\mathrm{d}}/R_\mathrm{d}$ for a sample of 60 dwarf galaxies, including BCDs, Irrs, and Sphs. $V_{R_\mathrm{d}}/R_\mathrm{d}$ is a direct measure of the central dynamical mass density in a galaxy (including gas, stars, and dark matter). In Sect. 5.4.1 we showed that, for gas-rich dwarfs, $V_{R_\mathrm{d}}/R_\mathrm{d}$ correlates with i) the central surface brightness, ii) the mean H I surface density over the stellar body, and iii) the SFR surface density. Starbursting dwarfs are in the upper parts of these relations, as they have high H I surface densities, high central surface brightnesses, and high circular-velocity gradients, indicating that they have a high central dynamical mass density. This implies that the starburst activity is closely related to the inner steepness of the potential well and the gas surface density. The nature of this connection is unclear. There are, however, two likely possibilities: i) the progenitors of BCDs are unusually compact Irrs with a steep potential well, or ii) there is a mechanism that concentrates the mass (gas, stars, and dark matter) in typical Irrs, eventually causing a starburst. These possibilities are discussed in the following.

If the progenitors of BCDs are compact Irrs, the high circular-velocity gradient would imply high values of the critical surface-density threshold for gravitational instabilities Σ_crit (Toomre 1964; Kennicutt 1989) and make the gaseous disk relatively stable against large-scale perturbations. For a self-gravitating gaseous disk, Σ_crit is given by

$$\Sigma_\mathrm{crit} = \alpha \frac{\sigma_\mathrm{gas}\kappa}{\pi G} \tag{5.15}$$

where α is a dimensionless parameter (near unity) that accounts for the finite thickness of the disk (e.g. Martin & Kennicutt 2001), σ_gas is the gas velocity dispersion, and κ is the epicyclic frequency given by

$$\kappa = 1.41 \frac{V_\mathrm{circ}(R)}{R} \sqrt{1 + \frac{d \log V_\mathrm{circ}(R)}{d \log R}}. \tag{5.16}$$

The possible role of Σ_crit in BCDs has been discussed by Meurer et al. (1998) and van Zee et al. (2001), who argued that, in these compact galaxies, the gas could pile up in the center and reach high surface densities, while the star formation would be delayed until the critical surface-density treshold is reached, leading to a starburst. We note that this should strictly apply only to the inner regions of the galaxy ($R \lesssim 2R_\mathrm{d}$), where the shape of the rotation curve is close to a solid body and, thus, $\Sigma_\mathrm{crit} \propto V_{R_\mathrm{d}}/R_\mathrm{d}$ (assuming that σ_gas and α are nearly constant with radius). In the outer regions ($R \gtrsim 2R_\mathrm{d}$), instead, the rotation curve becomes flat and $\Sigma_\mathrm{crit} \propto 1/R$, hence the gaseous disk might be

less stable. Thus, this picture does not require a "bursty" SFH for the whole galaxy, i.e. strong bursts separated by quiescent periods, as the star-formation may continue in the outer parts of the galaxy. Star-formation at large radii is actually observed in several Irrs and BCDs (e.g. Hunter & Elmegreen 2004).

Toomre's model for gravitational instabilities may also provide a simple explanation for the correlation between $V_{R_\mathrm{d}}/R_\mathrm{d}$ and $\overline{\Sigma}_\mathrm{H\,I}$ (Fig. 5.1, right). If $\Sigma_\mathrm{gas} \simeq \Sigma_\mathrm{crit} \propto V_{R_\mathrm{d}}/R_\mathrm{d}$ and the product $\alpha \times \sigma_\mathrm{gas}$ is approximately the same in every dwarf galaxy, we would expect the following relation:

$$\log\left(\frac{V_{R_\mathrm{d}}}{R_\mathrm{d}}\right) = \log(\Sigma_\mathrm{gas}) + \log\left(\frac{\pi G}{\alpha\sigma_\mathrm{gas}}\right). \tag{5.17}$$

Remarkably, the observed slope of the $V_{R_\mathrm{d}}/R_\mathrm{d} - \overline{\Sigma}_\mathrm{H\,I}$ relation is consistent with 1 within the uncertainties (see Eq. 5.11). Moreover, the value of the intersect (corrected for the presence of Helium) imply $\alpha \times \sigma_\mathrm{gas} = 3.6$ km s^{-1}, in close agreement with the value of $\sim$4 km s^{-1} found by Kennicutt (1989) and Martin & Kennicutt (2001) in the outer regions of spiral galaxies. Note that Eq. 5.15 and Eq. 5.17 are valid in the case of a self-graviting gaseous disk. If one considers also the gravitational effect of stars, the condition for the stability of the two-components disk is more complex (e.g. Rafikov 2001), and it is unclear whether the linear relation in Fig. 5.1 (right) may be simply explained.

There are several mechanisms that can cause a concentration of mass in a galaxy, both internal (bar-like torques) and/or external (interactions/mergers). First, we discuss internal mechanisms. BCDs and compact Irrs are not necessarily barred, thus a bar-driven inflow seems an unlikely general mechanisms. However, Hunter & Elmegreen (2004) speculated that dwarf galaxies may have bars made of dark matter, while Bekki & Freeman (2002) argued that rotating, triaxial dark-matter haloes can exert large-scale torques and lead to mass inflow. Elmegreen et al. (2012) proposed that massive clumps of gas and young stars can exchange angular momentum with halo stars and dark matter particles and, thus, may spiral inward to the galaxy center, leading to a central starburst. This scenario would imply an evolutionary trend from BCDs with an off-centered starbursts (e.g. NGC 2366 and I Zw 36) to BCDs with a centrally-concentrated starburst (e.g. NGC 1705 and NGC 4214). Simulations of high-redshift galaxies suggest that the clump-instability creates a central mass concentration similar to a bulge, that is photometrically distinct from the underlying exponential disk (e.g. Immeli et al. 2004; Bournaud et al. 2007). The compact Irrs identified in Sec. 5.4.1, instead, have surface brightness profiles described by a single HSB exponential (with the exception of the barred galaxies UGC 3711 and UGC 7261; cf. Swaters & Balcells 2002). BCDs often show surface brightness profiles with an inner light excess, but these light enhancements typically have very blue colors and do not appear to trace the stellar mass (e.g. Papaderos et al. 1996).

Regarding external mechanims, it is well established that galaxy interactions and mergers can cause gas inflow and lead to a central starburst (e.g. Barnes

& Hernquist 1996; Bekki 2008). Moreover, dwarf galaxies are thought to be relatively fragile systems and external perturbations may significantly change their mass distribution, possibly leading to an overall contraction of the stellar and gaseous disks (e.g. Hunter & Elmegreen 2004). About half of the BCDs in our sample have disturbed and asymmetric H I morphologies in their outer parts, suggesting either a recent interaction/merger between gas-rich dwarfs (see e.g. I Zw 18 in Lelli et al. 2012a) or gas accretion from the environment (e.g. Kereš et al. 2005; Dekel & Birnboim 2006). Disturbed H I morphologies have been found also in other studies of BCDs (e.g. López-Sánchez et al. 2010; Ashley et al. 2013) and several interacting BCDs are known (e.g. Cox et al. 2001; Ekta et al. 2006, 2009). Thus, the hypothesis that interactions/mergers cause the central concentration of mass (gas, stars, and/or dark matter) and trigger the starburst is in overall agreement with the observations.

5.5.2 BCDs and the evolution of dwarf galaxies

In the following, we discuss the possible evolutionary links between BCDs, Irrs, and Sphs. The emerging picture is that a BCD in isolation most likely evolves into a compact Irr, but environmental processes (such as ram-pressure stripping) may transform compact Irrs and BCDs into rotating Sphs.

The link between BCDs and compact Irrs

In Sect. 5.4.1 we pointed out that the global gas-depletion times of BCDs are much larger than the typical durations of a starburst (<1 Gyr). This implies that BCDs generally do not consume their entire gas reservoir. Moreover, both optical and X-rays observations suggest that BCDs do not expell a large quantity of gas out of their potential well (see also Chapter 4). Observations of the Na D absorption doublet have shown that ouflows are common in starbursting dwarfs, but the velocities of the outflowing gas do *not* clearly exceed the galaxy escape velocity (Schwartz & Martin 2004). Similarly, studies of the Hα kinematics have found that the warm gas is usually gravitationally-bound to the galaxy (e.g. Martin 1996, 1998; van Eymeren et al. 2009b,a, 2010). X-ray studies have revealed that some BCDs have diffuse coronae of hot gas at $T \simeq 10^6$ K (Ott et al. 2005a,b), which are presumably associated with outflows but have very low masses, only $\sim$1% of the H I masses. Thus, a BCD *in isolation* most likely evolves into another gas-rich dwarf as the starburst fades.

In Sect. 5.4.1 we also identified several compact Irrs that have structural and dynamical properties similar to BCDs. It is clear that, unless a redistribution of mass takes place, the descendants of BCDs must be compact Irrs. A strong redistribution of mass seems unlikely for two reasons: i) in dwarf galaxies there are no *known* internal mechanisms that are able to redistribute stars and dark matter, such as radial migrations due to bars and density waves (e.g. Minchev et al. 2011); and ii) stellar feedback seems unable to expell a large quantity of gas

from the potential well and, thus, cause a significant expansion of the stellar and dark matter components. In particular, Papaderos et al. (1996) and Gil de Paz & Madore (2005) showed that the scale-lengths of the old stellar component of BCDs should, on average, increase by a factor of ∼2 to be consistent with those of typical Irrs and Sphs. Papaderos et al. (1996) proposed a simple, spherically-symmetric model to quantify the effect of ouflows on the evolution of the stellar body of an isolated BCD; their equations 12 and 13 can be written as

$$\frac{R_{\rm d}^{\rm i}}{R_{\rm d}^{\rm f}} = 1 - \frac{M_{\rm out}}{M_{\rm bar}^{\rm i}} f_{\rm bar}^{\rm i} \tag{5.18}$$

where $R_{\rm d}^{\rm i}$ and $R_{\rm d}^{\rm f}$ are, respectively, the scale-lengths in the initial (starburst) and final (post-starburst) stages of the system, $M_{\rm out}$ is the gas mass that is ejected, $M_{\rm bar}^{i} = M_* + M_{\rm gas}$ is the baryonic mass in the initial stage, and $f_{\rm bar}^{\rm i} = M_{\rm bar}^{\rm i}/M_{\rm dyn}^{\rm i}$ is the initial baryonic fraction within the stellar body. In Chapter 4, we showed that BCDs have, on average, $f_{\rm bar} \simeq 0.3$ to 0.5, depending on the assumptions on the IMF and on the molecular gas content. In order to have $R_{\rm d}^{\rm i}/R_{\rm d}^{\rm f} = 1/2$, one would need unphysical values of $M_{\rm out}/M_{\rm bar}^{\rm i} \simeq 1$ to 1.7, that would leave no baryons in the potential well. Thus, even if outflows would expell a significant quantity of gas, they could not easily explain the differences in the scale-lengths of BCDs and typical Irrs/Sphs.

In this evolutionary context, the BCD NGC 6789 deserves special attention. NGC 6789 resides in the Local Void and is extremely isolated, as the nearest massive galaxy (NGC 6946) is at a projected distance of 2.5 Mpc (Drozdovsky et al. 2001). The SFHs from McQuinn et al. (2010a) and García-Benito & Pérez-Montero (2012) show that the starburst ended about ∼500 Myr ago and the galaxy is now forming stars at a lower rate. Thus, NGC 6789 is a post-starburst dwarf galaxy. The system still has a considerable gas reservoir ($\sim 2\times10^7$ $M_\odot$) and the gas depletion time is long (∼6 Gyr). The rotation curve rises steeply in the inner parts, indicating that there is a strong central concentration of mass. Thus, NGC 6789 did not consume its entire gas reservoir during the starburst and did not experience a strong redistribution of mass in the last ∼500 Myr, in agreement with our previous reasoning.

The link between BCDs and rotating Sphs

In Sect. 5.4.3, we showed that rotating Sphs in the Virgo cluster have central dynamical mass densities similar to those of BCDs and compact Irrs. It is likely, therefore, that rotating Sphs are the descendants of BCDs and compact Irrs, providing that some mechanism removes the gas from the galaxy. As we already pointed out, supernova feedback seems unable to entirely expell the ISM of a BCD, thus the best candidate is ram-pressure stripping due to either the hot intra-cluster medium (e.g. Kormendy & Bender 2012) or the hot coronae that are thought to surround massive galaxies (e.g. Gatto et al. 2013).

The rotating Sphs in our sample, however, are still pressure-supported in the inner regions (with $v_{\rm rot}/\sigma$ between $\sim$0.3 to $\sim$1), whereas the *gaseous disks* of BCDs and Irrs are rotation-supported (with $v_{\rm rot}/\sigma > 1$). In particular, one may expect that the newly-formed stars retain the angular momentum of the H I disk, which is the site of the recent star-formation. Thus, an additional mechanism that heats the stellar disk of a BCD/compact Irr may be required for a morphological transformation into a rotating Sph. Possible mechanisms are galaxy harassment by a galaxy cluster (e.g. Moore et al. 1998) or tidal stirring by a nearby massive companion (e.g. Mayer et al. 2006). We warn, however, that the comparison between different kinematical tracers (as stars and H I) may be misleading. Leaman et al. (2012) studied the stellar kinematics of the Local Group irregular WLM and found that its stellar disk has $v_{\rm rot}/\sigma \sim 1$, whereas the H I disk has $v_{\rm rot}/\sigma \sim 7$. Thus, the stellar and H I kinematics in a dwarf galaxy may be remarkably different, and the stellar component of an Irr may be very similar to that of a Sph. In this case, the evolution from a BCD/compact Irr to a rotating Sph would just require gas removal, given that the current starburst typically creates only a small fraction of the total stellar mass ($\sim$10%, e.g. McQuinn et al. 2010b) and, thus, the newly-formed stars cannot strongly affect the overall stellar kinematics.

The evolutionary sequence BCDs $\rightarrow$ compact Irrs $\rightarrow$ rotating Sphs may solve some long-standing issues about the direct transformation of Irrs into *bright* Sphs: i) Irrs are expected to fade after the cessation of the star-formation and this would result in central surface brightnesses that are significantly lower than those of the brightest Sphs in galaxy clusters (Bothun et al. 1986; Davies & Phillipps 1988), and ii) most bright Sphs show central nuclei whereas Irrs do not (e.g. Côté et al. 2006; Lisker et al. 2007). In fact, regardless of the details of the triggering mechanism, the occurrence of a starburst in an Irr should necessarily i) create a central concentration of mass and increase the central surface brightness, and might possibly ii) form a central nucleus by the inspiralling and merging of star clusters (Gnedin et al. 2013), which are often found in BCDs (e.g. Annibali et al. 2009, 2011). In particular, the nuclei of Sphs are generally bluer than the overall stellar body (e.g. Lotz et al. 2004), suggesting that they contain younger stellar populations than the rest of the galaxy. Moreover, several Sphs in the Virgo cluster show central star-formation and/or disk features (e.g. Lisker et al. 2006, 2007), further hinting at a possible link with BCDs and compact Irrs.

Finally, we point out that the rotating Sphs considered here have relatively-high luminosities ($-16 \lesssim M_{\rm R} \lesssim -18$ mag) and, thus, are at the top end of the $M - \mu_0$ relation (e.g. Kormendy et al. 2009). It is unclear whether Sphs with lower luminosities and surface brightnesses, as those in the Local Group, also show some ordered rotation (see e.g. Tolstoy et al. 2009) and what their location is in the $V_{\rm R_d}/R_{\rm d} - \mu_0$ diagram. Thus, the evolutionary scenario outlined above refers *only* to the brightest Sphs found in galaxy clusters. Typical LSB Irrs

might evolve into LSB Sphs without going through a starbursting phase (e.g. Weisz et al. 2011).

5.6 Conclusions

We studied the structure and evolution of dwarf galaxies using a new dynamical quantity: the circular-velocity gradient $d_R V(0)$. This provides a direct measure of the inner steepness of the potential well of a galaxy and, thus, of its central dynamical mass density (including gas, stars, and dark matter). For bulgeless, low-mass galaxies, $d_R V(0)$ can be simply estimated as $V_{R_\mathrm{d}}/R_\mathrm{d}$, where R_d is the exponential scale-length of the stellar body. We constructed a sample of 60 low-mass galaxies (including starbursting dwarfs, irregulars, and spheroidals), considering objects with high-quality H I and stellar rotation curves from the literature. Our results can be summarized as follows.

1. For gas-rich dwarfs (Irrs and BCDs), $V_{R_\mathrm{d}}/R_\mathrm{d}$ correlates with i) the central surface brightness μ_0^i; ii) the mean H I surface density over the stellar body; and iii) the SFR surface density.

2. Starbursting dwarfs (BCDs) are different from typical Irrs. BCDs have high central surface brightnesses, high H I surface densities, and high circular-velocity gradients, implying that they have a strong central concentration of dynamical mass (luminous and/or dark). This suggests that the starburst is closely linked to the inner shape of the gravitational potential and the gas density.

3. We identified several compact Irrs that have values of μ_0^i, R_d, and $V_{R_\mathrm{d}}/R_\mathrm{d}$ similar to those of BCDs. Compact Irrs are the best candidates to be the progenitors/descendants of BCDs.

4. Rotating Sphs in the Virgo cluster follow the same correlation between $V_{R_\mathrm{d}}/R_\mathrm{d}$ and μ_0^i determined by Irrs and BCDs. The Sphs in our sample have values of $V_{R_\mathrm{d}}/R_\mathrm{d}$ similar to those of BCDs and compact Irrs. This suggests that BCDs and compact Irrs may evolve into rotating Sphs, provided that some external mechanism removes the entire ISM.

5. Similarly to spiral galaxies, the star-formation activity in dwarfs can be described by a law of the form $\Sigma_\mathrm{SFR} = \epsilon\,\Sigma_\mathrm{gas}/\tau_\mathrm{orb}$, where Σ_gas considers the atomic gas only, τ_orb is the orbital time on the solid-body portion of the rotation curve, and the fraction ϵ of atomic gas converted into stars during every orbit is $\sim 2\%$.

Acknowledgements

We are grateful to Renzo Sancisi for sharing insights and ideas that fueled this investigation. We also thank Eline Tolstoy for stimulating discussions. FL acknowledges the Ubbo Emmius bursary program of the University of Groningen and the Leids Kerkhoven-Bosscha Fund. FF aknowledges financial support from PRIN MIUR 2010-2011, project "The Chemical and Dynamical Evolution of the Milky Way and Local Group Galaxies", prot. 2010LY5N2T.

Appendix 5.A Asymmetric-drift correction

To calculate the asymmetric-drift correction, we start from equation (4-33) of Binney & Tremaine (1987), which describes a stationary, axisymmetric stellar system embedded in a gravitational potential $\Phi(R, z)$:

$$V_{\rm circ}^2 = \overline{v_\phi}^2 - \sigma_{\rm R}^2 \left[\frac{\partial \ln \rho}{\partial \ln R} + \frac{\partial \ln \sigma_{\rm R}^2}{\partial \ln R} + 1 - \frac{\sigma_\phi^2}{\sigma_{\rm R}^2} + \frac{R}{\sigma_{\rm R}^2} \frac{\partial(\overline{v_{\rm R} v_z})}{\partial z} \right], \qquad (5.A.1)$$

where $v_{\rm R}$, v_z, and v_ϕ are the components (in cylindrical coordinates) of the velocity of a star, ρ is the stellar density, $\sigma_{\rm R}^2 = \overline{v_{\rm R}^2}$, $\sigma_{\rm z}^2 = \overline{v_{\rm z}^2}$, $\sigma_\phi^2 = \overline{v_\phi^2} - \overline{v_\phi}^2$, and $V_{\rm circ} = \sqrt{R(\partial\Phi/\partial R)}$. The observed stellar rotation curve $v_{\rm rot}$ provides $\overline{v_\phi}$. Note that equation 5.A.1 does *not* require that the velocity dispersion is smaller than the rotation velocity. Following Weijmans et al. (2008), we write

$$\overline{v_{\rm R} v_z} = \kappa(\sigma_{\rm R}^2 - \sigma_z^2) \frac{z/R}{1-(z/R)^2} \qquad 0 \le \kappa \le 1, \qquad (5.A.2)$$

where $\kappa = 0$ and $\kappa = 1$ correspond, respectively, to the extreme cases of a velocity ellipsoid aligned with the cilindrical (R, z, ϕ) and spherical (r, θ, ϕ) coordinate systems. Using higher-order velocity-moments of the collisionless Boltzmann equation, Weijmans et al. (2008) obtained the following expressions (see their Appendix A):

$$\frac{\sigma_\phi^2}{\sigma_{\rm R}^2} = \frac{1}{2} \left[1 + \alpha_{\rm R} + \kappa \frac{1-\sigma_z^2/\sigma_{\rm R}^2}{1-(z/R)^2} \alpha_z - \frac{\overline{(v_\phi - \overline{v_\phi})^3}}{\sigma_{\rm R}^2 \overline{v_\phi}} \right] \qquad (5.A.3)$$

and

$$\frac{\sigma_\phi^2}{\sigma_z^2} = \frac{\kappa z^2 (1+\alpha_{\rm R})}{\kappa z^2 (1+\alpha_{\rm R}) - \alpha_z (R^2 - z^2)}, \qquad (5.A.4)$$

where

$$\alpha_{\rm R} = \frac{\partial \ln \overline{v_\phi}}{\partial \ln R}, \quad \text{and} \quad \alpha_z = \frac{\partial \ln \overline{v_\phi}}{\partial \ln z}. \qquad (5.A.5)$$

The last term of equation 5.A.3 vanishes if the velocity ellipsoid is symmetric around $\overline{v_\phi}$. Since we want to estimate $V_{\rm circ}$ at $R \simeq R_{\rm d}$, this higher-order term can be safely ignored, as $\sigma_{\rm R}^2 \simeq \sigma_{\rm obs}^2 > \overline{v_\phi}^2$ in the inner galaxy regions.

We now assume that the galaxy is in cilindrical rotation, i.e. $v_{\rm rot} = \overline{v_\phi}(R)$. Observationally, it is difficult to obtain information on the rotation velocities above the galaxy plane. A negative velocity gradient in the vertical direction, however, would produce an observable feature: asymmetric line profiles with a tail toward the systemic velocity. This means that a Gauss-Hermite polynomial-fit to the line profiles should give high values of the h_3 term. This effect is

observed, for example, in the lagging H I haloes of spiral galaxies (e.g. Fraternali et al. 2002). The stellar, absorption-line profiles of gas-poor dwarfs, instead, are quite symmetric and have $|h_3| \lesssim 0.1$ (Halliday et al. 2001; Spolaor et al. 2010; Howley et al. 2013), implying that any vertical velocity gradient is relatively small. It is reasonable, therefore, to assume cilindrical rotation such that $\alpha_z = 0$. Thus, Eq. 5.A.4 gives $\sigma_\phi = \sigma_z$.

Since we are interested in the inner circular-velocity gradient, we also assume that the galaxy is in solid-body rotation, i.e. $\overline{v_\phi}(R) = A \times R$. All the Sphs in our sample, indeed, show nearly solid-body rotation curves out to the last measured point (cf. van Zee et al. 2004b) and thus $\alpha_R = 1$. Consequently, Eq. 5.A.3 gives $\sigma_\phi = \sigma_{\rm R}$ (neglecting the higher-order term). Therefore, using observationally-motivated assumptions, we find that the Sphs in our sample can be approximated as isotropic rotators with $\sigma_{\rm R} = \sigma_z = \sigma_\phi = \sigma_{\rm obs}$.

Finally, we assume that the scale-height of the galaxy is constant with radius. Thus, we have $\partial \ln \rho / \partial \ln R = \partial \ln \Sigma / \partial \ln R$, where Σ is the surface density profile (traced by the surface brightness profile). Assuming a Sersic profile (Sérsic 1963), the asymmetric-drift-corrected circular velocity is given by

$$V_{\rm circ}^2 = v_{\rm rot}^2 + \sigma_{\rm obs}^2 \left[\frac{b_n}{n} \left(\frac{R}{R_{\rm eff}} \right)^{1/n} - 2 \frac{\partial \ln \sigma_{\rm obs}}{\partial \ln R} \right], \tag{5.A.6}$$

where $R_{\rm eff}$ is the effective radius, n is the Sersic index, and b_n is a constant that depends on n (see Ciotti 1991; Ciotti & Bertin 1999).

For rotating Sphs, the surface brightness profile can be fitted by an exponential-law, thus $n = 1$ and $b_1 = 1.678$. We also assume that $\sigma_{\rm obs}$ is constant with radius, as the observations generally provide only the mean value $\overline{\sigma}_{\rm obs}$. Therefore, Eq. 5.A.6 simplifies to $V_{\rm circ}^2 = v_{\rm rot}^2 + \overline{\sigma}_{\rm obs}^2 (R/R_{\rm d})$, where $R_{\rm d} = 1.678 R_{\rm eff}$ is the exponential scale-length. In this case, the error $\delta_{V/R}$ on $V_{\rm R_d}/R_{\rm d}$ is given by

$$\begin{aligned} \delta_{V/R}^2 = \Bigg\{ & \left[\frac{v_{\rm rot}}{V_{\rm circ}} \frac{\delta_{v_{\rm l.o.s.}}}{R \sin(i)} \right]^2 + \left[\frac{v_{\rm rot}^2}{V_{\rm circ} R} \frac{\delta_i}{\tan(i)} \right]^2 \\ & + \left[\frac{\overline{\sigma}_{\rm obs}}{V_{\rm circ}} \frac{\delta_{\overline{\sigma}_{\rm obs}}}{R_{\rm d}} \right]^2 + \left[\frac{V_{\rm circ}}{R} \frac{\delta_D}{D} \right]^2 \Bigg\}_{R=R_{\rm d}}, \end{aligned} \tag{5.A.7}$$

where D and i are, respectively, the galaxy distance and inclination (cf. with Eq. 5.3).

Appendix 5.B Tables

Tables 5.B.1 and 5.B.3 - Structural and dynamical properties of gas-rich dwarfs (BCDs and Irrs)

Column (1) gives the galaxy name.
Column (2), (3), (4) give the assumed distance, the distance indicator, and the corresponding reference.
Column (5), (6), (7), and (8) give the R-band absolute magnitude $M_{\rm R}$, the central R-band surface brightness μ_0^i (corrected for inclination), the scale-length $R_{\rm d}$, and the reference for the surface photometry. The structural parameters were derived from an exponential fit to the outer parts of the surface brightness profiles. All the quantities have been corrected for Galactic extinction, but not for internal extiction.
Column (9) gives the galaxy inclination, derived by fitting a tilted-ring model to the H I velocity field and/or by building 3D model-cubes.
Column (10), (11), (12), and (13) give the circular velocity $V_{R_{\rm d}}$ at $R_{\rm d}$, the circular velocity $V_{\rm last}$ at the last measured point, the radius at $V_{\rm last}$, and the reference for the H I rotation curves. Values of $V_{\rm last}$ in *italics* indicate rotation curves that do not reach the flat part.
Column (15) gives the circular-velocity gradient $V_{R_{\rm d}}/R_{\rm d}$.

Tables 5.B.2 and 5.B.4 - Gas and star formation properties of gas-rich dwarfs (BCDs and Irrs)

Column (1) gives the galaxy name.
Column (2) and (3) give the gas metallicity and the respective references. Values in *italics* indicate abundances derived using "strong-line" calibrations; we assigned to them a conservative error of 0.2 (cf. Berg et al. 2012). All the other abundances have been derived using the T_e-method.
Column (4), (5), and (6) give the H I mass, the mean H I surface density within $R_{\rm opt} = 3.2R_{\rm d}$ (corrected for inclination), and the reference for the H I observations.
Column (7), (8), and (9) give the Hα+[N II] equivalent width, the Hα star formation rate (SFR), and the reference for the Hα observations. SFRs have been calculated using the Kennicutt (1998a) calibration and have not been corrected for internal extinction.
Column (10) and (11) give the ratio SFR/$M_{\rm bar}$ and the SFR surface density ($\Sigma_{\rm SFR} = {\rm SFR}/\pi R_{\rm opt}^2$). $M_{\rm bar}$ has been estimated using the baryonic Tully-Fisher relation as calibrated by McGaugh (2012) with an accuracy of $\sim$10%. Values of SFR/$M_{\rm bar}$ in *italics* indicate galaxies with rotation curves that do not reach the flat part, thus they may be slightly underestimated.
Column (12) and (13) give the global and local gas depletion times $\tau_{\rm global}$ and

$\tau_{\rm local}$. $\tau_{\rm global}$ considers the total atomic gas mass of the galaxy, whereas $\tau_{\rm local}$ considers the atomic gas mass within $R_{\rm opt}$.

Table 5.B.5 - Structural and dynamical properties of gas-poor dwarfs (Sphs)

Column (1) gives the galaxy name.
Column (2), (3), (4), (5), and (6) give the R-band absolute magnitude, the inclination i, the central surface brightness (corrected for i), the scale-length, and the reference for the surface photometry. The inclination was estimated from the observed ellipticities using Eq. 5.6 with $q_0 = 0.35$. The structural parameters were derived from an exponential fit to the outer parts of the surface brightness profiles. All the quantities have been corrected for Galactic extinction, but not for internal extinction.
Column (7), (8), (9), (10), and (11) give the rotation velocity at $R_{\rm d}$, the rotation velocity $v_{\rm last}$ at the last measured point, the radius at $v_{\rm last}$, the mean velocity dispersion, and the reference for the stellar spectroscopy. All rotation velocities have been corrected for inclination.
Column (12), (13) and (14) give the circular velocity at $R_{\rm d}$, the circular velocity at $R_{\rm last}$, and the circular-velocity gradient. All the circular velocities have been corrected for asymmetric-drift (see Appendix 5.A).

Table 5.B.1 – Sample of starbursting dwarfs. Structural and dynamical properties. References: (a) Tosi et al. (2001); (b) Tolstoy et al. (1995); (c) Karachentsev et al. (2003); (d) Jacobs et al. (2009); (e) Drozdovsky et al. (2001); (f) Izotov & Thuan (2002); (g) Aloisi et al. (2007); (h) Schulte-Ladbeck et al. (2001); (i) Aloisi et al. (2005); (j) Chapter 4; (k) Swaters & Balcells (2002); (l) Meurer et al. (1994); (m) Papaderos et al. (2002); (n) Elson et al. (2010); (o) Lelli et al. (2012b); (p) Lelli et al. (2012a).

Name	Dist	Method	Ref.	$M_{\rm R}$	$\mu^i_{0,R}$	$R_{\rm d}$	Ref.	i	$V_{R_{\rm d}}$	$V_{\rm last}$	$R_{\rm last}$	Ref.	$V_{R_{\rm d}}/R_{\rm d}$
	(Mpc)			(mag)	(mag/$''^2$)	(kpc)		($^\circ$)	(km/s)	(km/s)	(kpc)		(km/s/kpc)
(1)	(2)	(3)	(4)	(5)	(6)	(7)	(8)	(9)	(10)	(11)	(12)	(13)	(14)
NGC 1705$^\alpha$	5.1±0.6	TRGB	a	-16.3±0.2	21.1±0.1	0.46	j	45±5	58±8	71±10	5.7	j	126±25
NGC 2366	3.2±0.4	Ceph	b	-16.6±0.3	22.5±0.2	1.36	k	68±5	30±2	49±6	5.9	j	22±3
NGC 2915$^\beta$	3.8±0.4	TRGB	c	-15.9±0.2	20.5±0.1	0.46	l	52±3	32±15	85±5	9.3	n	70±33
NGC 4068	4.3±0.1	TRGB	d	-15.7±0.1	21.8±0.1	0.56	k	44±6	13±4	*39±5*	2.3	j	23±8
NGC 4214$^\alpha$	2.7±0.2	TRGB	d	-17.8±0.2	20.3±0.1	0.70	k	30±10	64±8	81±9	4.8	j	91±31
NGC 6789	3.6±0.2	TRGB	e	-15.1±0.1	21.1±0.2	0.23	j	43±7	23±4	*57±9*	0.7	j	100±22
UGC 4483	3.2±0.2	TRGB	f	-13.0±0.1	22.7±0.1	0.20	j	58±3	10±3	19±2	1.2	o	50±15
I Zw 18$^\gamma$	18.2±1.4	TRGB	g	-15.0±0.2	20.5±0.2	0.15	m	70±4	25±10	38±4	0.8	p	167±60
I Zw 36	5.9±0.5	TRGB	h	-14.9±0.1	22.5±0.2	0.29	j	67±3	16±2	29±2	1.1	j	55±8

Notes. $^{(\alpha)}$ The H I disk is warped, the inclination is given for $R \simeq R_{\rm d}$.
$^{(\beta)}$ We adopted the rotation curve derived by Elson et al. (2010) assuming a constant inclination of 52°.
$^{(\gamma)}$ The optical parameters have been derived by Papaderos et al. (2002) after subtracting the Hα emission.

Table 5.B.2 – Sample of starbursting dwarfs. Gas and star-formation properties. References: (a) Berg et al. (2012); (b) Croxall et al. (2009); (c) Izotov & Thuan (1999); (d) Chapter 4; (e) Elson et al. (2010); (f) Kennicutt et al. (2008); (g) Gil de Paz et al. (2003).

Name	log(O/H) +12	Ref.	$M_{\rm H\,I}$ ($10^8 M_\odot$)	$\overline{\Sigma}_{\rm H\,I}$ ($M_\odot$/pc^2)	Ref.	EW(Hα) (Å)	SFR ($M_\odot$/yr)	Ref.	SFR/$M_{\rm bar}$ (Gyr^{-1})	log($\Sigma_{\rm SFR}$) ($M_\odot$/yr/kpc^2)	$\tau_{\rm global}$ (Gyr)	$\tau_{\rm local}$ (Gyr)
(1)	(2)	(3)	(4)	(5)	(6)	(7)	(8)	(9)	(10)	(11)	(12)	(13)
NGC 1705	8.21±0.05	a	1.1±0.3	7.0±0.9	d	109±7	0.075	f	0.063	-1.96	1.9	0.8
NGC 2366	7.91±0.05	b	6.2±1.7	6.0±1.4	d	149±38	0.100	f	0.369	-2.77	8.2	4.7
NGC 2915	8.27±0.20	a	4.4±1.0	5.8±0.7	e	38±5	0.028	f	0.011	-2.39	20.9	1.9
NGC 4068	...	...	1.5±0.2	8.1±1.1	d	28±5	0.014	f	*0.129*	-2.89	14.2	8.3
NGC 4214	8.22±0.05	a	4.3±0.8	6.9±1.0	d	62±7	0.104	f	0.051	-2.18	5.5	1.4
NGC 6789	...	...	0.18±0.03	7.3±1.1	d	23±3	0.004	f	*0.008*	-2.63	6.0	4.1
UGC 4483	7.56±0.03	b	0.29±0.05	7.9±1.0	d	130±20	0.003	f	0.490	-2.63	12.9	4.5
I Zw 18	7.18±0.01	c	2.1±0.4	22.0±4.8	d	679±68	0.111	g	1.133	-0.81	2.5	0.2
I Zw 36	7.77±0.01	c	0.7±0.1	5.5±0.9	d	335±17	0.041	f	1.233	-1.82	2.3	0.5

Table 5.B.3 – Sample of irregulars. Structural and dynamical properties. References: (a) Tully (1988); (b) Tully et al. (2009); (c) Hoessel et al. (1998); (d) Thim et al. (2004); (e) Jacobs et al. (2009); (f) Drozdovsky & Karachentsev (2000); (g) Bono et al. (2010); (h) Swaters & Balcells (2002); (i) Tully et al. (1996); (j) Hunter & Elmegreen (2006); (k) Swaters et al. (2009); (l) Verheijen & Sancisi (2001); (m) Broeils (1992); (n) Kepley et al. (2007); (o) Weldrake et al. (2003).

Name	Dist	Method	Ref.	$M_{\rm R}$	$\mu^i_{0,R}$	$R_{\rm d}$	Ref.	i	$V_{R_{\rm d}}$	$V_{\rm last}$	$R_{\rm last}$	Ref.	$V_{R_{\rm d}}/R_{\rm d}$
	(Mpc)			(mag)	(mag/$''^2$)	(kpc)		($^\circ$)	(km/s)	(km/s)	(kpc)		(km/s/kpc)
(1)	(2)	(3)	(4)	(5)	(6)	(7)	(8)	(9)	(10)	(11)	(12)	(13)	(14)
UGC 731	11.8±4.3	TF	a	-17.1±0.8	22.9±0.1	2.62	h	57±3	50±4	74±4	10.3	k	19±7
UGC 2455$^\alpha$	6.4±1.2	TF	a	-17.7±0.4	20.1±0.1	0.72	h	51±3	23±10	*61±4*	3.7	k	32±15
UGC 3371	21.9±4.9	TF	b	-18.6±0.4	23.2±0.1	5.58	h	49±3	51±3	86±3	17.4	k	9±2
UGC 3711	8.2±1.5	TF	a	-17.4±0.4	21.1±0.1	0.87	h	60±3	79±4	95±4	3.6	k	91±17
UGC 3817	8.3±3.1	TF	a	-14.8±0.8	22.7±0.1	0.64	h	30±3	16±5	*45±5*	2.4	k	25±12
UGC 3966	7.4±1.4	TF	a	-15.2±0.4	22.5±0.1	0.67	h	41±3	38±5	50±5	2.7	k	57±13
UGC 4173	16.7±3.1	TF	a	-17.7±0.4	24.1±0.1	4.97	h	40±3	36±5	*57±5*	12.2	k	7±2
UGC 4325	10.0±1.8	TF	a	-18.0±0.4	21.4±0.1	1.74	h	41±3	73±3	92±3	5.8	k	42±8
UGC 4499	12.8±2.4	TF	a	-17.7±0.4	21.8±0.1	1.33	h	50±3	38±4	74±3	8.4	k	29±6
UGC 4543	30.0±5.5	TF	a	-19.2±0.4	22.4±0.1	3.34	h	46±3	59±4	67±4	17.4	k	18±4
UGC 5272	6.5±1.2	TF	a	-15.2±0.4	22.0±0.1	0.68	h	59±3	19±4	*45±4*	1.9	k	28±8
UGC 5414	9.4±1.7	TF	a	-17.4±0.4	21.8±0.1	1.38	h	55±3	35±3	*61±2*	4.1	k	25±5
UGC 5721	5.9±1.1	TF	a	-16.3±0.4	20.3±0.1	0.39	h	61±3	39±3	79±3	6.4	k	100±20
UGC 5829	8.0±1.5	TF	a	-17.0±0.4	22.6±0.1	1.50	h	34±3	34±5	*69±5*	6.4	k	23±6
UGC 5846	19.3±3.6	TF	a	-16.9±0.4	22.8±0.1	1.77	h	30±3	30±6	51±6	5.6	k	17±5
UGC 5918	7.1±1.3	TF	a	-15.2±0.4	23.8±0.1	1.59	h	46±3	30±4	*45±4*	4.1	k	19±4
UGC 6399	18.4±3.0	TF	b	-18.0±0.3	22.3±0.2	2.14	i	75±2	53±7	88±5	8.0	l	26±5
UGC 6446	18.0±3.0	TF	b	-18.5±0.4	22.2±0.1	2.70	i	51±3	62±4	82±4	15.7	l	23±4
UGC 6955	16.1±2.7	TF	b	-18.1±0.4	23.0±0.1	3.91	h	64±2	49±3	82±2	15.6	m	12±2
UGC 7232	2.8±0.5	TF	a	-14.8±0.4	20.7±0.1	0.20	h	59±3	19±4	*44±4*	0.8	k	95±26
UGC 7261	7.9±1.5	TF	a	-17.3±0.4	22.0±0.1	1.34	h	30±3	66±6	76±6	4.0	k	49±11
UGC 7323	5.8±1.0	TF	b	-18.2±0.4	21.3±0.1	1.51	h	47±3	49±4	*86±4*	4.2	k	32±6
UGC 7524$^\beta$	4.3±0.4	Ceph	d	-18.6±0.2	22.1±0.1	2.82	h	46±3	58±4	79±4	9.7	k	21±3
UGC 7559	5.0±0.2	TRGB	e	-14.6±0.1	23.9±0.1	1.08	h	61±3	21±4	33±4	3.3	k	19±4
UGC 7577	2.6±0.1	TRGB	e	-15.0±0.1	22.4±0.1	0.64	h	63±3	8±3	*18±3*	1.7	k	12±5
UGC 7603	10.5±1.7	TF	b	-17.8±0.3	21.3±0.3	1.06	h	78±3	30±3	64±3	9.2	k	28±5
UGC 7690$^\gamma$	7.5±1.4	TF	a	-16.9±0.4	20.2±0.1	0.43	h	41±3	44±4	56±4	3.8	k	102±22

Table 5.B.3 – continued.

Name	Dist (Mpc)	Method	Ref.	M_R (mag)	$\mu^i_{0,R}$ (mag/$''^2$)	R_d (kpc)	Ref.	i (°)	V_{R_d} (km/s)	V_{last} (km/s)	R_{last} (kpc)	Ref.	V_{R_d}/R_d (km/s/kpc)
(1)	(2)	(3)	(4)	(5)	(6)	(7)	(8)	(9)	(10)	(11)	(12)	(13)	(14)
UGC 7866	4.6±0.2	TRGB	e	-15.1±0.1	22.1±0.1	0.55	h	44±3	17±4	*33±4*	2.3	k	31±8
UGC 7916	7.2±2.6	TF	a	-14.6±0.8	24.4±0.2	1.47	h	74±3	21±3	*36±3*	3.7	k	14±5
UGC 7971	8.0±1.5	TF	a	-17.0±0.4	21.3±0.1	0.89	h	38±3	22±5	*45±5*	2.9	k	25±7
UGC 8320	4.6±0.2	TRGB	e	-15.9±0.1	22.3±0.1	0.79	h	61±3	21±4	49±4	4.0	m	27±5
UGC 8490[γ]	4.6±0.6	TRGB	f	-17.2±0.3	20.4±0.1	0.65	h	50±3	48±4	78±4	10.0	k	74±12
UGC 8837	7.2±0.1	TRGB	e	-16.5±0.1	23.7±0.3	1.73	h	80±3	25±3	*48±4*	4.2	k	14±2
UGC 9211	14.7±2.7	TF	a	-16.5±0.4	22.7±0.1	1.38	h	44±3	35±4	65±4	9.6	k	25±6
UGC 9992	11.2±2.1	TF	a	-16.0±0.4	21.9±0.1	0.86	h	30±3	28±6	34±6	4.1	k	33±10
UGC 10310	15.8±2.9	TF	a	-17.9±0.4	21.9±0.1	1.91	h	34±3	44±5	74±5	9.2	k	23±5
UGC 11557	23.7±4.4	TF	a	-19.0±0.4	20.9±0.1	3.01	h	30±3	53±6	85±6	10.3	k	18±4
UGC 11707	15.7±3.0	TF	a	-18.2±0.4	23.1±0.2	4.41	h	68±3	68±7	100±3	15.0	k	15±3
UGC 12060	15.1±2.8	TF	a	-17.7±0.4	21.8±0.1	1.52	h	40±3	61±4	74±4	9.9	k	40±8
UGC 12632	9.2±1.7	TF	a	-17.5±0.4	23.3±0.1	3.78	h	46±3	58±4	76±3	11.4	k	15±3
UGC 12732	12.4±2.3	TF	a	-17.8±0.4	22.4±0.1	2.13	h	39±3	53±5	*98±5*	14.4	k	25±5
WLM[δ]	1.0±0.1	Ceph	g	-14.1±0.2	22.5±0.2	0.57	j	70±4	19±2	*43±4*	3.7	n	33±5
NGC 6822[δ]	0.5±0.1	Ceph	g	-15.0±0.4	21.3±0.1	0.57	j	59±3	20±1	56±3	4.7	o	35±7

Notes. [α] the H I line profiles are very broad and complex; we assigned a larger error to V_{R_d} than given by Swaters et al. (2009).
[β] the galaxy is kinematically lopsided, but the H I kinematics is quite symmetric in the inner regions.
[γ] the H I disk is warped, the inclination is given for $R \simeq R_d$.
[δ] the V-band values from Hunter & Elmegreen (2006) have been converted to R-band assuming $V - R = 0.5$.

Table 5.B.4 – Sample of irregulars. Gas and star-formation properties. References:(a) Hunter & Hoffman (1999); (b) Berg et al. (2012); (c) van Zee & Haynes (2006); (d) Croxall et al. (2009); (e) Esteban et al. (2009); (f) Lee et al. (2005); (g) Swaters et al. (2002); (h) Verheijen & Sancisi (2001); (i) Broeils (1992); (j) Kepley et al. (2007); (k) Weldrake et al. (2003); (l) Kennicutt et al. (2008); (m) James et al. (2004).

Name	log(O/H) +12	Ref.	$M_{\rm H\,I}$	$\overline{\Sigma}_{\rm H\,I}$	Ref.	EW(Hα)	SFR	Ref.	SFR/$M_{\rm bar}$	$\log(\Sigma_{\rm SFR})$	$\tau_{\rm global}$	$\tau_{\rm local}$
			($10^8 M_\odot$)	($M_\odot$/pc^2)		(Å)	($M_\odot$/yr)		(Gyr^{-1})	($M_\odot$/yr/kpc^2)	(Gyr)	(Gyr)
(1)	(2)	(3)	(4)	(5)	(6)	(7)	(8)	(9)	(10)	(11)	(12)	(13)
UGC 731	*8.46±0.20*	a	16.1±11.8	5.5±0.7	g	...	...	...	...	...	...	...
UGC 2455	*8.39±0.20*	a	6.9±2.7	10.1±1.2	g	49±4	0.161	l	*0.247*	-2.01	5.7	1.4
UGC 3371	*8.48±0.20*	a	35.6±16.3	3.2±0.4	g	24±2	0.041	m	0.016	-4.39	115.5	104.0
UGC 3711	...	...	6.2±2.4	7.7±1.0	g	44±4	0.097	l	0.025	-2.40	8.5	2.6
UGC 3817	...	...	2.1±1.6	4.5±0.5	g	59±8	0.008	l	*0.041*	-3.22	34.9	9.9
UGC 3966	*8.15±0.20*	a	3.2±1.2	6.4±0.7	g	20±4	0.005	l	0.017	-3.46	85.1	24.6
UGC 4173	...	...	23.8±8.0	3.0±0.3	g	60±6	0.056	m	*0.113*	-4.15	56.5	56.5
UGC 4325	8.15±0.05	b	7.4±2.7	6.6±0.7	g	32±4	0.075	l	0.022	-3.11	12.9	11.4
UGC 4499	...	...	11.5±4.5	7.2±0.8	g	49±5	0.082	m	0.058	-2.84	18.6	6.6
UGC 4543	...	...	72.2±27.4	5.4±0.6	g	...	...	...	...	...	...	...
UGC 5272	7.87±0.05	b	1.9±0.7	8.9±1.2	g	45±4	0.016	l	*0.083*	-2.97	15.8	11.0
UGC 5414	...	...	5.7±2.1	6.0±0.7	g	49±5	0.051	m	*0.078*	-3.08	14.9	9.6
UGC 5721	*8.32±0.20*	a	5.1±2.0	11.7±1.6	g	53±4	0.037	l	0.020	-2.12	18.3	2.1
UGC 5829	*8.30±0.10*	c	8.8±3.4	6.7±0.7	g	38±4	0.049	l	*0.046*	-3.17	23.9	13.2
UGC 5846	...	...	15.3±5.9	5.1±0.5	g	...	...	...	...	...	...	...
UGC 5918	7.84±0.04	d	2.5±0.9	2.6±0.3	g	19±5	0.003	l	0.016	-4.43	110.8	93.7
UGC 6399	...	...	8.4±2.7	...	h	25±2	0.067	m	0.024	-3.34	16.7	...
UGC 6446	...	...	31.0±10.3	5.5±0.6	h	80±8	0.117	m	0.055	-3.30	35.2	14.7
UGC 6955	*8.26±0.20*	a	20.8±7.3	...	i	20±5	0.047	m	0.022	-4.02	58.9	...
UGC 7232	...	...	0.4±0.2	7.8±1.0	g	22±5	0.003	l	*0.017*	-2.63	17.7	4.4
UGC 7261	...	...	5.0±2.0	5.2±0.5	g	42±4	0.075	l	0.048	-2.89	8.9	5.3
UGC 7323	...	...	3.8±1.4	4.1±0.5	g	18±3	0.038	l	0.015	-3.29	13.3	10.5
UGC 7524	8.09±0.15	e	14.6±3.0	3.9±0.4	g	27±4	0.079	l	0.043	-3.51	24.6	16.8
UGC 7559	...	...	1.8±0.2	3.6±0.5	g	38±5	0.008	l	0.143	-3.67	29.9	22.5
UGC 7577	7.97±0.06	b	0.45±0.06	2.1±0.3	g	9±2	0.002	l	*0.405*	-3.82	29.9	18.4
UGC 7603	...	...	12.8±4.3	6.3±1.7	g	35±4	0.081	l	0.103	-2.65	21.0	3.7
UGC 7690	...	...	3.3±1.3	8.8±1.0	g	24±4	0.024	l	0.052	-2.39	18.3	2.9
UGC 7866	...	...	1.2±0.2	4.7±0.5	g	49±4	0.012	l	*0.215*	-2.91	13.3	5.1

Table 5.B.4 – continued.

Name	log(O/H) +12	Ref.	$M_{\rm H\,I}$ ($10^8 M_\odot$)	$\overline{\Sigma}_{\rm H\,I}$ ($M_\odot$/pc^2)	Ref.	EW(Hα) (Å)	SFR ($M_\odot$/yr)	Ref.	SFR/$M_{\rm bar}$ (Gyr^{-1})	log($\Sigma_{\rm SFR}$) ($M_\odot$/yr/kpc^2)	$\tau_{\rm global}$ (Gyr)	$\tau_{\rm local}$ (Gyr)
(1)	(2)	(3)	(4)	(5)	(6)	(7)	(8)	(9)	(10)	(11)	(12)	(13)
UGC 7916	...	...	2.6±1.9	3.1±0.6	g	63±22	0.014	l	*0.177*	-3.70	24.7	20.5
UGC 7971	*8.43±0.20*	a	2.5±0.9	5.7±0.6	g	25±4	0.017	l	*0.088*	-3.18	19.6	11.4
UGC 8320	*8.29±0.20*	a	3.5±0.5	...	i	22±4	0.008	l	0.029	-3.40	58.2	...
UGC 8490	...	...	7.0±2.0	9.1±1.1	g	54±5	0.063	l	0.036	-2.33	14.8	2.6
UGC 8837	7.87±0.07	b	3.2±0.3	1.8±0.6	g	37±4	0.022	l	*0.088*	-3.64	19.3	10.5
UGC 9211	...	...	14.2±5.4	6.2±0.7	g	57±12	0.036	l	0.043	-3.23	52.5	14.0
UGC 9992	7.88±0.12	c	3.5±1.4	5.3±0.5	g	20±4	0.009	l	0.143	-3.42	51.7	18.6
UGC 10310	*8.31±0.20*	a	12.9±4.9	6.2±0.7	g	63±6	0.147	m	0.104	-2.90	11.7	6.6
UGC 11557	...	...	25.0±9.6	5.0±0.5	g	35±3	0.486	m	0.198	-2.78	6.8	4.0
UGC 11707	...	...	36.3±14.3	5.2±0.8	g	...	...	...	...	...	...	...
UGC 12060	*8.34±0.20*	a	16.7±6.4	4.0±0.4	g	...	...	...	...	...	...	...
UGC 12632	*8.34±0.20*	a	15.4±5.9	3.4±0.4	g	40±6	0.060	l	0.038	-3.88	34.1	34.6
UGC 12732	...	...	32.3±12.4	4.7±0.5	g	88±9	0.086	m	*0.020*	-3.23	49.9	10.6
WLM	7.83±0.06	b	0.7±0.1	...	j	25±9	0.002	l	*0.012*	-3.72	46.5	...
NGC 6822$^\alpha$	8.11±0.10	f	1.5±0.6	...	k	47±12	0.011	l	0.024	-2.98	18.1	...

Notes. $^{(\alpha)}$ Weldrake et al. (2003) do not provide the total H I flux, thus we used the single-dish value from Koribalski et al. (2004) to calculate $M_{\rm H\,I}$.

Table 5.B.5 – Sample of rotating spheroidals. We assumed a distance of 16.1±1.2 Mpc for all the galaxies. References: (a) van Zee et al. (2004a); (b) van Zee et al. (2004b).

Name	$M_{\rm R}$	i	$\mu^i_{0,R}$	$R_{\rm d}$	Ref.	$v_{R_{\rm d}}$	$v_{\rm last}$	$R_{\rm last}$	$\overline{\sigma}_{\rm obs}$	Ref.	$V_{R_{\rm d}}$	$V_{\rm last}$	$V_{R_{\rm d}}/R_{\rm d}$
	(mag)	(°)	(mag/$''^2$)	(kpc)		(km/s)	(km/s)	(kpc)	(km/s)		(km/s)	(km/s)	(km/s/kpc)
(1)	(2)	(3)	(4)	(5)	(6)	(7)	(8)	(9)	(10)	(11)	(12)	(13)	(14)
VCC 178	-16.6±0.2	60±3	20.9±0.1	0.52	a	14±3	30±3	1.1	46±5	b	48±5	73±7	92±12
VCC 437	-18.1±0.2	54±3	21.7±0.1	1.60	a	49±5	49±5	1.6	50±5	b	70±5	70±5	44±5
VCC 543	-17.9±0.2	62±3	21.6±0.1	1.23	a	35±4	46±4	1.6	44±5	b	56±5	68±5	45±5
VCC 990	-17.6±0.2	50±3	20.0±0.1	0.53	a	18±3	43±3	1.3	43±5	b	46±5	80±7	87±11
VCC 1036	-18.3±0.2	69±3	21.4±0.2	1.32	a	32±2	52±2	2.1	37±4	b	49±3	70±4	37±4
VCC 1122	-17.3±0.2	70±3	21.5±0.2	0.90	a	17±3	28±3	1.4	40±4	b	43±4	57±5	48±6
VCC 2019	-17.6±0.2	47±3	20.6±0.1	0.73	a	28±3	42±3	1.1	41±4	b	50±4	65±4	68±8
VCC 2050	-16.8±0.2	66±3	21.3±0.2	0.62	a	11±3	20±3	1.0	37±6	b	39±6	51±7	60±10

References

Aloisi, A., Clementini, G., Tosi, M., et al. 2007, ApJL, 667, L151
Aloisi, A., van der Marel, R. P., Mack, J., et al. 2005, ApJL, 631, L45
Annibali, F., Tosi, M., Aloisi, A., & van der Marel, R. P. 2011, AJ, 142, 129
Annibali, F., Tosi, M., Monelli, M., et al. 2009, AJ, 138, 169
Ashley, T., Simpson, C. E., & Elmegreen, B. G. 2013, AJ, 146, 42
Barnes, J. E. & Hernquist, L. 1996, ApJ, 471, 115
Bekki, K. 2008, MNRAS, 388, L10
Bekki, K. & Freeman, K. C. 2002, ApJL, 574, L21
Berg, D. A., Skillman, E. D., Marble, A. R., et al. 2012, ApJ, 754, 98
Binggeli, B. 1994, in European Southern Observatory Conference and Workshop Proceedings, Vol. 49, European Southern Observatory Conference and Workshop Proceedings, ed. G. Meylan & P. Prugniel, 13
Binggeli, B., Sandage, A., & Tammann, G. A. 1985, AJ, 90, 1681
Binney, J. & Tremaine, S. 1987, Galactic dynamics
Bono, G., Caputo, F., Marconi, M., & Musella, I. 2010, ApJ, 715, 277
Bothun, G. D., Mould, J. R., Caldwell, N., & MacGillivray, H. T. 1986, AJ, 92, 1007
Bournaud, F., Elmegreen, B. G., & Elmegreen, D. M. 2007, ApJ, 670, 237
Broeils, A. H. 1992, Dark and visible matter in spiral galaxies
Ciotti, L. 1991, A&A, 249, 99
Ciotti, L. & Bertin, G. 1999, A&A, 352, 447
Côté, P., Piatek, S., Ferrarese, L., et al. 2006, ApJS, 165, 57
Cox, A. L., Sparke, L. S., Watson, A. M., & van Moorsel, G. 2001, AJ, 121, 692
Croxall, K. V., van Zee, L., Lee, H., et al. 2009, ApJ, 705, 723
Davies, J. I. & Phillipps, S. 1988, MNRAS, 233, 553
de Vaucouleurs, G., de Vaucouleurs, A., Corwin, Jr., H. G., et al. 1991, Third Reference Catalogue of Bright Galaxies. Volume I: Explanations and references. Volume II: Data for galaxies between 0^h and 12^h. Volume III: Data for galaxies between 12^h and 24^h.
Dekel, A. & Birnboim, Y. 2006, MNRAS, 368, 2
Dekel, A. & Silk, J. 1986, ApJ, 303, 39
Dellenbusch, K. E., Gallagher, III, J. S., & Knezek, P. M. 2007, ApJL, 655, L29
Dellenbusch, K. E., Gallagher, III, J. S., Knezek, P. M., & Noble, A. G. 2008, AJ, 135, 326
Drozdovsky, I. O. & Karachentsev, I. D. 2000, A&AS, 142, 425
Drozdovsky, I. O., Schulte-Ladbeck, R. E., Hopp, U., Crone, M. M., & Greggio, L. 2001, ApJL, 551, L135
Ekta, Chengalur, J. N., & Pustilnik, S. A. 2006, MNRAS, 372, 853
Ekta, B., Pustilnik, S. A., & Chengalur, J. N. 2009, MNRAS, 397, 963
Elmegreen, B. G., Zhang, H.-X., & Hunter, D. A. 2012, ApJ, 747, 105
Elson, E. C., de Blok, W. J. G., & Kraan-Korteweg, R. C. 2010, MNRAS, 404, 2061

Elson, E. C., de Blok, W. J. G., & Kraan-Korteweg, R. C. 2011, MNRAS, 415, 323
Esteban, C., Bresolin, F., Peimbert, M., et al. 2009, ApJ, 700, 654
Ferguson, H. C. & Binggeli, B. 1994, A&ARv, 6, 67
Fraternali, F., van Moorsel, G., Sancisi, R., & Oosterloo, T. 2002, AJ, 123, 3124
Freeman, K. C. 1970, ApJ, 160, 811
Gallagher, III, J. S. & Hunter, D. A. 1987, AJ, 94, 43
García-Benito, R. & Pérez-Montero, E. 2012, MNRAS, 423, 406
Gatto, A., Fraternali, F., Read, J. I., et al. 2013, MNRAS, 433, 2749
Gentile, G., Angus, G. W., Famaey, B., Oh, S.-H., & de Blok, W. J. G. 2012, A&A, 543, A47
Gil de Paz, A. & Madore, B. F. 2005, ApJS, 156, 345
Gil de Paz, A., Madore, B. F., & Pevunova, O. 2003, ApJS, 147, 29
Gnedin, O. Y., Ostriker, J. P., & Tremaine, S. 2013, ArXiv e-prints
Halliday, C., Davies, R. L., Kuntschner, H., et al. 2001, MNRAS, 326, 473
Hoessel, J. G., Saha, A., & Danielson, G. E. 1998, AJ, 115, 573
Holmberg, E. 1950, Meddelanden fran Lunds Astronomiska Observatorium Serie II, 128, 1
Howley, K. M., Guhathakurta, P., van der Marel, R., et al. 2013, ApJ, 765, 65
Hunter, D. A. & Elmegreen, B. G. 2004, AJ, 128, 2170
Hunter, D. A. & Elmegreen, B. G. 2006, ApJS, 162, 49
Hunter, D. A. & Hoffman, L. 1999, AJ, 117, 2789
Immeli, A., Samland, M., Gerhard, O., & Westera, P. 2004, A&A, 413, 547
Izotov, Y. I. & Thuan, T. X. 1999, ApJ, 511, 639
Izotov, Y. I. & Thuan, T. X. 2002, ApJ, 567, 875
Jackson, D. C., Skillman, E. D., Cannon, J. M., & Côté, S. 2004, AJ, 128, 1219
Jacobs, B. A., Rizzi, L., Tully, R. B., et al. 2009, AJ, 138, 332
James, P. A., Shane, N. S., Beckman, J. E., et al. 2004, A&A, 414, 23
Karachentsev, I. D., Makarov, D. I., Sharina, M. E., et al. 2003, A&A, 398, 479
Kelson, D. D., Illingworth, G. D., Tonry, J. L., et al. 2000, ApJ, 529, 768
Kennicutt, R. C. & Evans, N. J. 2012, ARA&A, 50, 531
Kennicutt, Jr., R. C. 1989, ApJ, 344, 685
Kennicutt, Jr., R. C. 1998a, ARA&A, 36, 189
Kennicutt, Jr., R. C. 1998b, ApJ, 498, 541
Kennicutt, Jr., R. C., Lee, J. C., Funes, José G., S. J., Sakai, S., & Akiyama, S. 2008, ApJS, 178, 247
Kepley, A. A., Wilcots, E. M., Hunter, D. A., & Nordgren, T. 2007, AJ, 133, 2242
Kereš, D., Katz, N., Weinberg, D. H., & Davé, R. 2005, MNRAS, 363, 2
Koribalski, B. S., Staveley-Smith, L., Kilborn, V. A., et al. 2004, AJ, 128, 16
Kormendy, J. 1985, ApJ, 295, 73
Kormendy, J. & Bender, R. 2012, ApJS, 198, 2
Kormendy, J., Fisher, D. B., Cornell, M. E., & Bender, R. 2009, ApJS, 182, 216

Leaman, R., Venn, K. A., Brooks, A. M., et al. 2012, ApJ, 750, 33
Lee, H., Skillman, E. D., & Venn, K. A. 2005, ApJ, 620, 223
Lee, J. C., Gil de Paz, A., Tremonti, C., et al. 2009, ApJ, 706, 599
Lelli, F., Fraternali, F., & Verheijen, M. 2013, MNRAS
Lelli, F., Verheijen, M., Fraternali, F., & Sancisi, R. 2012a, A&A, 537, A72
Lelli, F., Verheijen, M., Fraternali, F., & Sancisi, R. 2012b, A&A, 544, A145
Leroy, A. K., Walter, F., Brinks, E., et al. 2008, AJ, 136, 2782
Lisker, T., Glatt, K., Westera, P., & Grebel, E. K. 2006, AJ, 132, 2432
Lisker, T., Grebel, E. K., Binggeli, B., & Glatt, K. 2007, ApJ, 660, 1186
López-Sánchez, A. R., Koribalski, B., van Eymeren, J., et al. 2010, in Astronomical Society of the Pacific Conference Series, Vol. 421, Galaxies in Isolation: Exploring Nature Versus Nurture, ed. L. Verdes-Montenegro, A. Del Olmo, & J. Sulentic, 65
Lotz, J. M., Miller, B. W., & Ferguson, H. C. 2004, ApJ, 613, 262
Marlowe, A. T., Meurer, G. R., & Heckman, T. M. 1999, ApJ, 522, 183
Martin, C. L. 1996, ApJ, 465, 680
Martin, C. L. 1998, ApJ, 506, 222
Martin, C. L. & Kennicutt, Jr., R. C. 2001, ApJ, 555, 301
Mateo, M. L. 1998, ARA&A, 36, 435
Mayer, L. 2011, in EAS Publications Series, Vol. 48, EAS Publications Series, ed. M. Koleva, P. Prugniel, & I. Vauglin, 369–381
Mayer, L., Mastropietro, C., Wadsley, J., Stadel, J., & Moore, B. 2006, MNRAS, 369, 1021
McGaugh, S. S. 2012, AJ, 143, 40
McGaugh, S. S. & Wolf, J. 2010, ApJ, 722, 248
McQuinn, K. B. W., Skillman, E. D., Cannon, J. M., et al. 2010a, ApJ, 721, 297
McQuinn, K. B. W., Skillman, E. D., Cannon, J. M., et al. 2010b, ApJ, 724, 49
McQuinn, K. B. W., Skillman, E. D., Dalcanton, J. J., et al. 2012, ApJ, 759, 77
Meurer, G. R., Mackie, G., & Carignan, C. 1994, AJ, 107, 2021
Meurer, G. R., Staveley-Smith, L., & Killeen, N. E. B. 1998, MNRAS, 300, 705
Micheva, G., Östlin, G., Bergvall, N., et al. 2013, MNRAS, 431, 102
Minchev, I., Famaey, B., Combes, F., et al. 2011, A&A, 527, A147
Moore, B., Lake, G., & Katz, N. 1998, ApJ, 495, 139
Noeske, K. G., Guseva, N. G., Fricke, K. J., et al. 2000, A&A, 361, 33
Oh, S.-H., de Blok, W. J. G., Brinks, E., Walter, F., & Kennicutt, Jr., R. C. 2011, AJ, 141, 193
Ott, J., Walter, F., & Brinks, E. 2005a, MNRAS, 358, 1423
Ott, J., Walter, F., & Brinks, E. 2005b, MNRAS, 358, 1453
Papaderos, P., Izotov, Y. I., Thuan, T. X., et al. 2002, A&A, 393, 461
Papaderos, P., Loose, H.-H., Fricke, K. J., & Thuan, T. X. 1996, A&A, 314, 59
Rafikov, R. R. 2001, MNRAS, 323, 445
Roychowdhury, S., Chengalur, J. N., Begum, A., & Karachentsev, I. D. 2009,

MNRAS, 397, 1435
Sánchez-Janssen, R., Méndez-Abreu, J., & Aguerri, J. A. L. 2010, MNRAS, 406, L65
Sandage, A. & Hoffman, G. L. 1991, ApJL, 379, L45
Schulte-Ladbeck, R. E., Hopp, U., Greggio, L., Crone, M. M., & Drozdovsky, I. O. 2001, AJ, 121, 3007
Schwartz, C. M. & Martin, C. L. 2004, ApJ, 610, 201
Sérsic, J. L. 1963, Boletin de la Asociacion Argentina de Astronomia La Plata Argentina, 6, 41
Simpson, C. E. & Gottesman, S. T. 2000, AJ, 120, 2975
Spolaor, M., Hau, G. K. T., Forbes, D. A., & Couch, W. J. 2010, MNRAS, 408, 254
Swaters, R. A. & Balcells, M. 2002, A&A, 390, 863
Swaters, R. A., Sancisi, R., van Albada, T. S., & van der Hulst, J. M. 2009, A&A, 493, 871
Swaters, R. A., van Albada, T. S., van der Hulst, J. M., & Sancisi, R. 2002, A&A, 390, 829
Tammann, G. A. 1994, in European Southern Observatory Conference and Workshop Proceedings, Vol. 49, European Southern Observatory Conference and Workshop Proceedings, ed. G. Meylan & P. Prugniel, 3
Taylor, C. L., Kobulnicky, H. A., & Skillman, E. D. 1998, AJ, 116, 2746
Terlevich, R., Melnick, J., Masegosa, J., Moles, M., & Copetti, M. V. F. 1991, A&AS, 91, 285
Thim, F., Hoessel, J. G., Saha, A., et al. 2004, AJ, 127, 2322
Tolstoy, E., Hill, V., & Tosi, M. 2009, ARA&A, 47, 371
Tolstoy, E., Saha, A., Hoessel, J. G., & McQuade, K. 1995, AJ, 110, 1640
Toomre, A. 1964, ApJ, 139, 1217
Tosi, M., Sabbi, E., Bellazzini, M., et al. 2001, AJ, 122, 1271
Tully, R. B. 1988, Nearby galaxies catalog
Tully, R. B., Rizzi, L., Shaya, E. J., et al. 2009, AJ, 138, 323
Tully, R. B., Verheijen, M. A. W., Pierce, M. J., Huang, J.-S., & Wainscoat, R. J. 1996, AJ, 112, 2471
van Eymeren, J., Koribalski, B. S., López-Sánchez, Á. R., Dettmar, R.-J., & Bomans, D. J. 2010, MNRAS, 407, 113
van Eymeren, J., Marcelin, M., Koribalski, B., et al. 2009a, A&A, 493, 511
van Eymeren, J., Marcelin, M., Koribalski, B. S., et al. 2009b, A&A, 505, 105
van Zee, L. 2001, AJ, 121, 2003
van Zee, L., Barton, E. J., & Skillman, E. D. 2004a, AJ, 128, 2797
van Zee, L. & Haynes, M. P. 2006, ApJ, 636, 214
van Zee, L., Salzer, J. J., & Skillman, E. D. 2001, AJ, 122, 121
van Zee, L., Skillman, E. D., & Haynes, M. P. 2004b, AJ, 128, 121
van Zee, L., Skillman, E. D., & Salzer, J. J. 1998, AJ, 116, 1186
Verheijen, M. A. W. 2001, ApJ, 563, 694

Verheijen, M. A. W. & Sancisi, R. 2001, A&A, 370, 765
Weijmans, A.-M., Krajnović, D., van de Ven, G., et al. 2008, MNRAS, 383, 1343
Weisz, D. R., Dalcanton, J. J., Williams, B. F., et al. 2011, ApJ, 739, 5
Weisz, D. R., Skillman, E. D., Cannon, J. M., et al. 2008, ApJ, 689, 160
Weldrake, D. T. F., de Blok, W. J. G., & Walter, F. 2003, MNRAS, 340, 12

Chapter 6

What triggers starbursts in low-mass galaxies?

— **Federico Lelli, Marc Verheijen, and Filippo Fraternali** —

In preparation for submission to MNRAS

Abstract

Strong bursts of star-formation in galaxies may be triggered either by internal or external mechanisms. We study the large-scale H I emission in 18 nearby starbursting dwarfs, that have accurate star-formation histories from HST observations. We found that these objects show a broad, continuous range of H I morphologies. Several galaxies have heavily disturbed H I morphologies, with major asymmetries, long filaments, and/or severe offsets between the H I and stellar distributions, whereas other galaxies show only minor asymmetries in their outer regions. We quantify these asymmetries for both our sample and a control-sample of non-starbursting dwarf irregulars, drawn from the VLA-ANGST survey. Starbursting dwarfs appear to have more asymmetric H I morphologies than typical irregulars, suggesting that some external mechanism triggered the intense star-formation. Moreover, galaxies hosting an old burst ($\gtrsim$100 Myr) have more symmetric H I morphologies than galaxies hosting a young one ($\lesssim$100 Myr), indicating that the former ones probably had enough time to regularize their outer H I distribution since the onset of the burst. These results suggest that the starburst is triggered by interactions/mergers between gas-rich dwarfs and/or by direct gas infall from the IGM.

6.1 Introduction

The mechanisms that trigger strong bursts of star-formation in low-mass galaxies are poorly understood. Unlike spiral galaxies, gas-rich dwarfs usually do not have strong density waves and stellar bars, thus internal mechanisms such as bar-driven gas inflows are generally ruled out (e.g. Hunter & Elmegreen 2004). Other internal mechanisms, however, have been proposed, like torques due to massive star-forming clumps (Elmegreen et al. 2012), triaxial dark matter haloes (Bekki & Freeman 2002), or bars made of dark matter (Hunter & Elmegreen 2004). External mechanisms are also possible, like tidal perturbations from nearby companions (e.g. Noguchi 1988), interactions/mergers between gas-rich dwarfs (e.g. Bekki 2008), or cold gas accretion from the IGM (e.g. Silk et al. 1987). In particular, cosmological models predict that low-mass galaxies should accreate most of their gas through cold flows, reaching the central parts of the dark matter halo without being shock-heated to the virial temperature (e.g. Dekel & Birnboim 2006). This process may still take place at $z \simeq 0$ in low-density environments (Kereš et al. 2005), thus isolated starbursting dwarfs in the nearby Universe are prime locations to search for cold gas accretion.

In Chapter 4, we studied the H I content of 18 starbursting dwarfs (hereafter blue compact dwarfs, BCDs) and found that complex H I kinematics are much more common in BCDs (∼50%) than in typical irregulars (∼10%). This may be related to the starburst trigger (interactions/mergers or disk instabilities), but may also be a consequence of feedback from supernovae and stellar winds, making it difficult to distinguish between different triggering mechanisms. The other ∼50% of BCDs, instead, have a regularly-rotating H I disk, which can be used to derive rotation curves and investigate the internal distribution of mass. In Chapter 5, we found that BCDs generally have steeper rotation curves than typical irregulars (Irrs) of the same total mass (see also van Zee et al. 2001), suggesting that there is a close link between the starburst activity and the shape of the gravitational potential. A central concentration of mass (gas, stars, and dark matter) seems to be a characterizing property of BCDs and must be tightly linked to the mechanism that triggers the starburst.

Environmental studies can also provide important clues about the triggering mechanism. BCDs tend to populate low-density environments (e.g. Iovino et al. 1988; Salzer 1989; Telles & Maddox 2000; Lee et al. 2000) and are not necessarily associated with *bright* galaxies (e.g. Campos-Aguilar & Moles 1991; Campos-Aguilar et al. 1993; Telles & Terlevich 1995; Pustilnik et al. 1995), suggesting that tidal interactions with *massive* companions are *not* a dominant starburst trigger. The possibility of interactions with low-luminosity, low-surface-brightness (LSB) galaxies, however, remains open (e.g. Méndez et al. 1999; Méndez & Esteban 2000; Noeske et al. 2001; Pustilnik et al. 2001b), given that these objects are usually under-represented in optical catalogs. Moreover, if the starburst is due to a *past* interaction/merger with a LSB dwarf, the resulting tidal features would have very low surface brightnesses and be difficult

Table 6.1 – Galaxy Sample

Name	Alternative Name	R.A. (J2000)	Dec. (J2000)	V_{sys} – (km s^{-1}) –	V_{rot}	Dist (Mpc)	M_R (mag)	R_{opt} (kpc)	12+log(O/H)	Ref.
NGC 625	ESO 297-G005	01 35 04.3	-41 26 15	398±6	30±5	3.9±0.4	-17.25±0.24	3.3	8.08±0.12	a, g, l
NGC 1569	UGC 3056	04 30 49.0	+64 50 53	-80±10	50±5	3.4±0.2	-17.14±0.25	3.0	8.19±0.02	a, h, m
NGC 1705	ESO 158-G013	04 54 13.9	-53 21 25	635±2	72±10	5.1±0.6	-16.35±0.26	1.5	8.21±0.05	b, i, l
NGC 2366	UGC 3851	07 28 51.9	+69 12 34	103±1	49±6	3.2±0.4	-16.64±0.27	4.4	7.91±0.05	a, h, l
NGC 4068	UGC 7047	12 04 02.7	+52 35 28	206±2	39±5	4.3±0.1	-15.67±0.05	1.8	...	a, h
NGC 4163	UGC 7199	12 12 09.0	+36 10 11	158±4	10±5	3.0±0.1	-14.81±0.10	1.0	7.56±0.14	a, h, l
NGC 4214	UGC 7278	12 15 38.8	+36 19 39	291±1	81±9	2.7±0.2	-17.77±0.24	2.2	8.22±0.05	a, h, l
NGC 4449	UGC 7592	12 28 10.8	+44 05 37	210±5	35±5	4.2±0.5	-18.88±0.26	3.3	8.26±0.09	a, h, l
NGC 5253	Haro 10	13 39 56.0	-31 38 31	410±10	...	3.5±0.4	-17.61±0.27	2.1	8.12±0.05	a, g, k
NGC 6789	UGC 11425	19 16 41.9	+63 58 17	-151±2	57±9	3.6±0.2	-15.09±0.14	0.7	...	a, i
UGC 4483	...	08 37 03.4	+69 46 31	158±2	19±2	3.2±0.2	-12.97±0.19	0.6	7.56±0.03	a, i, l
UGC 6456	VII Zw 403	11 27 57.2	+78 59 48	-102±4	10±5	4.3±0.1	-14.41±0.05	1.2	7.69±0.01	a, j, n
UGC 6541	Mrk 178	11 33 28.9	+49 14 22	250±2	...	4.2±0.2	-14.61±0.10	0.9	7.82±0.06	c, j, l
UGC 9128	DDO 187	14 15 56.8	+23 03 22	150±3	24±4	2.2±0.1	-12.82±0.12	0.6	7.75±0.05	a, h, l
UGCA 290	Arp 211	12 37 22.1	+38 44 41	468±5	...	6.7±0.4	-14.09±0.18	0.9	...	d, i
I Zw 18	Mrk 116	09 34 02.0	+55 14 25	767±4	38±4	18.2±1.4	-14.99±0.26	0.5	7.20±0.01	e, j, k
I Zw 36	Mrk 209	12 26 16.8	+48 29 39	277±2	29±2	5.9±0.5	-14.88±0.23	0.9	7.77±0.01	f, i, k
SBS 1415+437	...	14 17 02.1	+43 30 19	616±2	18±2	13.6±1.4	-15.90±0.25	2.4	7.62±0.03	a, i, o

Notes. The values of the center are derived from R-band or V-band images; the rotation velocities V_{rot} are measured at the outermost radii accessible by H I data at relatively-high spatial resolutions (see Chapter 4 for details). Distances are derived from the tip of the red giant branch. The optical radius R_{opt} is defined as 3.2 exponential scale-lengths. The last column provides references for the distance, the integrated photometry, and the ionized gas metallicity, respectively.

References. (a) McQuinn et al. (2010); (b) Annibali et al. (2003); (c) Schulte-Ladbeck et al. (2000); (d) Crone et al. (2002); (e) Annibali et al. (2013); (f) Schulte-Ladbeck et al. (2001); (g) Lauberts & Valentijn (1989); (h) Swaters & Balcells (2002); (i) Gil de Paz et al. (2003); (j) Papaderos et al. (2002); (k) Izotov & Thuan (1999); (l) Berg et al. (2012); (m) Kobulnicky & Skillman (1997); (n) Thuan & Izotov (2005); (o) Guseva et al. (2003).

to unambiguosly identify, unless very deep optical imaging is available (e.g. López-Sánchez 2010; Martínez-Delgado et al. 2012).

Alternatively, deep 21 cm-line observations can be used to search for gas-rich companions, infalling gas, or signatures of past interactions/mergers (e.g. Sancisi et al. 2008). Taylor et al. (1993, 1995, 1996) obtained low-resolution *Very Large Array* (VLA) observations of 21 BCDs and 17 LSB Irrs, and concluded that BCDs have nearby "H I companions" more than twice as often as LSB Irrs, highlighting the possible importance of low-mass perturbers. Studies of the large-scale H I emission in individual objects have revealed that several BCDs show extended and filamentary H I structures, which may indicate either a recent interaction/merger or cold gas accretion from the environment; e.g. NGC 1569 (Stil & Israel 2002), IC 10 (Manthey & Oosterloo 2008), and NGC 5253 (López-Sánchez et al. 2012). In some cases, the presence of a nearby companion and/or stellar tidal features clearly points to an interaction/merger between gas-rich dwarfs; e.g. II Zw 40 (van Zee et al. 1998), II Zw 70/71 (Cox et al. 2001), and I Zw 18 (Lelli et al. 2012a). However, some BCDs seem to have relatively-symmetric and unperturbed H I disks, undermining the importance of external mechanisms in triggering the starburst; e.g. NGC 2915 (Elson et al. 2011) and VII Zw 403 (Simpson et al. 2011). The relative fraction of BCDs with extended symmetric/asymmetric H I morphologies in their outer regions is unclear, as well as the detailed relation between the extended H I emission and the starburst activity.

Here we present a detailed and systematic study of the large-scale H I emission in 18 starbursting dwarfs. The properties of our sample have been described in Chapter 4, and are summarized in Tables 6.1 and 6.2. In particular, the information provided by the star formation histories (SFHs) of these galaxies allows us to compare the starburst timescales with the dynamical timescales in the outer parts, and investigate the possible relation between the H I morphology and the starburst activity.

6.2 Data analysis

For the 18 galaxies in our sample, we collected both new and archival 21 cm-line observations. The collection and reduction of these observations are described in detail in Chapter 4, where we presented H I data at relatively-high spatial resolutions (ranging from $5''$ to $30''$ depending on the individual galaxy properties). Here we present H I data at lower spatial resolutions, which are more sensitive to the diffuse H I emission on large scales. We use the same dataset as in Chapter 4 except for two objects: NGC 4449 and UGC 4483. For NGC 4449, the H I datacube from THINGS (Walter et al. 2008) covers a relatively small region on the sky, thus we consider here the total H I map and velocity field from Hunter et al. (1998), which were obtained from VLA D-array observations in a 3×3 pointing mosaic (covering $\sim 1^\circ$). For UGC 4483,

Table 6.2 – Properties of the starburst.

Galaxy	b	SFR_0	SFR_p	$\Sigma_{SFR}(0)$	$\Sigma_{SFR}(t_p)$	$\log(sSFR_0)$	$\log(sSFR_p)$	t_p	Ref.
		$(10^{-3}M_\odot\ yr^{-1})$		$(10^{-3}M_\odot\ yr^{-1}\ kpc^{-2})$		—— (Gyr^{-1}) ——		Myr	
NGC 625	3.0±0.1	4±2	86±20	0.12±0.06	2.5±0.6	-2.66±0.63	-1.33±0.45	820±180	a
NGC 1569	21±1	80±15	240±10	2.8±0.5	8.5±0.3	-1.79±0.21	-1.31±0.11	40±10	a
NGC 1705	∼6	314±78	314±78	44±11	44±11	-0.65±0.56	-0.65±0.56	3.0±1.5	b
NGC 2366	5.6±0.4	43±9	160±10	0.7±0.1	2.6±0.2	-1.63±0.24	-1.06±0.13	450±50	a
NGC 4068	4.7±0.3	31±7	42±3	3.0±0.7	4.5±0.3	-1.70±0.26	-1.56±0.15	360±40	a
NGC 4163	2.9±0.6	5.2±1.6	12±3	1.6±0.5	3.8±0.9	-2.13±0.43	-1.77±0.39	450±50	a
NGC 4214	3.1±0.9	64±13	130±40	4.2±0.8	8.5±2.6	-1.49±0.32	-1.18±0.40	450±50	a
NGC 4449	6.0±0.5	970±70	970±70	28±2	28±2	-1.18±0.18	-1.18±0.18	5±3	a
NGC 5253	9.0±0.9	162±13	400±40	12±0.9	29±3	-1.82±0.16	-1.43±0.17	450±50	a
NGC 6789	3.8±1.3	3.0±1.3	15±5	1.9±0.8	9.7±3.2	-2.21±0.52	-1.51±0.44	565±65	a
UGC 4483	14±3	11±4	11±2	9.7±1.8	8.8±3.5	-0.80±0.27	-0.84±0.45	565±65	a
UGC 6456	7.6±1.1	23±3	23±3	5.1±0.7	5.1±0.7	-1.18±0.42	-1.18±0.42	16±8	a
UGC 6541	∼3	3.0±1.5	...	1.2±0.6	...	-1.27±0.71	...	...	c
UGC 9128	6.3±1.4	0.7±0.4	5±1	0.6±0.3	4.4±0.9	-2.11±0.59	-1.26±0.25	150±50	a
UGCA 290	∼3	11±8	42±15	4.3±3.1	16±6	-0.80±0.88	-0.22±0.61	15±5	d
I Zw 18	∼30	100±50	100±50	127±64	127±64	-0.07±0.73	-0.07±0.73	10±5	e
I Zw 36	∼7	25±12	...	9.8±4.7	...	-0.35±0.69	...	...	f
SBS 1415+437	∼12	40±7	150±10	2.2±0.4	8.3±0.5	-1.47±0.25	-0.90±0.19	450±50	a

Notes. For a detailed description of these quantities, see Sect. 6.4.3. For NGC 1705, UGC 6541, UGCA 290, I Zw 18, I Zw 36, and SBS 1415+437, the SFH at ages $\gtrsim$1 Gyr is uncertain due to the relatively-shallow photometric dept of the color-magnitude diagrams ($\lesssim$1 mag below the tip of the red giant branch), thus the values of b, $sSFR_0$, and $sSFR_p$ are approximate. The most problematic case is I Zw 18, where we prefer to use the SFR derived from Hα observations (Chapter 5) rather than the value derived from fitting the CMD.

References. (a) McQuinn et al. (2010); (b) Annibali et al. (2003); (c) Schulte-Ladbeck et al. (2000); (d) Crone et al. (2002); (e) Annibali et al. (2013); (f) Schulte-Ladbeck et al. (2001).

in Chapter 3 (Lelli et al. 2012b) we reduced and analysed archival H I data obtained with the B- and C-arrays of the VLA, but here we analyse the datacube from Ott et al. (2012) that includes also new D-array observations, probing low-column-density gas on large angular scales.

For every galaxy, we chose the optimal spatial resolution using the following approach. We first inspected the H I cube at the highest spatial and spectral resolutions available. Then, this cube was progressively smoothed in the image plane to $10''$, $20''$, $30''$, and $40''$, and total H I maps at different spatial resolutions were constructed by summing masked channel maps. The smoothing procedure was halted when the total H I map reached a 3σ column density sensitivity of $\sim 10^{20}$ atoms cm^{-2}, which is adeguate to investigate the H I morphology on large-scales (e.g. Swaters et al. 2002) and, at the same time, allows us to preserve a relatively-high angular resolution (typically $20''$ except for 4 cases, see Table 6.3). The masks were obtained by smoothing the cube in velocity to $\sim$10 km s^{-1} and in the image plane to $1'$ ($2'$ for NGC 2366, NGC 4214, and NGC 5253 given their large angular extent), and clipping at $3\sigma_{1'}$ ($\sigma_{1'}$ is the rms noise in the smoothed cube). For NGC 4214, the cube was smoothed in velocity to only $\sim$2.6 km s^{-1} because only a few line-free channels were available at its high-velocity end. All the masks were visually inspected; residual noise peaks and Galactic emission were interactively blotted out. Note that the original, high-resolution cubes were obtained using a robust weighting technique (Briggs 1995) with robust parameter $\Re \simeq 0$, thus they have relatively-low column-density sensitivity, but their beam profile is close to a Gaussian shape. We avoided using natural-weighted datacubes because the broad wings of their beam profiles may lead to spurious detections of diffuse emission, especially when the H I data are not cleaned down to the noise level (as is the case for the LITTLE-THINGS datacubes that are cleaned down to only 2.5σ, see Hunter et al. 2012).

Since we are interested in the large-scale, diffuse H I emission, it is important to accurately estimate the 3σ column density sensitivity of the total H I maps. The noise in a total H I map is not uniform but varies from pixel to pixel because at each spatial position one adds a different number of channel maps, given that only the pixels inside a given mask are considered. Following Verheijen & Sancisi (2001), we constructed signal-to-noise maps and calculated a pseudo-3σ column density contour $N(3\sigma)$ by averaging the values of the pixels with signal-to-noise ratio between 2.75 and 3.25. We also calculated the rms of these pixels and used it to estimate the typical uncertainty on $N(3\sigma)$. In particular, we halted our smoothing procedure when the value of $N(3\sigma)$ was equal to 1×10^{20} cm^{-2} within the errors. The derivation of the signal-to-noise maps is described in detail in Appendix 6.A.

Total H I fluxes were calculated from the smoothed maps, by considering only the pixels with a flux density higher than $0.5 \times N(3\sigma)$, that can be considered as a pseudo-1.5σ contour. The H I fluxes are in overall agreement

Table 6.3 – Properties of the H I datacubes.

Galaxy	Telescope	Source	Smoothed Beam		Ch. Sep.	Taper	Rms Noise	pseudo-$N(3\sigma)$	
			(asec×asec)	(pc×pc)	(km s^{-1})		(mJy/beam)	(10^{20} cm^{-2})	($M_\odot$ pc^{-2})
NGC 625	VLA	a	30.0×30.0	567×567	2.6	Hann.	2.6	1.1±0.5	0.9±0.4
NGC 1569	VLA	b	20.0×20.0	330×330	2.6	Hann.	1.1	1.6±0.7	1.3±0.6
NGC 1705	ATCA	c	20.0×20.0	494×494	3.5	Hann.	1.2	1.1±0.4	0.9±0.3
NGC 2366	VLA	b	20.0×20.0	310×310	2.6	Hann.	1.3	1.5±0.6	1.2±0.5
NGC 4068	WSRT	d	30.0×30.0	625×625	2.0	Unif.	4.4	1.4±0.5	1.2±0.4
NGC 4163	VLA	b	20.0×20.0	290×290	1.3	Hann.	1.3	0.9±0.3	0.8±0.3
NGC 4214	VLA	b	30.0×30.0	393×393	1.3	Hann.	3.0	1.2±0.6	1.0±0.5
NGC 4449	VLA	e	62.0×54.0	1262×1099	5.2	Hann.	1.3	∼0.7	∼0.6
NGC 5253	ATCA	f	40.0×40.0	679×679	9.0	Unif.	2.7	1.0±0.3	0.8±0.3
NGC 6789	WSRT	a	20.0×20.0	349×349	2.0	Unif.	1.3	1.0±0.3	0.8±0.3
UGC 4483	VLA	g	20.0×20.0	310×310	2.6	Hann.	1.6	1.1±0.3	0.9±0.3
UGC 6456	VLA	a	20.0×20.0	417×417	2.6	Hann.	2.4	1.6±0.7	1.3±0.6
UGC 6541	VLA	b	20.0×20.0	408×408	1.3	Hann.	1.8	1.4±0.4	1.2±0.3
UGC 9128	VLA	b	20.0×20.0	213×213	2.6	Hann.	1.6	1.3±0.4	1.0±0.3
UGCA 290	VLA	a	20.0×20.0	650×650	1.6	Unif.	2.0	1.1±0.3	0.9±0.3
I Zw 18	VLA	h	20.0×20.0	1765×1765	1.3	Hann.	1.0	1.0±0.6	0.8±0.4
I Zw 36	VLA	b	20.0×20.0	572×572	2.6	Hann.	1.9	1.3±0.4	1.0±0.3
SBS 1415+437	VLA	a	20.0×20.0	1319×1319	1.6	Unif.	2.8	1.3±0.3	1.0±0.3

References. (a) Chapter 4; (b) Hunter et al. (2012); (c) Elson et al. (2013); (d)Swaters et al. (2002); (e) Hunter et al. (1998); (f) López-Sánchez et al. (2012); (g) Ott et al. (2012); (h) Lelli et al. (2012a).

with those from single-dish observations: the differences are typically $\lesssim$15%, apart for two objects (NGC 1569 and UGC 6456) that are affected by Galactic emission. Our smoothed H I maps, therefore, recover most of the H I emission from the galaxy.

We also derived H I velocity fields by estimating an intensity-weighted mean (IWM) velocity from the masked datacube at the optimal resolution, clipping at 2σ and considering only the pixels within the pseudo-3σ contour of the total H I map. Since the H I profiles are broad and asymmetric, these low-resolution IWM velocity fields are uncertain and provide only an overall description of kinematics of the extended gas. For the 18 galaxies in our sample, a detailed analysis of the H I kinematics has been presented in Chapter 2 (Lelli et al. 2012a), Chapter 3 (Lelli et al. 2012b), and Chapter 4, and we refer to these Chapters for details.

6.3 The large-scale H I emission

In the following, we discuss the overall properties of the diffuse H I emission in our sample of starbursting dwarfs, while in Sect. 6.5 we describe each individual galaxy in detail. In Sect. 6.4, we introduce the asymmetry parameter A, that quantifies the H I morphology in the outer regions; A is then used to make a comparison with a control-sample of typical irregulars (Irrs) and to investigate the possible relations between the large-scale H I distribution and the starburst.

Figs 6.1 and 6.2 show the total H I maps of our 18 galaxies superimposed on optical images; in each map the iso-density contours correspond to 1, 4, and 16×10^{20} atoms cm^{-2}. In Fig. 6.1 each box has a physical size of 20×20 kpc, while in Fig. 6.2 the sizes of the boxes have been optimized to appreciate the details of each individual object. It is clear that the diffuse H I emission in BCDs presents a large variety of sizes and morphologies. Several galaxies show heavily disturbed H I distributions, characterized by large-scale asymmetries, long filaments, and/or a severe optical-H I offset (e.g. NGC 1569, NGC 1705, NGC 4449, UGC 6541, UGCA 290, I Zw 18, and I Zw 36). Other galaxies, instead, show lopsided H I morphologies, characterized by minor asymmetries and/or extensions in the outer parts (e.g. NGC 2366, NGC 4068, NGC 4214, UGC 4483, UGC 6456, UGC 9128, and SBS 1415+437). There is *not* a clear-cut separation between these two types of H I morphologies, since there are several "intermediate" cases that have relatively-regular H I distributions in the inner parts and small tails/filaments in the outer regions (e.g. NGC 625, NGC 4163, NGC 5253, and NGC 6789).

We estimated the extent of the H I distribution $E_{\rm H\,I}$ by measuring the projected distance between the optical center of the galaxy and the outermost pixel with an *observed* column density of 1×10^{20} atoms cm^{-2}. Note that $E_{\rm H\,I}$ is conceptually different from the H I radius $R_{\rm H\,I}$ (measured in Chapter 4), as the latter is defined as the radius where the azimuthally-averaged H I surface density

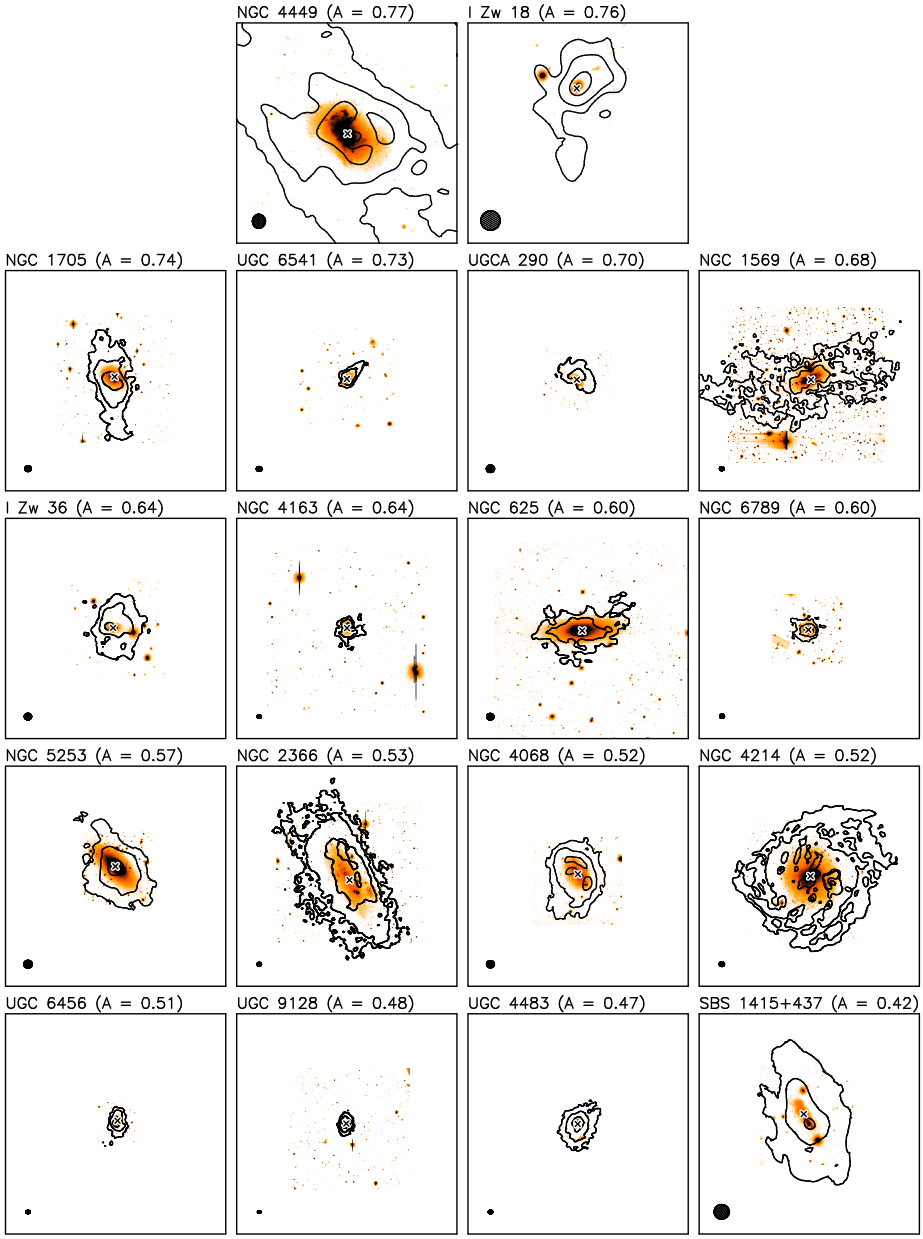

Figure 6.1 – Total H I maps for the 18 starbursting dwarfs in our sample, superimposed on optical images. Each box has a physical size of 20×20 kpc. The contours are at 1, 4, 16×10^{20} atoms cm^{-2}. The cross shows the optical center. The ellipse to the bottom-left shows the H I beam. The galaxies are ordered according to the value of the asymmetry parameter A (see Sect. 6.4 for details).

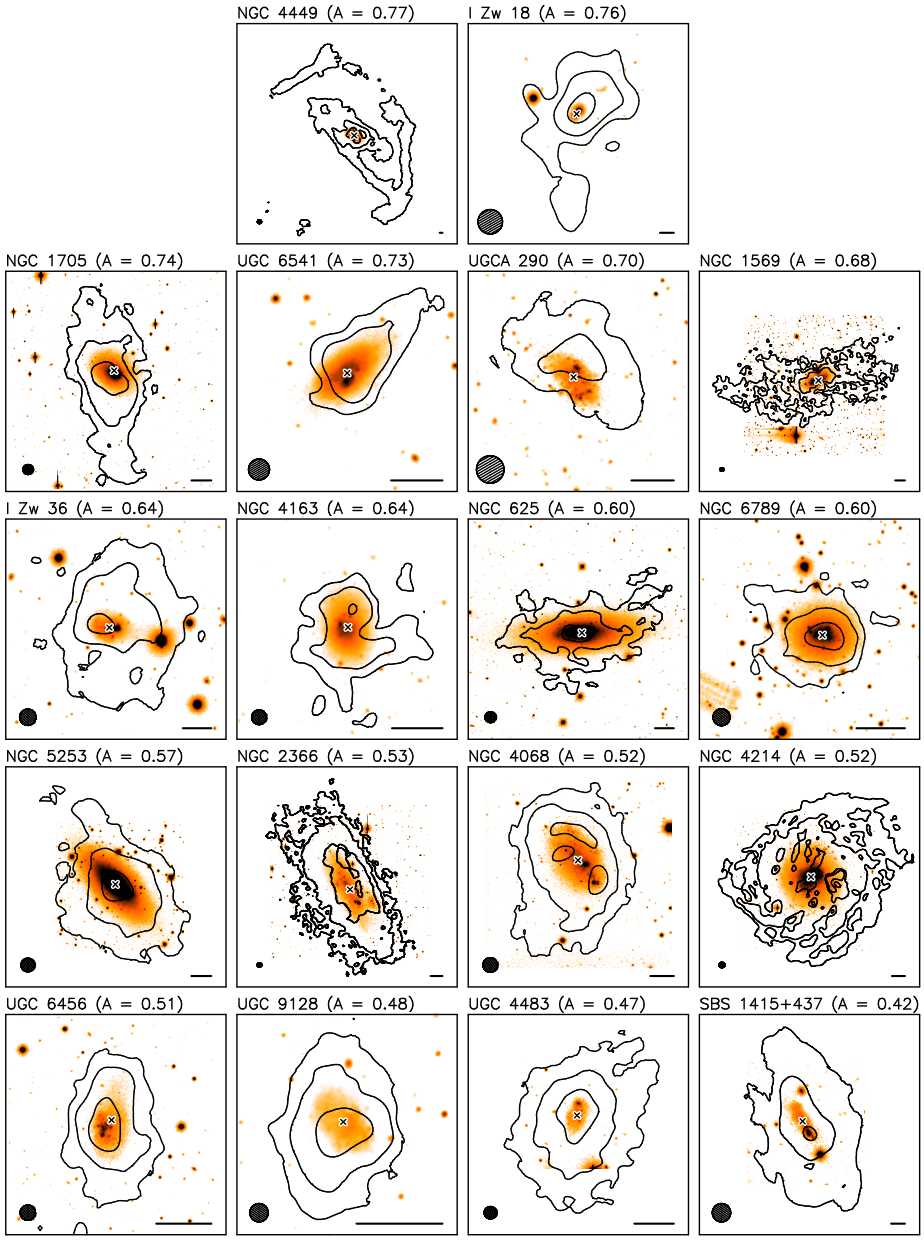

Figure 6.2 – Same as Fig. 6.1, but here the sizes of the boxes have been optimized to show the H I morphology of each galaxy in detail. The bar to the bottom-right corresponds to 1 kpc.

Table 6.4 – Properties of the large-scale H I emission.

Galaxy	$S_{\rm H\,I}$ (Jy km/s)	$M_{\rm H\,I}$ ($10^7 M_\odot$)	$E_{\rm H\,I}$ (amin)	(kpc)	$E_{\rm H\,I}/R_{\rm opt}$	$t_{E_{\rm H\,I}}$ (Gyr)	A
NGC 625	27.0	9.7±2.2	4.7	5.4	1.6	1.1	0.60
NGC 1569	106.6	29.1±4.5	10.8	10.7	3.6	1.3	0.68
NGC 1705	18.2	11.1±2.9	4.0	5.9	3.9	0.5	0.74
NGC 2366	254.8	62±17	10.1	9.4	2.1	1.1	0.53
NGC 4068	34.2	14.9±1.6	3.6	4.5	2.5	0.7	0.52
NGC 4163	7.2	1.5±0.2	2.3	2.0	2.0	1.2	0.64
NGC 4214	250.8	43±8	10.4	8.2	3.7	0.6	0.52
NGC 4449$^\alpha$	721.2	300±77	34.3	42	13	7.4	0.77
NGC 5253	47.6	13.8±3.4	4.6	4.7	2.2	...	0.57
NGC 6789	5.9	1.8±0.3	1.8	1.9	2.7	0.2	0.60
UGC 4483	12.0	2.9±0.5	2.7	2.5	4.2	0.8	0.73
UGC 6456	10.4	4.5±0.5	1.9	2.4	1.9	1.5	0.51
UGC 6541	2.8	1.2±0.2	1.9	2.3	2.5	...	0.73
UGC 9128	11.1	1.3±0.2	1.8	1.2	2.0	0.3	0.48
UGCA 290	1.35	1.4±0.2	1.1	2.1	2.3	...	0.70
I Zw 18	2.7	21±4	1.6	8.5	17	1.4	0.76
I Zw 36	8.2	6.7±1.3	1.9	3.3	3.7	0.7	0.64
SBS 1415+437	4.6	20.1±4.6	1.8	7.3	3.0	2.5	0.42

Notes. $^\alpha$the VLA data miss diffuse H I emission (Hunter et al. 1998), thus the values of $S_{\rm H\,I}$ and $M_{\rm H\,I}$ should be considered as lower limits.

profile (corrected for inclination) reaches 1 $M_\odot$ pc^{-2} ($\sim$1.2×10^{20} atoms cm^{-2}). Since $E_{\rm H\,I}$ is *not* obtained from an azimuthal average over the total H I map, it properly takes into account anomalous extensions in the H I distribution (such as tails or filaments), but may be affected by projection effects along the line of sight. Table 6.4 lists the values of $E_{\rm H\,I}$ and $E_{\rm H\,I}/R_{\rm opt}$, where the optical radius $R_{\rm opt}$ is the defined as 3.2 exponential scale-lengths (see Chapter 4) and is given in Table 6.1. For the 18 galaxies in our sample, $E_{\rm H\,I}/R_{\rm opt}$ ranges from $\sim$1.5 to $\sim$4, except for I Zw 18 ($E_{\rm H\,I}/R_{\rm opt} \simeq 17$) and NGC 4449 ($E_{\rm H\,I}/R_{\rm opt} \simeq 13$). These two objects show exceedingly extended H I tails with relatively-high column densities ($\sim 1-2\times10^{20}$ atoms cm^{-2}). Intriguingly, both I Zw 18 and NGC 4449 have a companion galaxy with $L_{\rm R} \simeq 0.5-1\times10^7\ L_\odot$ at a projected distance $\lesssim$ 10 kpc. For I Zw 18, there are strong indications that the extended H I emission is associated with the secondary body (see Lelli et al. 2012a). For NGC 4449, instead, the relation between the companion galaxy and the long H I filaments is unclear (see Martínez-Delgado et al. 2012).

Finally, we describe the kinematics of the large-scale H I emission. Figure 6.3 shows the velocity fields of our 18 galaxies; the size of each box is the same as in Fig. 6.2. As we stressed in Sect. 6.2, these velocity fields are uncertain due to the complex structure of the H I profiles, but they provide an overall

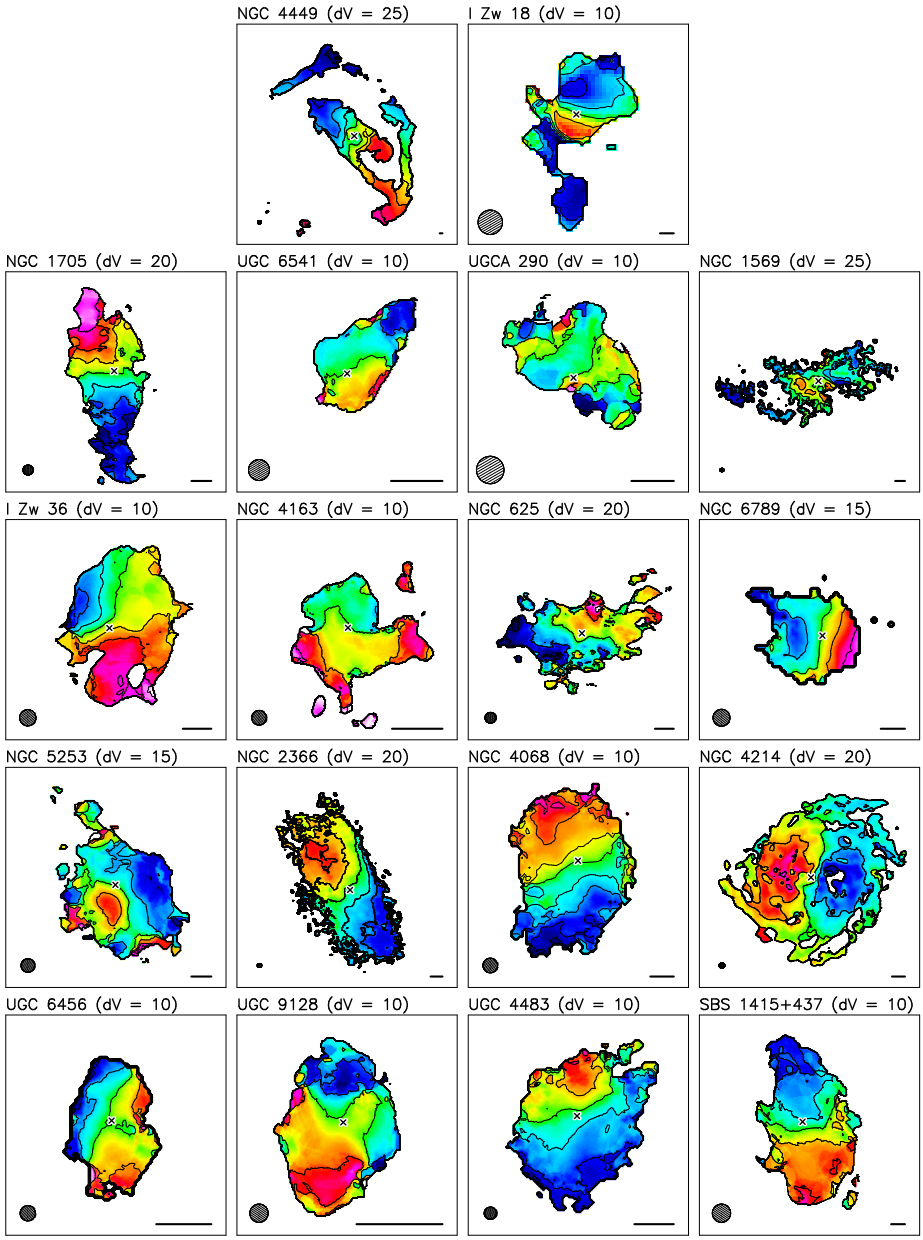

Figure 6.3 – Velocity fields for the 18 starbursting dwarfs in our sample, using the same box-sizes as in Fig. 6.2. The velocity separation *dV* between the contours is indicated. The cross shows the optical center. The ellipse to the bottom-left shows the H I beam. The bar to the bottom-right corresponds to 1 kpc.

description of the gas kinematics. For BCDs with a rotating H I disk, the outer gas is generally kinematically-connected to the inner H I distribution (except for I Zw 18, discussed in Lelli et al. 2012a). This suggests that the outer tails/extensions may be involved in the overall rotation and could possibly become regularized in a few orbital times. We calculated the orbital times $t_{\rm E_{H\,I}}$ at $E_{\rm H\,I}$ using the rotation velocities estimated in Chapter 4 (given in Table 6.1). These rotation velocities are typically estimated at $\sim$1 to 2 $R_{\rm opt}$, thus we are extrapolating their values to larger radii by assuming that the rotation curve is flat and the outer gas lies approximately in the same plane as the inner H I disk. The values of $t_{\rm E_{H\,I}}$ in Table 6.4, therefore, should be considered as order-of-magnitude estimates. Despite these uncertainties, the orbital times at $E_{\rm H\,I}$ are consistently of the order of $\sim$0.5 to 1 Gyr (except for NGC 4449 with $t_{\rm E_{H\,I}} \simeq 7$ Gyr), indicating that the outer asymmetries are relatively-recent and possibly short-lived (see also Sect. 6.4.3).

6.4 Quantifying the H I asymmetry

6.4.1 The asymmetry parameter

To investigate the relation between the large-scale H I emission and the starburst, it is desirable to quantify the degree of asymmetry/lopsidedness in the H I distribution of each individual galaxy. The infrared/optical morphologies of galaxies are usually quantified using the Concentration-Asymmetry-Smoothness (CAS) parameters (Conselice 2003) and the Gini-M_{20} parameters (Lotz et al. 2004). Recently, Holwerda et al. (2011a,b,c,d, 2013) used these parameters to quantify the H I morphologies in several samples of nearby galaxies. In particular, Holwerda et al. (2011c) used total H I maps from the WHISP survey and found that the CAS and Gini parameters weakly correlate with previous *visual* classifications of morphological lopsidedness (by Swaters et al. 2002 and Noordermeer et al. 2005). Particular combinations of the asymmetry parameter $\mathcal{A}$ and the Gini-M_{20} parameters, however, may be able to identify interacting galaxies (Holwerda et al. 2011a,d). Holwerda et al. (2013) used total H I maps at $\sim 5''$ resolution from LITTLE-THINGS (Hunter et al. 2012) and VLA-ANGST (Ott et al. 2012), and argued that the values of the CAS parameters do not strongly depend on the diffuse H I emission on large-scales, observed in total H I maps at lower spatial resolutions (see their Sect. 3.2 and Fig. 2). We consider here the asymmetry parameter $\mathcal{A}$. This is usually defined as

$$\mathcal{A} = \frac{\sum_{i,\,j} |I(i,j) - I_{180^\circ}(i,j)|}{\sum_{i,j} |I(i,j)|} \tag{6.1}$$

where $I(i,j)$ and $I_{180}(i,j)$ are, respectively, the flux densities of a pixel at position (i,j) in the original image and in an image rotated by 180° with respect to the galaxy center. This definition normalizes the residuals between

the original image and the rotated image to the total flux. It is clear, therefore, that asymmetries in the outer parts may have negligible weight in the sum, since the flux densities in the outer regions can be ∼2 orders of magnitude lower than those in the inner regions. Since we want to give more weight to the large-scale asymmetries in the outer parts, we define A as

$$A = \frac{1}{N} \sum_{i,j}^{N} \frac{|I(i,j) - I_{180^\circ}(i,j)|}{|I(i,j) + I_{180^\circ}(i,j)|} \tag{6.2}$$

where N is the total number of pixels in the image. This definiton normalizes the residuals at position (i, j) to the *local* flux density. In particular, if H I emission is detected only on one side of the galaxy, the residuals at (i, j) and $(i, j)_{180^\circ}$ get the maximum value $(= 1)$.

In Figs. 6.1 and 6.2, the total H I maps of our 18 galaxies are ordered according to their value of A. It is clear that A provides a reliable quantification of the H I asymmetry, in close agreement with our visual classification: galaxies with heavily-disturbed and/or strongly offset H I distributions have $A \gtrsim 0.6$, whereas galaxies with minor asymmetries and/or lopsided H I morphologies have $A \lesssim 0.6$. The value of A, however, depends on i) the assumed galaxy center, ii) the column density sensitivity of the H I observations, and iii) the spatial resolution in terms of both the actual beam-size in kpc and the relative number of beams across the H I map. In the following, we describe the effects of these factors on the value of A.

We adopted the optical centers derived in Chapter 4 and listed in Table 6.1. We did not consider the *kinematic* centers because 50% of the galaxies in our sample have either a kinematically-disturbed H I disk or an unsettled H I distribution, thus the kinematic parameters are either very uncertain or undefined (see Chapter 4). Moreover, the use of the optical center correctly returns high values of A for galaxies that show a strong offset between the H I distribution and the stellar body (e.g. NGC 1705 and UGCA 290), that may indicate a recent interaction/accretion event. We checked that small changes in the value of the centers ($\sim 2''$) do not significantly affect the value of A (the differences are $\lesssim 0.05$). This is expected because i) the typical uncertainties on the position of the optical center ($\sim 1''$ to $2''$) are much smaller than the H I beam ($\gtrsim 20''$), and ii) high-column-density asymmetries in the inner parts, given our definition of A, do not have much weight.

Regarding the column density sensitivity, the values of A listed in Table 6.4 have been calculated considering only pixels with $N_{\rm H\,I} \geq 10^{20}$ cm^{-2}, since this corresponds to the pseudo-3σ contour of our total H I maps (see Sec. 6.2 and Appendix 6.A). To test the effect of this column density threshold, in Fig. 6.4 (top) we compare the values of A obtained by considering thresholds of 1 and $2{\times}10^{20}$ cm^{-2}. The differences in A are within ∼0.1 and do not show a systematic trend, implying that the detailed shape of the outermost contour in the total H I map does not strongly affect the value of A. We warn, however,

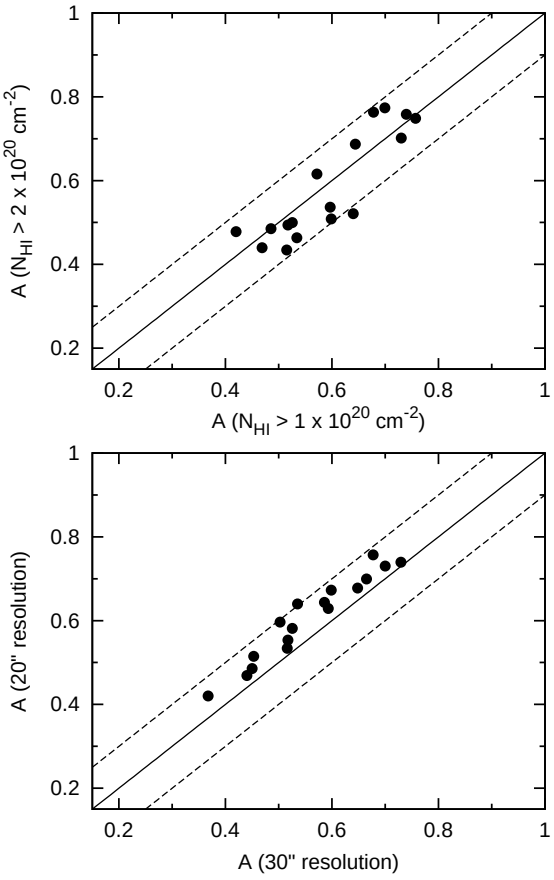

Figure 6.4 – The dependence of the asymmetry parameter A on the $N_{\rm H\,I}$-treshold (*top*) and the spatial resolution of the total H I maps (*bottom*). In the top panel, dots show the values of A obtained from the total H I maps in Figs. 6.1 and 6.2, using a $N_{\rm H\,I}$-treshold of 1 and 2×10^{20} atoms cm^{-2}. In the bottom panel, dots show the values of A using H I maps at $20''$ and $30''$, and a fixed $N_{\rm H\,I}$ of 10^{20} atoms cm^{-2}. The solid line corresponds to a null variation in the value of A, whereas the dashed lines correspond to variations of ± 0.1. See Sect. 6.4.1 for details.

that the use of a column-density threshold provides reliable results as long as i) one does *not* consider values much below the pseudo-3σ contour, introducing noise in the total H I maps, and ii) one does *not* consider high column density thresholds (e.g. $N_{\rm H\,I} \gtrsim 5 - 10 \times 10^{20}$ cm^{-2}), probing the small-scale clumpiness of the H I distribution. We also note that, when using a fixed column-density treshold for different galaxies, the inclination i of the H I disk may introduce some systematic effects, given that *projected* column densities correspond to different *face-on* surface densities. For an optically-thin H I disk, the projected column-density increases with $1/\cos(i)$, thus inclination effects on the column-density threshold become important only in edge-on disks with $i \gtrsim 70°$, for which projected column densities of $\sim 1 \times 10^{20}$ cm^{-2} would correspond to face-on surface densities that are lower by a factor $\gtrsim 3$. In our galaxy sample, the inclinations of the H I disks are $\lesssim 70°$ (see Chapter 4), thus projection effects are not a serious concern here.

The spatial resolution of the H I observations deserves some attention in the derivation of A. To quantify the effects of beam smearing, we constructed total H I maps at 20″ and 30″ resolution for all the galaxies in our sample (except for NGC 4449 that has H I data at a native resolution of ∼60″). The respective values of A, calculated using a threshold of $1{\times}10^{20}$ cm^{-2}, are compared in Fig. 6.4 (bottom). As expected, total H I maps at higher resolutions systematically yield higher values of A. The differences in A, however, appear reasonably small (within 0.1). Galaxies with a small number of beams along the major axis of the H I disk (e.g. NGC 4163, NGC 6789, I Zw 18) typically show the largest differences in A (∼0.1), whereas galaxies with well-resolved H I maps (e.g. NGC 2366, NGC 1569, and NGC 4214) show very small differences ($\lesssim$0.03). For the latter galaxies, a severe smoothing of the H I data down to 60″ (a factor 3) would still give differences in $A \lesssim 0.1$. Thus, we draw the following conclusions: i) to have a reliable estimate of A, one needs at least ∼5 resolution elements along the major axis of the total H I map, and ii) when the previous condition is met, differences in spatial resolution by a factor of ∼3 give relatively-small differences in A ($\lesssim 0.1$). The total H I maps in Figs. 6.1 and 6.2 are all reasonably well-resolved and have linear resolutions ranging from ∼0.3 to ∼0.7 kpc (see Table 6.3), thus it makes sense to compare the relative values of A. Exceptions are NGC 4449, I Zw 18, and SBS 1415+437, that have total H I maps with linear resolutions $\gtrsim$1 kpc. Despite the low linear resolution, NGC 4449 and I Zw 18 show the highest values of A in our sample, indicating that data at higher resolutions would only increase the difference with the other galaxies. On the contrary, SBS 1415+437 has the lowest value of A in our sample (see Figs. 6.1 and 6.2); this may be an effect of beam-smearing, thus the value of A for SBS 1415+437 may be slightly underestimated with respect to those of other galaxies. We did not build total H I maps at the same linear resolution (in kpc) for all the galaxies because it is not possible to find a compromise between the required number of beams along the H I major axis ($\gtrsim 5$ in order to have a proper estimate of A) and the 3σ column density sensitivity ($\lesssim 1 \times 10^{20}$ in order to probe the outer, diffuse H I emission).

6.4.2 Comparison with typical irregulars

In this section, we estimate A for a sample of typical Irrs, and make a comparison with our sample of starbursting dwarfs. We use total H I maps from the VLA-ANGST survey (Ott et al. 2012), which provides multi-configuration VLA observations for 29 low-mass galaxies included in the *Advanced Camera for Surveys Nearby Galaxy Survey Treasury* (ANGST; Dalcanton et al. 2009). Similarly to our 18 starbursting dwarfs, these Irrs have been resolved into single stars by HST, and SFHs are available for most of them (Weisz et al. 2011). In order to have two galaxy samples that span a similar range of stellar and H I masses, we excluded objects with $M_{\rm B} \lesssim -11$ (nearly equivalent to $M_* \lesssim 10^7$ M$_\odot$), given that such very low-mass dwarfs are not present in our

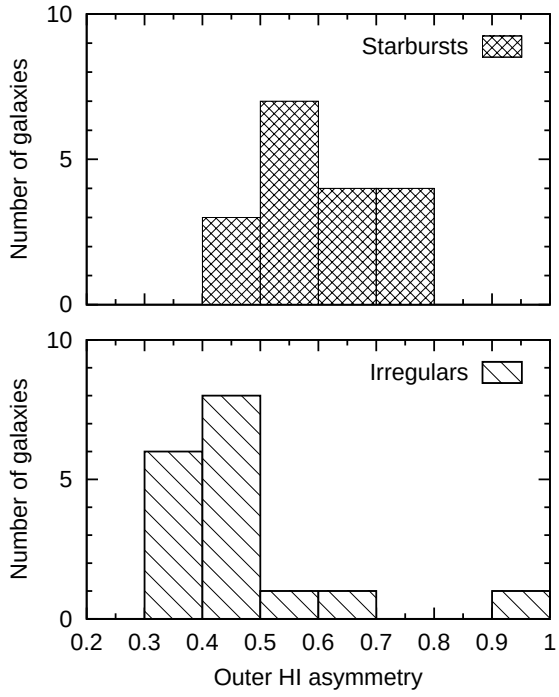

Figure 6.5 – The asymmetry parameter A for our sample of 18 starbursting dwarfs and for a control-sample of 17 typical Irrs, drawn from the VLA-ANGST survey. Starbursting dwarfs clearly have more asymmetric H I morphologies in the outer parts than typical Irrs of similar masses. See Sect. 6.4.2

sample of BCDs. We also excluded AO 0952+69 (Arp's loop), that may be a feature in the spiral arm of M81 (Ott et al. 2012), or a tidal dwarf galaxy (Weisz et al. 2011). The VLA-ANGST sample also contains 3 starbursting dwarfs that are included in our sample (NGC 4163, UGC 4483, and UGC 9128), which we use to test the consistency between our total H I maps and the VLA-ANGST ones. Our final control-sample of typical Irrs, therefore, contains 17 galaxies. Since the SFHs from Weisz et al. (2011) have been obtained by averaging the SFR over a single time-bin in the last $\sim$1 Gyr, we cannot check whether these galaxies have a recent birthrate parameter $b \lesssim 3$, confirming that they are non-starbursting Irrs. However, as far as we are aware of, these 17 galaxies do not show any sign of recent starburst activity and, thus, we consider them representative for quiescent Irrs.

The natural-weighted H I maps from VLA-ANGST have both an adequate number of resolution elements along the H I major axis, and a 3σ column density sensitivity $\lesssim 10^{20}$ cm^{-2} (see Ott et al. 2012), thus we can safely calculate A using a column-density threshold of 10^{20} cm^{-2} (as for our starbursting dwarfs). The linear resolutions of these H I maps range from $\sim$60 to $\sim$200 pc, significantly higher compared to our own H I maps (cf. with Table 6.3). As we discussed in Sect. 6.4.1, this could imply that the values of A for the starbursting dwarfs may be slightly underestimated with respect to those of the VLA-ANGST Irrs.

For UGC 4483 and UGC 9128, however, the VLA-ANGST H I maps and our total H I maps yield remarkably consistent results: UGC 4483 has $A = 0.469$ from our map and $A = 0.464$ from the VLA-ANGST one, while UGC 9128 has $A = 0.485$ from our map and $A = 0.480$ from the VLA-ANGST one. NGC 4163, instead, shows a significant discrepancy: our map yields $A = 0.64$ while the VLA-ANGST one returns $A = 0.50$. The VLA-ANGST map of NGC 4163, indeed, does not trace the full extent of the H I tail to the West and does not detect the cloud complexes to the South (compare our Fig. 6.2 with Fig. 18 of Ott et al. 2012). This is likely due to a different masking of the H I emission for the derivation of the total H I map. We are confident that these H I features are real given that they have been detected also by Swaters et al. (2002) using WSRT data.

Fig. 6.5 compares the values of A for our sample of starbursting dwarfs with those for the VLA-ANGST sample of typical Irrs. Clearly, starbursting dwarfs have systematically higher values of A than typical Irrs: the mean and median values of A are, respectively, 0.60 ± 0.10 and 0.60 for the sample of BCDs, and 0.47 ± 0.16 and 0.41 for the control-sample of Irrs. Moreover, since the total H I maps of the BCDs have lower linear resolutions than those of Irrs, the difference between the two samples may be even larger. Given the possible effects of beam smearing on A, we did not perform a statistical analysis of the two distributions (e.g. using a Kolmogorov-Smirnoff test). It is clear, however, that BCDs generally have more asymmetric H I morphologies in their outer regions than typical Irrs, suggesting that some *external mechanism* triggered the starburst. The two samples have some overlap between $0.4 \lesssim A \lesssim 0.6$ due to the presence of Irrs with lopsided H I morphologies. This is not surprising, as lopsidedness is a common phenomenon among gas-rich galaxies (e.g. Swaters et al. 2002).

Two galaxies from the control-sample have very high values of A, comparable with those of the most disturbed BCDs. These objects are NGC 404 ($A = 0.67$) and DDO 6 ($A = 1$). NGC 404 is at the high-mass end of the dwarf classification ($M_{\rm B} \simeq -16.2$) and shows an unusual lenticular morphology for a dwarf galaxy. Several authors (e.g. Thilker et al. 2010) argued that NGC 404 may have experienced a merger in the last $\sim$1 Gyr, given that it shows a very extended, outer H I ring (del Río et al. 2004); recent, low-level star-formation along the ring (Thilker et al. 2010); a counter-rotating, inner stellar core (Bouchard et al. 2010); and may also host an intermediate mass black hole (Binder et al. 2011). Considering all these facts, the relatively-high value of A may not be surprising, and demonstrates that our definition of A can successfully identify past interacting/merging systems. Regarding DDO 6, both Skillman et al. (2003) and Weisz et al. (2011) classified this object as a "transition" dwarf, i.e. a low-mass galaxy with detected H I emission but little or no Hα flux (Mateo 1998). In DDO 6, H I emission is detected only to the southern part of the galaxy (similarly to UGC 6541 in our sample), hence the galaxy has

an extremely high value of A. It would be interesting to investigate whether this galaxy has experienced a recent starburst. Intriguingly, the well-studied "transition" dwarf Antlia in the Local Group has been classified as a starburst by McQuinn et al. (2012), and shows a H I distribution similar to DDO 6 and UGC 6541 (see Ott et al. 2012; Antlia is not included here because it has $M_{\rm B} \lesssim -11$).

6.4.3 H I asymmetries versus starburst properties

We now investigate the possible relations between A and the properties of the starburst as derived from the HST studies of the resolved stellar populations. We consider the following quantities (see Table 6.2):

1. the birthrate parameter $b = {\rm SFR_p}/\overline{\rm SFR}_{0-6}$, where $\rm SFR_p$ is the peak SFR over the past 1 Gyr and $\overline{\rm SFR}$ is the average SFR over the past 6 Gyrs (see McQuinn et al. 2010);

2. the peak SFR surface density $\Sigma_{\rm SFR}(t_{\rm p}) = {\rm SFR_p}/(\pi R_{\rm opt}^2)$, where the optical radius $R_{\rm opt}$ is defined as 3.2 exponential scale-lengths (see Chapter 4 and Swaters et al. 2002);

3. the recent SFR surface density $\Sigma_{\rm SFR}(0) = {\rm SFR_0}/(\pi R_{\rm opt}^2)$, where $\rm SFR_0$ is the average SFR over the last 10 Myr;

4. the specific SFRs (sSFRs) given by ${\rm SFR_0}/M_*$ and ${\rm SFR_p}/M_*$;

5. the look-back time $t_{\rm p}$ at $\rm SFR_p$.

In particular, $t_{\rm p}$ allows us to distinguish between "old" bursts (with $t_{\rm p} \gtrsim 100$ Myr) and "young" bursts (with $t_{\rm p} \lesssim 100$ Myr), and can be considered as the typical "age" of the starburst. The SFHs of 5 galaxies (NGC 2366, NGC 4068, UGC 4483, UGC 9128, and SBS 1415+437) show two distinct peaks with similar SFRs (consistent within 1σ). In these cases, we consider the SFR and the look-back time of the older peak, since this is the one that formed more stars, given that the SFR is averaged over a larger time-bin (typically a factor of $\sim$4, see McQuinn et al. 2010). For UGC 6541 and I Zw 36, the recent SFHs are not well constrained (see Schulte-Ladbeck et al. 2000, 2001), thus we have no robust estimate of $\Sigma_{\rm SFR}(t_{\rm p})$, ${\rm sSFR_p}$, and $t_{\rm p}$.

Fig. 6.6 shows that there are no strong trends between A and the SFR indicators $\Sigma_{\rm SFR}(0)$, $\Sigma_{\rm SFR}(t_{\rm p})$, sSFR(0), or ${\rm sSFR}(t_{\rm p})$. We also found no correlation with b. The lack of any real trend has been tested by calculating the Pearson's correlation coefficient $\rho_{\rm cc}$, where $\rho_{\rm cc} = \pm 1$ for an ideal linear correlation/anticorrelation, whereas $\rho_{\rm cc} = 0$ if no correlation is present. We found values of $\rho_{\rm cc} \simeq 0.3$ to 0.4, except for the $A - \Sigma_{\rm SFR}(t_{\rm p})$ diagram that yields $\rho_{\rm cc} \simeq 0.6$. In particular, the 3 galaxies with the highest values of A (NGC 4449, I Zw 18, and NGC 1705) also have the highest values of $\Sigma_{\rm SFR}(t_{\rm p})$ and $\Sigma_{\rm SFR}(0)$.

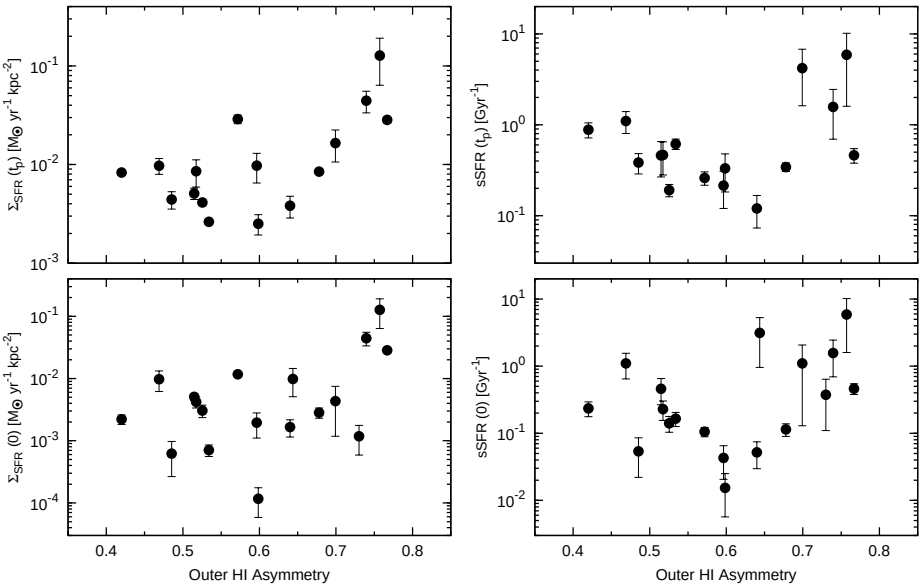

Figure 6.6 – The asymmetry parameter A versus the current SFR surface density $\Sigma_{\rm SFR}(0)$ (*top-left*), the peak SFR surface density $\Sigma_{\rm SFR}(t_{\rm p})$ (*bottom-left*), the current specific SFR (*top-right*), and the peak specific SFR (*bottom-right*). See Sect. 6.4.3 for details.

In these three cases, $t_{\rm p} \simeq 10$ Myr, thus $\Sigma_{\rm SFR}(t_{\rm p}) \simeq \Sigma_{\rm SFR}(0)$. Fig. 6.7 (left) shows that a very clear trend is present between A and $t_{\rm p}$ ($\rho_{\rm cc} \simeq -0.7$): galaxies hosting a "young" burst generally have a more asymmetric H I distribution than galaxies hosting an "old" one, further suggesting a close link between the outer, disturbed gas morphology and the central, recent starburst activity. Galaxies with minor asymmetries ($A \lesssim 0.6$) have values of $t_{\rm p} \simeq 500$ Myr (apart for UGC 6456), which are comparable within a factor of $\sim$2 with the orbital times $t_{\rm E_{H\,I}}$ at the outermost radii $E_{\rm H\,I}$. This is shown in Fig. 6.7 (right), where we plot A against the ratio $t_{\rm p}/t_{\rm E_{H\,I}}$. We recall, however, that $t_{\rm E_{H\,I}}$ is an order-of-magnitude estimate, thus the ratio $t_{\rm p}/t_{\rm E_{H\,I}}$ provides only a rough measure of the number of orbits that the outer gas may have completed since the epoch of the strongest star-formation activity. Despite these uncertainties, Fig. 6.7 (right) clearly indicates that galaxies hosting an "old" burst may have had enough time to complete an entire revolution around their center and, therefore, to regularize their outer H I distribution.

Finally, we discuss in some detail the "outlier" UGC 6456 (VII Zw 403) indicated in Fig. 6.7. This galaxy has been recently studied by Simpson et al. (2011), who pointed out the relatively-regular H I morphology and the lack of a clear external trigger. The total H I map and velocity field of Hunter et al. (2012), however, show a tail/extension to the South-West. We also detected this

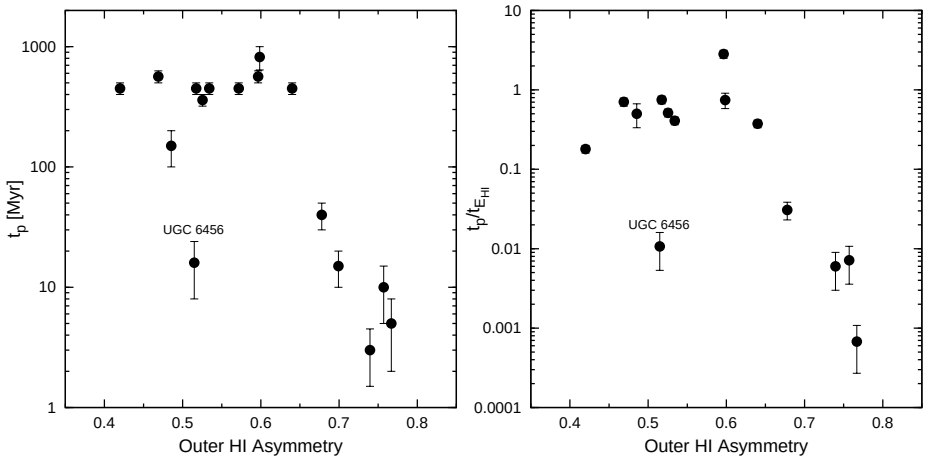

Figure 6.7 – The asymmetry parameter A versus the look-back time $t_{\rm p}$ at the peak of the SFH (*left*) and the ratio $t_{\rm p}/t_{\rm E_{H\,I}}$. See Sect. 6.4.3 for details.

feature in our total H I map, but it is below the 3σ column density sensitivity of the observations, having $N_{\rm H\,I} \lesssim 5 \times 10^{19}$ cm^{-2}. Deeper H I observations are needed to confirm whether this H I tail is real or an observational artefact. The location of UGC 6456 in Figs. 6.6 and 6.7 would change if one adopts column-density thresholds $\lesssim 5 \times 10^{19}$ cm^{-2}, but unfortunately these low values cannot be consistently adopted here due to the limited sensitivity of the H I observations for several galaxies in our sample.

6.5 Individual galaxies and their environment

In the following, we discuss in detail the H I properties of individual galaxies, and describe their nearby environment. We used the NASA/IPAC Extragalactic Database (NED[1]) to search for nearby galaxies with measured redshifts in a velocity range of $\pm$300 km s^{-1} with respect to the systemic velocity of the starbursting dwarf. Table 6.5 provides the 3 nearest galaxies to each BCD in our sample, together with their basic properties (from Karachentsev et al. 2013). We checked that these objects are actual galaxies by visual inspection, and excluded background/foreground galaxies when accurate, redshift-independent distances were available. Since most of the BCDs considered here have distances $D \lesssim$ 7 Mpc, Table 6.5 should be nearly complete down to dwarf galaxies with total magnitudes $M_{\rm B} \simeq -11$ and mean surface brightnesses $\mu_{\rm B} \simeq 25$ mag arcsec^{-2} (cf. with Karachentsev et al. 2004, 2013). Any galaxy with $M_{\rm B} \gtrsim -10$ would

[1]The NASA/IPAC Extragalactic Database (NED) is operated by the Jet Propulsion Laboratory, California Institute of Technology, under contract with the National Aeronautics and Space Administration.

be more than 10 times less massive than the BCDs in our sample, which have $M_{\rm R} \lesssim -14$ ($M_{\rm B} \lesssim -13$), thus it would probably be unable to induce the strong burst of star-formation. UGC 4483 and UGC 9128 have somewhat fainter luminosities ($M_{\rm R} \simeq -13$) but they are very nearby ($D \lesssim 3$ Mpc), thus possible companions with total magnitudes as low as $M_{\rm B} \simeq -10$ should be catalogued. SBS 1415+437 and I Zw 18, instead, are at distances of ∼14 Mpc and ∼18 Mpc, respectively, thus they may have faint companions that have not been identified by optical surveys. Note that an object with a proper velocity of ∼200 km s^{-1} (out of the Hubble flow) covers ∼200 kpc in 1 Gyr, thus one cannot exclude the possibility that a galaxy at a projected distance $D_{\rm p} \lesssim 200$ kpc from a BCD might have triggered the staburst by a past collision on an hyperbolic orbit (see e.g. Noguchi 1988). Most of the BCDs in our sample have such a potential perturber, except for NGC 1705, NGC 6789, and UGC 9128. Note that typical Irrs often have companions at $D_{\rm p} \lesssim 200$ kpc, thus one cannot claim that the presence of a companion is a *sufficient* condition for a starburst to occur.

Table 6.5 – Environment of the starbursting dwarfs in our sample. The projected distance $D_{\rm p}$ from the nearest galaxies and the difference between their respective systemic velocities $\Delta V_{\rm sys}$ were calculated using NED. The properties of the nearest galaxies are taken from Karachentsev et al. (2013), and given only when their distances are accurately estimated from the TRGB (the distance of NGC 2403 is estimated from Cepheids). Note that objects without an accurate distance estimate may be background/foreground galaxies. The properties of I Zw 18 C are taken from Lelli et al. (2012a). The morphological types are taken from both NED and Karachentsev et al. (2013).

Galaxy	Membership	Nearest galaxies	$D_{\rm p}$ (kpc)	$\Delta V_{\rm sys}$ (km s^{-1})	Type	Dist (Mpc)	$M_{\rm B}$ (mag)	$\log(M_{\rm H\,I})$ (10^7)	$W_{50,\,\rm H\,I}$ (km s^{-1})
NGC 625	Sculptor group	ESO245-005	203	−7	Im	4.4	-15.6	8.58	60
	(periphery)	CFC97 Sc 24$^{\alpha}$	402	-236	...	...	...	...	92
		GSD 106	619	132	...	...	...	...	...
NGC 1569	IC 432 group	UGCA 92	74	19	Irr	3.0	-15.6	8.17	56
		Cam B	190	157	Irr	3.3	-11.9	7.08	21
		UGCA 86	231	147	Im?	3.0	-17.9	...	...
NGC 1705	Field	LSBG F157-089$^{\beta}$	518	175	...	...	...	...	...
		MRSS 157-121650$^{\gamma}$	562	-50	...	...	...	...	...
		SGC 0409.0-5638	631	242	Irr	...	...	...	...
NGC 2366	M81 group	NGC 2363$^{\delta}$	2	-33	Irr	...	...	...	...
	(periphery)	NGC 2403	206	30	Scd	3.2	-19.2	9.26	240
		Holmberg II	254	39	Im	3.4	-16.7	8.61	64
NGC 4068	CVn I cloud	MCG +09-20-131	135	-47	Irr	4.6	-13.1	7.37	27
		ASK 185765.0$^{\epsilon}$	143	291	...	...	...	...	...
		UGC 7298	145	-33	Irr	4.2	-12.3	7.28	21
NGC 4163	CVn I cloud	MCG +06-27-017$^{\zeta}$	27	181	Im	4.8	-13.0	...	...
		NGC 4190	29	70	Im/BCD	2.8	-13.9	7.46	49
		DDO 113	30	126	Sph?	2.9	-11.5	< 5.56	32
NGC 4214	CVn I cloud	DDO 113	8	-7	Sph?	2.9	-11.5	< 5.56	...
		NGC 4190	23	-63	Im/BCD	2.8	-13.9	7.46	49
		NGC 4163	34	-133	BCD	3.0	-13.8	7.16	32
NGC 4449	CVn I cloud	DDO 125	44	-15	Im	2.7	-14.3	7.48	27
		MCG +07-26-012	77	226	Im	...	...	...	...
		DDO 120	155	252	Im	...	...	...	...

Table 6.5 – continued.

Galaxy	Membership	Nearest galaxies	$D_{\rm p}$ (kpc)	$\Delta V_{\rm sys}$ (km s^{-1})	Type	Dist (Mpc)	$M_{\rm B}$ (mag)	$\log(M_{\rm H\,I})$ (10^7)	$W_{50,\,\rm H\,I}$ km s^{-1}
NGC 5253	M83 group	ESO444-084$^{\eta}$	54	116	Sc	...	...	...	...
		NGC 5264	108	68	Im	4.5	-15.9	7.65	35
		HIDEEP J1337-33	111	181	Irr	4.4	-11.1	6.67	20
NGC 6789	Local Void	ABELL 2312:[MPC97] 04$^{\theta}$	297	59	...	...	...	...	...
		UGC 11411	400	220	BCD	...	...	...	...
		LEDA 166193	578	290	Irr	...	...	...	28
UGC 4483	M81 group	M81 Dwarf A	92	-45	Irr	3.5	-11.5	7.06	21
		Holmberg II	100	-16	Im	3.4	-16.7	8.61	64
		DDO 53	201	-138	Irr	3.6	-13.4	7.62	30
UGC 6456	M81 group	CGCG 351-049$^{\iota}$	151	8	...	...	...	...	...
	(periphery)	UGC 8245$^{\iota}$	358	172	Im	...	...	...	...
		DDO 82	683	158	Im	4.0	-14.7	...	...
UGC 6541	CVn I cloud	ASK 184683.0	213	208	...	...	...	...	...
	(periphery)	ASK 185765.0$^{\epsilon}$	289	247	...	...	...	...	...
		NGC 3741	292	-21	Im/BCD	3.0	-13.1	7.88	83
UGC 9128	Field	LSBG F650-01$^{\kappa}$	353	-167	...	...	...	...	...
		MAPS O-383-0548118$^{\lambda}$	359	-93	...	...	...	...	...
		SDSS J145657.7+221315$^{\lambda}$	365	-102	...	...	...	...	...
UGCA 290	NGC 4631 group?	UGC 7719	83	210	Sdm	...	...	...	57
		IC 3687	115	114	Im	4.6	-14.6	7.90	36
		BTS 142	122	251	Irr	...	...	...	23
I Zw 18	Field	I Zw 18 C	2	-16	Irr	18.2	-12.1	$\lesssim 8.08$	$\sim$45
		ASK 153750.0	639	243	...	...	...	...	...
		MGC +09-16-029	1052	-159	...	...	...	...	...
I Zw 36	CVn I cloud	UGC 7639$^{\mu}$	117	105	Im	...	...	...	...
		NGC 4248$^{\nu}$	183	207	...	...	...	...	...
		MAPS O-171-0165792	214	195	...	...	...	...	...

Table 6.5 – continued.

Galaxy	Membership	Nearest galaxies	$D_{\rm p}$ (kpc)	$\Delta V_{\rm sys}$ (km s^{-1})	Type	Dist (Mpc)	$M_{\rm B}$ (mag)	$\log(M_{\rm H\,I})$ (10^7)	$W_{50,\,\rm H\,I}$ km s^{-1}
SBS 1415+437	Field	MAPS O-221-0093662	179	105	...	...	...	...	...
		ASK 310753.0	492	18	...	...	...	...	...
		NGC 5608	493	47	Im	...	...	...	...

Notes. $^{(\alpha)}$ According to Karachentsev et al. (2004), this galaxy is not in the Sculptor group but lie outside the Local Volume. The value of $W_{50,\,\rm H\,I}$ is taken from Cote et al. (1997).
$^{(\beta)}$ This galaxy may be in the Dorado group ($D \simeq 17$ Mpc, Firth et al. 2006).
$^{(\gamma)}$ This object may be an ultra-compact dwarf in the Dorado group ($D \simeq 17$ Mpc, Evstigneeva et al. 2007).
$^{(\delta)}$ It is unclear whether this object is part of NGC 2366 or a separate galaxy (see Fig. 6.8).
$^{(\epsilon)}$ Trentham et al. (2001) included this galaxy in their study of the Ursa Major cluster. However, ASK 185765.0 is probably not a cluster member, given that its systemic velocity is $\sim$497 km s^{-1} (from the Sloan Digital Sky Survey).
$^{(\zeta)}$ Despite this galaxy is close to NGC 4163 on the sky, it seems to inhabit a more distant part of the CnV I cloud, having a distance of $\sim$4.8 Mpc from the TRGB.
$^{(\eta)}$ This edge-on spiral is not a member of the M83 group and probably is a background galaxy.
$^{(\theta)}$ This object is classified as a galaxy by NED. It is projected on the sky near the galaxy cluster ABELL 2312 (Maurogordato et al. 1997), but its systemic velocity indicates that it is a nearby object. In our opinion, it is unclear whether this is a galaxy or a Galactic object.
$^{(\iota)}$ This object is not associated to the M81 group and may be a background/foreground galaxy.
$^{(\kappa)}$ According to NED, this object may be a planetary nebula.
$^{(\lambda)}$ This object has also been classified as a X-ray source and a star.
$^{(\mu)}$ This object may have $D \simeq 7.1$ Mpc (from surface brightness fluctuations, Karachentsev et al. 2013) and be outside the CVn I cloud.
$^{(\nu)}$ This object may have $D \simeq 7.4$ Mpc (from the Tully-Fisher relation, Karachentsev et al. 2013) and be outside the CVn I cloud.

NGC 625 has a ∼2 kpc H I tail to the North-West, that shows a coherent kinematic structure at $V_{\rm los} \simeq 420$ km s^{-1}. A second tail/extension is present to the South-East, but it does not show a clear kinematic structure. Our total H I map and velocity field are in close agreement with those from Côté et al. (2000) and Cannon et al. (2004). NGC 625 is associated with the core of the Sculptor filament, but it is quite far from the central, massive galaxy NGC 253, being at a projected distance of ∼1.3 Mpc (Karachentsev 2005).

NGC 1569 has a heavily disturbed H I distribution. A H I cloud with $M_{\rm H\,I} \simeq 2 \times 10^7$ M$_\odot$ lies at $V_{\rm los} \simeq -150$ km s^{-1} to the East of the galaxy, and is connected to the main H I distribution by a thin bridge (see also Stil & Israel 1998). The datacube is strongly affected by Galactic emission, thus the total H I map and the velocity field are uncertain. Our results, however, are in close agreement with those from Stil & Israel (1998, 2002) and Johnson et al. (2012). NGC 1569 is part of the IC 432 group of galaxies (Grocholski et al. 2008) and has a nearby companion (UGCA 92) at a projected distance of ∼70 kpc with a similar systemic velocity (within ∼20 km s^{-1}).

NGC 1705 has an extended, warped H I disk. The H I disk has a relatively-regular morphology and kinematics, but it is strongly offset with respect to the stellar component: the optical and kinematic centers differ by ∼550 pc, while the optical and kinematic PAs differ by ∼45° (see Chapter 4). To the North-East, there is also a small H I extension with peculiar kinematics, that may be associated with the Hα wind (see Meurer et al. 1998; Elson et al. 2013). NGC 1705 appears very isolated: the two nearest objects (LSBG F157-089 and MRSS 157-121650) are at a projected distance of ∼0.5 Mpc, but may be members of the Dorado group at $D \simeq 18$ Mpc (see Firth et al. 2006 and Evstigneeva et al. 2007, respectively). Three other objects (NGC 1533, IC 2038, and IC 2039) lie at ∼7° from NGC 1705, but they seem to be background galaxies at distances of ∼20 Mpc (based on the TF relation).

NGC 2366 has a H I disk with a broad extension to the South-East and a strong kinematic distortion to the North-West. Fig. 6.8 (left) shows an optical image overlaid with the H I emission at 15″ resolution, integrated in a narrow spectral range near the systemic velocity (between ∼90 and ∼115 km s^{-1}). The gas to the North-West does not follow the rotation of the H I disk (see also Fig. 3 of Oh et al. 2008) and may be associated with the secondary star-forming body to the South-West (NGC 2363). Fig 6.8 (right) shows a Position-Velocity diagram taken along the dashed-line in Fig. 6.8 (left). Intriguingly, the PV-diagram displays a steep velocity gradient that coincides with the spatial position and optical systemic velocity of NGC 2363 (indicated by the star). However, given the overall rotation of the H I disk of NGC 2366, it is unclear whether this velocity gradient is due to rotation in a local potential well. The NGC 2363/NGC 2366 system probably is an on-going minor merger.

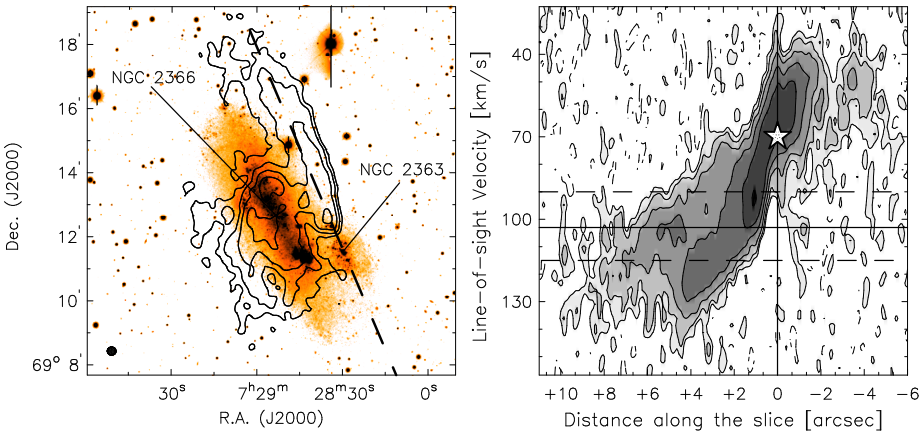

Figure 6.8 – Kinematically-anomalous gas in NGC 2363/NGC 2366. *Left*: V-band image overlaid with the H I emission at 15″ resolution, integrated in a narrow spectral range near the systemic velocity of NGC 2366 (from ∼90 to ∼115 km s^{-1}). The H I column densities are 2, 4, 8, 16 $M_\odot$ pc^{-2}. The arrows indicate the centers of NGC 2363 and NGC 2366. The circle to the bottom-left shows the H I beam. *Right*: Position-Velocity diagram taken along the dashed-line shown in the left-panel. The solid, horizontal line indicates the systemic velocity of NGC 2366 (103 km s^{-1}), while the dashed, horizontal lines show the velocity range that has been used to create the H I map in the left-panel. The vertical line corresponds to the spatial position of NGC 2363, while the star shows its optical systemic velocity (70 km s^{-1}), as given by NED. Contours are at -1.5 (dashed), 1.5, 3, 6, and 12 σ, where $\sigma = 0.66$ mJy/beam.

NGC 4068 shows a broad H I extension to the South-East. This object is in the Canes Venatici I (CVn I) cloud, which is an extended, loose group mainly inhabited by low-mass galaxies (Karachentsev et al. 2003).

NGC 4163 shows a H I tail to the West and, possibly, a second tail to the South (see also Hunter et al. 2012). NGC 4163 is in the CVn I cloud and is close to several other Irrs (at $D_{\rm p}$ ≃30 kpc), including the starbursting dwarf NGC 4214 and the "compact" irregular NGC 4190 (UGC 7232, see Chapter 5). Intriguingly, NGC 4190 has been classified as a BCD by Karachentsev et al. (2013) and shows a disturbed H I morphology (see Swaters et al. 2002).

NGC 4214 has a H I disk with a well-defined spiral pattern. The H I disk is strongly warped (see Chapter 4) and slightly more extended to the North-West. NGC 4214 is in the CVn I cloud and has a small companion galaxy (DDO 113) at a projected distance of ∼8 kpc. DDO 113 likely is a gas-poor spheroidal (Kaisin & Karachentsev 2008). This object, indeed, is within the field-of-view of the VLA, but no H I emission is detected.

NGC 4449 has an exceedingly extended H I distribution characterized by long filaments with column densities of ∼1 M$_\odot$ pc^{-2} (Hunter et al. 1998). A tidally-disturbed stellar body is present to the South-East of the galaxy, but it does not spatially coincide with any gaseous feature (Martínez-Delgado

et al. 2012), thus its relation with the extended H I emission remains unclear. NGC 4449 is one of the most massive galaxies in the CVn I cloud (Karachentsev 2005).

NGC 5253 has a ∼4 kpc H I tail to the North at $V_{\rm los} \simeq 400$ km s^{-1}. Our total H I map at $40'' \times 40''$ resolution is slightly different from that of López-Sánchez et al. (2012) at $57.8 \times 37.5''$ resolution, because we used a Gaussian-smoothed, robust-weighted datacube instead of a natural-weighted datacube. The former cube has a much more regular noise structure than the latter one, providing a better estimate of the 3σ colum density sensitivity. NGC 5253 is in the CenA/M83 group, and its projected distance from the massive spiral galaxy M83 is ∼150 kpc (Karachentsev 2005).

NGC 6789 has a regularly-rotating H I disk with several asymmetric features in the outer parts. This galaxy is in the Local Void and its nearest massive companion (NGC 6946) is at a projected distance of ∼2.5 Mpc (Drozdovsky et al. 2001).

UGC 4483 has a regularly-rotating H I disk with a small extension to the North-West. This galaxy is in the M81 group and lies between the group center and the NGC 2403 sub-group (Karachentsev et al. 2002).

UGC 6456 has a H I disk that is slightly more extended to the South. The datacube is affected by Galactic emission, making the total H I map uncertain. Our results, however, are in close agreement with those from Simpson et al. (2011). UGC 6456 lies in the periphery of the M 81 group (Karachentsev 2005).

UGC 6541 has a very asymmetric H I distribution. Gas emission is detected only in the Northern half of the galaxy. UGC 6541 is located to the North-Western edge of the the CVn I cloud (Karachentsev et al. 2003). Another BCD (NGC 3741, Karachentsev et al. 2013) lies at a projected distance of ∼300 kpc.

UGC 9128 has a relatively-regular H I distribution. The optical and kinematic position angles, however, differ by ∼30° (see also Chapter 4). This galaxy appears very isolated; the closest massive galaxy is the Milky Way at $D \simeq 2.2$ Mpc (Karachentsev et al. 2013).

UGCA 290 has a peculiar H I distribution that is off-set with respect to the stellar component. Our total H I map at $20'' \times 20''$ resolution is less extended than the one obtained by Kovač et al. (2009) using WSRT data at $52.2'' \times 30.9''$ resolution, but the H I fluxes are consistent within the uncertainties, indicating that our total H I map is not missing diffuse H I emission. UGCA 290 may be part of the NGC 4631 group; its projected distance from NGC 4631 is ∼700 kpc.

I Zw 18 has been discussed in details by Lelli et al. (2012a). The total H I map presented here is slightly different from that in Lelli et al. (2012a) because it was constructed using a mask at $60''$ resolution (instead of $45''$ resolution) for consistency with the other galaxies. The most likely interpretation of this system is an interaction/merger between two (or more) gas-rich dwarfs.

I Zw 36 has an extended and asymmetric H I distribution, that is kinematically-connected to a central rotating disk (see Chapter 4 and Ashley

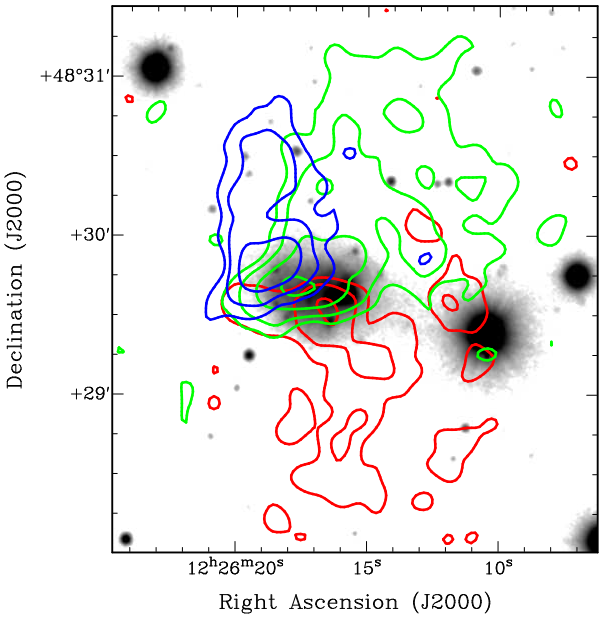

Figure 6.9 – Large-scale H I emission in I Zw 36 at 10″ resolution, integrated across 3 velocity ranges: 250 to 260 km s^{-1} (blue), 275 to 285 km s^{-1} (green), and 300 to 310 km s^{-1} (red). Contours are at 1.2, 2.4, 4.8, and 9.6 M$_\odot$ pc^{-2}.

et al. 2013). Data at 10″ resolution (see Fig. 6.9) reveal that the H I emission forms a tail-like structure to the South at receding velocities ($V_{\rm los} \simeq 300$ to 310 km s^{-1}; $V_{\rm sys} = 277$ km s^{-1}) and a broad extension to the North near the systemic velocity ($V_{\rm los} \simeq 270$ to 290 km s^{-1}), possibly connected to the approaching side of the disk ($V_{\rm los} \simeq 250$ to 260 km s^{-1}). There are no optical features associated with the extended gas down to $\mu_{\rm R} \simeq 26$ mag arcsec^{-2}. I Zw 36 is in the CVn I cloud.

SBS 1415+437 has an extended, lopsided H I disk. The galaxy is at a relatively-large distance (∼13.6 Mpc), thus it is possible that faint, nearby companions have not been identified by optical surveys.

6.6 Discussion

In Sect. 6.3, we found that starbursting dwarfs show a broad, continuous range of H I morphologies. Several BCDs in our sample have heavily disturbed H I morphologies, characterized by strong asymmetries, long filaments, and/or severe offsets between the stellar and H I distributions. Other galaxies, instead, show minor asymmetries, characterized by H I extensions and/or small tails in the outer parts. In Sect. 6.4, we introduced the parameter A, that quantifies the large-scale asymmetry in the outer parts, and measured it for both our sample of BCDs and a control-sample of typical Irrs. We found that starbursting dwarfs systematically have more asymmetric H I morphologies that typical Irrs,

suggesting that the starbursts have been triggered by some *external mechanism*. There is, however, a "grey area" for $0.4 \lesssim A \lesssim 0.6$, where one can find both starbursting and non-starbursting dwarfs with lopsided H I morphologies. Lopsidedness is a common phenomenon among spirals and irregular galaxies (e.g. Baldwin et al. 1980; Verheijen & Sancisi 2001; Swaters et al. 2002), and it has been suggested that it may be due to relatively-old interactions and/or accretion events (e.g. Sancisi et al. 2008). Our results are in line with this hypothesis, as we now discuss.

In Sect. 6.4, we also compared A with the starburst properties, as derived from the HST studies of the resolved stellar populations. We found that the H I asymmetry does not clearly correlate with any starburst indicator (the birthrate parameter, the specific SFR, or the SFR surface density), but there is a significant correlation between A and the look-back time at the peak of the star-formation activity $t_{\rm p}$ (see Fig. 6.7, left). Galaxies hosting an "old" burst ($\gtrsim$100 Myr) have low values of A, while galaxies hosting a "young" burst ($\lesssim$100 Myr) have a progressively more asymmetric H I distribution. This points to a close link between the outer, large-scale H I asymmetries and the central, recent starburst. In particular, galaxies with lopsided H I morphologies ($A \lesssim 0.6$) have values of $t_{\rm p} \simeq 500$ Myr, which are comparable with the orbital times in the outer regions (see Fig. 6.7, right), suggesting that the overall galaxy rotation could have had enough time to regularize the outer H I distribution since the epoch of the interaction/accretion event that possibly triggered the starburst. In particular, BCDs with extended, strongly-warped, and regularly-rotating H I disks, such as NGC 4214 (Chapter 4) and NGC 2915 (Elson et al. 2010), may represent an advanced stage of the interaction/accretion phenomenon, as it has already been suggested by Sancisi et al. (2008). On the other hand, a galaxy like NGC 1705, which has a warped H I disk that is strongly off-set with respect to the stellar component (see Chapter 4), may be in an earlier stage, where the outer H I gas is still in the process of settling down. This is in agreement with the very recent starburst activity ($t_{\rm p} \simeq 3$ Myr) observed in this galaxy (Annibali et al. 2003).

One may argue that the outer H I asymmetries could be the result of gaseous outflows due to stellar feedback. This possibility is very unlikely for the following reasons: i) gaseous outflows are expected to develop along the axis of rotation and to show some bipolar symmetry (e.g. Mac Low & Ferrara 1999), whereas the H I asymmetries discussed here often have a tail-like morphology and do not show any preferential direction with respect to the central galaxy (see Figs. 6.1 and 6.2); ii) the asymmetry parameter A shows no clear trend with the SFR surface density nor with the specific SFR (see Sect. 6.4.3); and iii) the energetics of the stellar feedback suggests that dwarf galaxies with circular velocities $\gtrsim$20 km s^{-1} do not expell a large quantity of gas out of their potential well, unless one assumes a very high feedback efficiency (see Chapter 4 and Ferrara & Tolstoy 2000). We conclude, therefore, that the large-scale H I asymmetries

Table 6.6 – Other starbursting dwarfs with high-quality H I observations.

Name(s)	Properties	References
II Zw 33 (Mrk 1039)	LSB companion II Zw 33 B	Walter et al. (1997)
HS 0822+3542	LSB companion SAO 0822+3542	Chengalur et al. (2006)
Mrk 324 (UGCA 439)	LSB companion EXG 0123-0040; H I tail?	van Zee et al. (2001)
NGC 2537 (Mrk 86)	Companion IC 2233 (Sd); outer H I arm	Matthews & Uson (2008)
UM 461/UM 462	BCD pair with lopsided H I disks	van Zee et al. (1998)
Haro 4 (Mrk 26)	Possible interaction with NGC 3510 (Sm)	Bravo-Alfaro et al. (2004)
Mrk 108 (IC 2450)	Interacting with NGC 2814 (Sb) & NGC 2820 (Sc)	Kantharia et al. (2005)
II Zw 70/ II Zw 71	Interacting pair	Cox et al. (2001)
SBS 0335-052	Interacting pair	Pustilnik et al. (2001a); Ekta et al. (2009)
SBS 1129+576/577	Interacting pair	Ekta et al. (2006)
II Zw 40 (UGC 116)	Advanced merger	van Zee et al. (1998)
IC 10 (UGC 192)	Long H I filaments and plumes	Manthey & Oosterloo (2008)
Haro 36 (UGC 7950)	H I filament	Ashley et al. (2013)
Mrk 1418 (UGC 5151)	H I plumes and clouds	van Zee et al. (2001)
FCC 35	High-velocity H I complex	Putman et al. (1998)
Haro 2 (Mrk 33)	H I extension and small tail/cloud	Thuan et al. (2004)
NGC 4861 (UGC 8098)	H I disk extended towards a H I cloud	Thuan et al. (2004)
Mrk 900 (NGC 7077)	Lopsided H I disk	van Zee et al. (2001)
Mrk 750	Lopsided H I disk	van Zee et al. (2001)
UM 439 (UGC 6578)	Lopsided H I disk	van Zee et al. (2001)
UM 323	Lopsided H I disk, possibly warped	van Zee et al. (2001)
UM 38	Relatively-regular H I disk	van Zee et al. (2001)
NGC 2915	Extended, warped H I disk	Meurer et al. (1996); Elson et al. (2010)

in the outer regions of BCDs indicate that the starburst is triggered by *external mechanisms*, such as interactions/mergers between gas-rich dwarfs or cold gas accretion from the IGM.

Recent H I studies by Ekta et al. (2008), Ekta & Chengalur (2010), and López-Sánchez et al. (2010) have also highlighted the importance of interaction/accretion events in triggering the starburst in BCDs. In Table 6.6, we list further examples of starbursting dwarfs with high-quality H I observations. This list is by no means complete. We have, however, carefully inspected the published total H I maps and velocity fields of these galaxies, and reported their main properties. These galaxies do *not* have accurate SFHs from HST observations, but are thought to be experiencing a starburst as suggested by their blue colors, high surface brightnesses, and/or strong emission lines. We also have no direct information on the "age" of the starburst. Based on their H I morphology and on the observed trend between A and $t_{\rm p}$, however, we suggest that we may be observing BCDs at different stages of the interaction/accretion process. In particular, we distinguish between four main "classes" or "evolutionary stages":

1. BCDs that have a nearby companion ($\lesssim$ 200 kpc) but show *no* sign of strong interactions, such as H I bridges or tails (e.g. II Zw 33, Walter et al. 1997). These systems may represent either an early-stage prior to a merger or a very-late stage after a fly-by.

2. BCDs that are clearly interacting with a companion (e.g. II Zw 70/II Zw 71, Cox et al. 2001) or are in an advanced stage of merging (e.g. II Zw 40, van Zee et al. 1998).

3. BCDs that are relatively isolated and show a heavily-disturbed H I morphology (e.g. IC 10, Manthey & Oosterloo 2008), that may be due to a recent interaction/merger and/or cold gas accretion from the environment.

4. BCDs that are relatively isolated and have an extended, lopsided H I disk (e.g. UM 439, van Zee et al. 1998) or a pronounced warp (e.g. NGC 2915, Elson et al. 2010).

Our galaxy sample includes BCDs from all these 4 classes. As we described in Sect. 6.5, NGC 4214 and NGC 4163 have several nearby companions belonging to the CVn I cloud and, thus, fit into class 1. Grocholski et al. (2008) argued that NGC 1560 and UGCA 290 may form a pair of galaxies in the IC 432 group similar to the LMC and the SMC in the Local Group; in this case, NGC 1569 would also belong to class 1. There may be more BCDs in this class, having galaxies at projected distances $D_{\rm p} \lesssim 200$ kpc and differences in their systemic velocities $\lesssim 300$ km s^{-1}, but the lack of accurate distance estimates for their potential companions prevents us from unambiguously classifying them (see Sect. 6.5). I Zw 18, NGC 4449, and NGC 2366 are probably undergoing a minor merger (see Lelli et al. 2012a, Martínez-Delgado et al. 2012, and Sect. 6.5,

respectively) and, thus, may belong to class 2. I Zw 36, UGC 6431, UGCA 290, and NGC 625 can be included in class 3, whereas UGC 4483, UGC 6456, UGC 9128, and SBS 1415+437 belong to class 4. NGC 6789 and NGC 5253 are somewhat intermediate between class 3 and 4, having $A \simeq 0.6$.

The observational evidence presented so far indicates that past and on-going interaction/accretion events play an important role in triggering the starburst in low-mass galaxies. Moreover, interaction/mergers between gas-rich dwarfs may provide the mechanism that forms the central concentration of mass observed in BCDs (see Lelli et al. 2012a,b and Chapter 5). Numerical simulations, indeed, indicate that interactions/mergers between gas-rich dwarfs may lead to an overall contraction of the disk and form a central mass concentration (e.g. Bekki 2008). However, to unambiguously identify galaxy interaction as the main triggering mechanism, one would need very deep optical observations (down to $\sim 29-30$ mag arcsec^{-2}) to search for stellar tidal features associated with the H I features, and/or for faint, low-surface-brightness companions. Several galaxies in our sample, indeed, show remarkably symmetric optical morphologies (down to $\sim$26 mag arcsec^{-2}), whereas the H I distribution is heavily pertured (see e.g. I Zw 36 in Fig. 6.9). In the case that stellar tidal features would still remain undetected by deep optical observations, the remaining possibility is that BCDs are directly accreting gas from the IGM. Cold flows of gas are predicted by ΛCDM models of galaxy formation (Kereš et al. 2005; Dekel & Birnboim 2006). In particular, Kereš et al. (2005) argued that these cold flows might still take place at $z \simeq 0$ in low-mass galaxies residing in low-density enviroments. As we discussed in Sect. 6.5, most BCDs in our sample inhabit similar environments as typical Irrs, such as galaxy groups and small associations. Thus, it is unclear why cosmological cold flows should be visible only in BCDs, unless they are highly stochastic and can rapidly trigger a central starburst by bringing large amounts of gas to the bottom of the potential well. It is also unclear what the relation would be between these cold flows and the central concentration of mass (luminous and/or dark). Three galaxies (NGC 1705, NGC 6789, and UGC 9128), however, *seem* very isolated and show relatively-regular optical morphologies down to $\mu \simeq 26$ R mag arcsec^{-2}. NGC 1705 shows a strong offset between the H I and stellar distribution, NGC 6789 has an anomalous H I extension to the West, while in UGC 9128 the optical and kinematical position angles differ by $\sim$30° (see Sect. 6.5 and Chapter 4). If the regular optical morphologies of these galaxies are confirmed by deeper optical images, they may represent cases of cold gas accretion in the nearby Universe.

6.7 Conclusions

We investigated the large-scale H I emission in a sample of 18 starbursting dwarf galaxies, using both new and archival data. We considered only galaxies that

have been resolved into single stars by HST observations, providing their recent SFHs and starburst timescales. Our main results can be summarized as follows.

1. Starbursting dwarfs display a broad, continuous range of H I morphologies. Several galaxies show heavily disturbed H I morphologies characterized by large-scale asymmetries, long filaments, and/or strong offsets between the stellar and H I distributions, whereas other galaxies show only minor asymmetries in the outer regions.

2. We defined the parameter A to quantify the H I asymmetry in the outer parts, and measured it for our sample of starbursting dwarfs and a control-sample of non-starbursting irregulars, drawn from the VLA-ANGST survey. We found that starbursting dwarfs generally have higher values of A than typical irregulars, suggesting that some external mechanism triggered the starburst.

3. We compared the values of A with the starburst properties. We found that galaxies hosting a "young" burst ($\lesssim$100 Myr) generally have more asymmetric H I morphologies than galaxies hosting an "old" one ($\gtrsim$100 Myr), further indicating that there is a close link between the outer, disturbed H I distribution and the central, recent star-formation. Galaxies hosting an "old" burst likely had enough time to partially regularize their outer H I distribution, since the "age" of the burst ($\sim$500 Myr) is comparable with the orbital time in the outer parts.

4. We investigated the nearby environment of the galaxies in our sample. Most of them have a potential perturber at a projected distance $\lesssim$ 200 kpc, thus the hypothesis of a past interaction cannot be excluded. Three galaxies (NGC 2366, NGC 4449, and I Zw 18) are probably undergoing a minor merger. Another three objects (NGC 1705, NGC 6789, and UGC 9128), instead, seem very isolated and show regular optical morphologies down to $\mu \simeq 26$ R mag arcsec^{-2}, thus they *may* represent cases of cold gas accretion in the nearby Universe.

Acknowledgements

We are grateful to Renzo Sancisi for sharing his valuable insights with us. We thank Juergen Ott for useful correspondence about the VLA-ANGST data, and Kristen McQuinn for sharing information about the stellar populations of the ANGST galaxies. We are grateful to Martin Vogelaar for implementing a special version of the Gipsy task "Visions". We also thank Ed Elson, Deidre Hunter, and Angel R. López-Sánchez for providing us with the H I data of NGC 1705, NGC 4449, and NGC 5253, respectively. Finally, we thank the members of the WHISP, THINGS, LITTLE-THINGS, and VLA-ANGST projects for having made the H I data publicly available. FL acknowledges the Ubbo Emmius

bursary program of the University of Groningen and the Leids Kerkhoven-Bosscha Fund. FF acknowledges financial support from PRIN MIUR 2010-2011, project "The Chemical and Dynamical Evolution of the Milky Way and Local Group Galaxies", prot. 2010LY5N2T.

Appendix 6.A The noise in a total H I map

In their appendix A, Verheijen & Sancisi (2001) describe how to calculate the noise in a total H I map obtained using a mask on an hanning-tapered datacube, in which all the channel maps are kept during the analysis. Here, we derive similar formulae that can be used to construct signal-to-noise maps in 2 different cases: i) a uniform-tapered datacube, as it is the case for the WHISP data and our new WRST and VLA observations; and ii) an online hanning-tapered datacube, in which half of the channel maps are discarded during the observations, as it is the case for the THINGS/LITTLE-THINGS data and other archival VLA observations.

Uniform taper

If the observations are made using an uniform velocity taper, the noise σ^u in two channel maps will be independent. When N uniform-tapered channel maps are added at the spatial position (x, y), the noise σ^u_N in the total H I map will increase by a factor $\sqrt{N}$, thus $\sigma^u_N(x, y) = \sqrt{N(x, y)}\sigma^u$. However, before the channel maps are added to form a total H I map, the continuum emission is subtracted, introducing further noise in the channel maps. Here we assume that the continuum map C^u is constructed by averaging N_1 and N_2 line-free channel maps at the high and low velocity ends of the datacube, respectively. Thus, one has

$$C^u = \frac{1}{2}\left(\frac{1}{N_1}\sum_{j=1}^{N_1} U_j + \frac{1}{N_2}\sum_{j=1}^{N_2} U_j\right), \tag{6.A.1}$$

and the noise σ^u_C in the continuum map is given by

$$\sigma^u_C = \frac{1}{2}\sqrt{\frac{1}{N_1} + \frac{1}{N_2}}\sigma^u. \tag{6.A.2}$$

If U_i is the value of a pixel in the i^{th} uniform-tapered channel map, the line-emission L^u_i is given by $L^u_i = U_i - C^u$ and the noise σ^{lu}_i in L^u_i is given by

$$\sigma^{lu}_i = \sqrt{1 + \frac{1}{4}\left(\frac{1}{N_1} + \frac{1}{N_2}\right)}\sigma^u \tag{6.A.3}$$

When N uniform-tapered and continuum-subtracted channel maps are added, the signal L^u_N at a position (x, y) of the total H I map is given by

$$L^u_N(x, y) = \sum_{j=1}^{N(x,y)} L^u_j = \sum_{j=1}^{N(x,y)} U_j - N(x, y) \times C \tag{6.A.4}$$

and the noise σ_N^{lu} is given by

$$\sigma_N^{lu}(x,y) = \sqrt{N(x,y)\sigma^{u^2} + N(x,y)^2\sigma_C^{u^2}} = \\ = \sqrt{1 + \frac{N(x,y)}{4}\left(\frac{1}{N_1} + \frac{1}{N_2}\right)}\sqrt{N(x,y)}\sigma^u. \tag{6.A.5}$$

Online hanning taper

If the observations are made using an hanning taper, the datacube is smoothed in velocity and the noise in two adjacent channel maps is no longer independent. When the online hanning smoothing option of the VLA is used, half of the channel maps are discarted. If U_i and O_i are, respectively, the values of a pixel in the i^{th} uniform-tapered and online hanning-tapered channel maps, one has

$$\begin{aligned} O_i &= \frac{1}{4}U_{i-1} + \frac{1}{2}U_i + \frac{1}{4}U_{i+1}, \\ O_{i+1} &= \frac{1}{4}U_i + \frac{1}{2}U_{i+1} + \frac{1}{4}U_{i+2}, \\ O_{i+2} &= \frac{1}{4}U_{i+1} + \frac{1}{2}U_{i+2} + \frac{1}{4}U_{i+3}, \end{aligned} \tag{6.A.6}$$

and the $i+1^{th}$ channel map is discarted during the observations. The remaining channel maps i^{th} and $i+2^{th}$ are *not* independent, because both contain a quarter of the emission U_{i+1}. Thus, when N online hanning-smoothed channel maps are added, the noise σ_N^o does not increase by a factor $\sqrt{N}$, but by a factor $\sqrt{N - \frac{3}{4}\frac{4}{\sqrt{2}\sqrt{6}}}$, as we show in the following. The noise σ^o in the online hanning smoothed channel maps is equal to $\frac{\sqrt{6}}{4}\sigma^u$ (see Verheijen & Sancisi 2001). The total signal O_N is given by

$$O_N = O_i + O_{i+2} + O_{i+4} + O_{i+6} + ... + O_{i+2(N-1)}. \tag{6.A.7}$$

Table 6.7 – Adding N online hanning-tapered channel maps.

Channel	U_{i-1}	U_i	U_{i+1}	U_{i+2}	U_{i+3}	...	U_{i+2N-3}	U_{i+2N-2}	U_{i+2N-1}
i	1/4	1/2	1/4						
$i+2$			1/4	1/2	1/4				
...					...	...	...		
$i+2N-2$							1/4	1/2	1/4
	1/4	1/2	1/2	1/2	1/2	...	1/2	1/2	1/4

As it is shown by Table 6.7, one has

$$O_N = \frac{1}{4}U_{i-1} + \frac{1}{2}U_i + \frac{1}{2}U_{i+1} + ... + \frac{1}{2}U_{i+2N-2} + \frac{1}{4}U_{i+2N-1}, \tag{6.A.8}$$

and the noise σ_N^o is given by

$$\begin{aligned}\sigma_{\rm N}^o &= \sqrt{\left(\frac{1}{4}\right)^2 + \left(\frac{1}{2}\right)^2 (2N-2) + \left(\frac{1}{4}\right)^2}\sigma^u = \\ &= \frac{1}{\sqrt{2}}\sqrt{N-\frac{3}{4}}\sigma^u = \sqrt{N-\frac{3}{4}}\frac{4}{\sqrt{2}\sqrt{6}}\sigma^o.\end{aligned} \tag{6.A.9}$$

The continuum map C^o is now constructed by averaging N_1 and N_2 line-free channel maps at high and low velocity ends of the online hanning-tapered datacube, thus the noise σ_C^o in C^o is given by

$$\begin{aligned}\sigma_C^o &= \frac{1}{2\sqrt{2}}\sqrt{\frac{1}{N_1^2}\left(N_1-\frac{3}{4}\right)+\frac{1}{N_1^2}\left(N_2-\frac{3}{4}\right)}\sigma^u \\ &\equiv \frac{1}{\sqrt{2}}A\sigma^u = \frac{4}{\sqrt{2}\sqrt{6}}A\sigma^o\end{aligned} \tag{6.A.10}$$

The line-emission in the i^{th} channel maps is given by $L_i^o = O_i - C^o$ and the noise in L_i^o is given by

$$\sigma_i^{lo} = \sqrt{1+\frac{4}{3}A^2}\sigma^o \tag{6.A.11}$$

When N online hanning-tapered and continuum-subtracted channel maps are added, the signal L_N^o at a position (x, y) of the total H I maps is given by

$$\begin{aligned}L_N^o(x,y) = &\frac{1}{4}U_{i-1} + \frac{1}{2}U_i + ... + \frac{1}{2}U_{i+2N-2} + \frac{1}{4}U_{i+2N-1} + \\ &- N(x,y)\times C^o\end{aligned} \tag{6.A.12}$$

and the noise σ_N^{lo} at (x, y) is given by

$$\sigma_N^{lo}(x,y) = \sqrt{N(x,y) - \frac{3}{4} + N^2(x,y)A^2}\frac{4}{\sqrt{2}\sqrt{6}}\sigma^o \tag{6.A.13}$$

Note that this equation differs by a factor $1/\sqrt{2}$ from the one given by Verheijen & Sancisi (2001), which is valid in the case that all the hanning-tapered channel maps are kept during the data analysis.

References

Annibali, F., Cignoni, M., Tosi, M., et al. 2013, ArXiv e-prints
Annibali, F., Greggio, L., Tosi, M., Aloisi, A., & Leitherer, C. 2003, AJ, 126, 2752
Ashley, T., Simpson, C. E., & Elmegreen, B. G. 2013, ArXiv e-prints
Baldwin, J. E., Lynden-Bell, D., & Sancisi, R. 1980, MNRAS, 193, 313
Bekki, K. 2008, MNRAS, 388, L10
Bekki, K. & Freeman, K. C. 2002, ApJL, 574, L21
Berg, D. A., Skillman, E. D., Marble, A. R., et al. 2012, ApJ, 754, 98
Binder, B., Williams, B. F., Eracleous, M., et al. 2011, ApJ, 737, 77
Bouchard, A., Prugniel, P., Koleva, M., & Sharina, M. 2010, A&A, 513, A54
Bravo-Alfaro, H., Brinks, E., Baker, A. J., Walter, F., & Kunth, D. 2004, AJ, 127, 264
Briggs, D. S. 1995, in Bulletin of the American Astronomical Society, Vol. 27, Bulletin of the American Astronomical Society, 1444–+
Campos-Aguilar, A. & Moles, M. 1991, A&A, 241, 358
Campos-Aguilar, A., Moles, M., & Masegosa, J. 1993, AJ, 106, 1784
Cannon, J. M., McClure-Griffiths, N. M., Skillman, E. D., & Côté, S. 2004, ApJ, 607, 274
Chengalur, J. N., Pustilnik, S. A., Martin, J., & Kniazev, A. Y. 2006, MNRAS, 371, 1849
Conselice, C. J. 2003, ApJS, 147, 1
Côté, S., Carignan, C., & Freeman, K. C. 2000, AJ, 120, 3027
Cote, S., Freeman, K. C., Carignan, C., & Quinn, P. J. 1997, AJ, 114, 1313
Cox, A. L., Sparke, L. S., Watson, A. M., & van Moorsel, G. 2001, AJ, 121, 692
Crone, M. M., Schulte-Ladbeck, R. E., Greggio, L., & Hopp, U. 2002, ApJ, 567, 258
Dalcanton, J. J., Williams, B. F., Seth, A. C., et al. 2009, ApJS, 183, 67
Dekel, A. & Birnboim, Y. 2006, MNRAS, 368, 2
del Río, M. S., Brinks, E., & Cepa, J. 2004, AJ, 128, 89
Drozdovsky, I. O., Schulte-Ladbeck, R. E., Hopp, U., Crone, M. M., & Greggio, L. 2001, ApJL, 551, L135
Ekta, Chengalur, J. N., & Pustilnik, S. A. 2006, MNRAS, 372, 853
Ekta, Chengalur, J. N., & Pustilnik, S. A. 2008, MNRAS, 391, 881
Ekta, B. & Chengalur, J. N. 2010, MNRAS, 403, 295
Ekta, B., Pustilnik, S. A., & Chengalur, J. N. 2009, MNRAS, 397, 963
Elmegreen, B. G., Zhang, H.-X., & Hunter, D. A. 2012, ApJ, 747, 105
Elson, E. C., de Blok, W. J. G., & Kraan-Korteweg, R. C. 2010, MNRAS, 404, 2061
Elson, E. C., de Blok, W. J. G., & Kraan-Korteweg, R. C. 2011, MNRAS, 415, 323
Elson, E. C., de Blok, W. J. G., & Kraan-Korteweg, R. C. 2013, MNRAS, 429, 2550

Evstigneeva, E. A., Drinkwater, M. J., Jurek, R., et al. 2007, MNRAS, 378, 1036
Ferrara, A. & Tolstoy, E. 2000, MNRAS, 313, 291
Firth, P., Evstigneeva, E. A., Jones, J. B., et al. 2006, MNRAS, 372, 1856
Gil de Paz, A., Madore, B. F., & Pevunova, O. 2003, ApJS, 147, 29
Grocholski, A. J., Aloisi, A., van der Marel, R. P., et al. 2008, ApJL, 686, L79
Guseva, N. G., Papaderos, P., Izotov, Y. I., et al. 2003, A&A, 407, 105
Holwerda, B. W., Pirzkal, N., de Blok, W. J. G., & Blyth, S. 2013, ArXiv e-prints
Holwerda, B. W., Pirzkal, N., de Blok, W. J. G., et al. 2011a, MNRAS, 416, 2437
Holwerda, B. W., Pirzkal, N., de Blok, W. J. G., et al. 2011b, MNRAS, 416, 2401
Holwerda, B. W., Pirzkal, N., de Blok, W. J. G., et al. 2011c, MNRAS, 416, 2415
Holwerda, B. W., Pirzkal, N., de Blok, W. J. G., & van Driel, W. 2011d, MNRAS, 416, 2447
Hunter, D. A. & Elmegreen, B. G. 2004, AJ, 128, 2170
Hunter, D. A., Ficut-Vicas, D., Ashley, T., et al. 2012, AJ, 144, 134
Hunter, D. A., Wilcots, E. M., van Woerden, H., Gallagher, J. S., & Kohle, S. 1998, ApJL, 495, L47
Iovino, A., Melnick, J., & Shaver, P. 1988, ApJL, 330, L17
Izotov, Y. I. & Thuan, T. X. 1999, ApJ, 511, 639
Johnson, M., Hunter, D. A., Oh, S.-H., et al. 2012, AJ, 144, 152
Kaisin, S. S. & Karachentsev, I. D. 2008, A&A, 479, 603
Kantharia, N. G., Ananthakrishnan, S., Nityananda, R., & Hota, A. 2005, A&A, 435, 483
Karachentsev, I. D. 2005, AJ, 129, 178
Karachentsev, I. D., Dolphin, A. E., Geisler, D., et al. 2002, A&A, 383, 125
Karachentsev, I. D., Karachentseva, V. E., Huchtmeier, W. K., & Makarov, D. I. 2004, AJ, 127, 2031
Karachentsev, I. D., Makarov, D. I., & Kaisina, E. I. 2013, AJ, 145, 101
Karachentsev, I. D., Sharina, M. E., Dolphin, A. E., et al. 2003, A&A, 398, 467
Kereš, D., Katz, N., Weinberg, D. H., & Davé, R. 2005, MNRAS, 363, 2
Kobulnicky, H. A. & Skillman, E. D. 1997, ApJ, 489, 636
Kovač, K., Oosterloo, T. A., & van der Hulst, J. M. 2009, MNRAS, 400, 743
Lauberts, A. & Valentijn, E. A. 1989, The surface photometry catalogue of the ESO-Uppsala galaxies
Lee, J. C., Salzer, J. J., Law, D. A., & Rosenberg, J. L. 2000, ApJ, 536, 606
Lelli, F., Verheijen, M., Fraternali, F., & Sancisi, R. 2012a, A&A, 537, A72
Lelli, F., Verheijen, M., Fraternali, F., & Sancisi, R. 2012b, A&A, 544, A145
López-Sánchez, Á. R. 2010, A&A, 521, A63
López-Sánchez, A. R., Koribalski, B., van Eymeren, J., et al. 2010, in

Astronomical Society of the Pacific Conference Series, Vol. 421, Galaxies in Isolation: Exploring Nature Versus Nurture, ed. L. Verdes-Montenegro, A. Del Olmo, & J. Sulentic, 65
López-Sánchez, Á. R., Koribalski, B. S., van Eymeren, J., et al. 2012, MNRAS, 419, 1051
Lotz, J. M., Primack, J., & Madau, P. 2004, AJ, 128, 163
Mac Low, M. & Ferrara, A. 1999, ApJ, 513, 142
Manthey, E. & Oosterloo, T. 2008, in American Institute of Physics Conference Series, Vol. 1035, The Evolution of Galaxies Through the Neutral Hydrogen Window, ed. R. Minchin & E. Momjian, 156–158
Martínez-Delgado, D., Romanowsky, A. J., Gabany, R. J., et al. 2012, ApJL, 748, L24
Mateo, M. L. 1998, ARA&A, 36, 435
Matthews, L. D. & Uson, J. M. 2008, AJ, 135, 291
Maurogordato, S., Proust, D., Cappi, A., Slezak, E., & Martin, J. M. 1997, A&AS, 123, 411
McQuinn, K. B. W., Skillman, E. D., Cannon, J. M., et al. 2010, ApJ, 721, 297
McQuinn, K. B. W., Skillman, E. D., Dalcanton, J. J., et al. 2012, ApJ, 759, 77
Méndez, D. I. & Esteban, C. 2000, A&A, 359, 493
Méndez, D. I., Esteban, C., & Balcells, M. 1999, AJ, 117, 1229
Meurer, G. R., Carignan, C., Beaulieu, S. F., & Freeman, K. C. 1996, AJ, 111, 1551
Meurer, G. R., Staveley-Smith, L., & Killeen, N. E. B. 1998, MNRAS, 300, 705
Noeske, K. G., Iglesias-Páramo, J., Vílchez, J. M., Papaderos, P., & Fricke, K. J. 2001, A&A, 371, 806
Noguchi, M. 1988, A&A, 201, 37
Noordermeer, E., van der Hulst, J. M., Sancisi, R., Swaters, R. A., & van Albada, T. S. 2005, A&A, 442, 137
Oh, S., de Blok, W. J. G., Walter, F., Brinks, E., & Kennicutt, R. C. 2008, AJ, 136, 2761
Ott, J., Stilp, A. M., Warren, S. R., et al. 2012, AJ, 144, 123
Papaderos, P., Izotov, Y. I., Thuan, T. X., et al. 2002, A&A, 393, 461
Pustilnik, S., Ugryumov, A. V., Lipovetsky, V. A., Thuan, T. X., & Guseva, N. 1995, ApJ, 443, 499
Pustilnik, S. A., Brinks, E., Thuan, T. X., Lipovetsky, V. A., & Izotov, Y. I. 2001a, AJ, 121, 1413
Pustilnik, S. A., Kniazev, A. Y., Lipovetsky, V. A., & Ugryumov, A. V. 2001b, A&A, 373, 24
Putman, M. E., Bureau, M., Mould, J. R., Staveley-Smith, L., & Freeman, K. C. 1998, AJ, 115, 2345
Salzer, J. J. 1989, ApJ, 347, 152
Sancisi, R., Fraternali, F., Oosterloo, T., & van der Hulst, T. 2008, A&ARv, 15, 189

Schulte-Ladbeck, R. E., Hopp, U., Greggio, L., & Crone, M. M. 2000, AJ, 120, 1713
Schulte-Ladbeck, R. E., Hopp, U., Greggio, L., Crone, M. M., & Drozdovsky, I. O. 2001, AJ, 121, 3007
Silk, J., Wyse, R. F. G., & Shields, G. A. 1987, ApJL, 322, L59
Simpson, C. E., Hunter, D. A., Nordgren, T. E., et al. 2011, AJ, 142, 82
Skillman, E. D., Côté, S., & Miller, B. W. 2003, AJ, 125, 593
Stil, J. M. & Israel, F. P. 1998, A&A, 337, 64
Stil, J. M. & Israel, F. P. 2002, A&A, 392, 473
Swaters, R. A. & Balcells, M. 2002, A&A, 390, 863
Swaters, R. A., van Albada, T. S., van der Hulst, J. M., & Sancisi, R. 2002, A&A, 390, 829
Taylor, C., Brinks, E., & Skillman, E. D. 1993, AJ, 105, 128
Taylor, C. L., Brinks, E., Grashuis, R. M., & Skillman, E. D. 1995, ApJS, 99, 427
Taylor, C. L., Thomas, D. L., Brinks, E., & Skillman, E. D. 1996, ApJS, 107, 143
Telles, E. & Maddox, S. 2000, MNRAS, 311, 307
Telles, E. & Terlevich, R. 1995, MNRAS, 275, 1
Thilker, D. A., Bianchi, L., Schiminovich, D., et al. 2010, ApJL, 714, L171
Thuan, T. X., Hibbard, J. E., & Lévrier, F. 2004, AJ, 128, 617
Thuan, T. X. & Izotov, Y. I. 2005, ApJS, 161, 240
Trentham, N., Tully, R. B., & Verheijen, M. A. W. 2001, MNRAS, 325, 385
van Zee, L., Salzer, J. J., & Skillman, E. D. 2001, AJ, 122, 121
van Zee, L., Skillman, E. D., & Salzer, J. J. 1998, AJ, 116, 1186
Verheijen, M. & Sancisi, R. 2001, A&A, 370, 765
Walter, F., Brinks, E., de Blok, W. J. G., et al. 2008, AJ, 136, 2563
Walter, F., Brinks, E., Duric, N., & Klein, U. 1997, AJ, 113, 2031
Weisz, D. R., Dalcanton, J. J., Williams, B. F., et al. 2011, ApJ, 739, 5

Chapter 7

A scaling relation for disk galaxies: circular-velocity gradient *versus* central surface brightness

— **Federico Lelli, Filippo Fraternali, and Marc Verheijen** —

Monthly Notices of the Royal Astronomical Society: Letters, 2013,
doi:10.109/mnrasl/slt053

Abstract

For disk galaxies, a close relation exists between the distribution of light and the shape of the rotation curve. We quantify this relation by measuring the inner circular-velocity gradient $d_R V(0)$ for spiral and irregular galaxies with high-quality rotation curves. We find that $d_R V(0)$ correlates with the central surface brightness μ_0 over more than two orders of magnitude in $d_R V(0)$ and four orders of magnitudes in μ_0. This is a scaling relation for disk galaxies. It shows that the central stellar density of a galaxy closely relates to the inner shape of the potential well, also for low-luminosity and low-surface-brightness galaxies that are expected to be dominated by dark matter.

7.1 Introduction

Scaling relations are an ideal tool to investigate the structure, the formation, and the evolution of galaxies. For disk galaxies, the Tully-Fisher (TF) relation (Tully & Fisher 1977) is one of the best-studied scaling laws. It was originally proposed as a correlation between the absolute magnitude of a galaxy and the width of its global H I line profile. It is now clear that the fundamental relation is between the total baryonic mass of the galaxy and the circular velocity along the flat part of the outer rotation curve ($V_{\rm flat}$), thought to be set by the dark matter (DM) halo (e.g. McGaugh et al. 2000; Verheijen 2001; Noordermeer & Verheijen 2007).

While $V_{\rm flat}$ is related to the total dynamical mass of a galaxy, the inner shape of the rotation curve provides information on the steepness of the potential well. For disk galaxies (Sb and later types), the rotation curve is generally described by an inner rising part (nearly solid-body) and an outer flat part (e.g. Bosma 1981; Begeman 1987; Swaters et al. 2009). For bulge-dominated galaxies, instead, the rotation curve shows a very fast rise in the center, often followed by a decline and the flattening in the outer parts (e.g. Casertano & van Gorkom 1991; Noordermeer et al. 2007).

The relation between the optical properties of a galaxy and the shape of its rotation curve has been debated for many years (e.g. Rubin et al. 1985; Corradi & Capaccioli 1990; Persic & Salucci 1991). Several authors pointed out that the shape of the luminosity profile and the shape of the rotation curve are closely related (Kent 1987; Casertano & van Gorkom 1991; Broeils 1992; Sancisi 2004; Swaters et al. 2009). In particular, de Blok & McGaugh (1996) and Tully & Verheijen (1997) compared the properties of two *disk* galaxies on the same position of the TF relation but with different central surface brightness, and found that high-surface-brightness (HSB) galaxies have steeply-rising rotation curves compared to low-surface-brightness (LSB) ones. Thus, for a given total luminosity (or $V_{\rm flat}$), an exponential light distribution with a shorter scale-length corresponds to a steeper potential well (see also Amorisco & Bertin 2010). For HSB spirals, maximum-disk solutions can explain the dynamics in the central regions with reasonable values of the stellar mass-to-light ratio M_*/L (e.g. van Albada & Sancisi 1986; Palunas & Williams 2000), suggesting that either baryons dominate the gravitational potential or DM closely follows the distribution of light. Garrido et al. (2005) also found a clear trend between the inner slope of the rotation curve and the central surface brightness of 18 HSB spiral galaxies. For LSB galaxies, maximum-disk solutions can reproduce the inner parts of the rotation curves, but they often require high values of M_*/L that cannot be explained by stellar population models (e.g. de Blok et al. 2001; Swaters et al. 2011), leading to the interpretation that LSB galaxies are dominated by DM at all radii. Finally, galaxies with a central "light excess" with respect to the exponential disk (e.g. a bulge) show a corresponding "velocity excess" in the inner parts of the rotation curve (e.g. Márquez & Moles

1999; Swaters et al. 2009). This is usually referred to as the "Renzo's rule" (Sancisi 2004): for any feature in the luminosity profile of a galaxy there is a corresponding feature in the rotation curve, and vice versa.

In this Letter, we show that the inner circular-velocity gradient $d_R V(0)$ of a galaxy strongly correlates with the central surface brightness μ_0 over more than two orders of magnitude in $d_R V(0)$ and four orders of magnitude in μ_0, thereby extending and firmly establishing the correlation hinted at by Fig. 8 of Garrido et al. (2005). This is a scaling relation for disk galaxies. We discuss the implications of this relation for the stellar and DM properties of galaxies.

7.2 Data Analysis

7.2.1 The circular-velocity gradient

We define the circular-velocity gradient $d_R V(0)$ as the inner slope of a galaxy rotation curve, i.e. dV/dR for $R \to 0$. $d_R V(0)$ can be estimated if the rising part of the rotation curve is well sampled, but this requires high-quality data and a careful modelling of the gas kinematics in the inner parts. To minimize the uncertainties, we use four samples of galaxies with high-quality rotation curves: Swaters et al. (2009, hereafter S09), de Blok et al. (2008, hereafter dB08 or THINGS), Verheijen & Sancisi (2001, hereafter VS01), and Begeman (1987, hereafter B87). The rotation curves were derived using interferometric H I observations and corrected for beam-smearing effects. We select only galaxies viewed at inclination angles i between 40° and 80°, as the rotation velocities of face-on disks require a large correction for i, while the observed rotation curves of edge-on disks may be affected by unseen holes in the central H I distribution. We projected each derived rotation curve on to the corresponding position-velocity diagram to verify that they have been properly determined. We exclude the galaxies from S09 and VS01 with low-quality data ($q > 2$; see S09). The spiral NGC 3521 (from dB08) is close to edge-on in the inner regions and we neglect the two innermost velocity points. Five galaxies are in common between B87 and dB08. We use the new rotation curves from THINGS except for two galaxies (NGC 2903 and NGC 3198), as the inner parts of their rotation curves are better traced by B87, who applied a careful beam-smearing correction (see Figs. 9 and 12 of dB08). The sample of S09 has one object (NGC 2366) in common with dB08 and another one (UGC 6446) in common with VS01; we use the rotation curves from S09. In all these cases the differences in $d_R V(0)$ are, however, within a factor of 2. The final sample comprises 63 galaxies with morphological types ranging from Sab to Sd/Im.

To this high-quality sample, we add 11 rotation curves of S0/Sa galaxies (with $40° \leq i \leq 80°$) from Noordermeer et al. (2007, hereafter N07). Since early-type galaxies usually lack H I emission in their central regions, the rotation curves were derived combining Hα long-slit spectroscopy (for the inner parts)

with H I observations (for the outer parts). We exclude UGC 12043 as the Hα observations of this galaxy have very low velocity resolution. The values of $d_R V(0)$ for early-type galaxies are more uncertain than those for late-type galaxies.

We derive $d_R V(0)$ by fitting the inner rotation curve with a polynomial function of the form

$$V(R) = \sum_{\rm n=1}^{m} a_{\rm n} \times R^n \tag{7.1}$$

and consider the linear term $a_1 = \lim_{R\to 0} dV/dR = d_{\rm R}V(0)$. The fit is error-weighted and constrained to pass through $V = 0$ at $R = 0$. The value of a_1 depends on i) the radial range used in the fit, and ii) the order of the polynomial m. We define R_{90} as the radius where the rotation curve reaches 90% of its maximum velocity, and fit only the points within R_{90}. This choice allows us to maximize the number of points along the rising part of the rotation curve without including points along the flat part. Rotation curves with less than 3 points within R_{90} are excluded, as they are not well-resolved in the inner parts. 16 galaxies from the high-quality sample and 3 galaxies from N07 are excluded by this criterion, thus the high-quality and total samples reduce to 47 and 55 objects, respectively. For a pure exponential disk with scale-length $R_{\rm d}$, $R_{90} \simeq 1.2R_{\rm d}$. Thus, the first fitted point of the rotation curve is typically at $R \lesssim 0.4R_{\rm d}$ and the derived value of $d_{\rm R}V(0)$ is representative of the innermost galaxy regions that are accessible by the available rotation curves. To derive the best-fitting order of the polynomial, we proceed as follows. We start with a linear fit ($m = 1$) and progressively increase m until the reduced χ^2 (χ^2_ν) approaches 1. In practice, we minimize the function $P_\chi(\chi^2;\nu) - 0.5$, where $P_\chi(\chi^2;\nu)$ is the integral probability of χ^2 and ν is the number of degrees of freedom; the procedure is halted in case χ^2_ν would drop below 1. Visual inspection showed that this method works better than the F-test (e.g. Bevington & Robinson 2003), that in some cases returns high values of m and thus increases the number of free parameters in the fit.

We test our automatic procedure on a set of model rotation curves, calculated by summing the contributions of a disk, a bulge, and a DM halo. We add typical errors to the velocity points ($\sim$5 km s^{-1}) and try several spatial samplings. We find that, even if the rotation curve is poorly sampled ($\sim$5 points within R_{90}), the actual value of $d_{\rm R}V(0)$ can be recovered with a error of $\sim$30%. However, if the rotation curve has an inner "bump" (due to a compact bulge), $d_{\rm R}V(0)$ may be under estimated by a factor of $\sim$2.

Fig. 7.1 shows the results for four representative galaxies that require polynomial fits of different orders. Late-type galaxies (Sb to Im) are generally well fitted by polynomials with $m = 1$ (e.g. UGC 7559) or $m = 2$ (e.g. NGC 3198), but several cases do require $m \geq 3$ (e.g. NGC 5055). Early-type galaxies (S0/Sa) often require high-order polynomials ($m \geq 4$, e.g. UGC 11670),

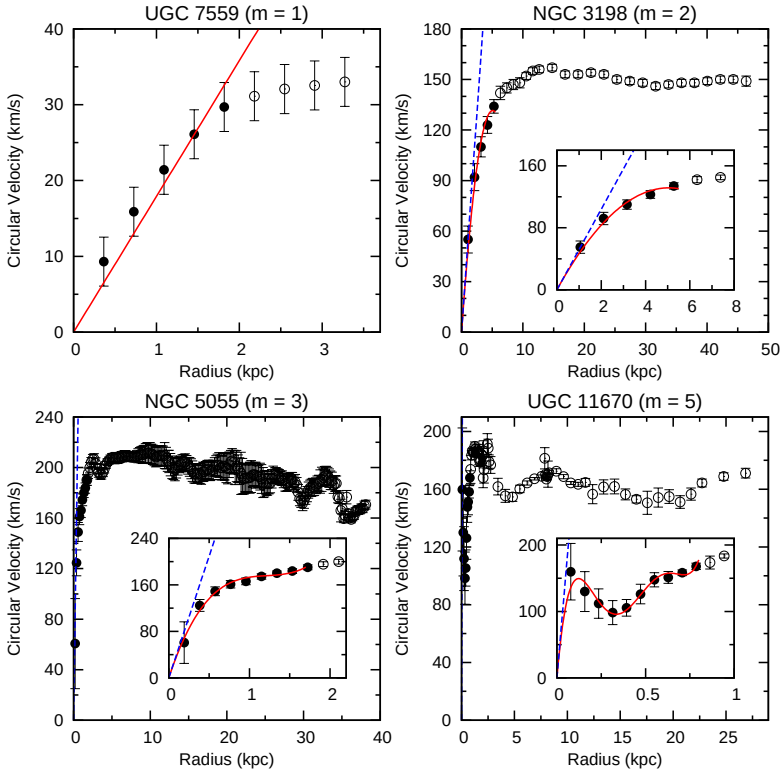

Figure 7.1 – Results of the polynomial fit for four representative galaxies. The filled circles show the points of the rotation curve within R_{90}, while the open circles show the points excluded in the fit. The solid, red line shows the fitted polynomial function, while the dashed, blue line shows its linear term. The order m of the polynomial is indicated. See Sect. 7.2.1 for details.

as their rotation curves may have complex shapes characterized by a steeply-rising part followed by a decline and a second rise. For some bulge-dominated galaxies from N07, the value of $d_R V(0)$ is rather uncertain, since there may be no data points in the inner radial range where the linear term a_1 is representative of the rotation curve (see Fig. 7.1, bottom-right). Table 7.1 provides the fit results for all the galaxies in our sample.

The error $\delta_{d_{\rm R}V(0)}$ on $d_R V(0)$ is estimated as

$$\delta_{d_{\rm R}V(0)} = \sqrt{\delta_{a_1}^2 + \left(d_{\rm R}V(0)\frac{\delta_i}{\tan(i)}\right)^2 + \left(d_{\rm R}V(0)\frac{\delta_{\rm D}}{D}\right)^2} \qquad (7.2)$$

where δ_{a_1} is the nominal error on the fitted linear term a_1, δ_i is the error on the disk inclination i, and $\delta_{\rm D}$ is the error on the galaxy distance D. $\delta_{\rm D}$ typically

gives a negligible contribution for galaxies with distances derived using the tip of the red giant branch (TRGB) and/or Cepheids (Ceph), whereas it can dominate the error budget for galaxies with distances estimated from the TF relation or the Hubble flow.

7.2.2 The central surface brightness

For the high-quality sample of disk-dominated galaxies, we consider two ways to estimate the central surface brightness: i) the disk central surface brightness $\mu_{\rm d}$, obtained from an exponential fit to the outer parts of the luminosity profile, and ii) the observed central surface brightness μ_0, obtained from a linear extrapolation of the luminosity profile in the inner few arcseconds to $R = 0$ (see Swaters & Balcells 2002). μ_0 takes into account possible deviations from a pure exponential disk. This may carry valuable information on the mass distribution, e.g. if a pseudo-bulge/bar is present, but may also reflect variations in the stellar populations and/or in the internal extinction, e.g. if the star-formation activity is enhanced in the central parts. We use the observed central surface brightness μ_0. Since we are considering disk-dominated galaxies (Sb and later types), we correct μ_0 for inclination; we assume an optically-thin disk. Given the ambiguity in using either μ_0 or $\mu_{\rm d}$, we include the difference $\Delta\mu = \mu_{\rm d} - \mu_0$ in the error δ_{μ_0}. This is estimated as

$$\delta_{\mu_0} = \sqrt{(\Delta\mu/2)^2 + [2.5\log(e)\tan(i)\delta_i]^2}. \tag{7.3}$$

For the galaxies from S09, we use the values listed in Table A.5 of Swaters & Balcells (2002) (Harris R-band). For the galaxies from VS01, we use the surface photometry from Tully et al. (1996) (Cousins R-band). For the galaxies from dB08 and B87, we use the surface photometry from three different sources (in order of preference): Swaters & Balcells (2002) (Harris R-band), Kent (1987) (r-band), and Muñoz-Mateos et al. (2009) (Harris R-band or r'-band). The optical filters are comparable, but there can be systematic differences of $\sim$0.1 mag (within the typical errors). Two galaxies from dB08 (NGC 925 and NGC 7793) and one galaxy from B87 (NGC 5371) have no R-band photometry available and have been excluded, reducing the total sample to 52 objects.

The S0/Sa galaxies from N07 require a different approach, because i) the surface brightness rapidly increases in the central regions due to the presence of a dominant bulge; and ii) several galaxies are at large distances ($\gtrsim$30 Mpc), thus the linear resolution of the optical observations is not very high ($\gtrsim$150 kpc). For these galaxies, Noordermeer & van der Hulst (2007) provide the R-band disk central surface brightness $\mu_{\rm d}$, extrapolated from an exponential fit and corrected for i, and the bulge central surface brightness $\mu_{\rm b}$, extrapolated from a Sersic fit to the inner parts after subtracting the disk contribution. We estimate μ_0 by summing the contributions of $\mu_{\rm d}$ and $\mu_{\rm b}$; the latter value is *not* corrected for i as the bulge is assumed to be spherical. The errors are given by Eq. 7.3, where $\Delta\mu$ is now the difference between μ_0 and the innermost value of μ observed.

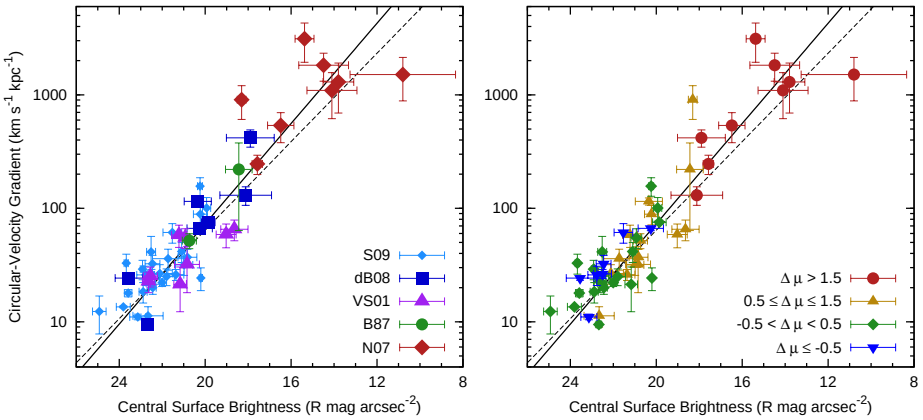

Figure 7.2 – The circular-velocity gradient versus the central surface brightness. The solid and dashed lines show a liner fit to the data points for the total and high-quality samples, respectively. *Left:* galaxies coded by the reference for the rotation curve (S09: Swaters et al. 2009, dB08: de Blok et al. 2008, VS01: Verheijen & Sancisi 2001, B87: Begeman 1987, N07: Noordermeer et al. 2007). *Right:* galaxies coded by the value of $\Delta\mu = \mu_{\rm d} - \mu_0$ (in R mag arcsec^{-2}), that quantifies the "light excess" over an exponential profile.

7.3 The $d_R V(0) - \mu_0$ scaling relation

In Fig. 7.2 (left), we plot μ_0 against $d_R V(0)$ for the total sample of 52 galaxies. There is a clear, striking relation. A linear, error-weighted fit to the data yields

$$\log[d_R V(0)] = (-0.22 \pm 0.02)\,\mu_0 + (6.28 \pm 0.40). \qquad (7.4)$$

As discussed in Sect. 7.2, the values of $d_R V(0)$ for the S0/Sa galaxies from N07 are uncertain. However, it is clear that these bulge-dominated galaxies follow the same trend defined by disk-dominated ones. Fig. 7.2 (left) also shows a linear fit excluding the objects from N07 (dashed line). This gives only slightly different values of the slope (-0.19 ± 0.03) and the intersect (5.70 ± 0.57). Considering the different types of galaxies and the uncertainties involved, the relation shown in Fig. 7.2 is remarkably tight and extended, spanning more than two orders of magnitude in $d_R V(0)$ and four orders of magnitude in μ_0.

The values of the slope and the intersect are likely more uncertain than the formal errors, due to several effects in the determination of $d_R V(0)$ and μ_0. Possible concerns are i) the different linear resolutions (in kpc) of the H I and optical observations, and ii) the effects on μ_0 of internal extinction, recent star-formation, and/or a LINER core. We performed several fits using different methods to estimate μ_0 and $d_R V(0)$, such as calculating V/R at the innermost point of the rotation curve. We obtained slopes always between -0.25 and -0.15, and we think that the actual slope must be constrained between these values.

The scatter around the relation is largely due to observational uncertainties on $d_R V(0)$. Major sources of uncertainties are i) the galaxy distance, ii) the inclination, and iii) the innermost points of the rotation curve (see Eq. 7.2). However, part of the scatter is likely to be intrinsic, partially due to differences in the 3-dimensional (3D) distribution of baryons and in the structural component that defines μ_0 (a disk, a bulge, a bar, or a nuclear star cluster).

To investigate the role played by different structural components, in Fig. 7.2 (right) we plot the same data points coding the galaxies by the value of $\Delta\mu = \mu_{\rm d} - \mu_0$. This quantifies the deviation from an exponential law in the inner parts of the luminosity profile (in R mag arcsec^{-2}). We distinguish between four cases: i) galaxies dominated by a bulge ($\Delta\mu > 1.5$), ii) galaxies with a small central concentration of light ($0.5 \leq \Delta\mu \leq 1.5$) like a pseudo-bulge or a bar, iii) galaxies with an exponential disk ($-0.5 < \Delta\mu < 0.5$), and iv) galaxies with a central light depression ($\Delta\mu \leq -0.5$). The upper-right end of the relation ($\mu_0 \gtrsim 18$ mag arcsec^{-2}) is populated by bulge-dominated galaxies. It is clear that, for these galaxies, the use of $\mu_{\rm d}$ instead of μ_0 would shift them away from the relation, as $\mu_{\rm d} \lesssim$ 19-20 R mag arcsec^{-2} (the "Freeman value", Freeman 1970). On the lower-left end of the relation, instead, one can find both pure exponential disks and galaxies with central light concentrations/depressions. For these disk-dominated galaxies, the use of $\mu_{\rm d}$ instead of μ_0 would still lead to a correlation, but this would have a steeper slope ($\sim$-0.25). For galaxies with similar values of μ_0, $d_R V(0)$ do not seem to depend on the detailed shape of the luminosity profile (simple exponential or with a central light depression/concentration).

7.4 Discussion

The correlation between the central surface brightness μ_0 and the circular-velocity gradient $d_R V(0)$ implies that there is a close link between the stellar density and the gravitational potential in the central parts of galaxies. This holds for both HSB and LSB objects, covering a wide range of masses and asymptotic velocities ($20 \lesssim V_{\rm flat} \lesssim 300$ km s^{-1}).

The relation between the distribution of light and the distribution of mass has been extensively discussed in the past (see Sancisi 2004 and references therein). However, only few attempts have been made to parametrize this relation, notably by S09. Fig. 10 of S09 plots the logarithmic slope between 1 and 2 disk scale-lengths $S_{1,2} = \log[V(2h)/V(h)]/\log(2)$ versus the "light excess" with respect to an exponential disk $\Delta\mu = \mu_{\rm d} - \mu_0$. It shows that a "light excess" (a bulge-like component) corresponds to a "velocity excess" in the rotation curve with respect to the expectations for the underlying exponential disk. The limitation of that parametrization is that it does not capture the dynamical difference between HSB and LSB disks, that are known to have steeply-rising and slowly-rising rotation curves, respectively (e.g. Tully & Verheijen 1997). In Fig. 10 of S09, indeed, both HSB and LSB exponential disks have $\Delta\mu \simeq 0$

and $S_{1,2} \simeq 0.5$. The latter result is due to the fact that $S_{1,2}$ is, by definition, a scale-invariant quantity, that is not expected to depend on μ_0 or $V_{\rm max}$. In contrast, $d_R V(0)$ measures the inner slope of the rotation curve in physical units (km s^{-1} kpc^{-1}) and is directly related to the central dynamical surface density (in $M_\odot$ pc^{-2}), providing insights in the underlying physics, as we now discuss.

For a 3D distribution of mass, the rotation velocity V of a test particle at radius R is given, to a first approximation, by

$$\frac{V^2}{R} = \alpha \frac{G M_{\rm dyn}}{R^2} \tag{7.5}$$

where G is Newton's constant, $M_{\rm dyn} = 4/3\pi R^3 \overline{\rho}_{\rm dyn}$ is the dynamical mass within R, and α is a factor that depends on the detailed mass distribution (for a spherical distribution of mass α=1, while for a thin exponential disk $\alpha \simeq 0.76$ at $R = 0.5 R_0$). For $R \rightarrow 0$, we have

$$\frac{dV}{dR} = \frac{V}{R} = \sqrt{\beta G \rho_{\rm dyn,0}} = \sqrt{\beta G \frac{\rho_{\rm bar,0}}{f_{\rm bar,0}}} \tag{7.6}$$

where $\beta = 4/3\pi\alpha$, $\rho_{\rm dyn,0}$ and $\rho_{\rm bar,0}$ are, respectively, the central dynamical and baryonic mass densities, and $f_{\rm bar,0} = \rho_{\rm bar,0}/\rho_{\rm dyn,0}$ is the baryon fraction in the central regions. Note that $f_{\rm bar,0}$ may strongly differ from the "cosmic" baryon fraction, and can vary widely from galaxy to galaxy, depending on the formation and evolution history. Observationally, we measure μ_0 which is related to $\rho_{\rm bar,0}$ by

$$\mu_0 = -2.5 \log[\rho_{\rm bar,0}\, \Delta z\, (M_{\rm bar}/L)^{-1}] \tag{7.7}$$

where Δz is the typical thickness of the stellar component (either a disk or a bulge) and $M_{\rm bar}/L$ is the baryonic mass-to-light ratio, including molecules and other *dark* baryonic components. Thus, we expect the following relation

$$\log[d_R V(0)] = -0.2\, \mu_0 + 0.5 \log\left(\beta G \frac{M_{\rm bar}/L}{\Delta z\, f_{\rm bar,0}}\right). \tag{7.8}$$

In Sect. 7.3, we mentioned that the slope of our relation is not well-determined due to several uncertainties in the measurements of $d_R V(0)$ and μ_0. However, it is consistent with -0.2 and can be constrained between -0.15 and -0.25. In case the slope would be exactly -0.2, the second term of Eq. 7.8 would be a constant, implying a puzzling fine-tuning between the 3D distribution of baryons (β and Δz), the baryonic mass-to-light ratio ($M_{\rm bar}/L$), and the DM content ($f_{\rm bar,0}$).

Despite the uncertain value of the slope, the results presented here show a clear relation between the central stellar density in a galaxy and the steepness of the potential well (see also Sancisi 2004; Swaters et al. 2011). This implies a

close link between the density of the baryons, regulated by gas accretion, star-formation, and feedback mechanisms, and the central density of the DM halo, together shaping the inner potential well. This may represent a challenge for models of galaxy formation and evolution. Future observational studies may help to better constrain the slope of the relation, while theoretical work should aim to understand its origin.

7.5 Conclusions

We measured the circular-velocity gradient $d_R V(0)$ for a sample of spiral and irregular galaxies with high-quality rotation curves. We found a linear relation between $\log[d_{\rm R} V(0)]$ and the central surface brightness μ_0 with a slope of about -0.2. This is a scaling-relation for disk galaxies that holds for objects of very different morphologies, luminosities, and sizes, ranging from dwarf irregulars to bulge-dominated spirals. This relation quantifies the coupling between visible and dynamical mass in the central parts of galaxies, and shows that the central stellar density closely relates to the inner shape of the potential well.

Acknowledgements

We are grateful to Renzo Sancisi for stimulating discussions and insights. We also thank Erwin de Blok and Rob Swaters for providing us with the high-quality rotation curves. FF aknowledges financial support from PRIN MIUR 2010-2011, project "The Chemical and Dynamical Evolution of the Milky Way and Local Group Galaxies", prot. 2010LY5N2T.

Table 7.1 – Galaxy sample. The galaxies are listed according to the reference for the rotation curve. The last column provides references for the distance and the surface photometry: a) Tully (1988); b) Tully et al. (2009); c) Tolstoy et al. (1995); d) Hoessel et al. (1998); e) Jacobs et al. (2009); f) Thim et al. (2004); g) Karachentsev et al. (2003); h) Saha et al. (2006); i) Tully et al. (1996); j) Nasa/Ipac Extragalactic Database (NED); k) Willick et al. (1997); l) Swaters & Balcells (2002); m) Kent (1987); n) Muñoz-Mateos et al. (2009); o) Bottema (1989); Noordermeer & van der Hulst (2007).

Name	Type	Dist (Mpc)	Method	i (°)	$\mu_{0,R}$ (mag/$''^2$)	$V_{\rm max}$ (km/s)	$d_R V(0)$ (km/s/kpc)	R_{90} (kpc)	m	χ^2_ν	Ref.
(1)	(2)	(3)	(4)	(5)	(6)	(7)	(8)	(9)	(10)	(11)	(12)
Galaxies from Swaters et al. (2009)											
UGC 731	Im	11.8±4.3	TF	57±3	22.5±0.2	74±3	41±15	5.1	3	0.42	a, l
UGC 2455	IBm	6.4±1.2	TF	51±3	20.2±0.1	61±4	24±5	3.3	2	1.23	a, l
UGC 3371	Im	21.9±4.0	TF	49±3	22.9±0.2	86±3	18±4	11.1	3	0.90	b, l
UGC 3711	IBm	8.2±1.5	TF	60±3	19.6±0.8	95±3	...	0.6	...	...	b, l
UGC 3851	IBm	3.4±0.3	Ceph	59±3	22.5±0.2	55±3	22±2	2.4	1	0.63	c, l
UGC 3966	Im	7.4±1.4	TF	41±3	23.4±0.4	50±4	...	1.1	...	...	a, l
UGC 4173	Im	16.7±3.1	TF	40±3	22.7±0.7	57±4	11±2	8.5	2	0.24	a, l
UGC 4305	Im	3.0±0.2	Ceph	40±3	22.5±0.4	37±3	26±2	1.1	1	0.04	d, l
UGC 4325	Sm?	10.0±1.8	TF	41±3	21.5±0.1	93±3	...	1.4	...	...	a, l
UGC 4499	SBdm	12.8±2.4	TF	50±3	21.0±0.4	74±3	32±6	3.7	2	0.01	a, l
UGC 4543	Sdm	30.0±5.5	TF	46±3	20.6±0.7	67±4	...	2.2	...	...	a, l
UGC 5272	Im	6.5±1.2	TF	59±3	22.8±0.4	45±3	26±5	1.4	1	0.42	a, l
UGC 5414	IBm	9.4±1.7	TF	55±3	22.4±0.3	61±2	32±6	2.7	2	0.06	a, l
UGC 5721	SBd?	5.9±1.1	TF	61±3	19.9±0.2	79±3	101±24	1.3	2	2.70	a, l
UGC 5918	Im	7.1±1.3	TF	46±3	23.7±0.1	44±4	33±6	2.6	2	0.20	a, l
UGC 6446	Sd	18.0±3.0	TF	52±3	20.8±0.4	80±2	37±6	6.5	3	0.20	b, l
UGC 7047	Im	4.3±0.1	TRGB	46±3	22.0±0.1	38±4	22±2	1.6	1	0.51	e, l
UGC 7232	Im pec	2.8±0.5	TF	59±3	21.5±0.4	44±3	61±12	0.6	1	1.02	a, l
UGC 7323	SBdm	5.8±1.0	TF	47±3	21.1±0.1	86±4	42±8	2.9	2	1.38	b, l
UGC 7399	SBdm	8.0±1.5	TF	55±3	20.2±0.3	109±2	89±17	4.6	3	1.11	a, l
UGC 7524	Sm	4.3±0.4	Ceph	46±3	21.4±0.4	84±4	26±3	6.2	2	1.17	f, l
UGC 7559	IBm	5.0±0.2	TRGB	61±3	23.6±0.2	33±3	18±1	1.8	1	0.66	e, l

Table 7.1 – continued.

Name	Type	Dist (Mpc)	Method	i (°)	$\mu_{0,R}$ (mag/$''^2$)	$V_{\rm max}$ (km/s)	$d_R V(0)$ (km/s/kpc)	R_{90} (kpc)	m	χ^2_ν	Ref.
(1)	(2)	(3)	(4)	(5)	(6)	(7)	(8)	(9)	(10)	(11)	(12)
UGC 7577	Im	2.6±0.1	TRGB	63±3	23.1±0.4	18±3	11±1	1.5	1	0.09	e, l
UGC 7603	SBd?	10.5±1.7	TF	78±3	21.8±0.4	64±3	25±4	3.8	2	0.29	b, l
UGC 7690	Im	7.5±1.4	TF	41±3	20.3±0.1	61±4	...	0.5	...	...	a, l
UGC 7866	IBm	4.6±0.2	TRGB	44±3	22.4±0.1	33±4	20±2	1.7	1	1.64	e, l
UGC 7916	Im	7.2±2.6	TF	74±3	24.9±0.3	36±3	12±4	2.6	1	0.96	a, l
UGC 7971	Sm	8.0±1.5	TF	38±3	21.4±0.1	45±4	...	1.7	...	...	a, l
UGC 8490	Sm	4.6±0.6	TRGB	50±3	20.2±0.1	80±4	157±29	1.3	3	0.77	g, l
UGC 8837	IBm	7.2±0.1	TRGB	80±3	23.8±0.3	48±3	13±1	3.1	1	0.02	e, l
UGC 9211	Im	14.7±2.7	TF	44±3	22.9±0.1	66±4	29±6	3.2	2	0.06	a, l
UGC 11707	Sdm	15.7±3.0	TF	68±3	21.7±0.7	100±3	36±7	8.0	3	0.36	a, l
UGC 12060	IBm	15.1±2.8	TF	40±3	21.4±0.2	75±4	...	2.2	...	...	a, l
UGC 12632	Sm	9.2±1.7	TF	46±3	22.1±0.6	76±3	27±5	6.0	2	0.70	a, l
Galaxies from de Blok et al. (2008)											
DDO 154	IBm	4.0±0.1	TRGB	66±3	23.5±0.6	50±5	24±1	4.0	2	1.79	e, l
IC 2574	SBm	3.9±0.1	TRGB	53±3	22.7±0.1	78±5	9±1	8.0	1	0.70	e, l
NGC 925	SBd	9.3±0.2	Ceph	66±3	...	120±6	19±1	9.7	2	0.26	h, -
NGC 2403	SBcd	3.1±0.2	Ceph	63±3	20.3±0.6	144±4	115±8	10.2	5	1.12	h, m
NGC 2841	Sb	14.1±0.4	Ceph	74±3	18.1±1.1	324±4	...	3.8	...	...	h, m
NGC 2976	Sc pec	3.6±0.1	TRGB	64±3	20.2±0.6	86±3	67±3	2.1	2	1.27	e, l
NGC 3031	Sab	3.6±0.3	Ceph	59±3	16.4±1.3	260±7	...	2.4	...	...	h, m
NGC 3521	SBbc	11.2±1.8	TF	73±3	18.1±1.2	233±4	130±24	2.6	2	0.64	b, n
NGC 3621	Sd	7.2±0.2	Ceph	65±3	19.8±0.3	159±3	75±3	18.8	5	0.71	h, n
NGC 3627	SBb	12.6±0.5	Ceph	62±3	17.8±1.0	207±11	...	2.7	...	...	h, n
NGC 4736	Sab	4.7±0.1	TRGB	41±3	16.1±1.2	198±5	...	0.4	...	...	e, n
NGC 4826	Sab	4.7±0.1	TRGB	65±3	18.2±0.6	189±27	...	0.2	...	...	e, n
NGC 5055	Sbc	7.9±1.3	TF	59±3	17.9±1.1	212±8	418±72	1.7	3	0.57	b, n

Table 7.1 – continued.

Name	Type	Dist (Mpc)	Method	i (°)	$\mu_{0,R}$ (mag/$''^2$)	$V_{\rm max}$ (km/s)	$d_RV(0)$ (km/s/kpc)	R_{90} (kpc)	m	χ^2_ν	Ref.
(1)	(2)	(3)	(4)	(5)	(6)	(7)	(8)	(9)	(10)	(11)	(12)
NGC 7331	Sb	15.1±0.7	Ceph	76±3	17.7±1.4	268±13	...	3.1	...	...	h, n
NGC 7793	Sd	3.6±0.1	TRGB	50±3	...	118±4	152±9	3.1	4	0.57	e, -
Galaxies from Verheijen & Sancisi (2001)											
NGC 3877	Sc	15.5±3.0	Cluster	76±1	18.6±0.6	171±5	65±13	3.8	2	0.59	i, i
NGC 3917	Scd	15.5±3.0	Cluster	79±2	21.2±0.3	138±5	21±9	5.3	4	0.58	i, i
NGC 3953	SBbc	15.5±3.0	Cluster	62±1	17.0±0.1	234±8	...	4.5	...	...	i, i
NGC 3972	Sbc	15.5±3.0	Cluster	77±1	20.9±0.2	134±5	55±11	4.5	2	0.60	i, i
NGC 4100	Sbc	15.5±3.0	Cluster	73±2	19.0±0.5	195±6	59±14	3.8	2	0.76	i, i
UGC 6399	Sm	15.5±3.0	Cluster	75±2	22.6±0.3	88±5	23±5	3.8	1	2.67	i, i
UGC 6917	SBd	15.5±3.0	Cluster	56±2	21.2±0.3	111±6	58±13	4.5	3	0.86	i, i
UGC 6983	SBcd	15.5±3.0	Cluster	49±1	20.8±0.6	113±4	32±14	5.3	4	0.71	i, i
UGC 7089	Sdm	15.5±3.0	Cluster	80±3	22.5±0.3	79±7	25±5	5.3	2	0.48	i, i
Galaxies from Begeman (1987)											
NGC 2903	SBbc	8.5±1.4	TF	60±3	18.4±0.6	216±3	220±156	2.5	5	2.67	b, m
NGC 3198	SBc	14.5±2.0	Ceph	71±3	20.7±0.3	157±2	52±8	5.3	2	0.88	h, m
NGC 5033	Sc	18.8±3.0	TF	66±1	18.5±0.7	225±8	...	0.9	...	...	b, m
NGC 5371	SBbc	37.8±7.0	TF	53±2	...	242±3	278±65	6.9	4	5.26	a, -
NGC 6503	Scd	5.3±0.6	TRGB	74±2	19.4±0.4	121±2	...	1.3	...	...	g, o
Galaxies from Noordermeer et al. (2007)											
UGC 2916	Sab	63.4±4.4	Vflow	42±3	16.5±0.6	232±4	538±159	1.1	2	1.33	j, p
UGC 2953	Sab pec	21.6±4.0	TF	50±3	14.5±1.2	334±9	1825±505	5.6	10	5.70	b, p
UGC 3205	Sab	48.9±14.7	Vflow	67±3	18.3±0.2	247±4	905±298	3.5	7	0.20	j, p
UGC 3546	SBa	28.4±5.2	TF	55±3	17.2±0.6	267±12	...	0.6	...	...	a, p
UGC 3580	Sa pec	25.1±4.4	TF	63±3	17.6±0.2	131±2	246±48	18.2	10	3.25	b, p
UGC 6786	S0	29.4±10.8	TF	68±3	10.8±2.4	230±6	1510±626	3.9	7	0.55	a, p
UGC 6787	Sab	21.9±4.0	TF	69±3	13.8±0.7	278±12	1298±607	0.4	2	2.54	a, p

Table 7.1 – continued.

Name	Type	Dist (Mpc)	Method	i (°)	$\mu_{0,R}$ (mag/$''^2$)	$V_{\rm max}$ (km/s)	$d_R V(0)$ (km/s/kpc)	R_{90} (kpc)	m	χ^2_ν	Ref.
(1)	(2)	(3)	(4)	(5)	(6)	(7)	(8)	(9)	(10)	(11)	(12)
UGC 8699	SBab	39.4±6.7	TF	73±3	14.1±1.2	205±2	1093±476	0.9	3	2.12	b, p
UGC 9133	Sab	50.5±8.8	TF	53±3	14.3±0.1	312±6	...	0.3	...	...	k, p
UGC 11670	S0/a	14.2±5.2	TF	70±3	15.4±0.4	191±7	3117±1180	0.8	5	0.33	a, p
UGC 11852	SBa?	81.4±14.2	TF	50±3	16.2±0.6	234±10	...	0.4	...	...	k, p

References

Amorisco, N. C. & Bertin, G. 2010, A&A, 519, A47
Begeman, K. 1987, PhD thesis, University of Groningen
Bevington, P. R. & Robinson, D. K. 2003, Data reduction and error analysis for the physical sciences
Bosma, A. 1981, AJ, 86, 1825
Bottema, R. 1989, A&A, 221, 236
Broeils, A. H. 1992, PhD thesis, University of Groningen
Casertano, S. & van Gorkom, J. H. 1991, AJ, 101, 1231
Corradi, R. L. M. & Capaccioli, M. 1990, A&A, 237, 36
de Blok, W. J. G. & McGaugh, S. S. 1996, ApJL, 469, L89
de Blok, W. J. G., McGaugh, S. S., & Rubin, V. C. 2001, AJ, 122, 2396
de Blok, W. J. G., Walter, F., Brinks, E., et al. 2008, AJ, 136, 2648
Freeman, K. C. 1970, ApJ, 160, 811
Garrido, O., Marcelin, M., Amram, P., et al. 2005, MNRAS, 362, 127
Hoessel, J. G., Saha, A., & Danielson, G. E. 1998, AJ, 115, 573
Jacobs, B. A., Rizzi, L., Tully, R. B., et al. 2009, AJ, 138, 332
Karachentsev, I. D., Sharina, M. E., Dolphin, A. E., et al. 2003, A&A, 398, 467
Kent, S. M. 1987, AJ, 93, 816
Márquez, I. & Moles, M. 1999, A&A, 344, 421
McGaugh, S. S., Schombert, J. M., Bothun, G. D., & de Blok, W. J. G. 2000, ApJL, 533, L99
Muñoz-Mateos, J. C., Gil de Paz, A., Zamorano, J., et al. 2009, ApJ, 703, 1569
Noordermeer, E. & van der Hulst, J. M. 2007, MNRAS, 376, 1480
Noordermeer, E., van der Hulst, J. M., Sancisi, R., Swaters, R. S., & van Albada, T. S. 2007, MNRAS, 376, 1513
Noordermeer, E. & Verheijen, M. A. W. 2007, MNRAS, 381, 1463
Palunas, P. & Williams, T. B. 2000, AJ, 120, 2884
Persic, M. & Salucci, P. 1991, ApJ, 368, 60
Rubin, V. C., Burstein, D., Ford, Jr., W. K., & Thonnard, N. 1985, ApJ, 289, 81
Saha, A., Thim, F., Tammann, G. A., Reindl, B., & Sandage, A. 2006, ApJS, 165, 108
Sancisi, R. 2004, in IAU Symposium, Vol. 220, Dark Matter in Galaxies, ed. S. Ryder, D. Pisano, M. Walker, & K. Freeman, 233
Swaters, R. A. & Balcells, M. 2002, A&A, 390, 863
Swaters, R. A., Sancisi, R., van Albada, T. S., & van der Hulst, J. M. 2009, A&A, 493, 871
Swaters, R. A., Sancisi, R., van Albada, T. S., & van der Hulst, J. M. 2011, ApJ, 729, 118
Thim, F., Hoessel, J. G., Saha, A., et al. 2004, AJ, 127, 2322
Tolstoy, E., Saha, A., Hoessel, J. G., & McQuade, K. 1995, AJ, 110, 1640
Tully, R. B. 1988, Nearby galaxies catalog

Tully, R. B. & Fisher, J. R. 1977, A&A, 54, 661
Tully, R. B., Rizzi, L., Shaya, E. J., et al. 2009, AJ, 138, 323
Tully, R. B. & Verheijen, M. A. W. 1997, ApJ, 484, 145
Tully, R. B., Verheijen, M. A. W., Pierce, M. J., Huang, J.-S., & Wainscoat, R. J. 1996, AJ, 112, 2471
van Albada, T. S. & Sancisi, R. 1986, Royal Society of London Philosophical Transactions Series A, 320, 447
Verheijen, M. A. W. 2001, ApJ, 563, 694
Verheijen, M. A. W. & Sancisi, R. 2001, A&A, 370, 765
Willick, J. A., Courteau, S., Faber, S. M., et al. 1997, ApJS, 109, 333

Chapter 8

Conclusions and future prospects

8.1 Summary and highlights

In this Ph.D. thesis, we investigated the structure, dynamics, and evolution of starbursting dwarf galaxies (hereafter blue compact dwarfs, BCDs). We considered 18 nearby objects that have been resolved into single stars by HST, providing their star-formation histories (SFHs) from the modelling of color-magnitude diagrams. For these 18 BCDs, we collected both new and archival 21 cm-line observations. By combining the HST information with H I observations, we could study in detail the possible relations between the starburst and the gas distribution and kinematics. To investigate the evolutionary links between BCDs and other types of low-mass galaxies, we compared the properties of these starbursting dwarfs with those of gas-rich irregulars (Irrs) and gas-poor spheroidals (Sphs). Here we summarize our main results, and discuss prospects for future research.

8.1.1 H I distribution and kinematics in BCDs

BCDs have, on average, higher central H I *densities and more complex* H I *kinematics than typical Irrs.*

The azimuthally-averaged H I surface density profiles of BCDs are different from those of other gas-rich galaxies. The BCDs in our sample have, on average, central H I surface densities a factor of ∼2 higher than typical Irrs (Chapter 4), in overall agreement with previous H I studies. Moreover, the H I distribution over the stellar body is clumpy, and the peak H I column densities can reach very high values, up to ∼50-100 $M_{\odot}$ pc^{-2} in I Zw 18 at a linear resolution of ∼200 pc (Chapter 2). The average extent of the H I disk with respect to the stellar body, instead, is similar for BCDs, Irrs, and gas-rich spirals ($R_{\rm H\,I}/R_{\rm opt} \simeq 1.7$).

Complex H I kinematics are more common in BCDs (∼50%) than in typical Irrs (∼10%); this may be related to stellar feedback and/or to the mechanism that triggered the starburst (interactions/mergers and/or disk instabilities). For 9 galaxies with a regularly-rotating H I disk, we derived rotation curves by building 3D disk models (Chapters 2, 3, and 4). The rotation curves of BCDs typically show a steep rise in the inner parts and a flat part in the outer regions. In 4 galaxies, we also found evidence for radial motions. We do not know the direction of these radial motions, but if we assume that they are an inflow, the inferred gas accretion rates would be ∼1 order of magnitude higher than the current star-formation rates (SFRs). Probably, these radial motions are recent and short-lived, given that their timescales are comparable to the orbital times and the burst durations.

8.1.2 Luminous and dark matter in BCDs

BCDs have both baryonic and gas fractions similar to typical Irrs, suggesting that the starburst does not eject a large fraction of gas out of the potential well.

For BCDs with accurate estimates of the rotation velocity, we calculated the dynamical mass $M_{\rm dyn}$ and the baryonic fraction $f_{\rm bar} = M_{\rm bar}/M_{\rm dyn}$ within the optical radius (Chapter 4). The baryonic mass $M_{\rm bar}$ was estimated using the stellar mass provided by the HST studies of the resolved stellar populations, which depends *only* on the assumed initial mass function (IMF) and on the gas-recycling efficiency. On average, BCDs have $f_{\rm bar} \simeq 0.3$ for a Kroupa IMF and $f_{\rm bar} \simeq 0.4$ for a Salpeter IMF. The average baryonic fraction may increase up to 0.5 if molecules are also taken into account, but one has to rely on indirect estimates of the molecular gas mass.

For 4 galaxies with a regularly-rotating H I disk centered on the stellar body, we decomposed the rotation curves into mass components. In particular, we broke the disk-halo degeneracy by using the stellar masses from the HST observations, under the assumption that the stellar mass-to-light ratio does not vary strongly with radius. We found that baryons (gas and stars) are generally not sufficient to explain the inner rise of the rotation curve, although they constitute $\sim$ 20 to 40% of the total mass within $\sim$2 disk scale-lengths.

Despite the starburst having injected $\sim 10^{56}$ erg in the ISM during the past $\sim$500 Myr, BCDs have both baryonic and gas fractions similar to non-starbursting Irrs. This suggests that *either* BCDs do not expell a large amount of gas out of their potential well, *or* their gas fractions must have been much higher at the beginning of the burst. The former hypothesis seems more likely, given that we found no significant trend between the gas fractions and the starburst properties.

8.1.3 Starbursts and the evolution of dwarf galaxies

BCDs have a strong central concentration of dynamical mass (gas, stars, and dark matter) and likely evolve into "compact" Irrs and/or rotating Sphs; the starburst activity is closely related to the inner shape of the potential well.

BCDs have, on average, steeper rotation curves than typical Irrs (Chapters 2, 3, and 5), indicating that they have a high central dynamical mass density. In Chapter 5, we measured the inner circular-velocity gradient $d_R V(0)$ for 60 low-mass galaxies (including BCDs, Irrs, and rotating Sphs), using H I and/or stellar rotation curves from the literature. For gas-rich dwarfs, we found that $d_R V(0)$ correlates with the central surface brightness μ_0, the mean atomic gas surface density $\Sigma_{\rm gas}$ within the stellar body, and the SFR surface density $\Sigma_{\rm SFR}$. BCDs are in the upper parts of these relations, having high values of $d_R V(0)$. Similarly to spiral galaxies and massive starbursts, the star-formation activity in dwarfs can be parametrized as $\Sigma_{\rm SFR} = \epsilon \Sigma_{\rm gas}/\tau_{\rm orb}$, where $\tau_{\rm orb}$ is the orbital time on the solid-body portion of the rotation curve and ϵ ($\simeq 0.02$) is the fraction of atomic gas converted into stars during every orbit.

We identified several "compact" Irrs, that have values of $d_R V(0)$ similar to BCDs. These compact irregulars are candidate progenitors/descendants of BCDs. Rotating Sphs in the Virgo cluster follow the same correlation between

$d_R V(0)$ and μ_0 as gas-rich dwarfs. They have values of $d_R V(0)$ comparable to BCDs and compact Irrs, suggesting that evolutionary links between these types of dwarfs are possible. The evolutionary sequence BCD → compact Irr → rotating Sph is in overall agreement with the observational evidence, but an *external mechanism* is required to entirely remove the ISM from a compact Irr/BCD, such as ram-pressure stripping or galaxy harassment.

Toomre's criterion for large-scale gravitational instabilities provides a simple explanation for the correlation between $d_R V(0)$ and $\Sigma_{\rm gas}$. Moreover, if the progenitors of BCDs are compact Irrs, their steeply-rising rotation curves would imply high values of the critical surface-density threshold for gravitational instabilities, thus the gas could pile up in the center and reach high surface densities, eventually leading to a starburst. Alternatively, interactions/mergers between Irrs may lead to an overall contraction of their stellar and gaseous disks due to the loss of angular momentum, forming a central mass concentration and triggering the starburst.

8.1.4 Triggering the starburst in BCDs

BCDs have, on average, more asymmetric large-scale H I *distributions than typical Irrs, suggesting that an external mechanism triggered the starburst.*

The large-scale, diffuse H I emission in BCDs shows a broad variety of morphologies (Chapter 6). Several BCDs have heavily disturbed H I morphologies, characterized by strong asymmetries, long filaments, and severe offsets between the stellar and H I distributions, whereas other BCDs show only minor asymmetries. We quantified these asymmetries for both our sample of BCDs and a control-sample of typical Irrs. BCDs generally have more asymmetric H I morphologies than non-starbursting Irrs, indicating that some *external mechanism* triggered the starburst, such as interactions/mergers between gas-rich dwarfs or cold gas accretion from the IGM. Moreover, galaxies hosting an old burst ($\gtrsim 100$ Myr) have more symmetric H I morphologies than galaxies hosting a young burst ($\lesssim 100$ Myr), suggesting that the former ones had enough time to regularize their outer H I distributions since the epoch of the major interaction/accretion event.

We investigated the environment of the BCDs in our sample, and found that most of them have a potential perturber at a projected distance $\lesssim 200$ kpc and with a similar systemic velocity (within ± 300 km s^{-1}). In several cases, however, the lack of accurate distances prevents us to exclude possible background/foreground objects. Three galaxies (I Zw 18, NGC 4449, and NGC 2366) are probably undergoing a minor merger with a smaller companion. Another three galaxies (NGC 1705, NGC 6789, and UGC 9128), instead, appear very isolated and have relatively-regular optical morphologies down to $\mu_{\rm R} \simeq 26$ mag arcsec^{-2}. If these unperturbed stellar morphologies are confirmed by deeper optical images, these galaxies may represent cases of cold gas accretion in the

nearby Universe, although the link to the central mass concentration would remain to be explained.

8.1.5 The coupling between baryonic and dynamical mass

For rotating galaxies, the central baryonic density closely relates to the central dynamical mass density.

For disk galaxies, a close relation exists between the distribution of light and the steepness of the inner rotation curve. We quantify this relation by measuring the inner circular-velocity gradient $d_R V(0)$ for 52 spiral and irregular galaxies with high-quality rotation curves. We found that $d_R V(0)$ correlates with the central surface brightness μ_0 over more than two orders of magnitude in $d_R V(0)$ and four orders of magnitude in μ_0. This is a scaling relation for disk galaxies that holds for objects of very different morphologies, luminosities, and sizes, ranging from dwarf irregulars to bulge-dominated spirals. The $d_R V(0) - \mu_0$ relation indicates that the central stellar density closely relates to the inner shape of the potential well, also for low-luminosity and low-surface-brightness galaxies that are expected to be dominated by dark matter.

8.2 Prospects for future research

8.2.1 Larger samples, better statistics

In this Ph.D. thesis, we studied 18 starbursting dwarf galaxies. The size of this sample allowed us to perform an in-depth study of the gas kinematics in each individual object and, at the same time, to draw general conclusions about starbursting dwarfs as a galaxy population. We remind, however, that accurate dynamical masses could be derived for 11 objects and rotation curves for 9 objects, while detailed mass models could be built for only 4 galaxies. Clearly, a detailed study of a larger sample of BCDs would provide better statistics and strengthen the results presented here. Moreover, when we compared the dynamical properties of gas-rich and gas-poor dwarfs, we considered only 8 Sphs, given that stellar rotation curves and R-band structural parameters were available in the literature for a limited number of objects. On-going and future studies of the stellar kinematics in Sphs will provide larger datasets, and allow us to make a more extensive comparison between the dynamical properties of gas-rich and gas-poor dwarfs. In particular, larger galaxy samples are needed to investigate whether the dynamical properties of BCDs, Irrs, and rotating Sphs show any dependence on the environment.

8.2.2 Star-formation histories of compact irregulars

The compact Irrs identified in Chapter 5 are candidate progenitors/descendants of BCDs. To further investigate their relation with starbursting dwarfs, it

would be interesting to resolve them into single stars and derive their recent SFH. For the nearest objects ($D \lesssim 5$ Mpc), this can be achieved with HST observations, whereas for the most distant galaxies we should wait for next-generation facilities, such as the *European Extremely Large Telescope* (E-ELT). The compact Irr UGC 7232 (NGC 4190) has already been observed with HST by the ANGST project, but its recent SFH has not been studied in detail. Alternatively, one may attempt to constrain the recent SFH of compact Irrs by a detailed modelling of their spectral energy distribution (from far-UV to radio wavelengths) and/or by fitting stellar populations synthesis models to high-quality integrated spectra, although these techniques would provide recent SFHs that are less accurate than those from resolved stellar populations.

8.2.3 Searching for tidal features with deep photometry

The disturbed H I morphologies of BCDs suggest that some external mechanism triggered the starburst, such as interactions/mergers between gas-rich dwarfs or direct gas infall from the IGM. It would be useful to obtain very deep optical images for these objects (down to $\mu_{\rm B} \simeq 29 - 30$ mag arcsec^{-2}) to search for possible stellar tidal features and/or faint, low-surface-brightness companions. If these galaxies would still show *no* signs of tidal interactions at these low surface brightness levels, cold gas accretion would then be the most likely triggering mechanism.

8.2.4 The slope and scatter of the $d_R V(0) - \mu_0$ relation

The slope and the intrinsic scatter of the $d_R V(0) - \mu_0$ relation are not very well constrained. The situation can be improved in several ways:

1. In Chapter 7, we considered 52 galaxies with high-quality and high-resolution rotation curves from the literature. Clearly, more objects would improve our statistics and help to constrain the slope of the relation. In particular, only a few rotation curves were available for bulge-dominated galaxies. These objects lie in the top-right part of the relation and are crucial to constrain its slope. It would be helpful, therefore, to derive high-quality rotation curves for a large sample of bulge-dominated spirals and/or lenticulars, possibly using integral-field spectroscopy.

2. The errors on $d_R V(0)$ are generally dominated by distance uncertainties. More accurate distances (from Cepheids and/or the tip of the red giant branch) would substantially reduce the erros on $d_R V(0)$ and, possibly, the scatter along the relation. For the most distant objects, however, the Tully-Fisher relation would still be the only distance indicator available, thus improvements in its calibration are of great interest.

3. We estimated μ_0 from R-band observations. We made this choice because R-band surface brightness profiles were available from the literature for most of the galaxies. Surface brightness profiles in the K-band or at 3.6 μm would provide a better proxy for the central stellar density. This would improve our estimate of μ_0 and, possibly, reduce the scatter along the relation due to differences in dust attenuation and/or stellar populations.

In our opinion, the slope and the scatter of the $d_R V(0) - \mu_0$ relation provide crucial information on the link between baryonic and dynamical mass in the central parts of galaxies. Their exact values could put strong constrains on models of galaxy formation in a ΛCDM cosmology, as well as on alternative theories such as MOND. Future studies, therefore, should aim at improving our understanding of this relation, both from an observational and a theoretical perspective.